EXAMINATION OF THE STRUCTURE AND EVOLUTION OF ION ENERGY PROPERTIES OF A 5 kW CLASS LABORATORY HALL EFFECT THRUSTER AT VARIOUS OPERATIONAL CONDITIONS

by

Frank Stanley Gulczinski III

A dissertation submitted in partial fulfillment
of the requirements for the degree of
Doctor of Philosophy
(Aerospace Engineering)
in The University of Michigan
1999

Doctoral Committee:

Associate Professor Alec D. Gallimore
Professor Ronald M. Gilgenbach
Professor Tamas I. Gombosi
Dr. Gregory G. Spanjers, U. S. Air Force Research Laboratory

We are dreamers, shapers, singers, and makers.
We study the mysteries of laser and circuit, crystal and scanner,
holographic demons and invocations of equations.
These are the tools we employ and we know many things.

Elric to Captain Sheridan in Babylon 5: "The Geometry of Shadows"

ACKNOWLEDGMENTS

John Donne wrote, “No man is an island, entire of itself”, and as no man is an island, no dissertation is ever the work of one man alone. There are many co-workers, colleagues, and friends without whose assistance and support this dissertation would not be possible. First, I’d like to thank my advisor and the director of PEPL, Professor Alec Gallimore. He introduced me to the wonderful world of electric propulsion and let me loose in the finest university electric propulsion lab in the nation. It’s not just the facilities that make PEPL special, but also the other students I’ve had a chance to work with. Over the years, they have included: James Haas, Matt Domonkos, Dr. Colleen Marrese, Sang-Wook Kim, George Williams, Jon Van Noord, Dr. Sven “Check your Grounding” Bilén, Dr. Shawn Ohler, Dr. Doug Carlson, Dr. John Foster, Shane Malone, Krista Campbell, and the new generation of PEPL “whiz-kids”: Rich Hofer, Tim Smith, and Peter Peterson. Time spent working with them on projects, both technical and non-technical, made my experiences here even more valuable. Special thanks to Dr. Brad King for all of his assistance with the MBMS and the “dark art” of time-of-flight mass spectroscopy. I’d also like to thank the Department of Aerospace Engineering’s technical and administrative staff, including Dave McClean, Tom Griffin, Gary Gould, Warren Eaton, Terry Larrow, Margaret Fillion, Bonnie Willey, Caroline Rehberg, and Kenna Gaynor for helping me to build and purchase the equipment necessary for my thesis.

I’d like to thank the other members of my dissertation committee: Professor Tamas Gombosi, Professor Ronald Gilgenbach, and Dr. Gregory Spanjers of the Air Force Research Laboratory, for taking the time to help me turn my thesis dream into a reality.

Financial support for my work came from a number of sources, most notably the Air Force Office of Scientific Research under Dr. Mitat Birkan, and the Air Force Research Laboratory under Dr. Ronald Spores. As an Air Force Palace Knight, I had the opportunity to work with the talented personnel of the Air Force Research Laboratory's Electric Propulsion Lab at Edwards Air Force Base, CA; including my mentor – Dr. Ronald Spores, Dr. Greg Spanjers, Dr. Keith McFall, Mr. Daron Bromaghim, Mr. Alan Sutton, Mr. Dennis Tilley, Mr. Jamie Malak, Mr. William Hargus, Captain Jason LeDuc, and my supervisors – Dr. Robert Cohn, Mr. Jeff Veselenak, and Dr. Leslie Perkins. I'd also like to thank Mr. Michael Patterson and NASA's John H. Glenn Research Center at Lewis Field for their generous equipment loans.

On a personal level, I'd like to thank my family for their support. My parents, Frank and Tina Gulczinski, and my grandparents, Jacob and Edna Cipriani and Frank and Marie Gulczinski, provided me with the upbringing and motivation that made all of this possible. Finally, I'd like to thank my fiancée Jill-Renee Winter for being my emotional rock during the most frustrating and exciting year of my life.

Once again, thanks to everyone. It's been a great decade and one heck of a ride.

F.S.G. III

August 17, 1999

PREFACE

This thesis represents an effort to design, build, and characterize a 5 kW class Hall thruster for laboratory work. Particular attention was paid to plume ions because they cause interaction issues for satellite manufacturers and users due to their potential for damaging spacecraft surfaces and interfering with spacecraft operations.

A brief discussion of the history and physics of electric propulsion is provided, with more detail given for Hall thrusters. A procedure for Hall thruster design was developed based on Russian thruster design equations and a parameter study of existing commercial Hall thrusters. This method was used to design the University of Michigan / United States Air Force P5 5 kW class Hall thruster for experimental work. This thruster was designed for easy diagnostic access and modification. Performance measurements of the P5 indicated that it operated on par with commercial thrusters.

To further characterize and analyze the ion acceleration structure of the P5, an extensive study of ion energy distributions and ionic species composition was made using the Molecular Beam Mass Spectrometer (MBMS), a time-of-flight mass spectrometer with a 45-degree electrostatic energy analyzer. Measurements were taken at various angles with respect to the thruster at two axial locations in order to gain insight into the acceleration structure and how it is affected by the Hall thruster's annular configuration. These measurements were performed at several operating conditions to investigate how changes to the discharge voltage and current affected the acceleration structure. The effects of the facility on the data were also investigated.

Ion energy distribution measurements indicated an overall inward focus to the plume of the P5, with many ions accelerated from the annular discharge chamber across centerline of the thruster. This structure was consistent at all thruster operating conditions. Time of flight measurements indicated that the plume was composed primarily of singly ionized xenon, with detectable fractions of doubly, triply, and quadruply ionized xenon. It was found that by sampling the plasma in the near field, the effects of interactions with background neutral xenon could be minimized. Comparisons of the results with those obtained using laser induced fluorescence indicate agreement once the proper transformation of parameters is employed

Two appendices are included. This first is a mission analysis study that identified the 5 kW Hall thruster as a prime candidate for primary propulsion for satellite orbit transfer missions. The second contains the engineering drawings for the P5.

TABLE OF CONTENTS

LIST OF FIGURES

LIST OF TABLES

NOMENCLATURE*

a	Theoretical Maximum Efficiency	[-]
A	Anode Flow Area	[m^2]
b	Efficiency Parameter	[$(m/s)^2$]
b_{ch}	Width: Discharge Chamber	[mm]
b_m	Width: Magnetic Pole Separation	[mm]
b_o	Width: Ion Beam	[mm]
$\mathbf{B}$	Magnetic Field	[T] or [Gauss]
B_r	Radial Magnetic Field	[Gauss]
B_{rmax}	Maximum Radial Magnetic Field	[Gauss]
B_z	Axial Magnetic Field	[Gauss]
$C_{feedback}$	A250 Feedback Capacitance	[F]
d	Energy Analyzer Plate Separation	[m]
d_{ch}	Discharge Chamber Diameter	[mm]
d_{gate}	Electrostatic Gate Length	[m]
d_s	Sampling Skimmer Diameter	[m]
d_{tof}	Time of Flight Path Length	[m]
e	Electron Charge	[1.602×10^{-19} C]
$\mathbf{E}$	Electric Field	[V/m]
E_i	Ion Kinetic Energy	[J] or [eV]

* Nomenclature for Chapters 1 – 7 only. Nomenclature for Appendix A is not included.

E_{peak}	Ion Kinetic Energy where Signal Intensity is Maximum	[J]
E_{prod}	Ion Production Energy	[eV]
E_t	Ion Kinetic Energy where Signal Intensity is e^{-1} times Maximum	[J]
f	A250 Frequency Response	[s^{-1}]
f_i	Ion Species Fraction	[-]
$f(E_i)$	Maxwellian Ion Energy Distribution	[-]
$f(v_i)$	Maxwellian Ion Velocity Distribution	[-]
F_i	Overall Ion Species Fraction	[-]
g	Gravitational Acceleration	[9.806 m/s^2]
I_{BEAM}	Beam Current	[A]
I_{CEM}	Channel Electron Multiplier Output Current	[A]
I_D	Discharge Current	[A]
I_i	Species Ion Current	[A]
I_{sp}	Specific Impulse	[s]
I_{sp}^{1+}	Specific Impulse, Singly Charged Ions Only	[s]
$\mathbf{j}$	Electric Current	[A]
k	Boltzmann's Constant	[$1.38*10^{-23}$ J/K]
K_1	Charge Exchange Cross Section Constant	[-]
K_2	Charge Exchange Cross Section Constant	[-]
K_{45}	45 Degree Energy Analyzer Constant	[-]
l	Energy Analyzer Length	[m]
L_a	Length: Front of Magnetic Pole to Anode	[m] or [mm]
L_b	Length: Ionization Region	[mm]
L_c	Length: Maximum Radial Magnetic Field	[mm]

	to ½ Maximum Radial Magnetic Field	
L_{ch}	Length: Discharge Chamber	[mm]
m	Propellant Mass	[kg]
$\dot{m}_a$	Anode Mass Flow Rate	[kg/s] or [sccm]
$\dot{m}_n$	Neutral Mass Flow Rate	[kg/s]
m_e	Electron Mass	[$9.11*10^{-31}$ kg]
m_i	Ion Mass	[kg]
m_p	Proton Mass	[$1.67*10^{-27}$ kg]
m_n	Neutral Mass	[kg]
M_i	Atomic Mass Number	[AMU]
M_{max}	Mass of Heaviest Species	[AMU]
n	Number Density	[m^{-3}]
n_n	Neutral Number Density	[m^{-3}]
p	Pressure	[Pa]
P_{coll}	Collisional Probability	[-]
P_D	Discharge Power	[W]
q_i	Ion Unit Charge	[-]
q_{MAX}	Charge of Most Ionized Species	[-]
$R_{feedback}$	A250 Feedback Resistance	[Ω]
s	Electrostatic Gate Width	[m]
S	Collisional Path Length	[m]
t	Thrusting Time	[s]
t_d	Electrostatic Gate Transverse Time	[s]
t_{gate}	Electrostatic Gate Opening Time	[s]
$t_{gate\text{-max}}$	Maximum Electrostatic Gate Opening Time	[s]
$t_{gate\text{-min}}$	Minimum Electrostatic Gate Opening Time	[s]
t_{tof}	Time of Flight Time	[s]

T	Thrust	[N]
T^{1+}	Thrust, Singly Charged Ions Only	[N]
T^{*}	Temperature	[K]
T_i	Ion Temperature	[eV]
v	Exhaust Velocity	[m/s]
v_{drift}	Maxwellian Drift Velocity	[m/s]
v_i	Ion Velocity	[m/s]
v_n	Neutral Velocity	[m/s]
v_r	Relative Velocity	[m/s]
V_{A250}	A250 Amplifier Output Voltage	[V]
V_c	Cathode Voltage	[V]
V_D	Discharge Voltage	[V]
V_{gate}	Electrostatic Gate Voltage	[V]
V_i	Accelerating Potential	[V]
V_p	Energy Analyzer Pass Voltage	[V]
V_{peak}	Value of Ion Energy/Unit Charge where Signal Intensity is Maximum	[V]
V_t	Value of Ion Energy/Unit Charge where Signal Intensity is e^{-1} times the Maximum	[V]
w	Energy Analyzer Entrance Slit Width	[m]
x	Energy Analyzer Coordinate	[m]
y	Energy Analyzer Coordinate	[m]
y_{gate}	Electrostatic Gate Beam Deflection	[m]
z	Axial Coordinate	[m]
b	Maxwellian Distribution Parameter	$[(m/s)^{-2}]$
Dt_{tof}	Time Between Arrival of Time of Flight Peaks	[s]

DV_i	Energy Analyzer Error Term	[V]
h	Thruster Efficiency	[-]
h^{1+}	Thruster Efficiency, Singly Charged Ions Only	[-]
q	Energy Analyzer Entrance Angle	[degrees]
l	Mean Free Path	[m]
r_n	Neutral Density	[kg/m^3]
s	Collisional cross Section	[m^2]

LIST OF APPENDICES

CHAPTER I

ELECTRIC PROPULSION AND THRUSTER DESIGN

The ideas of electric propulsion are not new. The basic concepts were first referred to by Robert Goddard just after the turn of the century.[1] Serious research began in the 1950's in the United States and the former Soviet Union. However, it was primarily in the 1990's that the technology began to emerge from the laboratory to enter the commercial arena. This occurred for a combination of reasons including the availability of high power satellite systems capable of providing the power necessary for on-orbit electric propulsion, increased competition among satellite operators, and an influx of innovative ideas from the former Soviet Union made possible by the end of the Cold War.

1.1. Overview of Electric Propulsion

Electric propulsion is a type of rocket propulsion for space vehicles and satellites, which utilizes electric and/or magnetic processes to accelerate a propellant to a much higher velocity than chemical rockets can using combustion. Whereas combustion is limited by the energy stored within the chemical bonds of the propellant, electric propulsion is limited only by the on-board power available to the thruster and by the material limits of the thrusters themselves. As propellant velocity is increased, so is the specific impulse, I_{sp}, of the engine. Specific impulse is a unit of merit for rocket propulsion that essentially measures the rocket's fuel efficiency. It is defined as the total impulse (the rocket's thrust multiplied by the thrusting time) per unit propellant mass:

EQN 1.1

$$I_{sp} = \frac{T}{g}\frac{t}{m} = \frac{v}{g}$$

where v is the exhaust velocity, T is the thrust, t is the thrusting time, m is the propellant mass, and g is the gravitational acceleration. The specific impulses for various electric propulsion thrusters and for state of the art chemical orbital maneuvering systems are given in Table 1.1. Descriptions of the various types of electric propulsion will be given in Section 1.2.

Thruster Type	Specific Impulse Range
On-Orbit Chemical Propulsion	220 - 315 seconds
Resistojet	300 seconds
Arcjet	500 - 1000 seconds
Pulsed Plasma Thruster	850 seconds
Hall Thruster	1000 - 3000 seconds
Ion Engine	2000 - 4000 seconds
Magnetoplasamadynamic Thruster	3000 - 6000 seconds

Table 1.1. Specific Impulses of Various Orbital Maneuvering Systems

Because of its higher specific impulse, an electric propulsion system can perform the same orbital maneuver as a chemical system while using less on-board propellant. The concomitant reduction in required propellant mass results in increased payload mass capability. This makes electric propulsion very attractive for orbital insertion and orbit maintenance of reconnaissance and communications satellites for a number of reasons. By reducing the amount of propellant needed to perform a given maneuver, a satellite can increase the number of maneuvers possible – or conversely the lifetime of the satellite – with the same overall propellant mass. Alternatively, the propellant mass can be decreased to maintain the same satellite lifetime, allowing additional payload hardware to be added while keeping the same total satellite mass. Of course, a combination of these two options is possible, depending on the needs of the satellite operator. A third option is to decrease the total overall mass of the satellite in order to launch it using a smaller (and less expensive) launch vehicle – a change that can save tens if not hundreds of millions of dollars per launch. A more detailed examination of electric propulsion missions is included in Appendix A.

There are three major obstacles to the widespread use of electric propulsion for on-orbit missions. First, the satellite must provide the power needed for the electric propulsion system. For a low earth orbit (LEO) to geosynchronous earth orbit (GEO) transfer, power levels on the order of 15 to 20 kW are required for a satellite launched by a medium launch vehicle such as a Delta II or Atlas IIAS with launch masses on the order of 4000 to 8000 kg.[2] Second, because of the lower mass throughput of an electric propulsion thruster, the thrust is lower than for a chemical system. This results in longer trip times for the same mission. For LEO to GEO transfers, calculations show that trip times on the order of 180 to 360 days would be practical. However, given the dramatic increases in payload mass delivered, this type of delay may be practical for some satellite users. The following chart shows the mass delivered to GEO for various launch vehicles and trip times with a comparison to chemical propulsion systems.

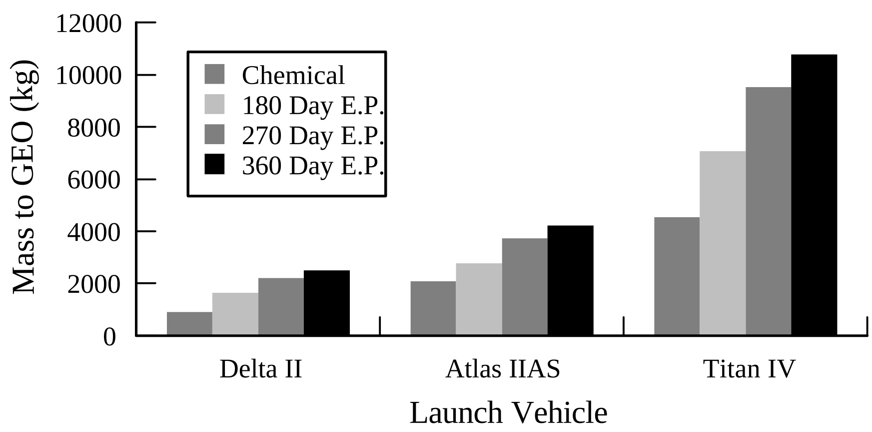

Figure 1.1. Mass Delivered from LEO to GEO for Chemical Systems and Electric Propulsion

It should be noted that the LEO to GEO transfer is one of the extreme cases for on-orbit electric propulsion. Other missions, including the use of electric propulsion thrusters for circularizing an orbit established by chemical propulsion and for stationkeeping of LEO and GEO satellites have been studied and the power and time requirements for these missions are far less strenuous.

The third obstacle to electric propulsion is concern over the effects that an electric propulsion system may have on the satellite that it is maneuvering. Because the plume of an electric propulsion thruster is composed of highly energetic charged particles, plume impingement on a satellite surface may damage it. This thesis is dedicated to quantifying the distribution of ion concentration and energy within a plume and understanding how this is related to the creation of ions within the thruster for one of the most promising candidates for electric propulsion missions – the 5 kW class Hall effect thruster.

1.2. Physics of Electric Propulsion

There are three basic types of electric propulsion devices. They are classified, based on the method used for propellant acceleration; as electrothermal, electrostatic, and electromagnetic.

Electrothermal thrusters are those in which propellant acceleration is achieved through electrical heating. The two basic types are the resistojet and the arcjet. The resistojet is essentially an enhanced chemical thruster in which electrical heating is used to further expand and accelerate propellant that has already undergone a chemical reaction. In an arcjet, the propellant passes through an electric arc that heats the propellant before it expands out of a nozzle. The typical propellants for both types of thrusters are light compounds such as hydrazine (N_2H_4) and ammonia (NH_3), though water resistojets have also been developed. These were chosen because of their use in chemical propulsion systems, allowing a resistojet or arcjet to be retrofitted to an existing system with minimum alterations.

Electrostatic systems are those in which an electric field is used to accelerate an ionized propellant. There are two basic types: the ion engine and the Hall thruster. The Hall thruster is the primary emphasis of this thesis – its history and operation will be discussed in Sections 1.3 and 1.4. Ion engines were developed at NASA's Lewis Research Center (now the John H. Glenn Research Center at Lewis Field) in the late 1950's under the guidance of Dr. Harold Kaufman.[3] In an ion engine, the propellant is injected into a discharge chamber where it is ionized by electron bombardment. The ionized propellant is then accelerated through a series of charged grids to provide thrust. A second cathode outside the engine provides electrons to neutralize the propellant. The original models used primarily mercury or cesium for propellants because these elements are heavy, which maximizes thrust per input power and reduces neutral propellant losses, and have low ionization potentials, which enhances the overall efficiency of the engine. In the 1980's, emphasis shifted to xenon and other noble gases because of concern over spacecraft contamination and environmental issues during ground testing. As part of its New Millennium program, NASA has developed NASA's Solar Electric Propulsion Technology Application Readiness (NSTAR) engine for use on the first New Millennium mission, Deep Space 1.[4]

Electromagnetic thrusters are those in which crossed electric and magnetic fields result in a $\mathbf{j} \times \mathbf{B}$ acceleration on an ionized propellant. Electromagnetic thrusters run the gamut of power levels from very low to very high power. At the low power end is the pulsed plasma thruster, which typically operates at 30 W or less (average power) and is used for fine repositioning of small satellites. In the pulsed plasma thruster, Teflon is ablated from a solid block and accelerated by crossed electric current and a self-induced magnetic field. The high end of the power spectrum is the steady state magnetoplasmadynamic (MPD) thruster, which operates in the range of hundreds of kilowatts to megawatts. MPD thrusters accelerate propellant ions using crossed electric current and self-induced and/or applied magnetic fields. Early work concentrated on lithium as a propellant, but this work has been mostly abandoned in the west for environmental reasons, although Russian engineers continue to conduct experiments with 500 kW lithium MPD thrusters. Work in the west continues using other propellants because, if the power is available, MPD thrusters are excellent candidates for manned exploration of the solar system.

1.3. History of Hall Effect Thruster Development

Initial work on Hall-effect thrusters began in the 1960's in the United States and the former Soviet Union. Work in the United States aimed at producing a thruster capable of operating in the range of 5000 to 10000 s specific impulse. This range was of interest due to projections of the availability of very high specific power nuclear power sources for use on manned interplanetary missions. In this specific impulse range, ion production efficiency is low due to the highly energetic nature of electrons backflowing to the anode. Because of these problems in achieving the same levels of efficiency reached by the ion engine, work ceased in the United States around 1970.[5]

In the Soviet Union work continued on both high-power Hall thrusters for interplanetary missions and low power models for use as ion accelerators and aboard earth orbiting satellites.[6] Work on the ion acceleration mechanism led to improvements in efficiency and further research and development efforts. Two basic types of Hall thrusters were developed: the stationary plasma thruster (SPT), shown in Figure 1.2, developed under the leadership of A.I. Morozov at the Kurchatov Institute, and the thruster with anode layer (TAL), shown in Figure 1.3, developed under the leadership of A.V. Zharinov at TSNIIMASH.[7] Details on the differences between these types of Hall thrusters will be presented in Section 1.5.

The first flight test of a Hall thruster was of a 60 mm stationary plasma thruster (designated SPT-60) on board the Soviet Meteor spacecraft in February 1972. Approximately one hundred other stationary plasma thrusters of various sizes, including the SPT-50, SPT-70, and SPT-100 (the numerical designation in the name of a SPT refers to the outer diameter of its discharge chamber in millimeters), were flown on Soviet spacecraft over the next 20 years. With the end of the Cold War, this technology became available for evaluation and use in the west. Though there was initial skepticism over the claims of Soviet scientists, evaluation by western experts in the Soviet Union showed that these thrusters met or exceeded the claims of their developers. Initial work in the United States to further quantify SPT and TAL performance and flight qualify them for western spacecraft was done primarily at the NASA Lewis Research Center[8] and the Jet Propulsion Laboratory.[9]

Initial interest in the west concentrated on the 1.5 kW class of Hall thrusters. These thrusters, including the SPT-100, the D-55 TAL, and the T-100 SPT, have typical performance parameters of approximately 1600 s specific impulse, 80 mN thrust, and an efficiency of 50%. The efficiency is defined as the ratio of the power converted to thrust to the discharge power:

EQN 1.2
$$h = \frac{\tfrac{1}{2}T^2 / \dot{m}_a}{P_D} = \frac{\tfrac{1}{2}T^2 / \dot{m}_a}{V_D I_D} = \frac{\tfrac{1}{2} T I_{sp} g}{V_D I_D} .$$

Several thrusters of this class have been flight qualified, and in the year 2000 a 1.5 kW Hall thruster will be used for stationkeeping on a GEO communications satellite. They are also under consideration for stationkeeping on constellations of LEO communications satellites. With the 1.5 kW class thrusters reaching an operational stage, research has shifted toward the development of thrusters for other missions, including sub-kilowatt thrusters for small satellites and 5 kW or larger Hall thrusters for orbit transfer missions.

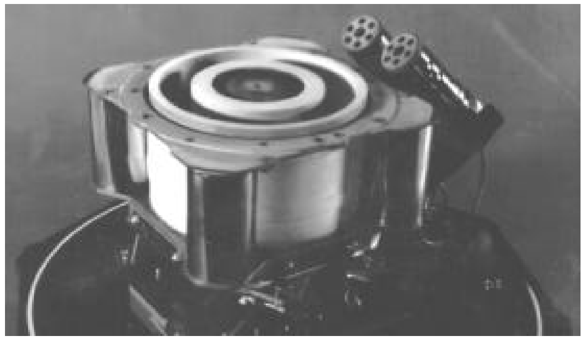

Figure 1.2. SPT-100 Stationary Plasma Thruster

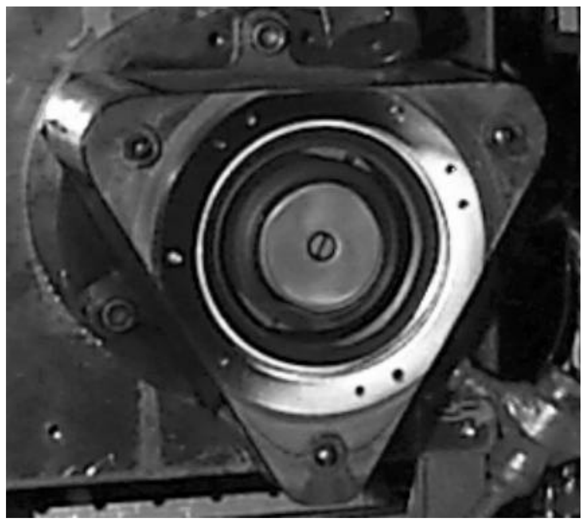

Figure 1.3. D-55 Thruster with Anode Layer

1.4. Physics of the Hall Thruster

The Hall thruster is sometimes referred to as a gridless ion engine. Though this description is far from completely accurate, it does provide a good starting point for describing their operation. Please refer to Figure 1.4 during this discussion. There are three fundamental components to a Hall thruster. First, there is an electrical circuit consisting of an annular anode and a cathode located outside the thruster proper. In most cases, the anode also acts as the propellant distribution device. Second, there is a magnetic circuit, consisting of inner and outer magnetic cores and pole pieces (inner and outer are with respect to the anode) which creates a magnetic field perpendicular to the annulus. Finally, there is a discharge region, downstream of the anode, where injected propellant is ionized and accelerated. The propellant is typically xenon, but other noble gases such as krypton and argon have also been used. In the SPT, this area is enclosed in a ceramic discharge chamber, whereas in the TAL it is surrounded by conducting walls at anode potential. Common Hall thruster terminology refers to the direction from the anode to free space as axial, the direction that the primary magnetic field exists in as radial, and the direction around the discharge chamber as azimuthal.

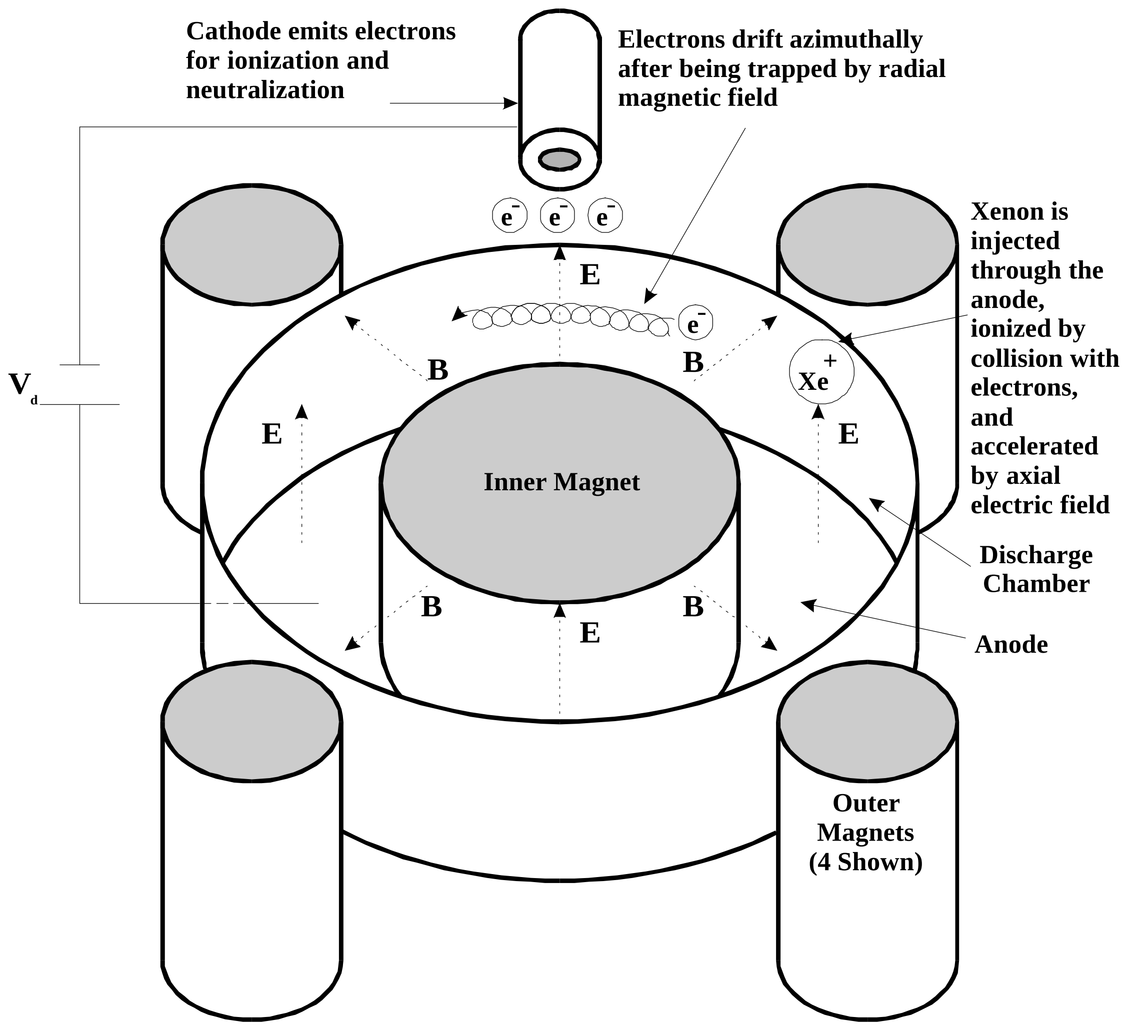

Figure 1.4. Hall Thruster Physics

To operate a Hall thruster, the magnetic circuit creates a magnetic field in the radial direction while an axial electric field is created between the anode and cathode. The presence of these crossed fields traps electrons emitted from the cathode, which then gyrate around the magnetic field lines while drifting azimuthally around the discharge region. This azimuthal drift is the result of the crossed radial magnetic and axial electric fields and is known as the Hall effect. It is caused by the fact that the electron is gyrating in a plane parallel to the electric field. The resulting gyroradius is larger when the electron is being accelerated by the electric field (moving toward the anode) than when it is being decelerated by it (moving away from the anode), giving a net azimuthal drift. Propellant atoms introduced from (or near) the anode collide with these electrons and become positive ions. These ions see a potential variation in the axial direction between the anode and the "virtual cathode" created by the trapped electrons and accelerate. It is because of this process that Hall thrusters are sometimes referred to as gridless ion engines. The velocity of the ions is proportional to the square root of the accelerating potential that they experience and is given by:

EQN 1.3
$$v_i = \sqrt{\frac{2q_i e V_i}{m_i}} \,.$$

Electrons are knocked out of their orbits by collisions with the walls and other particles and flow to the anode to complete the discharge circuit. Additional electrons emitted from the cathode are used to neutralize the propellant ions to prevent spacecraft charging.

The key to the proper operation of a Hall thruster is the design of the magnetic field and how it relates to the rest of the thruster's geometry. The strength of the magnetic field must be such that electrons are trapped within the discharge chamber while the ions are allowed to escape. This is ensured by having the length of the discharge region, L_a, be greater than the electron gyroradius and much less than the ion gyroradius:

EQN 1.4
$$\frac{\sqrt{2m_e V_d / e}}{B} < L_a << \frac{\sqrt{2m_i V_d / q_i e}}{B}.$$

This relationship will be critical to thruster scaling discussed in Section 1.5.

Though the crossed electric and magnetic fields do have an effect on the ions, providing them with a small azimuthal velocity, the axially directed electric field provides the useful component of thrust. It is for this reason that the Hall thruster is classified as an electrostatic device rather than an electromagnetic device.

The shape of the magnetic field is of prime importance to the stable operation of the Hall thruster. The necessary criteria for stable ion flow is that the magnetic field increase in the axial direction, $dB/dz > 0$.[10] The maximum of the magnetic field marks the end of the acceleration region and, by virtue of the design of the magnetic circuit, it should be located between the inner and outer poles. This field structure is shown in Figure 1.5. Other magnetic field structures, such as that found in an end-Hall thruster[11] do not meet this criterion, and therefore these thrusters cannot attain the levels of stability and performance obtained by SPT and TAL type Hall thrusters. When electrons are trapped within the magnetic field their ability to escape through collisions, especially wall collisions, will be inversely proportional to the strength of the magnetic field. This is seen in EQN 1.4, which shows that the gyroradius decreases as the field increases making a collision with the walls less likely. Therefore, the electrons will concentrate at or near the point of maximum radial magnetic field. Since the electrons are the carriers of potential variation, most of the change in potential will occur near the location where the magnetic field is maximum. This potential distribution is shown in Figure 1.6.

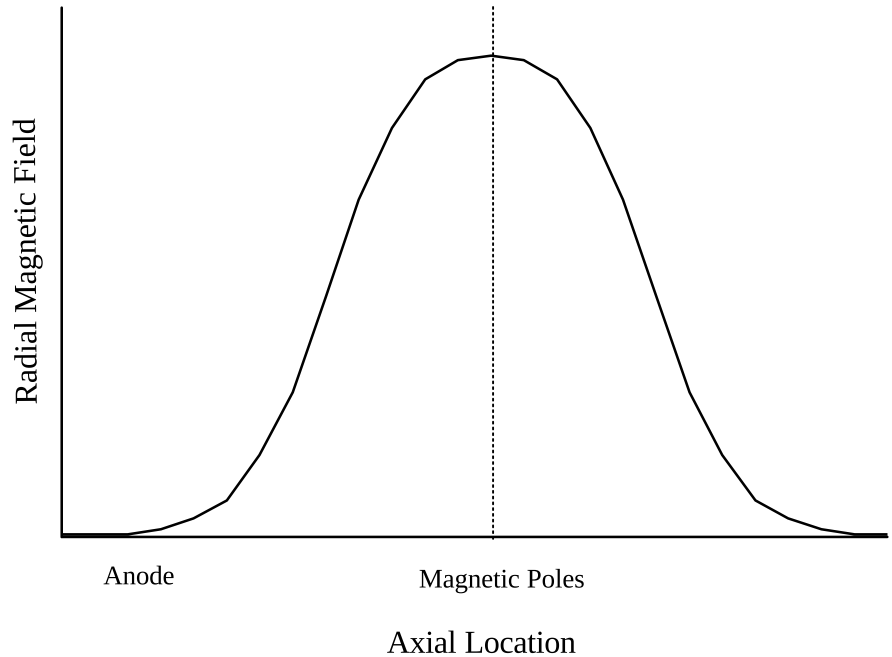

Figure 1.5. Idealized Radial Magnetic Field Distribution

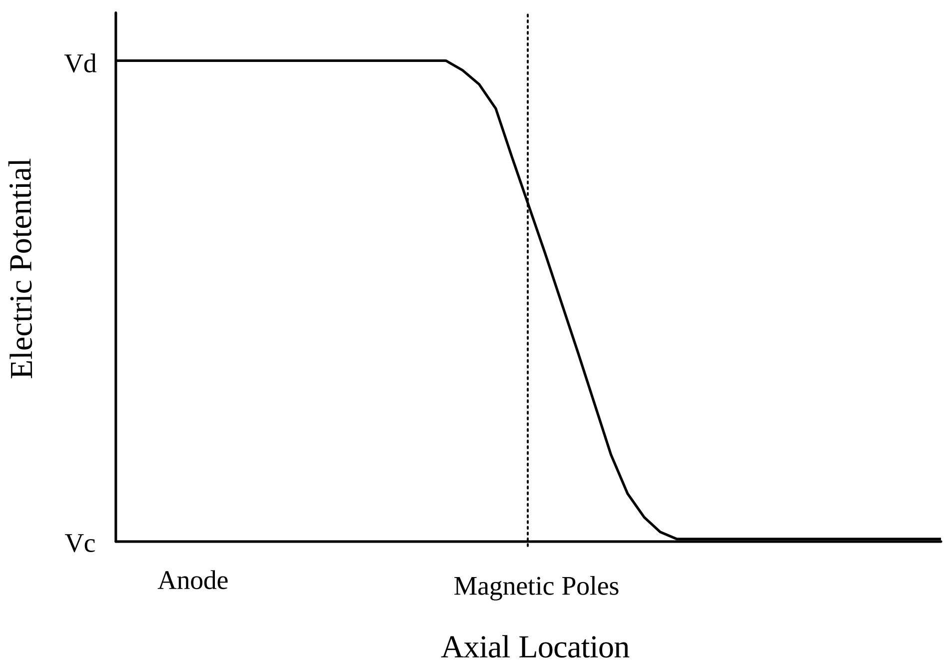

Figure 1.6. Idealized Electric Potential Distribution

Since most of the ionizing collisions occur in regions of high electron density, most ions will experience an accelerating potential near to, but less than, that between anode and cathode. The radial magnetic field has a finite axial width, thus electrons will be trapped - and therefore ions created and accelerated - over an axial range. Because there is a gradual fall in potential, there will a spread in the ion energies.

1.5. Thruster Design and Sizing

Hall thruster design is an empirical science at this time, since it is not possible to design a thruster with acceptable performance levels based solely on basic principles. Instead, it is necessary to build on years of design experience, most of which has been conducted by Russian scientists and engineers.

The first key point to note is that there are two distinct types of Hall thruster. The stationary plasma thruster and the thruster with anode layer. The SPT has a discharge chamber with ceramic walls that is longer than it is wide. Electron and ion collisions with the ceramic walls provide low energy secondary electrons that serve to keep the electron temperature within the discharge chamber low, allowing for an extended ionization and acceleration process. The TAL has a conducting discharge chamber, comprised of the anode, and inner and outer magnetic poles, that is wider than it is deep. The ion beam is confined to a narrow portion of the discharge chamber via control over the propellant injection in order to minimize erosion of the poles. Since there are few secondary electrons, the electron temperature increases toward the anode, leading to a sharp increase in the plasma potential near the anode. It is within this “anode layer” that most of the ionization and acceleration occurs. These conditions are stated mathematically in the following equations,[7] where L_{ch} is the length of the discharge chamber, b_{ch} is its width, L_b is the length over which the electron density is sufficient for ionization and acceleration to occur, and b_o is the width of the ion beam:

For the stationary plasma thruster:

EQN 1.5 $$\frac{L_{ch}}{b_{ch}} > 1, \ \frac{L_{ch}}{L_b} \geq 1, \ \frac{b_o}{b_{ch}} = 1, \ \frac{b_{ch} - b_o}{b_o} = 0$$

For the anode layer thruster:

EQN 1.6 $$\frac{L_{ch}}{b_{ch}} < 1, \ \frac{L_{ch}}{L_b} < 1, \ \frac{b_o}{b_{ch}} < 1, \ \frac{b_{ch} - b_o}{b_o} \approx 1$$

For equivalent power levels, the two types of thrusters have similar performance characteristics. This work will not debate the relative merit of one versus the other for operational systems. However, for research purposes, the SPT has several advantages. First, as will be described in Section 2.2, the University of Michigan and the United States Air Force Research Laboratory have designed and built a laboratory model 5 kW Hall thruster. A set of design equations that relate dimensions of a SPT such as the discharge chamber width and depth to its diameter were presented at an electric propulsion seminar given at the Massachusetts Institute of Technology in 1991 by Russian Hall thruster designers.[12] These equations provide the basis for the UM/USAF design. No equivalent design equations for the TAL are known to have been published. Second, the larger discharge chamber and acceleration region of the stationary plasma thruster makes it more accessible to the internal diagnostics that are a large part of this design goal. Finally, the lower electron temperatures provide a more benign environment to carry out the aforementioned internal measurements.

The design equations are given below. They relate thruster dimensions to the diameter of the discharge chamber. They are based on trial-and-error development by Russian scientists and engineers, not basic theory. These dimensions are defined in Figure 1.7.

EQN 1.7 $$b_m = 0.3 d_{ch} \; [mm]$$

EQN 1.8 $$b_{ch} = 6 + 0.375 b_m \; [mm]$$

EQN 1.9 $$L_c = 0.32 b_m \; [mm]$$

EQN 1.10 $$L_a = 2 L_c \; [mm]$$

EQN 1.11 $$L_{ch} \geq 1.1 L_a \; [mm]$$

where d_{ch} is the diameter of the discharge chamber, b_m is the separation of the front magnetic pole pieces, L_c is the distance from the maximum of the magnetic field to the point where it is one half maximum, and L_a is the distance from the front of the magnetic pole to the anode. These equations, combined with the discharge chamber diameter, provide a basis for designing a Hall thruster.

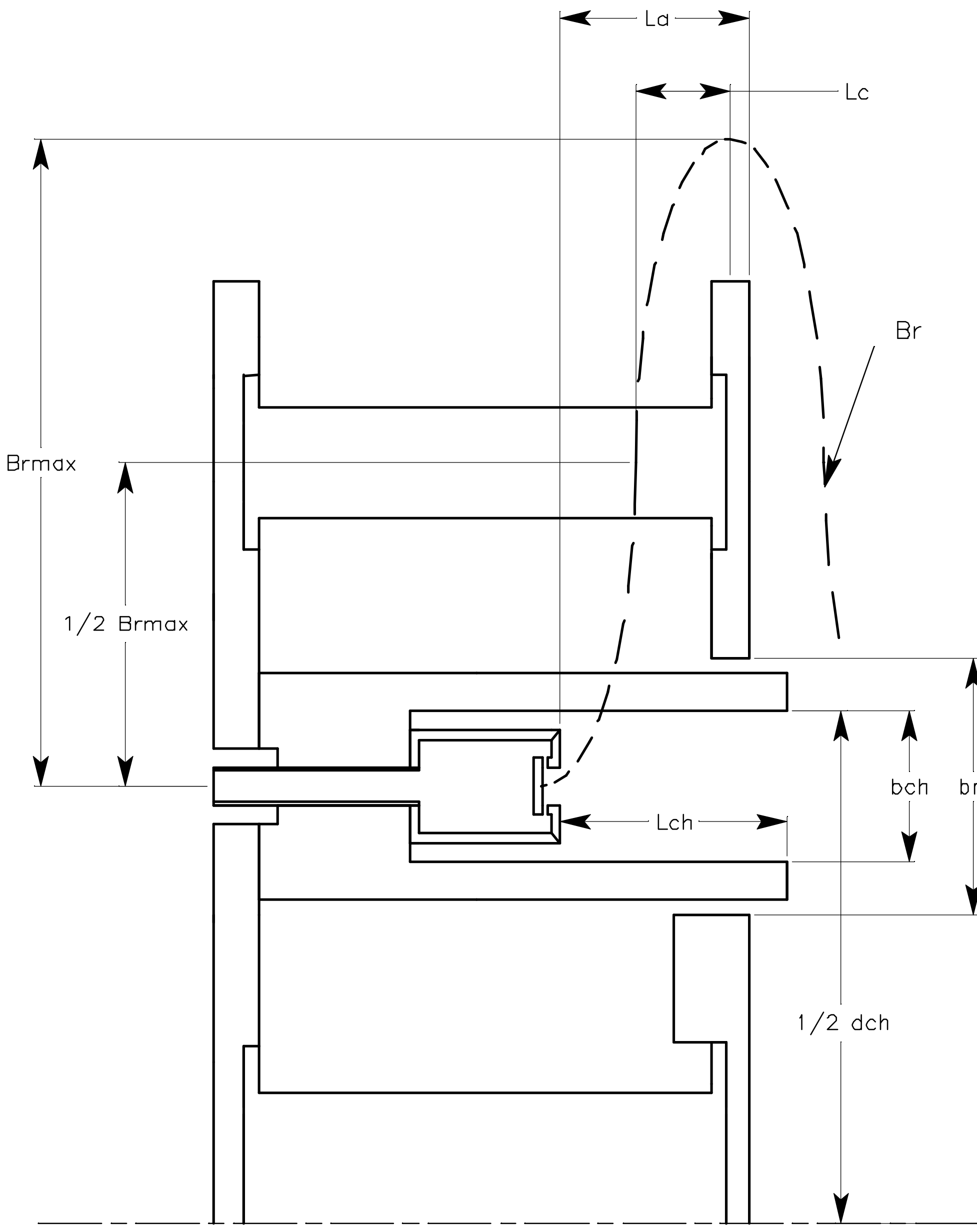

Figure 1.7. Design Equation Dimensions

In order to determine the discharge chamber diameter, it is first necessary to examine how the size of a Hall thruster relates to its operational characteristics. The two most common parameters used in describing a Hall thruster are its discharge chamber size and its nominal power level, and these are in most cases interchangeable. For example, a stationary plasma thruster with an 100 mm discharge chamber will have a nominal power level of 1.35 kW. However, one of the finest attributes of the Hall thruster is that varying the discharge voltage and current, the performance can be changed. Increasing the discharge voltage, V_d, will increase the accelerating potential on the ions, V_i, and will thus increase their velocity and the specific impulse of the thruster since:

EQN 1.12
$$I_{sp} = \frac{\overline{v_i}}{g} = \frac{1}{g}\sqrt{\frac{2q_i eV_i}{m_i}}$$

(the average ion velocity is used in performance equations because the plasma is not composed solely of singly ionized particles and not all ions see the same accelerating potential). Increases in discharge current are obtained by increasing the anode mass flow rate. This increases the thrust, since:

EQN 1.13
$$T = \dot{m}_a \overline{v_i}\ .$$

Note that the thrust will also increase with increasing discharge voltage, but only proportionally to its square root. By varying the thrust and specific impulse that an engine can deliver, multiple missions (e.g., orbit raising, stationkeeping, and de-orbit) are possible using a single thruster.

The range of performance that can be obtained with a given thruster is usually limited by the material properties of the thruster itself. If a small thruster is operated at too high of a power level, it will suffer excessive heating (due to its smaller mass and lower ability to dissipate heat) and be prone to breakdowns. Additionally, when attempts are made to create very small thrusters, there are difficulties relating to the magnetic field. From EQN 1.4, it is seen that in order to decrease the characteristic dimension of a Hall thruster, the magnetic field must be increased. For very small thrusters, the required magnetic fields are very difficult to generate. There are fewer problems taking a large thruster to lower power levels, though stability is often an issue and it is inefficient from a satellite mass standpoint to do so.

Therefore, it is best to design a thruster for a nominal power level, with the expectation that it can be run at higher and lower powers. Since mission requirements are most directly driven by the specific impulse of a thruster, it is best to begin by determining a relationship between the nominal specific impulse and nominal power level of the thruster. By examining existing thrusters[12,13,14,15] it is possible to extract such a relationship. Figure 1.8 shows the nominal powers and specific impulses for commercial stationary plasma thrusters, as well as an exponential curve fit used to relate the two.

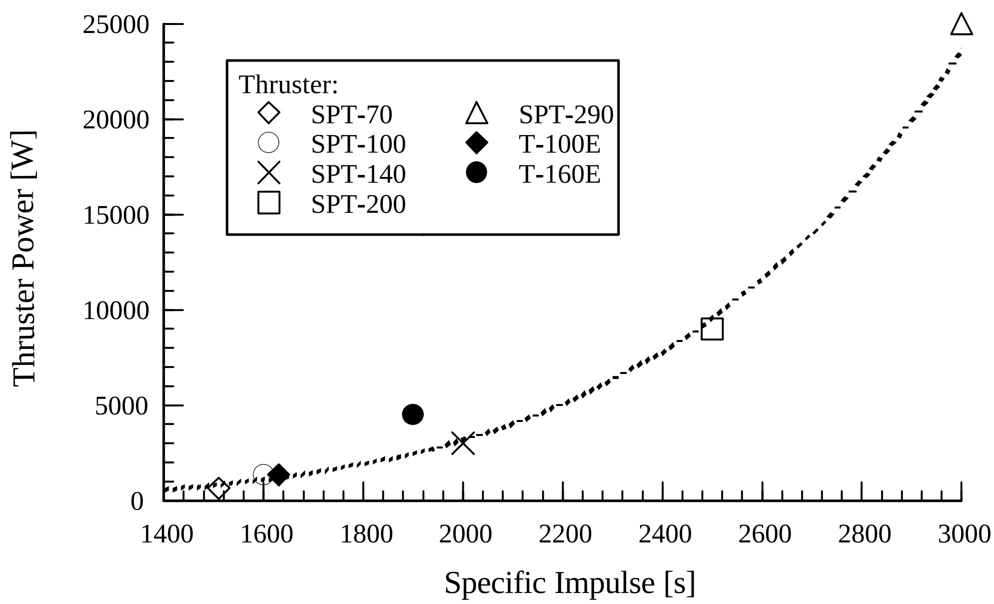

Figure 1.8. Relationship between thruster power and specific impulse

With power and specific impulse, the propellant mass flow rate can be determined if the thruster efficiency can be estimated. Hall thruster efficiency versus specific impulse has been shown to fit the functional form:[16]

EQN 1.14
$$\eta = \frac{a}{1 + \frac{b}{(gI_{sp})^2}} .$$

This form is the same as that developed by Brophy at the Jet Propulsion Laboratory to estimate ion engine efficiency.[17] The parameter *a* is the theoretical maximum efficiency based on fundamental engineering losses (particle collisions with walls, electrical circuit resistance, power processing unit losses, etc.), and is estimated at 0.8. The second parameter, *b*, relates to the discharge energy required for production of an ion: $b=2eE_{prod}/m_i$. An excellent fit to known thruster efficiencies, shown in Figure 1.9, can be obtained for $b=1.42*10^8$, which results in a production energy of 96.6 eV/ion. This agrees with the value of approximately 100 eV/ion measured by Kaufman.[5]

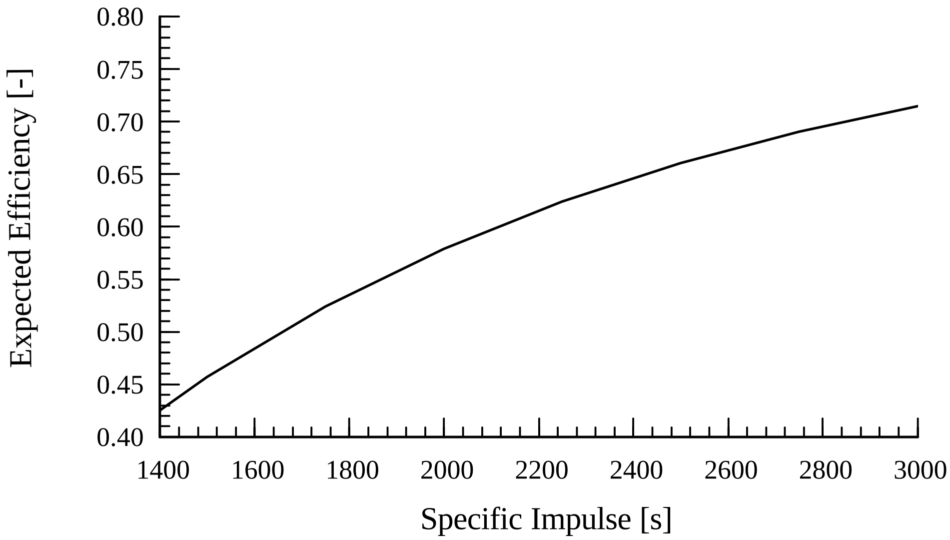

Figure 1.9. Relationship between thruster efficiency and specific impulse

The mass flow rate can now be determined using the relationship:

EQN 1.15
$$\dot{m}_a = \frac{2\eta P_D}{(I_{sp}g)^2} .$$

To determine thruster diameter, we examine the relationship for flow through an orifice, $\dot{m}_n = \rho_n A v_n = m_n n_n A v_n$ for the neutral propellant. Assuming a constant neutral drift velocity, for the density (and thus the probability of a neutral undergoing an ionizing collision) to be constant, the mass flow rate must increase in proportion to the area of the injection area. Therefore, the square of the thruster diameter should be proportional to the mass flow rate. Plotting this for commercially available thrusters, it is seen that this relationship is linear and can be used to determine thruster diameter.

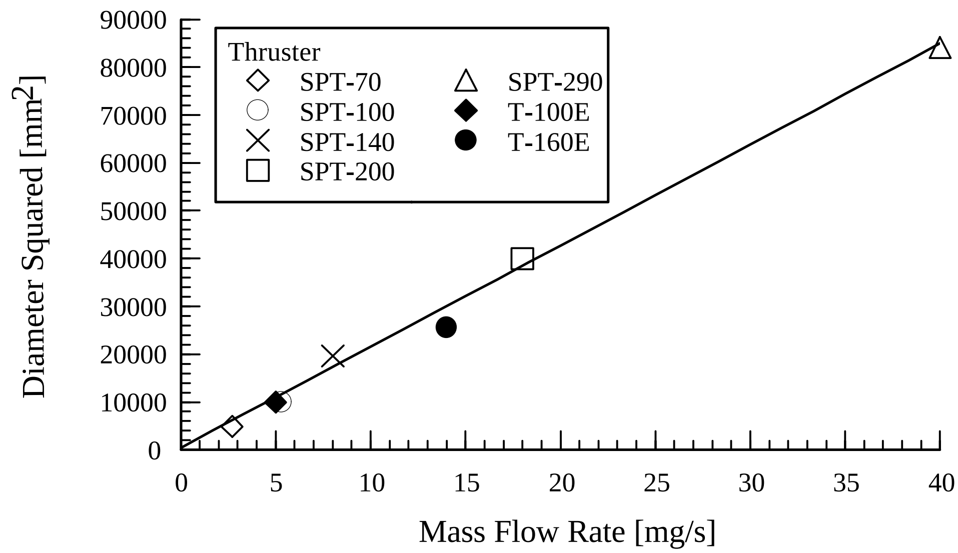

Figure 1.10. Thruster diameter versus mass flow rate

Using this method, it is possible to determine the discharge chamber diameter for a Hall thruster based solely on the desired power or specific impulse. This information can be combined with the design equations presented earlier to give other thruster parameters, such as discharge chamber width and depth; providing most of the information necessary to design a Hall thruster.

CHAPTER II

EXPERIMENTAL FACILITIES

In this chapter, the experimental facilities and procedures used in this thesis will be described.

2.1. Large Vacuum Test Facility

Tests were performed at the University of Michigan's Plasmadynamics and Electric Propulsion Laboratory (PEPL) in its 6 m by 9 m Large Vacuum Test Facility (LVTF). This is the same facility used in previous work at PEPL,[18] but prior to tests presented in this thesis, the LVTF was refitted with four CVI model TM-1200 Re-Entrant Cryopumps. Each cryopump is surrounded by a liquid nitrogen baffle, as shown in Figure 2.1. These cryopumps have replaced the diffusion pumps previously used for high vacuum work. They provide a xenon pumping speed measured at 140,000 l/s with a base pressure of $2*10^{-7}$ Torr. Pressure was determined by averaging the measurements of two ion gauges: a Varian model 571 gauge with a HPS model 919 Hot Cathode Controller and a Varian model UHV-24 nude gauge with a Varian UHV senTorr Vacuum Gauge Controller. The Varian nude gauge, the senTorr controller, and the connecting cable were calibrated as a unit on nitrogen. A calibration factor of 2.87 was used to correct for xenon.[19] The pressure during testing ranged from $5.5*10^{-6}$ Torr to $8.5*10^{-6}$ Torr, depending on the anode mass flow rate. Propellant flow was controlled by two MKS Model 1100 Flow Controllers, which were calibrated using a known volume and the ideal gas law corrected for the compressibility of xenon.

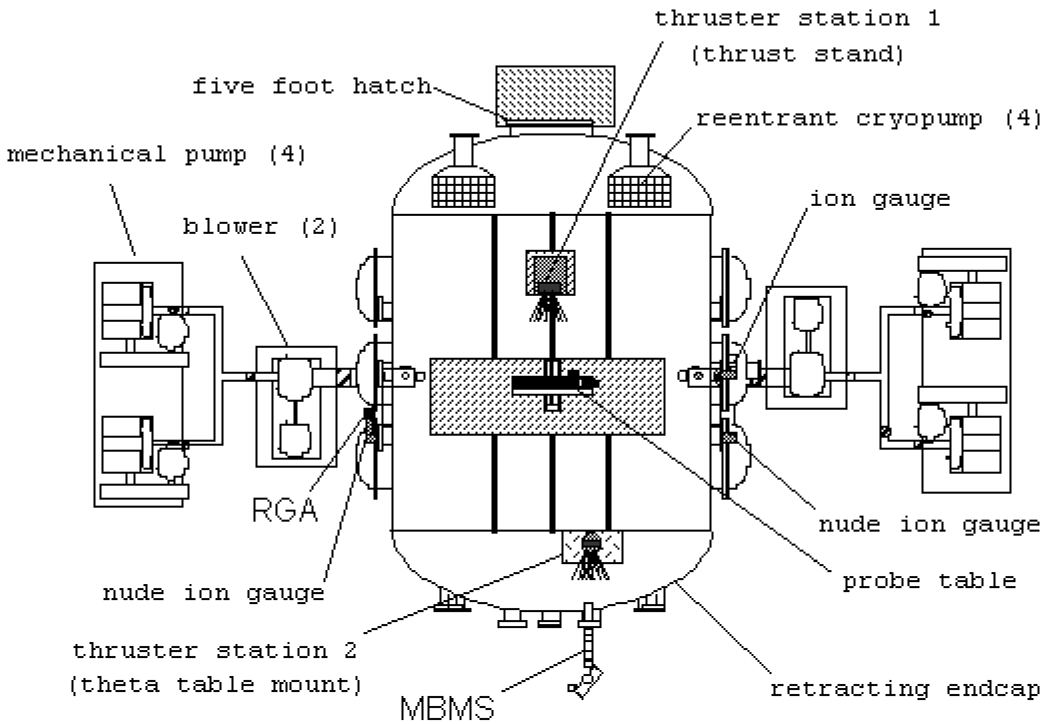

Figure 2.1. PEPL Large Vacuum Test Facility Schematic

2.2. UM/USAF Hall Thruster

Previous Hall thruster research has concentrated primarily on the 1.5 kW class of thrusters since they were of primary interest for commercial and military satellite use. However, driven by industry trends and IHPRPT (Integrated High Payoff Rocket Propulsion Technology) goals, the Hall thruster market is expanding beyond the 1.5 kW class. Of interest are sub-kW thrusters for small satellites and high power thrusters for orbit transfer missions, particularly the 5 kW class. Several commercial thrusters are under development for this role. These include the SPT-140[20] and T-160[21] stationary plasma thrusters, the D-100[22] anode layer thruster, and the Busek-Primex BPT-4000.[23] The University of Michigan and the United States Air Force (USAF) have moved toward studies of 5 kW class Hall thrusters. Unfortunately, from a research standpoint, 5 kW

Hall thrusters are few in number; and those that do exist are intended primarily for flight qualification use and are not well suited for basic research purposes.

With these facts in mind, the University of Michigan and the USAF decided to jointly develop a 5 kW class Hall thruster for basic research purposes. The goal was to develop a thruster that would be well suited for diagnostic access, particularly internal access, to gain a better understanding of the basic physics of its operation. Additionally, the thruster would be easily modifiable so that the effects of changes in thruster configuration could be examined. This thruster would also remain permanently in the possession of the University of Michigan and USAF, allowing them to undertake uninterrupted long-term research projects.

The design of the thruster was a three-step process. First, an analysis of Hall thruster characteristics, as presented in Section 1.5, was used to determine the nominal diameter and specific impulse; as well as the predicted anode mass flow rate, thrust, and efficiency, of a 5 kW class thruster. The result of this analysis was a thruster discharge chamber diameter of 169 mm with a nominal specific impulse goal of 2200 s. This specific impulse is near the IHPRPT specified goal for thrusters performing orbit transfer missions, giving a maximum payload fraction delivered to geosynchronous orbit. Second, the stationary plasma thruster design equations were used to determine the other Hall thruster dimensions (discharge chamber width, discharge chamber depth, pole separation, etc.) with respect to the thruster diameter. Finally, QuickField™ 3.4 - a 2 ½ dimensional magnetic field code - was used to design the magnetic circuit. This critical portion of the thruster design will be discussed in further detail.

The first step of the magnetic circuit design was to examine the magnetic flux through the cores and pole pieces to ensure that the material was not magnetically saturating. Typical values for 1.5 kW SPT magnetic fields across the discharge chamber are on the order of several hundred Gauss. Scaling relations indicated that a peak field of 280 Gauss would be necessary for the 5 kW Hall thruster being designed. To ensure that sufficient magnetic field strength was available, a 25% margin was added to the 280 Gauss and the thickness of the magnetic pole pieces were designed so that they would not saturate with a field of at least 350 Gauss across the discharge chamber. The predicted and measured radial magnetic fields, B_r, are shown in Figure 2.2 at the radial center of the discharge chamber (midway between the inner and outer front pole pieces). The axial reference point for this figure is the downstream edge of the front magnetic poles at 0 mm, with the downstream end of the anode at -31.8 mm and the upstream end of the anode (where it contacts the ceramic discharge chamber) at -57.2 mm. It is seen that the predicted field matches very well with the measured field, and both show the same shape as the idealized radial magnetic field in Figure 1.5.

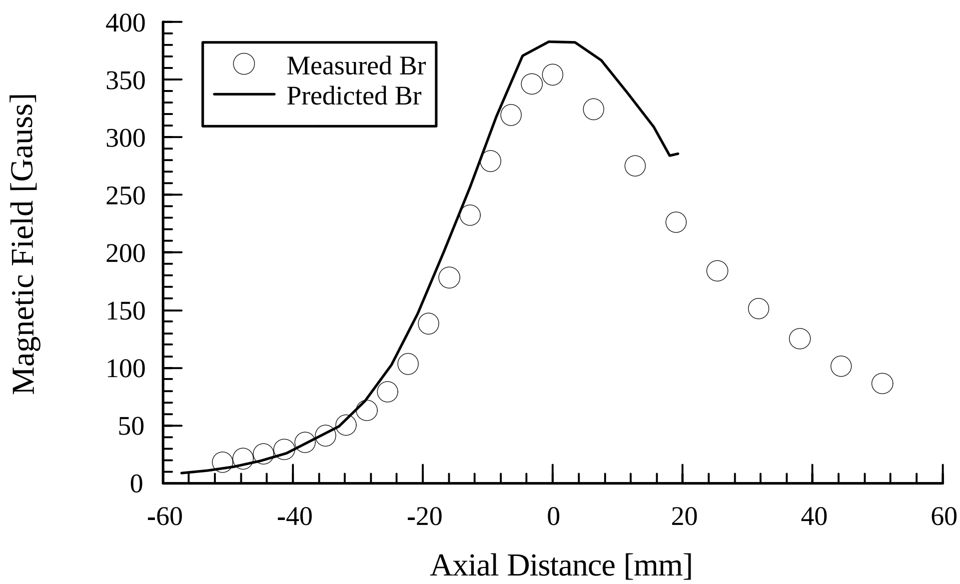

Figure 2.2. Predicted and measured radial magnetic fields

If the field were entirely radial, the thruster would behave very well with a magnetic circuit consisting of only poles and cores. However, the magnetic field will also have an axial component that can be detrimental to thruster operations. Figure 2.3 shows the magnetic field lines as predicted by QuickField for a configuration consisting of only cores and pole pieces. The predicted values of the radial, axial (B_z) and total magnetic fields ($B^2=B_r^2+B_z^2$) along the discharge chamber centerline are given in Figure 2.4. There are large magnetic field components in the axial direction and near the anode, the field is almost entirely axial. As discussed in Section 1.4, electrons tend to move to the areas of magnetic field maxima. A field structure such as that seen in Figure 2.4 will drive the electrons to the anode, resulting in high current and low thruster efficiency.

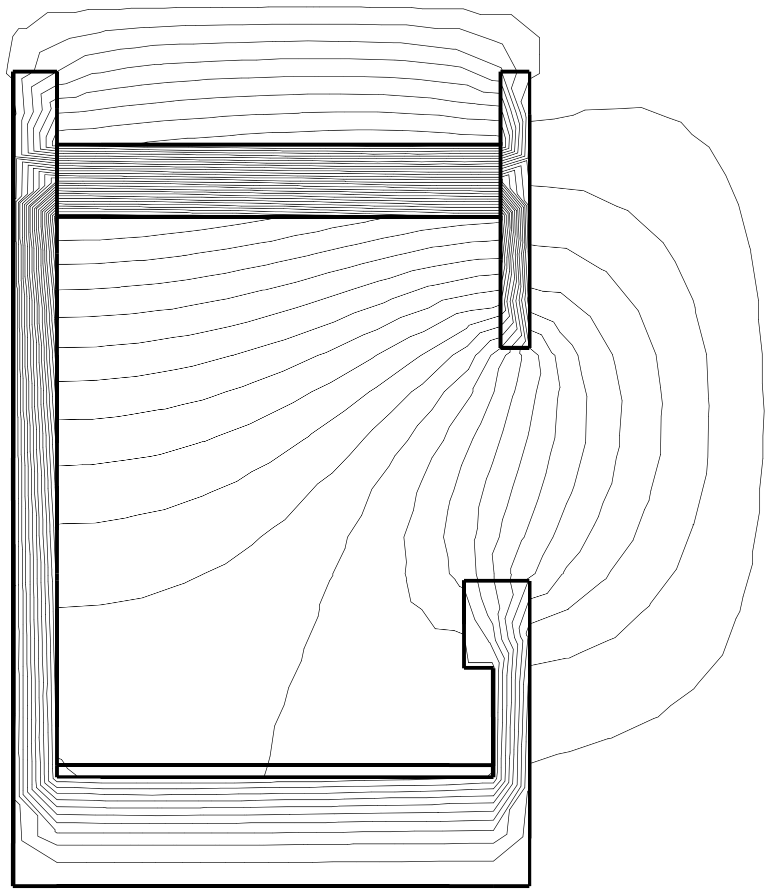

Figure 2.3. Magnetic Field Lines: No Shields

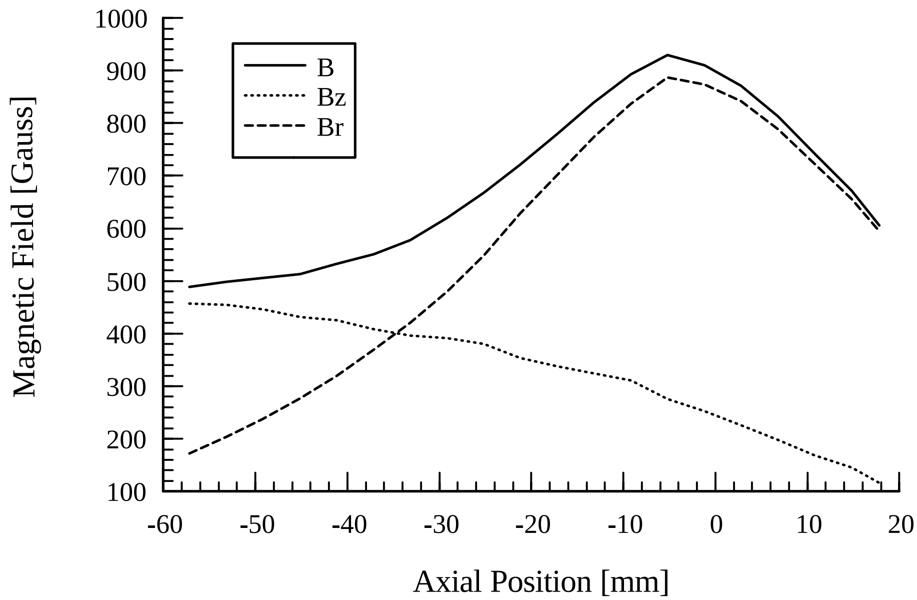

Figure 2.4. Predicted Fields for Shieldless Configuration

To prevent this from occurring, a conduit is needed that will carry the axial magnetic field so that it does not penetrate the discharge chamber. The solution is a set of two magnetic shields placed on opposite sides of the discharge chamber, extending from the back pole piece to just upstream of the front outer and inner poles. Many configurations were simulated before one was selected that maintained the proper radial field while minimizing the axial field. This configuration is shown in Figure 2.5. It is seen that the shields carry the axial portions of the magnetic field away while maintaining a proper radial field across the discharge chamber. The radial, axial, and total fields along discharge chamber centerline are shown in Figure 2.6. This is a proper magnetic field configuration, with the maximum radial field at the front pole pieces, sufficient field strength for thruster operation, and a small axial field near the anode. The predicted radial fields are the ones used in comparison with the measured fields in Figure 2.2, and the measured axial fields agree equally well with their predicted values.

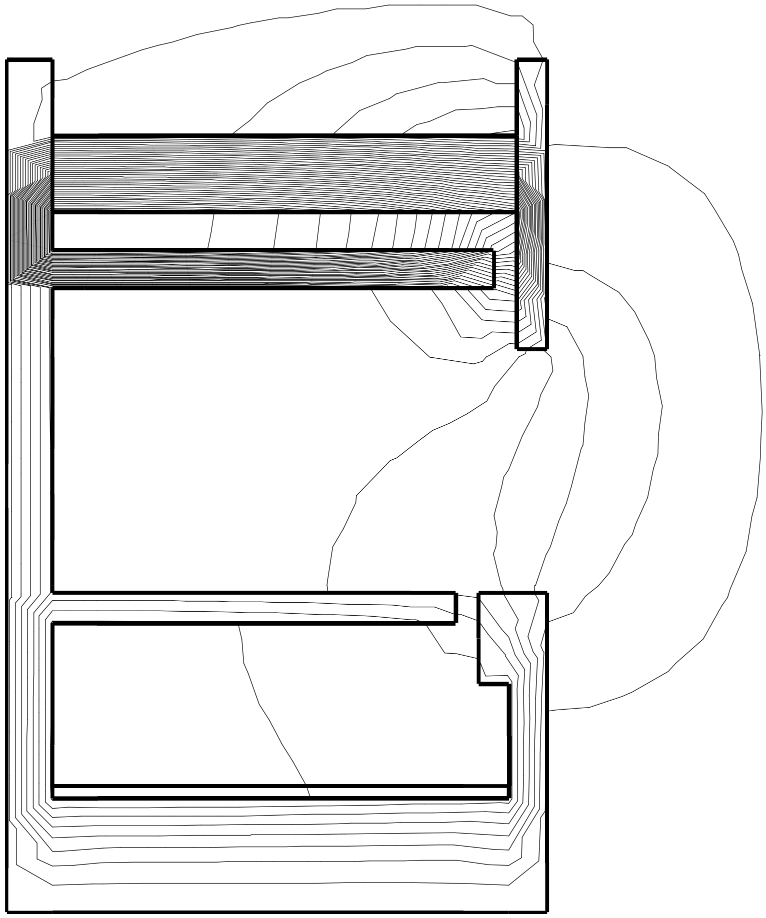

Figure 2.5. Magnetic Field Lines: Shields

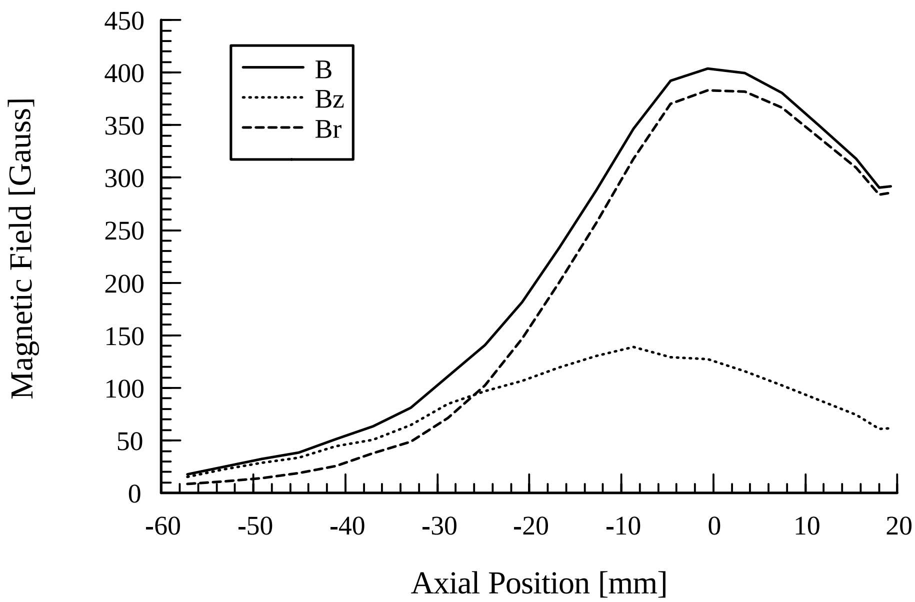

Figure 2.6. Final Configuration Predicted Fields

With the magnetic circuit design completed, a final thruster design was prepared. The resulting design underwent a critical design review in late November 1997 at the University of Michigan and, following several minor changes, fabrication began at the Air Force Research Laboratory in December 1997. The thruster, shown in a schematic in Figure 2.7 and a photograph in Figure 2.8, was completed in March 1998 and dubbed the P5. The magnetic components of the thruster were machined from cast iron due to its excellent magnetic properties and ease of machining. The anode was fabricated from 347 stainless steel. The discharge chamber was machined from a 50% boron nitride / 50% silicon dioxide ceramic and the inner pole piece guard disk was machined from pure boron nitride. A complete set of engineering drawings is included in Appendix B.

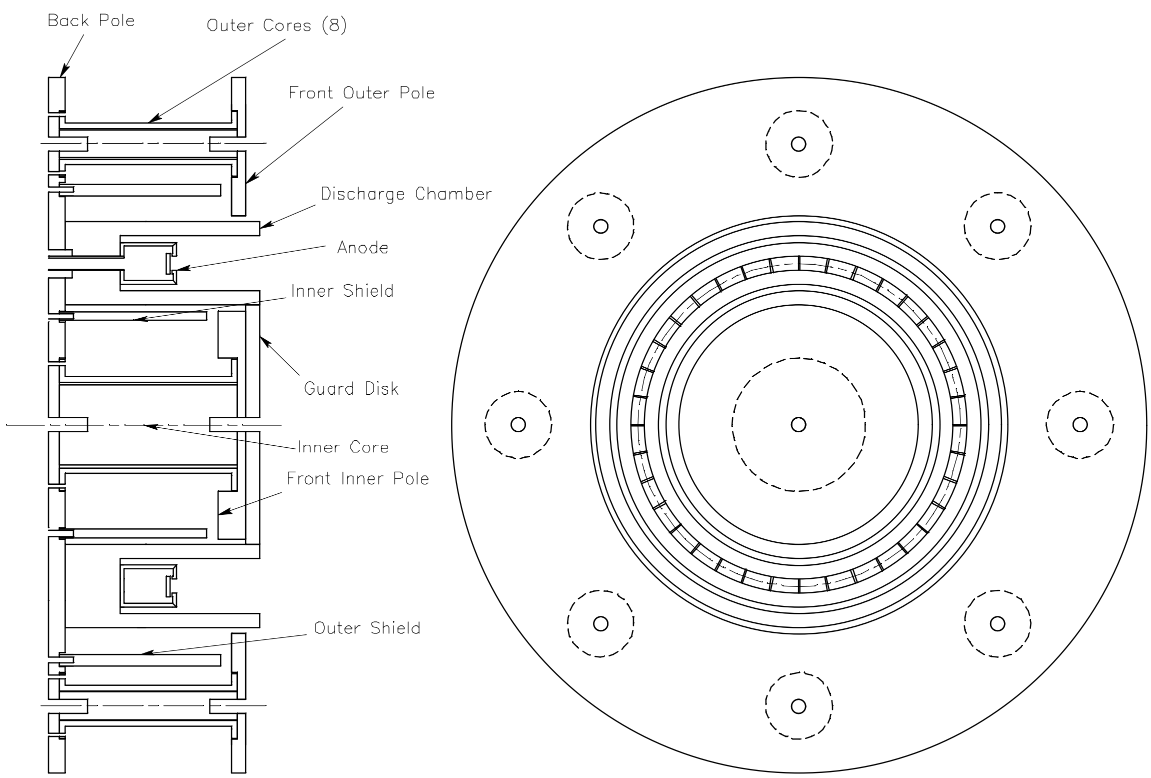

Figure 2.7. P5 Schematic

Figure 2.8. P5 Photograph

To ensure that measurements taken on the P5 would be relevant to the understanding of the operation of commercial thrusters, performance and probe data were taken.[24] The results are reproduced here for convenience. To make performance measurements, the thruster was mounted on an inverted pendulum thrust stand designed at NASA.[25] Performance was measured at discharge voltages ranging from 200 V to 500 V, and at discharge currents of 5.5 A, 7.6 A, and 10 A. These currents correspond to anode flow rates of 58 sccm, 79 sccm, and 105 sccm, respectively. For all cases, the cathode flow rate was set at 6 sccm.

In addition to thrust measurements, Faraday and Langmuir probe measurements were taken in a radial sweep, 50 cm from the thruster. The Faraday probe[25] had an area of 4.34×10^{-4} m^2 and was biased to -50 V to repel electrons. The Langmuir probe[26] had a collection area of 2.85×10^{-4} m^2, a length-to-diameter ratio of 16, and used a 497 Ω shunt resistor to measure current. Faraday probe measurements were taken on a continuous sweep from +70° to -70° relative to the thruster centerline, while Langmuir probe measurements were taken over the same interval at discrete 10° increments. Measurements were attempted at each performance operating condition.

The performance measurements are shown in Figure 2.9 - Figure 2.11. Both cathode and anode mass flow are accounted for in the calculation of specific impulse and efficiency, though the magnet power - which ranged from 17 W to 64 W - was not. For each performance parameter, the data for the three anode mass flow rates are presented versus discharge voltage. During testing the tank pressure was $5.5*10^{-6}$ Torr for an anode mass flow rate of 58 sccm, $7.1*10^{-6}$ Torr for 79 sccm, and $8.5*10^{-6}$ Torr for 105 sccm. These pressures are corrected for xenon and are the average of the readings on two ion gauges. The thrust measurements had an error of +1.2 / -8.0 mN. The specific impulse measurements had an error that decreased with increasing anode mass flow rate: +20 / -131 s at 58 sccm, +15 / -97 s at 79 sccm, and +11 / - 75 s at 105 sccm. The error in efficiency measurements also decreased with increasing anode mass flow rate: +1.2 / -8.3% at 58 sccm, +1.0 / -6.6% at 79 sccm, and +0.7 / -4.9% at 105 sccm.

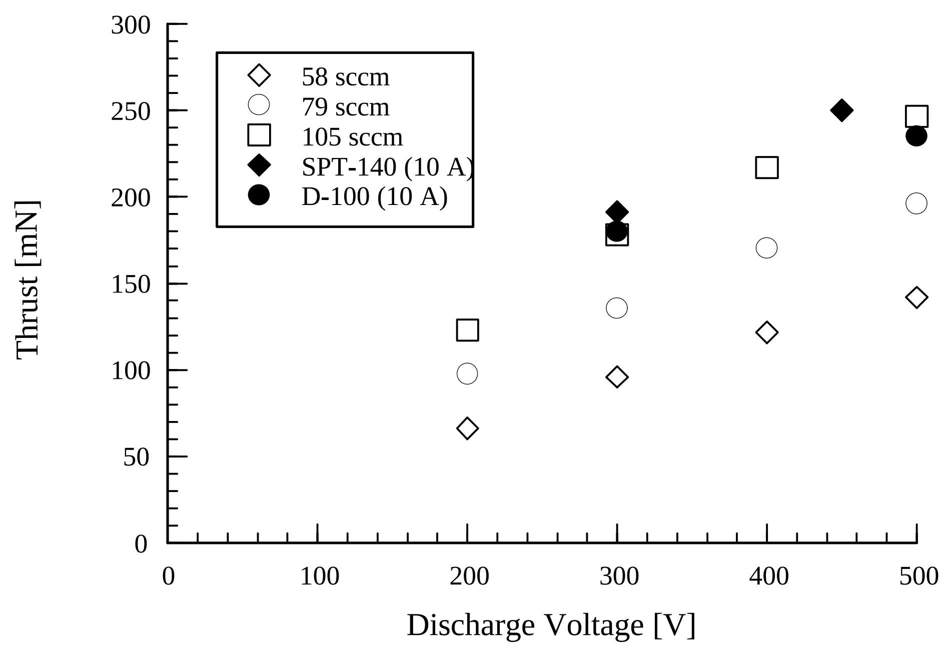

Figure 2.9. Thrust versus Discharge Voltage

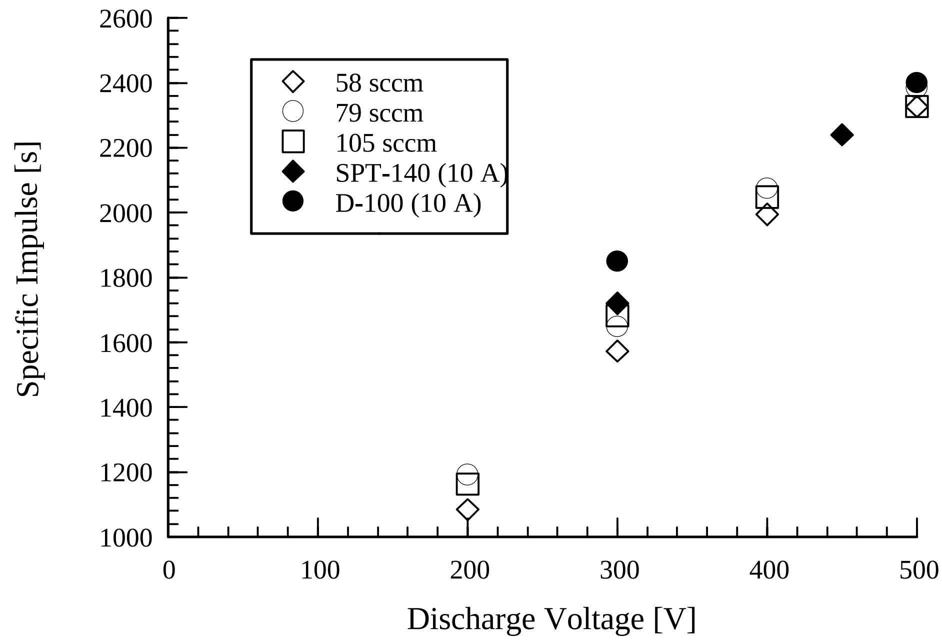

Figure 2.10. Specific Impulse versus Discharge Voltage

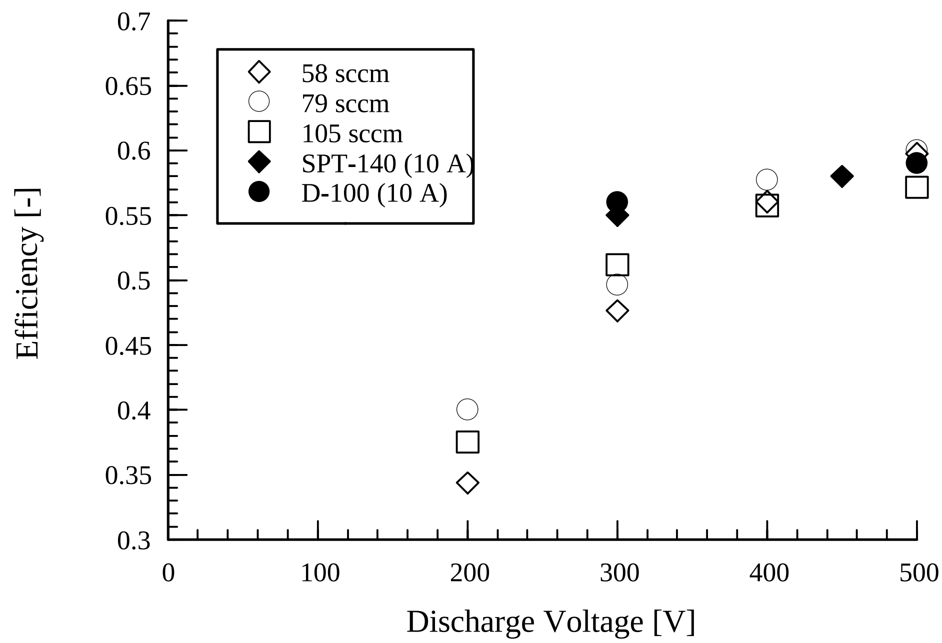

Figure 2.11. Efficiency versus discharge voltage

This data is in excellent agreement with the performance values for commercial thrusters included for comparison.[27,28] The SPT-140 was tested at Fakel at pressures of $2.5*10^{-4}$ to $3.6*10^{-4}$ Torr and the D-100 was tested at JPL in a 3.1 m by 5.1 m vacuum chamber that had a base pressure of $1*10^{-7}$ Torr and a measured xenon pumping speed of 48,000 l/s.

Ion current density information calculated from the Faraday probe measurements is given in Figure 2.12 through Figure 2.14 for the three anode mass flow operating points. Stable operation at 200 V, 105 sccm (10 A) could not be maintained during Faraday probe measurements. Therefore, an additional data point at 350 V was added for this mass flow rate. The estimated error in the ion current density was ± 5%, with an uncertainty in position of ± 3°. For all cases, approximately 80% of the ion current between ± 70° was between ± 20°. Integrating these results over the plume area gives a total current that is equivalent to, but less than, the discharge current. For the first two flow rates, the peak ion current density increases with increasing discharge voltage, indicating decreased plume divergence due to greater ion velocity. For the third flow rate, 105 sccm, the peak ion current density increases at first, then plateaus with increasing discharge voltage. The peak value is less than at 79 sccm, but the angular spread of the profile is greater, indicating increased divergence at this flow rate.

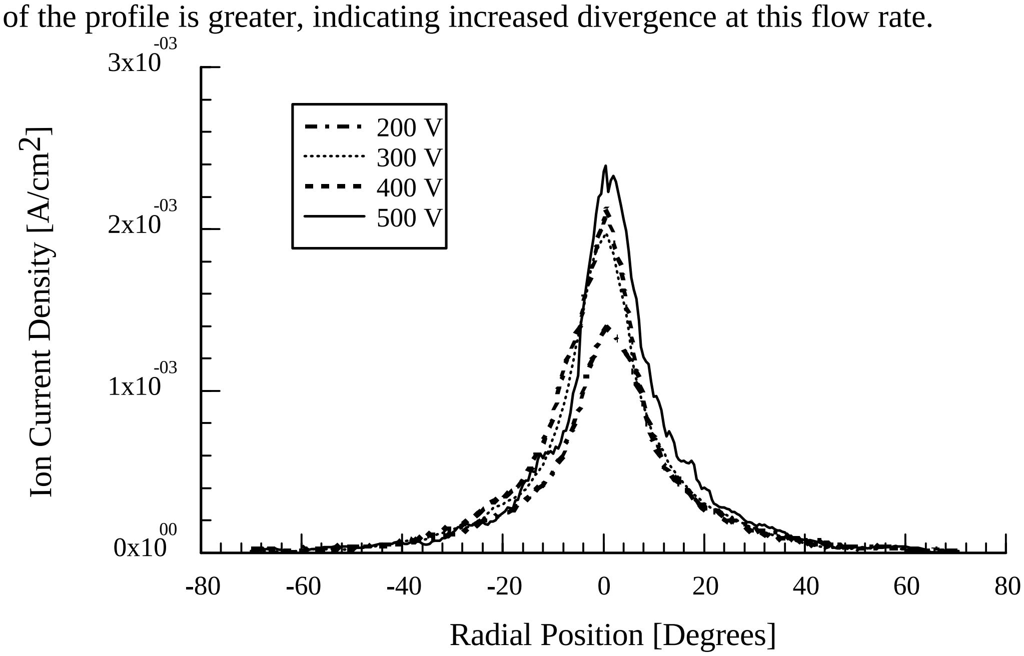

Figure 2.12. Ion Current Density at 58 sccm

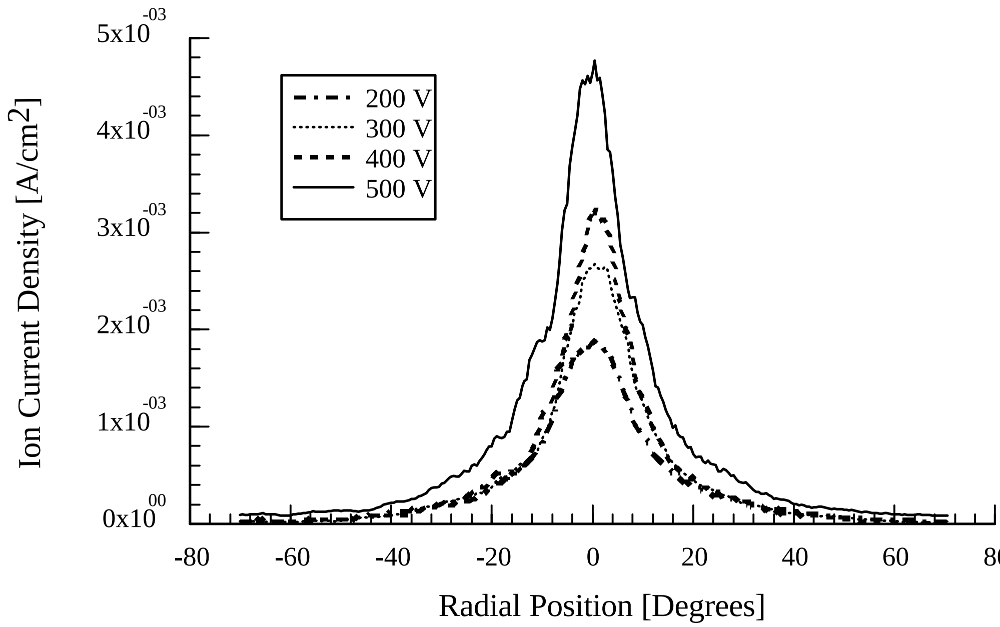

Figure 2.13. Ion Current Density at 79 sccm

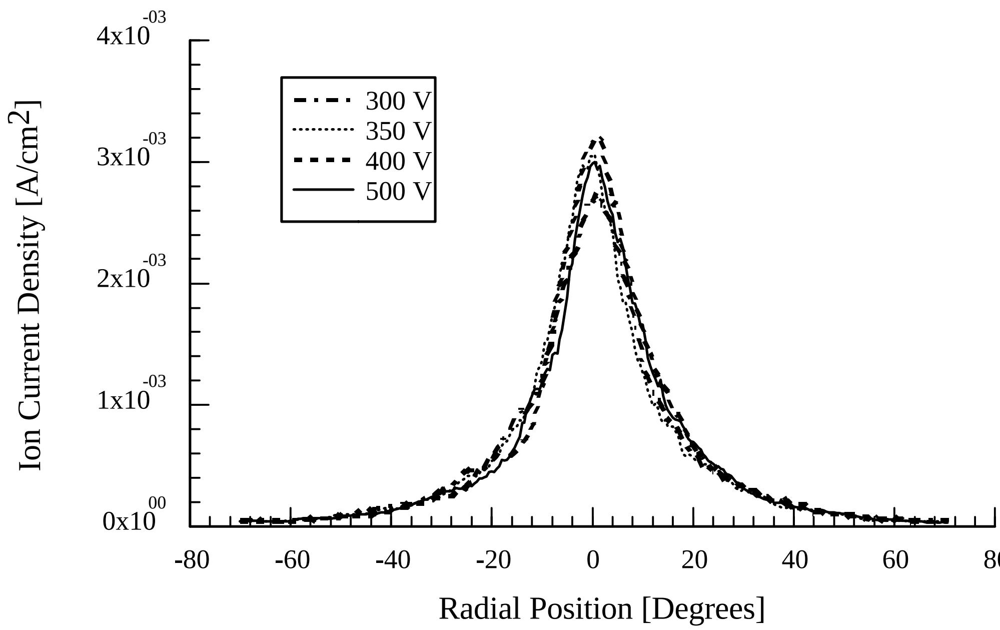

Figure 2.14. Ion Current Density at 105 sccm

Electron temperature data from the Langmuir probe measurements is shown in Figure 2.15 through Figure 2.17. Due to difficulties with probe ablation, Langmuir probe measurements were taken at 79 sccm and 500 V only from 70° to -50° and at 105 sccm only at 500 V. The estimated error in the electron temperature was ± 5%, with an uncertainty in position of ± 3°. These results show that the most energetic electrons are directed along the thruster centerline, while low energy electrons expand outward with the plume ions.

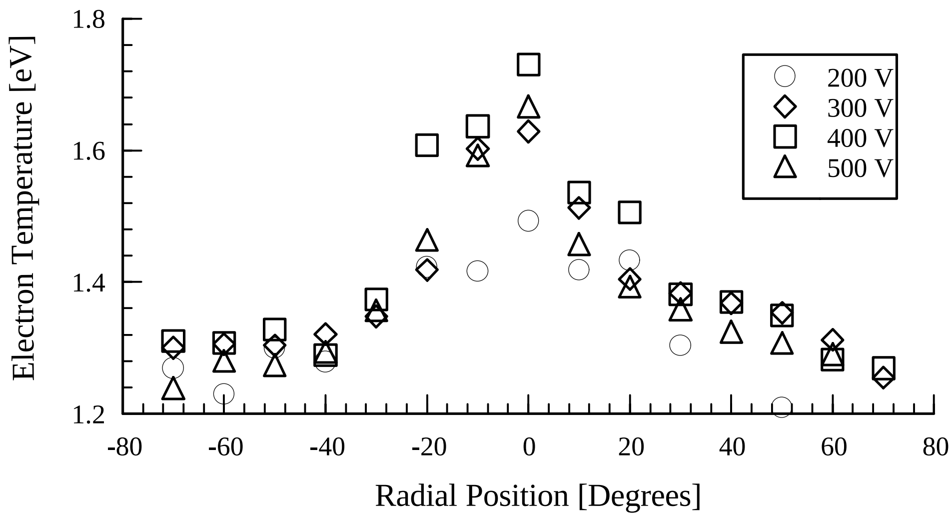

Figure 2.15. Electron Temperature at 58 sccm

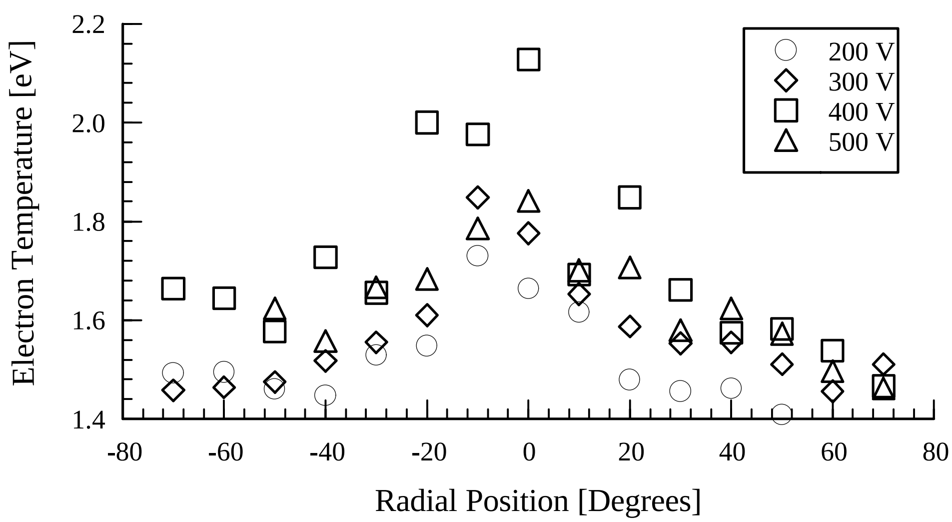

Figure 2.16. Electron Temperature at 79 sccm

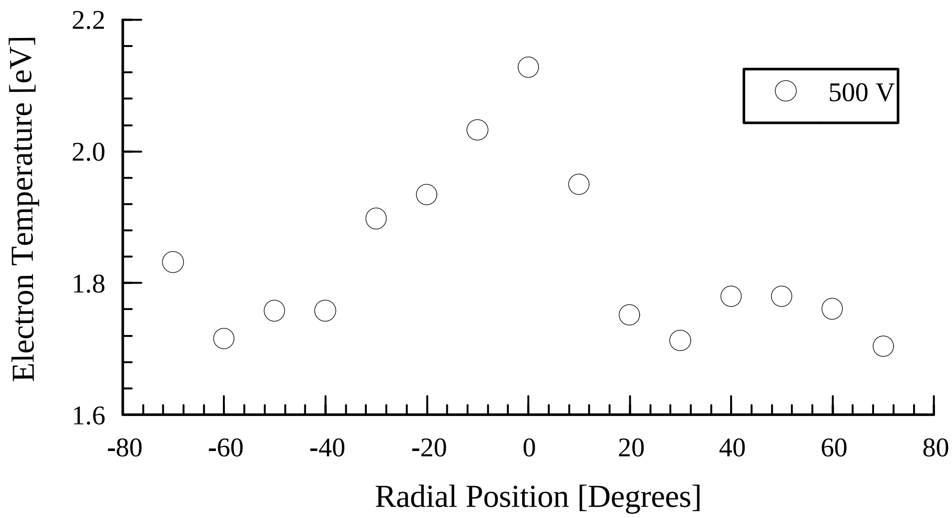

Figure 2.17. Electron Temperature at 105 sccm

Electron number density data from the Langmuir probe measurements is shown in Figure 2.18 and Figure 2.19. From theory, the error in electron number density is ± 50%. These results are similar to the ion current density data, showing that the electrons follow the ions in order to maintain quasineutrality within the plume.

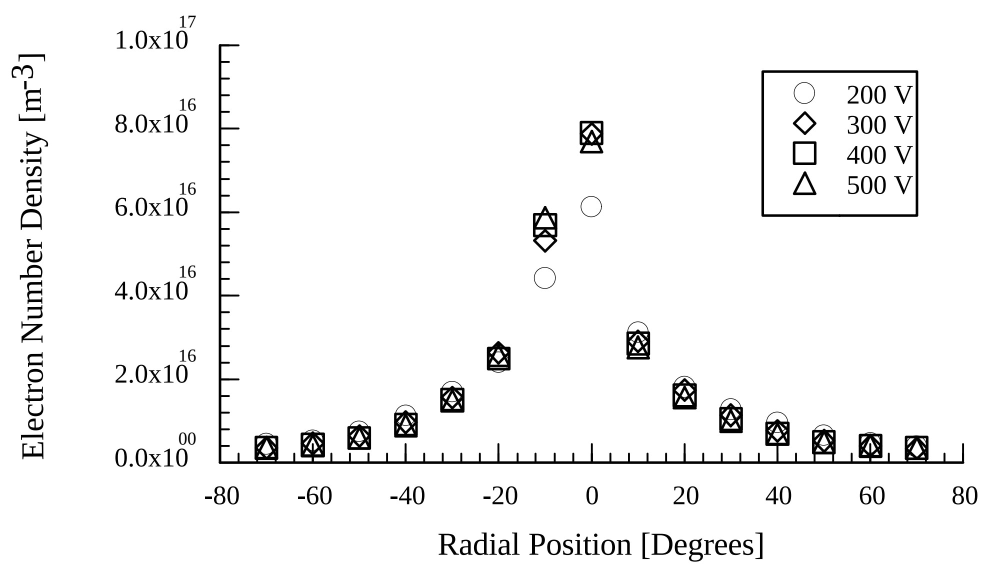

Figure 2.18. Electron Number Density at 58 sccm

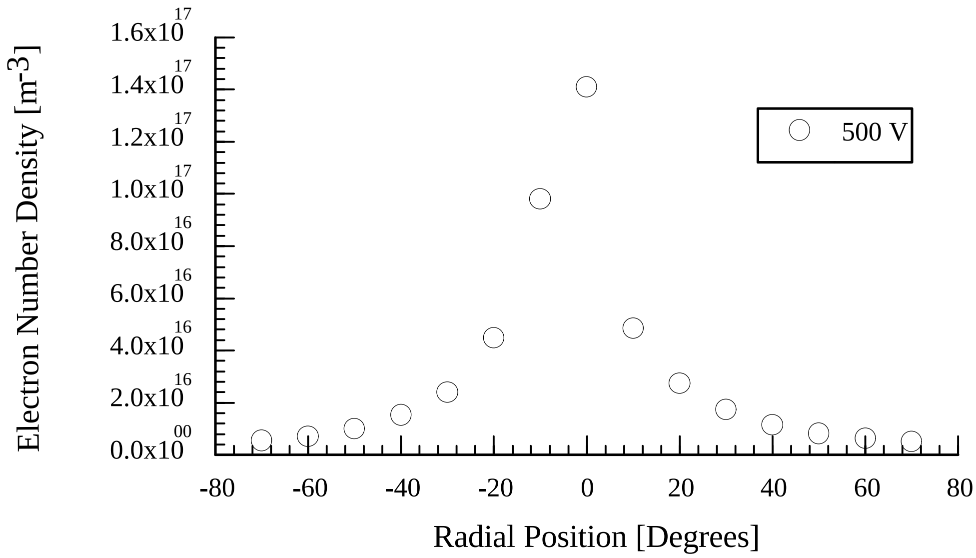

Figure 2.19. Electron Number Density at 105 sccm

Plasma potential data from Langmuir probe measurements are given in Figure 2.20 through Figure 2.22. These results typically show a maximum in plasma potential at high angles, with a local maxima near 0°. The estimated error in plasma potential is the same as for electron temperature, ± 5%, and the error in position is ± 3°.

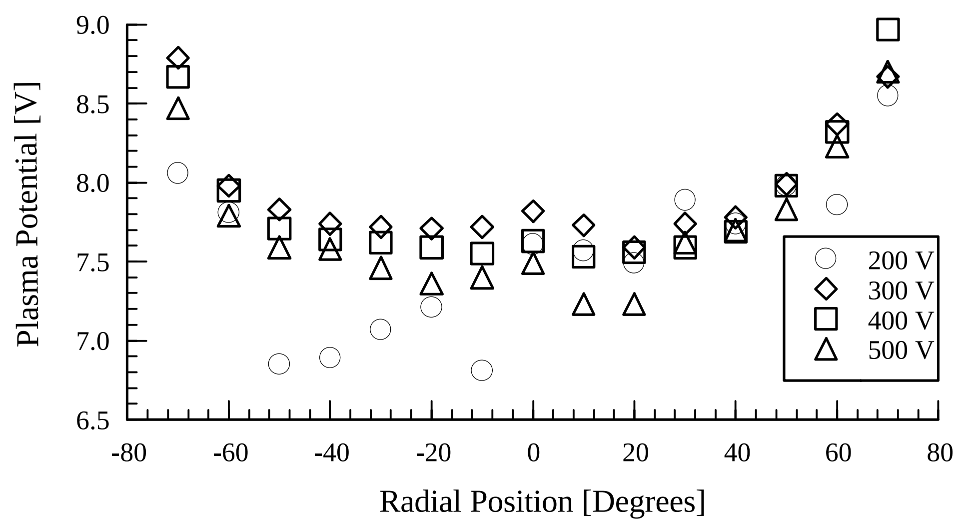

Figure 2.20. Plasma Potential at 58 sccm

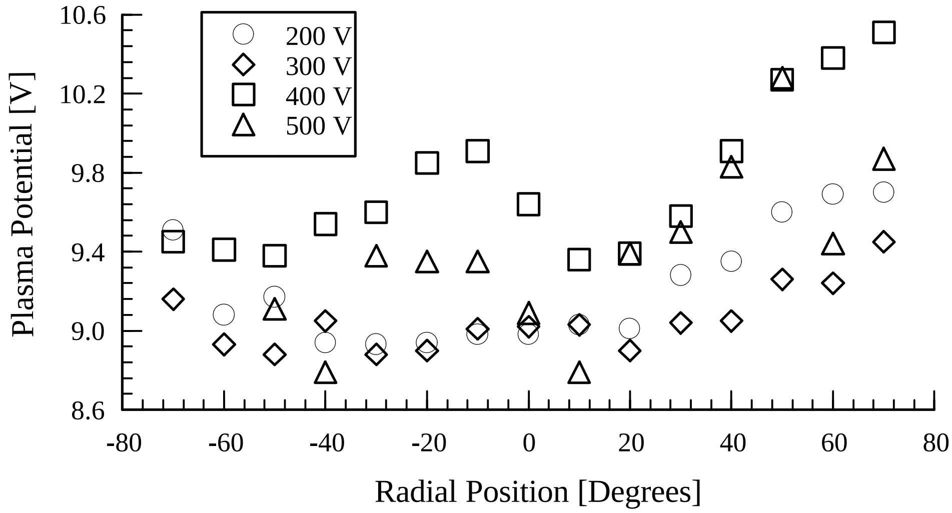

Figure 2.21. Plasma Potential at 79 sccm

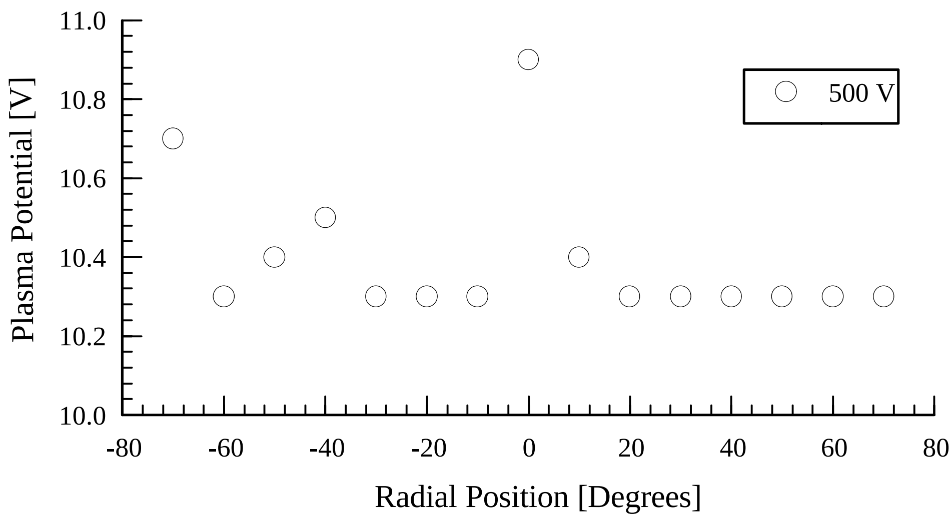

Figure 2.22. Plasma Potential at 105 sccm

Floating potential data from Langmuir probe measurements are given in Figure 2.23 through Figure 2.25. They show that the floating potential increases as centerline is approached, at a rate that is much greater than the other quantities measured by the Langmuir probe. Again, the estimated error is the same as for electron temperature, ± 5%, and the error in position is ± 3°.

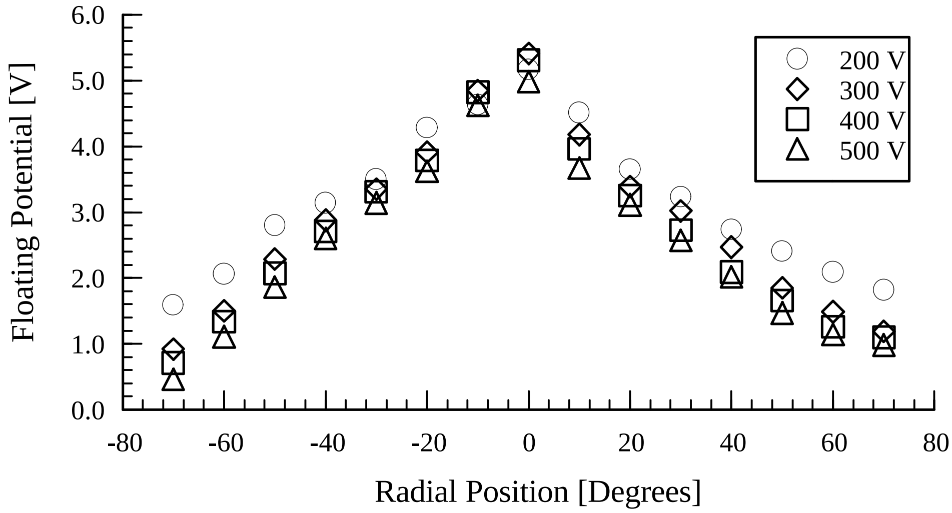

Figure 2.23. Floating Potential at 58 sccm

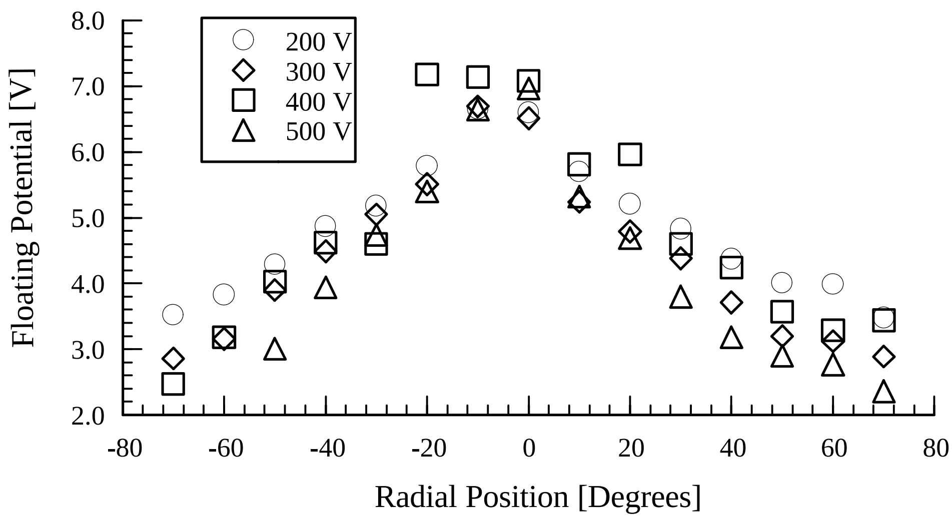

Figure 2.24. Floating Potential at 79 sccm

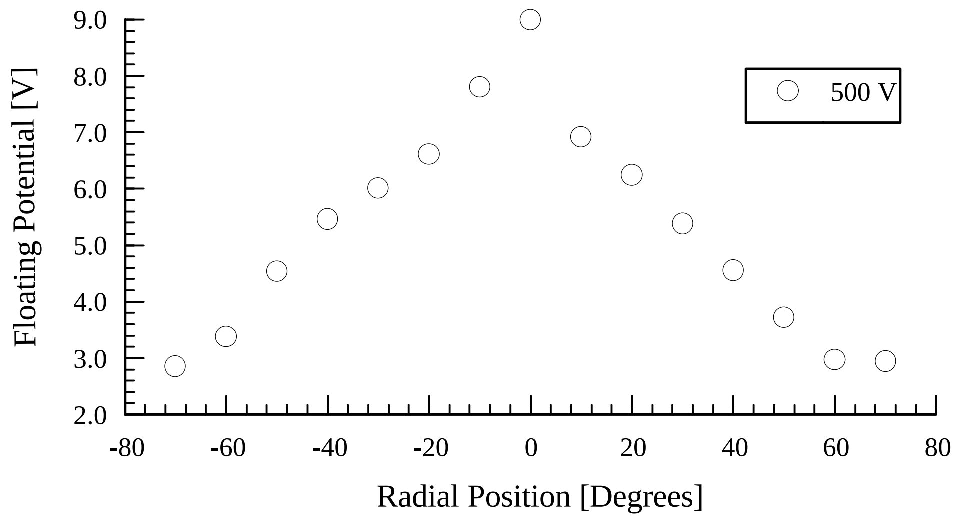

Figure 2.25. Floating Potential at 105 sccm

The current and voltage characteristics of the thruster were also examined. Current/Voltage characteristics were determined by igniting the main discharge and increasing the discharge voltage until a stable current plateau is reached. The electromagnet currents were kept constant up to 200 V, then adjusted to minimize the discharge current. The results are shown in Figure 2.26 for the three operating anode mass flow rates. The thruster ignited at a discharge voltage of ~65 V. A current overshoot occurs, with a maxima at ~100 V, before the current plateaus to a steady value with increasing discharge voltage. Characteristics such as these are seen for all flight type Hall thrusters. The overshoot is present for thrusters where the electromagnet current is kept constant during startup, and is absent for those which have the electromagnets in series with the main discharge.

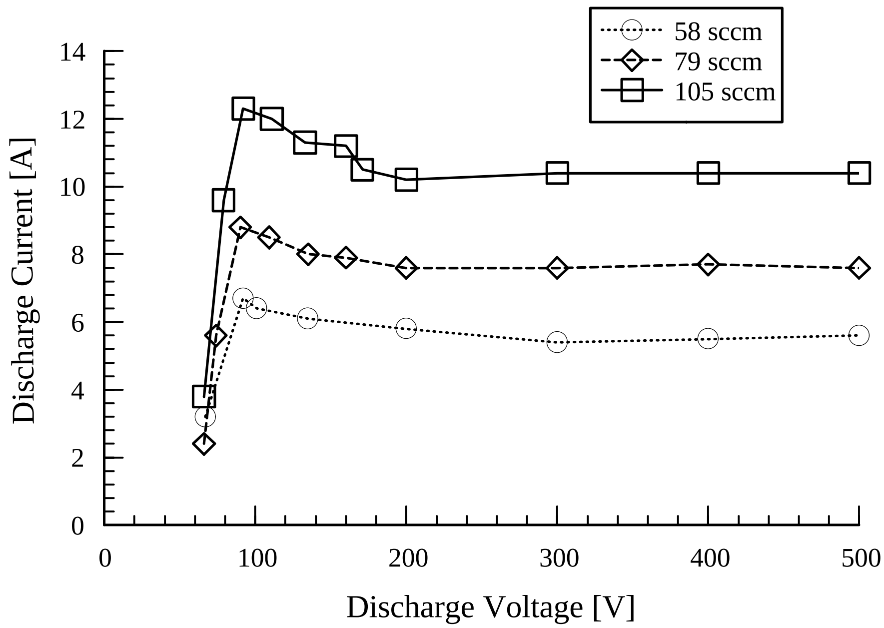

Figure 2.26. Current/Voltage Characteristics

An oscilloscope trace taken of the thruster current and voltage at 5 kW (487 V, 10.3 A) shows significant oscillation at millisecond time scales. Fluctuations such as these have been measured on other Hall thrusters, and typically do not have an adverse effect on thruster operation.

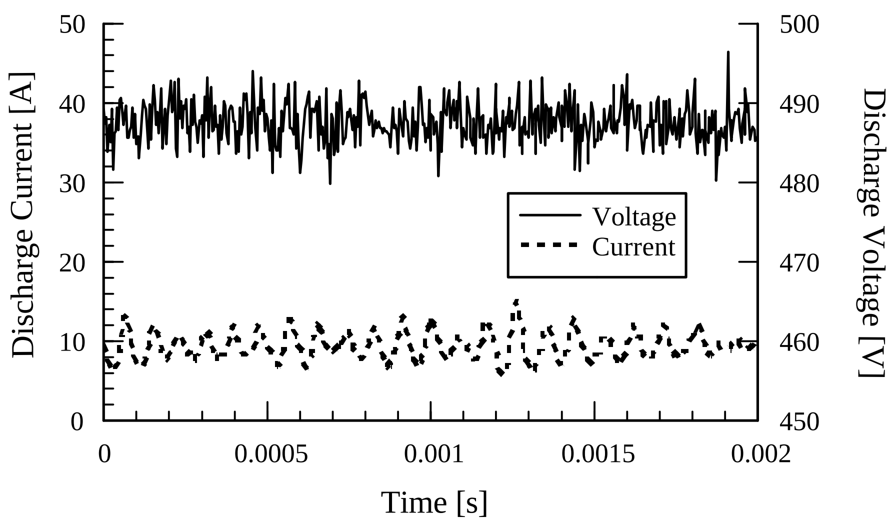

Figure 2.27. Oscilloscope Readings of Current and Voltage

The performance and probe measurements taken on this Hall thruster indicate that it behaves in the same manner as flight ready hardware, thus confirming the validity of the parameter based design method. Issues such as lifetime and mass savings were not taken into account when it was designed. It is believed that the data taken on this thruster using other methods will be equally valid and representative of flight type units. Therefore, the thruster is well suited for its role as a laboratory tool.

2.3. Molecular Beam Mass Spectrometer

Several techniques can be used to examine the ion energy distribution within the plume of a Hall thruster. Retarding potential analyzers[29] (RPAs) can be used to perform an analysis of the ion energy distribution function, but there are several obstacles to their use. Most importantly, the analysis of RPA data is dependent on the assumption that the plasma is composed of only one ionic species. However, various investigations have shown that though the dominant species in a Hall thruster plume is singly ionized xenon, higher charged species exist. Therefore, the interpretation of RPA data is erroneous for the multi-species Hall thruster plume. Additionally, RPA data must be numerically differentiated in order to be used, a step that inevitably amplifies noise in the distribution function.

Another technique for studying ion energy is laser induced fluorescence (LIF).[30,31] LIF investigations of singly ionized xenon have provided measurements of average ion velocity that are in agreement with other techniques such as the RPA. However, LIF measurements report profile width as an ion temperature on the order of 1 eV, whereas RPA data indicate a spread in the ion energy distribution function on the order of 100 eV. It is not entirely clear if these measurements of profile width are, in fact, equivalent; or, if they are equivalent, what is the cause of the discrepancy. It is possible to investigate other charge state species using LIF, including neutrals.[32] However, the transitions for multiply charged xenon are found in the ultraviolet, a region where it is very difficult to obtain the type of laser operation necessary for LIF velocity measurements.

Manzella investigated the species composition of the plume using emission spectroscopy.[33] This investigation showed that the plume was comprised of ~89% Xe^{+} and ~12% Xe^{2+}. However, it was based on a Boltzmann equilibrium model that was not truly applicable to Hall thruster plumes. The correct model, based on collisional-radiative equilibrium, was not developed due to a lack of knowledge of the complicated xenon excitation rates.

It can be seen that there are difficulties using these techniques to measure ion energy and species composition. Emission spectroscopy and LIF provide these quantities separately, but both require a model of the plasma's equilibrium state. LIF is capable of looking at different charge species, but to do so is non-trivial. The RPA can be used to obtain measurements of ion energy, but these are frequently noisy and ignore the multiple charge states found in the plume of the Hall thruster. An instrument was desired that would allow for measurements of both the ion energy and species composition of a Hall thruster's plume that, if not simultaneous, could be performed in close temporal proximity. Such an instrument is the molecular beam mass spectrometer (MBMS) developed for use at PEPL by King.[34]

The MBMS is a time-of-flight mass spectrometer with a 45-degree parallel plate energy analyzer. It is essentially two instruments in one that when used together can give direct measurements of both ion energy and species composition. The mass spectrometer is mounted to one end of the LVTF (Figure 2.1). Ions pass into the MBMS through a sampling orifice. Two diffusion pumps are used to evacuate the MBMS in order to reduce the change for collisions between beam ions and background gas. The beam enters the 45-degree energy analyzer, which allows ions of a specific energy-to-charge ratio to pass through and reach the detector. This ratio is selected by setting the electric field between the plates of the analyzer. By sweeping the value of this field, an entire ion energy distribution function can be determined without the need for any numerical differentiation as with the RPA. The setup for ion energy measurements is described in detail in Section 2.3.1.

For species composition, the time-of-flight mass spectrometer is used. This is the same physical system, with an electrostatic beam gate placed downstream of the sampling orifice. By pulsing the gate open and recording the time it takes for the ions to reach the detector at the end of the energy analyzer, the individual species of the plasma can be detected. This can be done because, while all of the ions passing through the analyzer for a given pass voltage have the same energy-to-charge ratio, the Hall thruster accelerates them to different velocities based on their charge state, as seen from EQN 1.3. Since their velocities are different, they will arrive at the detector at different times. The time-of-flight mass spectrometer is described in further detail in Section 2.3.2.

This work expands and improves on previous MBMS research in a number of ways. First, the refit of the LVTF with cryopumps (See Section 2.1) has dramatically improved its pumping capability, allowing for lower tank pressures during testing. From the ideal gas law, $p = nkT^*$, with lower pressure comes lower density (assuming that the temperature is unchanged). We see that the mean free path, l, increases by using the following relationship, assuming that the gas is in kinematic equilibrium:

EQN 2.1 $$l = \frac{1}{\sqrt{2}ns}.$$

The charge exchange collision cross section, s, for a Xe^+ + Xe collision can be computed from:[35]

EQN 2.2 $$s = \left(K_1 \ln v_r + K_2\right)^2 \times 10^{-20}\, m^2$$

where K_1 = -0.8821, K_2 = 15.1262, and v_r is the relative interparticle speed. It is assumed that the velocity of the neutral background gas is much less than the ions, such that $v_r = v_i - v_n \approx v_i = I_{sp} g$. With increased mean free path, there is a lower probability of collisions over a path length, *s*, between xenon ions and background neutral gases based on the collision survival equation:[36]

EQN 2.3 $$P_{coll}(s) = 1 - e^{-s/l}\ .$$

Therefore, by lowering the tank pressure, the mean free path is increased and the probability of collisions decreases. The collision probabilities based on the corrected tank pressures for diffusion pump and cryopump operations in the far field are given in Table 2.1. However, as will be discussed in Section 7.3, the actual pressure in front of the far field sampling skimmer was higher than the global tank pressure given here. Thus, the mean free paths will be shorter and the collision probabilities higher. This effect is dependant on the angle at which the thruster is positioned (See Table 7.1).

	Corrected Tank Pressure [Torr]	Mean Free Path [m]	0.5 m Collision Probability	1.0 m Collision Probability
Diffusion Pumps	$5.0 * 10^{-5}$	1.0	38.5%	62.2%
Cryopumps	$5.5 * 10^{-6}$	9.1	5.4%	10.4%

Table 2.1. Influence of Chamber Pressure on Ion-Neutral Collisions

Whereas previous research concentrated on a single thruster operating point, this work looks at three operational conditions to determine how changing the discharge voltage and current affects the ion energy distributions. This knowledge will be critical to any user who wishes to vary the operational characteristics of the Hall thruster in order to perform different missions. The operational characteristics investigated are summarized in Table 2.2. Condition 1 represents running the thruster in a mode similar to a 1.5 kW Hall thruster such as the SPT-100 or D-55 TAL. Condition 3 is the full power 5 kW case. Condition 2 is an intermediate case that shares a current with Condition 1 and a voltage with Condition 3, allowing for comparisons while changing only one variable.

	Discharge Voltage [V]	Discharge Current [A]	Total Flow Rate [sccm]	Tank Pressure [Torr]
Condition 1	300	5.3	64	$5.5*10^{-6}$
Condition 2	500	5.3	64	$5.5*10^{-6}$
Condition 3	500	10.0	111	$8.5*10^{-6}$

Table 2.2. Thruster Operating Points

By interrogating the ion energy in the near field region (~10 cm from the end of the discharge chamber) and the very near field (~1 cm from the end of the discharge chamber) and comparing it to far field measurements taken beyond 50 cm from the thruster, insight into the evolution and structure of the ion energy distributions can be obtained. To allow for near field measurements of the plume, an extension was created that moved the sampling orifice closer to the thruster without moving the thruster closer to the end of the vacuum chamber. Operating the thruster within 50 cm of the end of the vacuum chamber causes excessive sputtering of wall materials and can result in electrical shorts in the thruster, especially at a discharge current of 10 A. Details of the sampling orifice are given in Section 2.3.4

2.3.1. Ion Energy Measurements

The 45-degree energy analyzer, shown in Figure 2.28, is an electrostatic filter that passes ions of a specific energy-per-charge to a detector. The ions enter through a slit and experience a constant electric field of magnitude V_p/d at an angle of $90^{\circ}-q$ with respect to the direction of travel, providing a constant acceleration in the negative y direction (field correction plates prevent field distortion due to the surrounding ground potential). The ions experience a parabolic trajectory given by the equation:

EQN 2.4 $$y = x - \frac{q_i e V_p}{2dm_i} \frac{x^2}{v_i^2 \sin^2 q}.$$

The origin of the coordinate system is the center of the entrance slit.

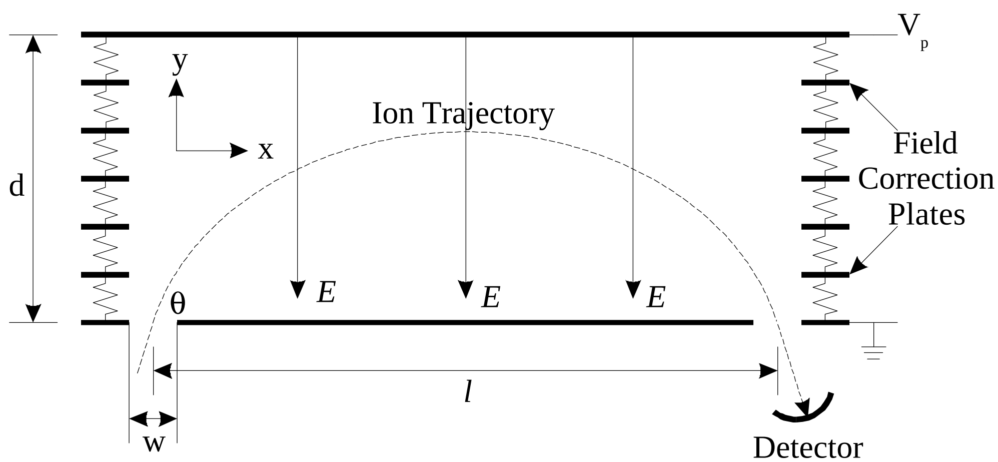

Figure 2.28. Schematic of 45-Degree Energy Analyzer

Substituting the kinetic energy of the ion, $E_i = ½\, m_i v_i^2$, for the ion velocity and setting $q = 45°$, the resulting trajectory is given by:

EQN 2.5 $$y = x - \frac{V_p}{2d} \frac{x^2}{\left(E_i \big/ q_i e \right)}.$$

For an ion to reach the detector, it must pass through the exit slit located at the point $x = l$, $y = 0$. This condition defines the 45 degree spectrometer constant, K_{45}, as:

EQN 2.6 $$K_{45} = \frac{V_p}{\left(E_i \big/ q_i e \right)} = \frac{2d}{l}.$$

Therefore, for a given pass voltage, V_p, only ions with the energy-to-charge ratio of $E_i/q_i e$ will reach the detector. The ion velocity from EQN 1.3 can be inserted into the ion kinetic energy equation to show that $E_i = q_i e V_i$. This allows EQN 2.6 to be rewritten as:

EQN 2.7 $$K_{45} = \frac{V_p}{V_i} = \frac{2d}{l}.$$

Since the plume of a Hall thruster consists of ions with different charges, EQN 2.7 has important consequences for the measurement of ion energy distributions with the 45-degree energy analyzer. A singly charged ion, accelerated to a velocity, v_i, by a given accelerating potential, V_i, will reach the detector if the pass voltage is $K_{45}V_i$. However, a doubly charged ion, accelerated to $\sqrt{2}v_i$ by the same potential (from EQN 1.3), will also reach the detector because it has the same energy-to-charge ratio E_i/q_ie. This fact is key when analyzing ion energy spectra from the 45-degree energy analyzer, since it indicates that the only way that a multiply charged ion can be directly measured is if it undergoes a collision with another ion or neutral atom within the plasma that alters its energy or charge state.

Due to the large path lengths necessary for time-of-flight mass spectroscopy (as described in Section 2.3.2), there is a considerable amount of expansion of the plasma before it reaches the detector. Therefore, a sensitive current detector was needed in order to measure the low level signals. The detector used was a K and M Electronics model 7550m ceramic channel electron multiplier (CEM) capable of amplifying input ion current by up to 1.2 x 10^8 with a maximum output current of approximately 5 μA. A large negative potential (ranging from –1600 V to –2000V, depending on the desired gain) is placed upon the inlet of the semiconducting CEM collection channel. This high negative potential draws ions into the CEM at high energies while repelling electrons. When the ions impact on the channel walls, which are coated by a material (proprietary to K and M Electronics) that has a high secondary electron impact yield due to ions and electrons, they eject a number of secondary electrons. These electrons climb toward the channel exit (which is grounded), impacting on the walls and ejecting more electrons as they go – thereby amplifying the current. Since the number of secondary electrons ejected by a collision is a function of the material properties of the channel coating material and not the charge of the ion, a doubly charged ion will produce the same amount of current as a singly charged ion. Thus, unlike electrostatic probes, the CEM does not measure charge but rather ion impacts.

The current output from the CEM was measured using a Keithley model 486 Picoammeter, with an overall range of 2 fA to 2 mA. The accuracy of the picoammeter varied with measurement range: ± 0.3% at 2 nA, ± 0.2% at 20 nA, and ± 0.15% at 200 nA and 2 μA. The pass voltage was provided using a Keithley model 2410 SourceMeter that was swept from 0 to 1000 V in to provide a complete spectrum of ion energy data. This sourcemeter had a rated accuracy of better than 0.012% over the full range of interest. The output from both instruments was fed into a computer based data acquisition system for recording and processing. A complete system schematic is shown in Figure 2.29.

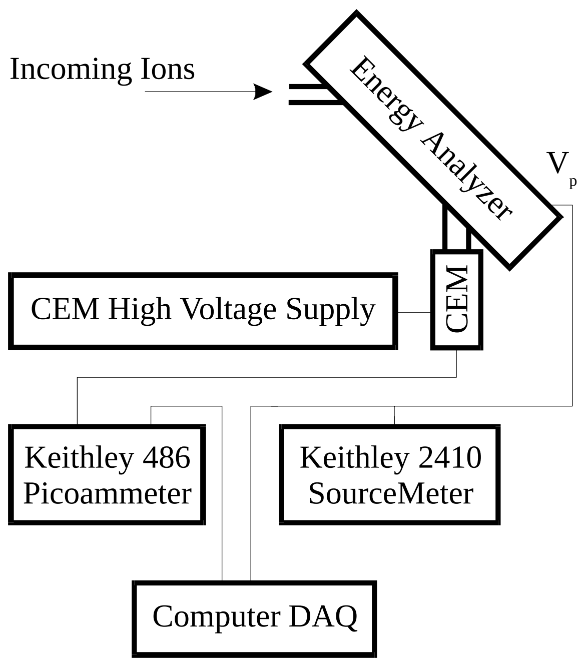

Figure 2.29. Ion Energy Component Schematic

The analyzer itself was constructed from 1.5 mm thick aluminum plates. The slotted field correction plates were used to eliminate field distortion due to the grounded vacuum chamber walls and ensure a homogenous electric field. They were biased using a resistor-string voltage divider to maintain the proper field. The entire analyzer was mounted on a frame of nylon threaded rod and inserted into a section of vacuum chamber consisting of two off-the-shelf 20.3 cm outer diameter by 40.6 cm long ConFlat fittings.

The depth of the analyzer, *d*, must be great enough to ensure that the ions do not impact the repelling plate of the energy analyzer. This value can be determined by combining EQN 2.5 and EQN 2.6 to give:

EQN 2.8

$$y = x - \frac{x^2}{l}.$$

Therefore, for $y < d$ at the apex of the parabola, $x = l/2$, the depth must be greater than ¼ the length, $d > l/4$.

The resolution of the energy analyzer is based on the fact that the finite width of the slots allows ions to enter at non-nominal trajectories and still reach the detector. The resolution is given by:

EQN 2.9

$$\frac{\Delta V_i}{V_i} = \frac{w \sin q}{l}.$$

Combining a desired resolution of less than 0.5% error with the calculations for depth and the physical dimensions of the vacuum chamber sections gives the dimensions of the 45-degree energy analyzer. These values along with the other relevant parameters are given in Table 2.3.

Parameter	Value
Depth, *d*	160 mm
Length, *l*	584 mm
Slot Width, *w*	3 mm
Spectrometer Constant, K_{45}	0.549
Resolution, DV_i/V_i	0.004

Table 2.3. 45-Degree Energy Analyzer Parameters

2.3.2. Time-of-flight Mass Measurements

Time-of-flight mass spectroscopy is based on the simple principle that particles traveling at different velocities will transverse the same path length in different times:

EQN 2.10
$$t_{tof} = \frac{d_{tof}}{v_i} .$$

The ion velocity from EQN 1.3 can be substituted into EQN 2.10 and combined with the definition, $m_i = M_i m_p$, where M_i is the atomic mass number and m_p is the proton mass to give:

EQN 2.11
$$\frac{d_{tof}^2}{t_{tof}^2} = \frac{2q_i eV_i}{M_i m_p} = \frac{2E_i}{M_i m_p}$$

which holds for all time-of-flight mass spectrometers. However, as described in Section 2.3.1, a 45 degree energy analyzer is used to admit only ions of the set energy-to-charge ratio $E_i/q_i e = V_i$ to the detector. Therefore, using the definition of the 45-degree spectrometer constant from EQN 2.7, we can relate the ion's flight time to their mass-to-charge ratio as:

EQN 2.12
$$\frac{M_i}{q_i} = \frac{2eV_p}{m_p K_{45} d_{tof}^2} t_{tof}^2 .$$

From this relationship, we can see that there are two mechanisms by which ions flowing through the time-of-flight mass spectrometer can achieve different velocities and arrive at the detector at different times: by having different masses, M_i, or by having different charges, q_i.

Ions of different masses arise from separate atomic species. For example, if a Hall thruster were to be operated with a propellant mixture of xenon and argon[37] (to lower the propellant cost), a majority of the discharge plume would consist of singly ionized xenon and singly ionized argon. Both ions will be accelerated by the same potential, V_i, (perhaps differing slightly due to the difference in ionization potential between the two species) and will therefore pass through the 45-degree energy analyzer at the same pass voltage. However, since the masses of the ions are different - 131.3 AMU for xenon and 39.9 AMU for argon - we see from EQN 1.3 that they will travel at different velocities. Thus, the argon ions will arrive at the detector in 55% of the time that it takes the xenon ions to arrive.

The second mechanism for ion separation is difference in charge. This allows for the interrogation of multiply charged species within the plume of a Hall thruster. For example, if both singly and doubly charged xenon ions are formed at the same location within the Hall thruster, they will see the same accelerating potential. Since they see the same accelerating potential (and thus have the same energy-to-charge ratio $V_i = E_i/q_i e$), they will both pass through the 45-degree energy analyzer at the same pass voltage. However, the doubly charge xenon will be accelerated to a velocity that is $\sqrt{2}$ times greater than the singly charged xenon and will arrive at the detector first. The difference in velocity due to the difference in mass between the two ions, the mass of an electron, is negligible.

To obtain mass-to-charge spectra, the ion beam entering the mass spectrometer is pulsed using a high voltage electrostatic beam gate. Two different gates were used; one for far field measurements, the details of which are given in Section 2.3.3, and one for near field and very near field measurements that will be discussed in Section 2.3.4. Both operated by creating an electric field perpendicular to the ion beam path that deflects the beam into the MBMS chamber wall. The gate is opened by removing the potential across it, allowing ions to flow freely toward the detector. The distance from the front of the beam gate to the detector is the time-of-flight length, d_{tof}, and the opening of the gate marks the beginning of the time-of-flight period, t_{tof}. When the ions reach the 45-degree energy analyzer, only those ions meeting the pass voltage criteria are transmitted through to the detector. Recording the output of the detector on an oscilloscope, we see the ions arriving grouped according to their mass-to-charge ratio. Thus, individual peaks of the spectra represent either ions of different mass or different charge. By varying the pass voltage of the 45-degree energy analyzer, mass-to-charge spectra can be measured over a wide range of ion energies.

The design of the time-of-flight system is strongly dependent on desired resolution and can be influenced by knowledge of the species expected in the plume. The key component of the system is the gate; its method of operation is shown in Figure 2.30. Before the gate is opened at t = 0, all ions are deflected by the electric field so that they do not reach the detector. When the gate is opened, ions already within the gate, between points 1 and 2, have already begun to deflect and thus will not reach the detector. The first ions to reach the detector are those located at point 1, which reach the detector after travelling a distance d_{tof}. When the gate is closed at $t = t_{gate}$, ions within the gate will be deflected and will not reach the detector. Thus the last ions to reach the detector will be those located at point 2. The distance between point 1 and point 2 is equal to the length of the gate, d_{gate} and so these trailing edge ions will only have traveled a distance d_{tof} - d_{gate}.

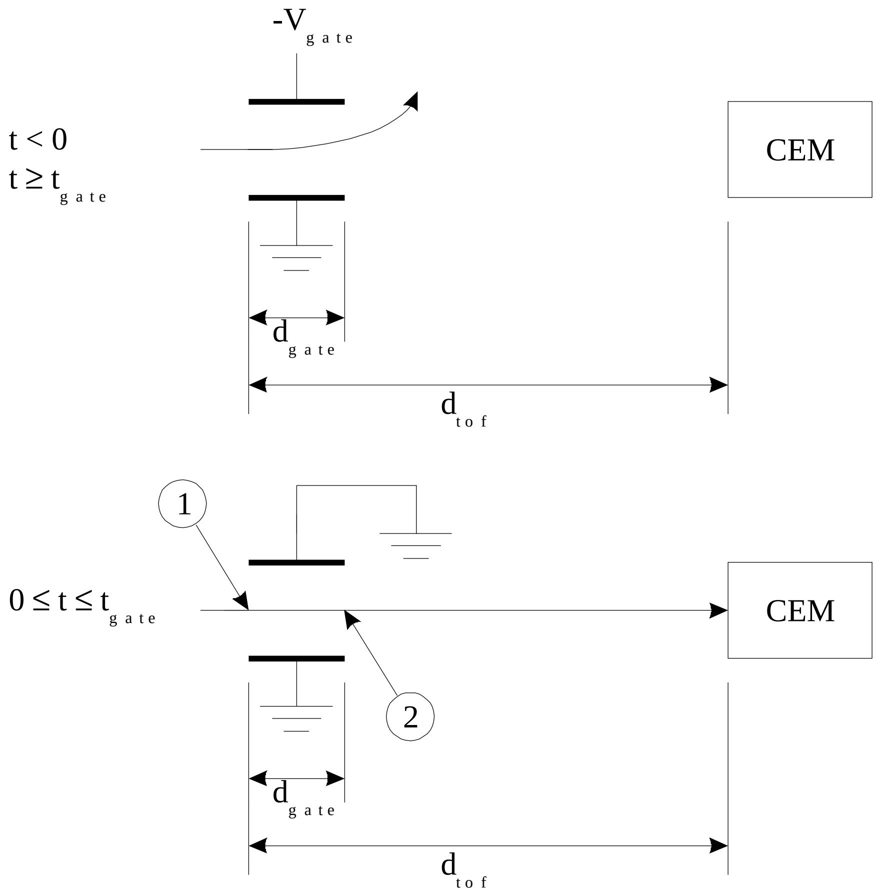

Figure 2.30. Time-of-flight Gating Scheme

When the ions reach the detector, a spectrum like the simplified and idealized one shown in Figure 2.31 is obtained. This figure shows two ions X_0 and X_1. The width of an ion pulse is dependant on both the time that the gate is open and its length. The leading edge of the pulse travels a length d_{tof} and arrives at time t_{tof}. The trailing edge of the pulse, however, only travels a distance d_{tof} - d_{gate}, and thus arrives at the detector at a time:

EQN 2.13 $$t = t_{gate} + \frac{d_{tof} - d_{gate}}{v_i} = t_{gate} + t_{tof} - t_d$$

with t_d defined as the time it takes an ion to traverse the gate. Therefore the width of the pulse from the leading edge to the trailing edge is t_{gate} - t_d. If the pulse is wide, that is $t_{gate} >> t_d$, the pulse will be transmitted at full intensity and the ratio of ion currents can be used to determine the ratio of species densities. If the pulse is narrower, such that t_{gate} is only slightly longer than t_d, the pulse will not have ample time to fully transmit and the trailing edge will be clipped. The resultant ion current will not properly reflect species density.

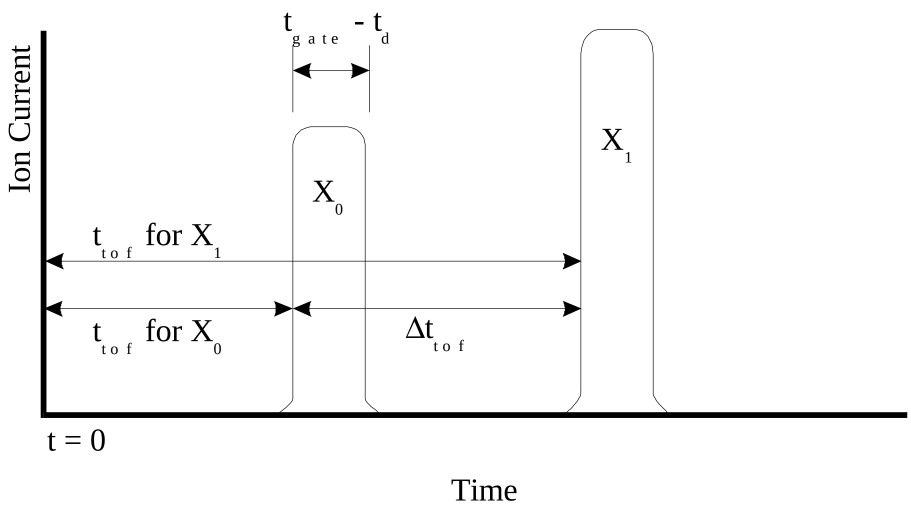

Figure 2.31. Idealized Time-of-flight Spectrum

There is, unfortunately, a competing criterion for the length of the gate pulse. From Figure 2.31, we see that the time between the arrival of the two mass peaks is Dt_{tof}. If the gate pulse is made too long, such that t_{gate} - t_d is greater than Dt_{tof}, the trailing edge of X_1 will merge with the leading edge of X_0 and the peaks will be unresolvable. Thus, a balance must be struck between having a gate pulse that is long enough to allow full transmission of each ion pulse while being short enough to prevent a loss of mass (or charge) resolution. This can be expressed quantitatively.

First, the gate time must be much larger than the time that it takes for the slowest, and therefore heaviest or lowest charged, ion to pass through the gate:

EQN 2.14 $$t_{gate-\min} >> \frac{d_{gate}}{v_i} = d_{gate}\sqrt{\frac{m_p}{2eV_i}\left(\frac{M_i}{q_i}\right)_{MAX}}\ .$$

Second, the gate time must be shorter than the time between the arrival of adjacent ion pulses. Thus, it must be less than Dt_{tof}:

EQN 2.15 $$t_{gate} < \Delta t_{tof} = d_{tof}\sqrt{\frac{m_p}{2eV_i}}\left(\sqrt{\frac{M_1}{q_1}} - \sqrt{\frac{M_0}{q_0}}\right) = C_1(V_i)\left(\sqrt{\frac{M_1}{q_1}} - \sqrt{\frac{M_0}{q_0}}\right)$$

where $C_1(V_i)$ is constant for a given accelerating potential. Examining EQN 2.15 we see that, as expected, this criterion is most restrictive if the ions have similar velocities, that is $M_1/q_1 \cong M_0/q_0$. Assuming that a resolution of both at least one AMU and one unit charge is desired, unless very light ions or very high charge states are being investigated, a change of 1 AMU will result in a smaller velocity spread and a greater restriction. For example, taking a fictitious singly charged ion with a mass of 100 AMU (which is the general region of interest for electrostatic thruster propellants) we see that the time of flight difference between it and a doubly charged ion of the same atom will be $Dt_{tof} = 2.93C_1(V_i)$. If instead we wish to detect the difference between the singly charged ion with a mass of 100 AMU and a singly charged ion with a mass of 99 AMU, the time of flight difference will be $Dt_{tof} = 0.05C_1(V_i)$. Thus, the criterion is set by the more restrictive case where two ions of the same charge state differ by one AMU ($M_1 = M_0 + 1$, $q_1 = q_0$):

EQN 2.16 $$t_{gate} < \Delta t_{tof} = d_{tof}\sqrt{\frac{m_p}{2eV_i}}\left(\sqrt{\frac{M_1}{q_1}} - \sqrt{\frac{M_1-1}{q_1}}\right).$$

The gate time from EQN 2.16 is minimized for heavy ions such. This gives the maximum gate time for one AMU resolution of heavy ions:

EQN 2.17 $$t_{gate-\max} < d_{tof}\sqrt{\frac{m_p}{2eV_i}}\left(\sqrt{\left(\frac{M_i}{q_i}\right)_{MAX}} - \sqrt{\left(\frac{M_i-1}{q_i}\right)_{MAX}}\right).$$

Using EQN 2.14 and EQN 2.17 together, the gate time is bounded:

EQN 2.18

$$d_{gate}\sqrt{\frac{m_p}{2eV_i}\left(\frac{M_i}{q_i}\right)_{MAX}} < t_{gate} < d_{tof}\sqrt{\frac{m_p}{2eV_i}}\left(\sqrt{\left(\frac{M_i}{q_i}\right)_{MAX}} - \sqrt{\left(\frac{M_i - 1}{q_i}\right)_{MAX}}\right).$$

From EQN 2.18, a relationship between the length of the gate and the time-of-flight drift length can be determined:

EQN 2.19

$$\frac{d_{gate}}{d_{tof}} < 1 - \sqrt{\frac{M_{MAX} - 1}{M_{MAX}}}$$

which dictates the geometry of the time-of-flight system given the assumption that the heaviest ions in the flow must be resolved to within one AMU and that all ions have the same charge.

With the determination of a gate length, the other parameters of the gate can be related. When a constant electric field is applied across the gate region, an ideal ion beam will deflect as shown in Figure 2.32 and the deflection within the gate can be related to the gate voltage using:

EQN 2.20

$$\frac{V_{gate}}{y_{gate}} = \frac{4sV_i}{d_{gate}^2}$$

where s is the width of the gate, y_{gate} is the ion beam deflection within the gate, and d_s is the diameter of the sampling skimmer - which in the ideal case will be equal to the diameter of the beam. In order for the gate to be closed, the beam must deflect sufficiently that it does not enter the 45-degree energy analyzer, the opening of which has a width with respect to the ion beam of 0.707w, or 2.12 mm.

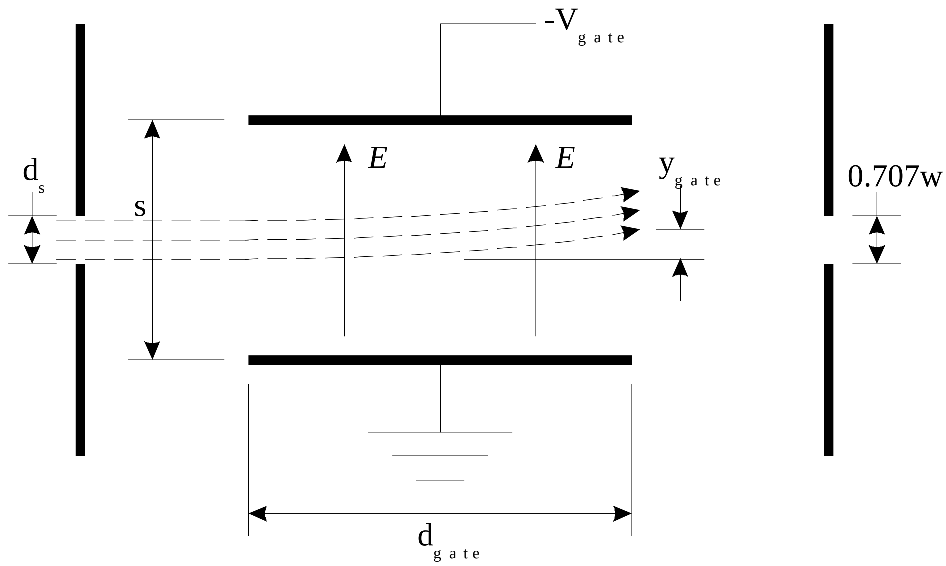

Figure 2.32. Ideal electrostatic beam gate

The gate voltage was supplied by a Directed Energy, Inc. GRX-3 high voltage pulser, capable of producing square output pulses with an amplitude of ± 3kV with a rise time of 20 ns and a settling time of 40 ns. A BK Precision Model 3300 low voltage pulse generator was used to set the pulse duration and duty cycle. High voltage was supplied by an external, custom-built, power supply. The gate pulse was used to trigger a Tektronix TDS-540 digital oscilloscope via a Tektronix P6015A 1000-to-1 voltage probe to begin time-of-flight data acquisition. This information was transferred to a computer based data acquisition system for recording and processing. A complete system schematic is shown in Figure 2.33.

The short pulse duration needed for high resolution time-of-flight mass spectrometry results in a very low current level reaching the detector. It was therefore necessary to use a two-stage high-speed, high-gain current to voltage amplifier[34] to boost the signal output of the CEM before sending it to the oscilloscope. Pulses ranged from 1 nA to 1 μA with durations on the order of 1 μs. The first stage pre-amplifier was a low noise, high frequency Amptek model A250 amplifier. The A250 was configured as a transimpedance (current-to-voltage) amplifier by using a feedback resistor that gave a resulting output voltage of $V_{A250} = I_{cem}R_{feedback}$. A feedback capacitor is necessary to prevent unstable amplifier oscillations. This capacitor/resistor combination sets the frequency response of the output pulse as $f = (R_{feedback}C_{feedback})^{-1}$. Thus, increasing the gain of the amplifier lowers its frequency response. The components ($R_{feedback}$ = 50 kΩ, $C_{feedback}$ = 2 pF) gave a response of 10 MHz and a gain of 50 V/mA. This gain was insufficient for detection, so a second amplifier was needed. This post-amplifier was an Analog Devices AD829 op-amp. It provided a voltage-to-voltage amplification of 50. This gave an overall amplification of 2.5 V/μA for this two-stage amplifier. Combined with the maximum gain of the electron multiplier, the time-of-flight system had a maximum amplification of 300 V/pA of ion beam current.

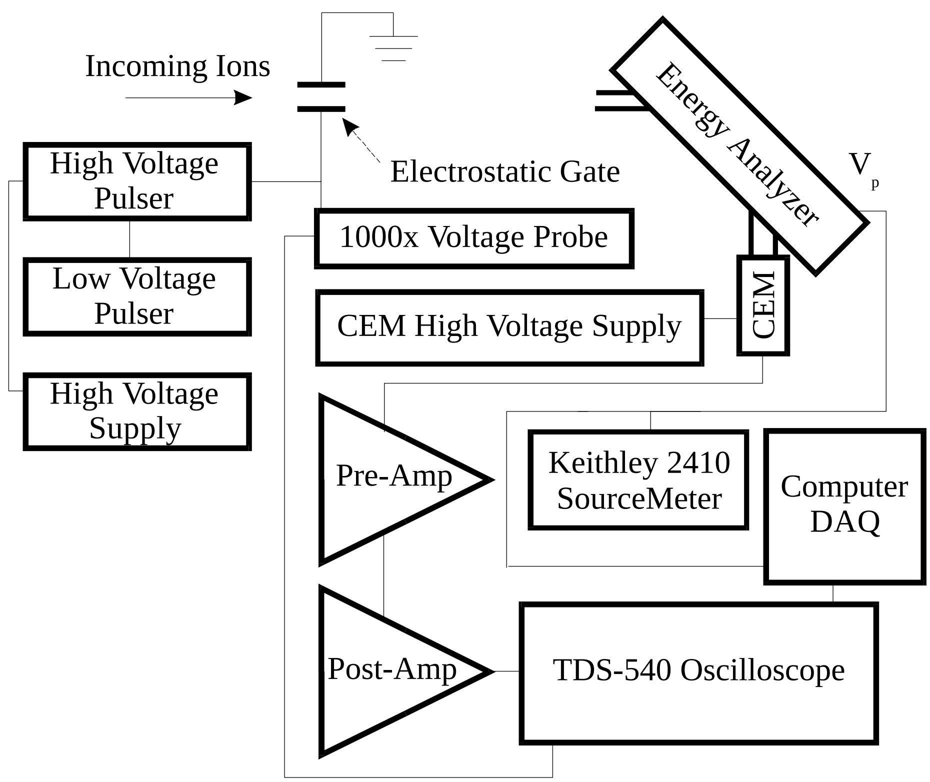

Figure 2.33. Time-of-flight Component Schematic

Of significant concern for these measurements was the lack of calibrated ion sources for ions of the energies examined in this work. Without such a source, it would not be possible to determine if the spectrometer constant, K_{45}, was correct, so that the values of pass voltage programmed into the sourcemeter correspond to the proper accelerating potentials (See EQN 2.7). However, the time-of-flight measurements convert peak arrival time to mass-to-charge ratio using EQN 2.12, which also contains the spectrometer constant. If the spectrometer constant were incorrect, the peaks would not arrive at the proper mass-to-charge ratio (which they do). Therefore, there is an independent check, if not a calibration, of the spectrometer constant.

2.3.3. Far Field Configuration

The configuration of the far field ion energy and time-of-flight system was driven by requirements of the high frequency time-of-flight system. A baseline time-of-flight of approximately 100 μs for the heaviest, slowest ion species was chosen based on available instrumentation. Singly ionized xenon is the slowest species under investigation, and a nominal ion acceleration of 300 V results in velocities on the order of 20000 m/s. This gives a nominal flight path of 2 m. Constructing the system of off-the-shelf vacuum hardware resulted in a far-field time-of-flight path length, d_{tof} = 2.34 m. A schematic of the system is shown in Figure 2.34.

Two oil diffusion pumps were used to differentially pump the system. The first, located upstream of the energy analyzer was a Varian model HS-10 10 inch diffusion pump. The second, located beneath the energy analyzer was a Varian model M6 6 inch pump. These were fitted with water cooled inlet baffles to minimize oil backstreaming into the MBMS and backed by a Kinney model KDH-80 80-cfm rotary mechanical pump. Pressure inside the MBMS was measured using a Varian model 531 thermocouple gauge monitored by a Varian model 801 thermocouple gauge display and two Varian model 571 ionization gauges monitored by Varian BA senTorr Vacuum Gauge

Controllers. An eight inch gate valve was placed between the MBMS and the LVTF to allow them to be pumped and vented independently.

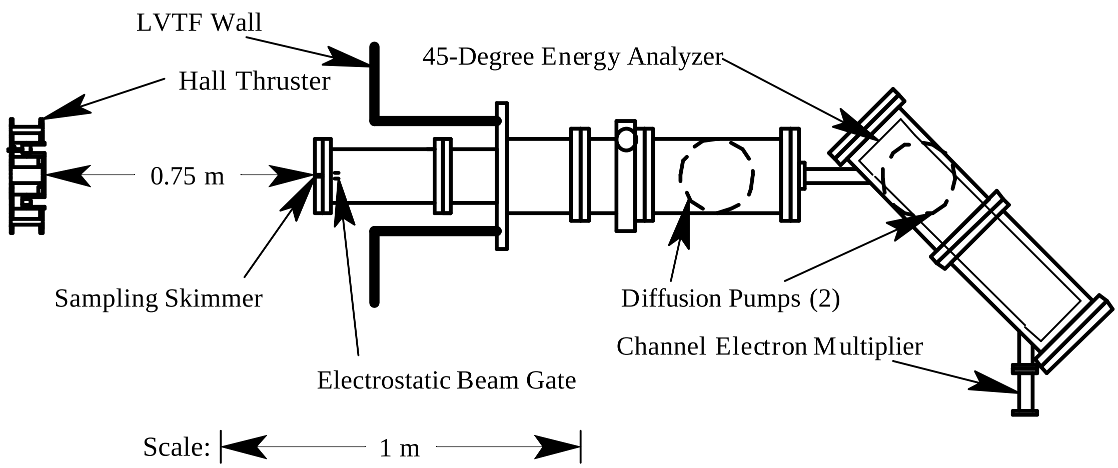

Figure 2.34. Far Field Configuration Schematic (Top View)

With a time-of-flight path length chosen, a starting point for gate design can be determined. Choosing xenon with M_{MAX} = 131 AMU, EQN 2.19 gives a d_{gate}/d_{tof} ratio of less than 0.0038; which for d_{tof} = 2.34 m gives a maximum gate length of 9 mm. The diameter of the sampling skimmer, d_s, was 5 mm which will also be the diameter of the beam. In order to ensure that the gate electrodes do not obscure the beam line, the electrode separation was set to s = 19 mm. Using EQN 2.20, the electric field within the gate, V_{gate}/s to deflect a 300 V ion by 2.12 mm to miss the entrance to the 45-degree energy analyzer would need to be at least 31000 V/m. For the separation of 19 mm, the gate repelling voltage would need to be on the order of 600 V.

However, the actual ion beam within the gate is not the ideal one shown in Figure 2.32. The beam will diverge upon entering the MBMS due to ionic repulsion as shown in Figure 2.35. The beam will continue to diverge within and beyond the gate, making an analytic solution for the gate voltage as in EQN 2.20 far more difficult. Instead, King tested the gate and determined that a gate voltage greater than -2000 V would be necessary to completely close the gate. This high voltage caused electric arcs across the gate and prevented normal operation of the system. From EQN 2.20, we see that in order to lower the gate voltage, it is necessary to increase the gate length.

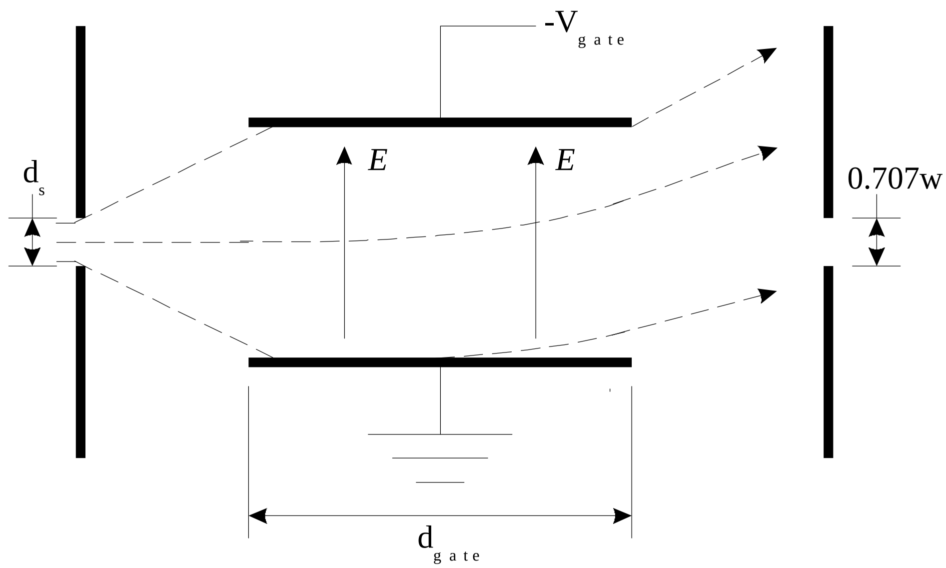

Figure 2.35. Real beam Gate with Ionic Repulsion

After testing several configurations, it was determined that a gate width of 13 mm would be sufficient to properly close the gate without arcing using a gate voltage of approximately -1500 V. This gave a d_{gate}/d_{tof} ratio of 0.0055. Thus, it is no longer possible to resolve ions in the range of 131 AMU to within one AMU and still transmit the peak at full intensity. Since the primary goal of this part of the study was to investigate the relative concentration of xenon charge states (which requires transmission at full intensity) and not isotopes that differ by one AMU, the more restrictive criterion of a one AMU resolution can be dropped by increasing t_{gate} to provide ample time for the ions to pass through the longer gate. To check that the necessary charge resolution is still available, we use EQN 2.14 and EQN 2.15 to reformulate EQN 2.19 for ions that have the same mass but differ in charge by one unit ($M_1 = M_0$, $q_0 = q_1 + 1$) to give:

EQN 2.21
$$\frac{d_{gate}}{d_{tof}} < 1 - \sqrt{\frac{q_{MAX} - 1}{q_{MAX}}}\ .$$

The highest charge state xenon that has been experimentally observed in a Hall thruster was Xe^{4+} by Kim using an E X B probe.[38] Setting $q_{max} = 4$, gives $d_{gate}/d_{tof} < 0.13$, which is easily met by the system employed here.

Therefore, the gate time can be increased in order to prevent peak clipping. Ion peaks will still arrive at the same time as specified by EQN 2.12, but will now have a width of several AMU/unit charge. The minimum gate time must be set to ensure that the slowest ions are transmitted at full intensity. This is determined by setting an acceleration voltage, V_i, of 100 V in EQN 2.14 for singly charged xenon. This gives a minimum gate time, $t_{gate\text{-}min} = 1.1$ μs. Similarly, a maximum gate time can be determined from EQN 2.15, using $q_1 = 3$ and $q_0 = 4$, to give $t_{gate\text{-}max} = 15$ μs. The only additional constraint is the overall time constant of the amplifier system, which is on the order of 50 μs. The maximum gate time is less than this, so amplifier response will not be a problem.

The final configuration for far field time-of-flight measurements is summarized in Table 2.4.

Parameter	Value
Time-of-flight Length, d_{tof}	2.34 m
Gate Length, d_{gate}	13 mm
Gate Width, s	19 mm
Collection Skimmer Diameter, d_s	5 mm
Energy Analyzer Entrance Width, $w\sin 45°$	2.12 mm

Table 2.4. Time-of-flight System Parameters

Far field measurements were attempted at three axial locations: 1.0 m, 75 cm, and 50 cm. At 1.0 m, Ion energy measurements were made successfully at all three thruster conditions. However, signal levels were too low to successfully take time-of-flight measurements. At 50 cm, there was sufficient signal for time-of-flight measurements but at this axial location - especially at the higher power Conditions 2 (5.3 A, 500 V) and 3 (10 A, 500 V) - the thruster reacted badly to being operated in such close proximity to the end of the chamber. Thruster current would increase by approximately 20% when the thruster was turned directly toward the flange on which the sampling skimmer was mounted. It is believed that this effect resulted from xenon propellant being neutralized by collisions with the flange, then drifting back upstream to enter the thruster and be ionized again. Thus the anode mass flow rate was artificially increased and as demonstrated in Figure 2.26, increased anode mass flow rate leads to increased current. Post-experimental inspection of the thruster indicated that it had been sputter coated by materials from the end-cap region of the chamber, including stainless steel and Graphoil sheeting used for protection of chamber surfaces. Therefore, further runs were not made at 50 cm, and a compromise location of 75 cm was chosen. Both ion energy and time-of-flight measurements were successfully made at this location, and this was used for all further far field measurements.

As an aside, modifications to King's far field configuration were attempted to increase system resolution. A new gate was designed, built, and tested. This gate employed a set of parallel grids oriented 10° to the perpendicular to the flow, as shown in Figure 2.36. A large positive potential was applied to the first grid to repel, rather than deflect, the ion beam. The second grid was grounded to provide an end to the gate. The grids were placed at an angle to prevent ions formed beyond the first grid (by electron impact ionization) from being accelerated by the grid into the detector. This gate was significantly shorter than the original (6.5 mm as constructed) and thus theoretically could provide better resolution. Unfortunately, the grids perturbed and attenuated the flow to such a degree that no examination of resolution could be performed.

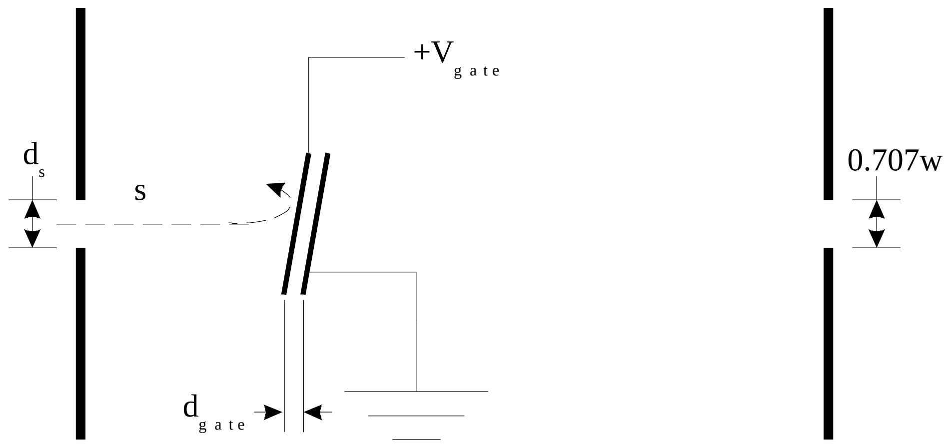

Figure 2.36. Repulsive gate concept

The primary signal loss mechanisms in the MBMS is beam expansion. Radial beam expansion can be determined by using ion beam expansion models that assume that all electrons are stripped from the beam as it enters the sampling skimmer.[39,40] Based on the ion density measured at 50 cm using the Langmuir probe for Condition 1 (see Figure 2.18), these models indicate that by the time the beam reached the detector, it would have expanded to approximately 360000 times the radius it had when it passed through the sampling skimmer. However, Langmuir probe measurements taken downstream of the sampling skimmer (i.e., within the MBMS), indicated the presence of electrons. Ion densities calculated from these measurements indicate a more conventional $1/z^2$ beam expansion. For this case, the beam expands to approximately 60 times the radius it had when passing through the skimmer. In either case, a vast percentage of the signal fails to reach the detector. To improve this, it was decided to develop a focusing lens for the gap between the skimmer and the 45-degree energy analyzer entrance slit. A single element electrostatic Einzel lens was chosen for its simplicity. An Einzel lens normally consists of three elements along the ion beam, the center one biased positive to the outer ones. However, since experiments showed that the influence of the outer electrodes on the centerline potential is negligible, they were omitted.[41,42] A positive potential applied to the center electrode will repel the ion beam from the wall, countering its expansion, and focusing it onto the detector. A three-dimension ion optics code, SIMION 3D Version 6.0, was used to simulate the effects of the lens on the ion beam. Unfortunately, uncertainties regarding the ion and electron densities within the drift section, coupled with difficulties determining the proper parameters for beam repulsion in the code, resulted in computational simulations that lacked sufficient detail. A lens was constructed from existing components and tested, but signal strength showed no noticeable improvement. Due to time constraints, work on the lens was abandoned. However, the concept remains valid and both ion energy and time-of-flight measurements would benefit from a properly implemented set of ion focusing optics.

2.3.4. Near Field Configuration

Based on the attempts to take far field data at 50 cm, it was decided that, rather than move the thruster closer to the orifice to make near field measurements, an extension to the system would be built. The extension, shown with the complete system in Figure 2.37 and in detail in Figure 2.38 added approximately 67 cm to the system.

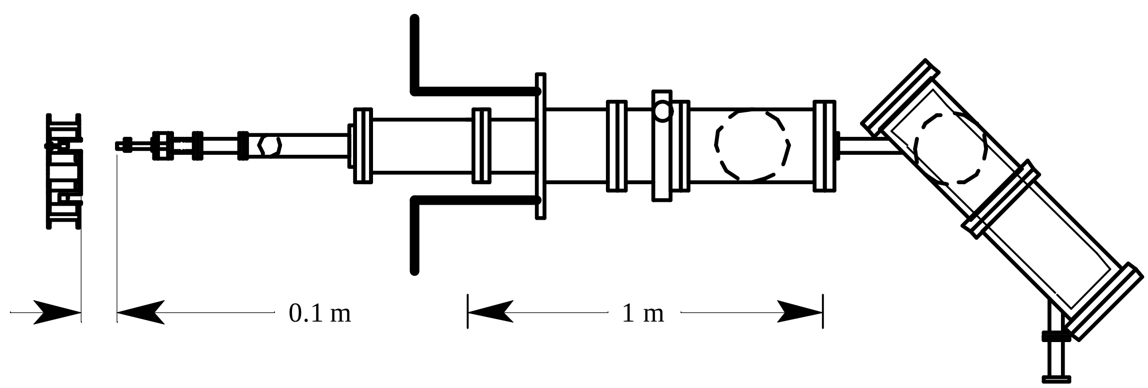

Figure 2.37. Near Field Configuration Schematic (Top View)

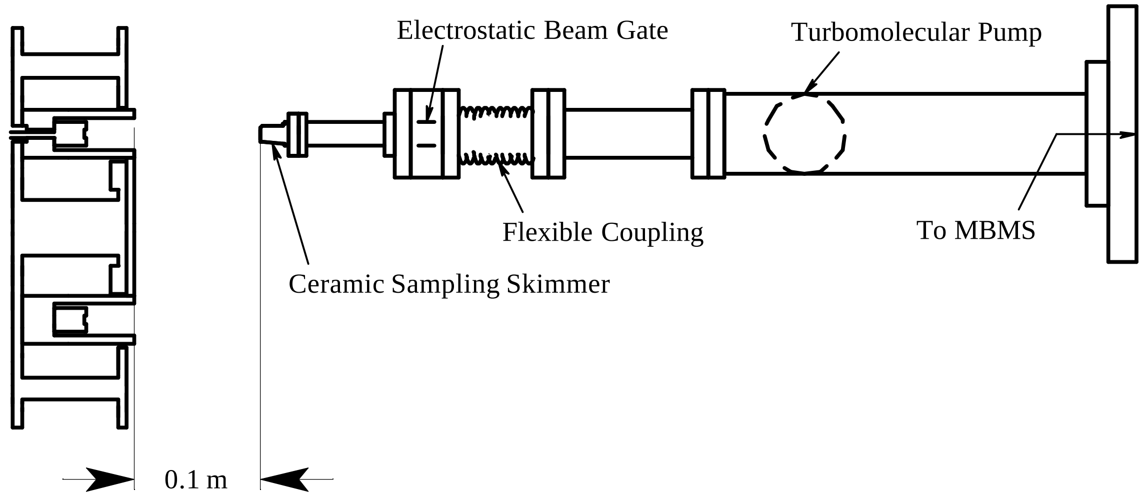

Figure 2.38. Sampling Skimmer for Near Field Configuration (Top View)

The near field skimmer was constructed from off-the-shelf vacuum components that necked down as they neared the thruster. The first section, which was connected to a Varian Model V70LP turbomolecular pump for differential pumping, had an outer diameter of 6.35 cm. The water cooled turbomolecular pump, rated at 68 l/s on nitrogen, used the LVTF itself as a backing pump and lowered the pressure within this section by a factor of 15. The next two components, including the flexible coupling, had an outer diameter of 3.81 cm. The flexible coupling was installed for two reasons. First, it made it possible to align the sampling orifice with the entrance slit to the 45-degree energy analyzer. Second, when the LVTF is pumped down to vacuum, the end cap contracts slightly inward. The sampling skimmer was fixed with respect to the thruster using an optics mounting post, and the flexible coupling took up the displacement of the end cap. The final section of hardware was 1.91 cm in diameter. On it was mounted a porcelain sampling skimmer with an orifice approximately 6.9 mm in diameter.

Obtaining time-of-flight data in the near field configuration presented additional difficulties due to gating problems. The first approach used the existing gate in its original, far field location. Unfortunately, due to the fact that the ion beam no longer passed through a skimmer directly in front of the gate it had expanded and overwhelmed the gate, preventing proper operation. The next approach was to place a skimmer in front of the gate, within the MBMS. This approach solved the opening and closing problem, but in this configuration the beam intensity was reduced due to expansion losses from a second orifice and collisions due to pressure build up in front of the orifice. It was finally decided that a new gate would need to be manufactured that could be placed near the new entrance orifice. The most practical location for the gate was within the 2.54 cm long Conflat flange section that was attached to the mounting post (See Figure 2.38). Placing a gate here would increase the time-of-flight length, d_{tof}, to 2.92 m. From EQN 2.19, we need a gate length of less than 11 mm for one AMU resolution of xenon. However, based on previous gate design experiences and given the nature of the desired data, it was decided to lengthen the gate and use the same gate dimensions that had been used in the original gate. The gate, shown in Figure 2.39, had a length of 13 mm and a width of 19 mm. The gate width was set to be larger than the inner diameter of the upstream section of the sampling skimmer to avoid interfering with the beam.

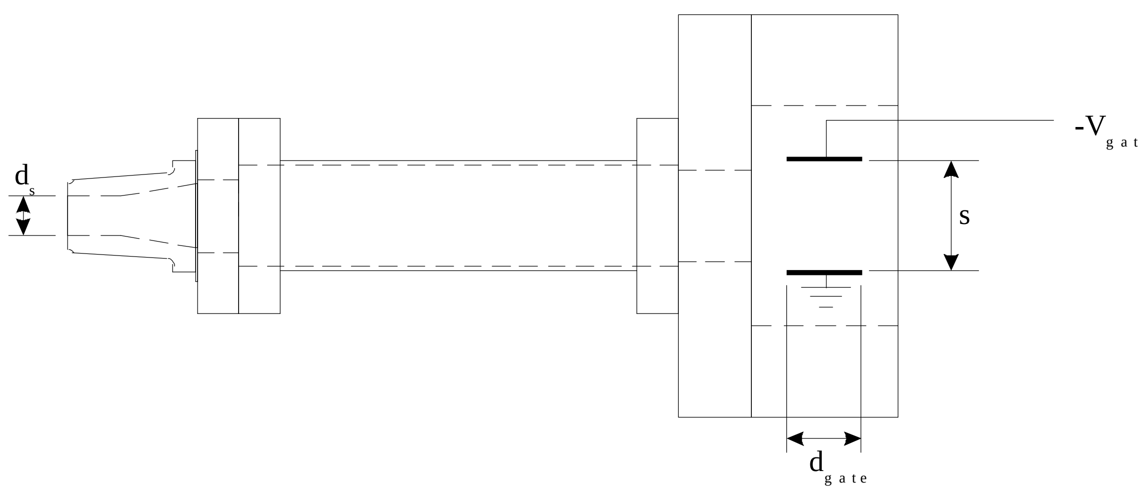

Figure 2.39. Miniaturized gate for Near Field Measurements

Using this near field skimmer system, ion energy measurements were successfully taken at all three operational conditions. The current rise from background propellant was small, approximately 4% of the discharge current. Time-of-flight measurements were taken at Condition 1 and Condition 2. However, when operating at Condition 3 (10 A, 500 V), the thruster current crept upward, due to the longer experimental times required for time-of-flight measurements.

2.3.5. Very Near Field Configuration

In an attempt to obtain measurements in the very near field region (1 cm), the system was again modified. It was decided not to move the thruster any closer to the near field sampling skimmer. Instead, the porcelain sampling tip was replaced by an alumina tube that provided an inlet 1 cm from the discharge chamber. The very near field configuration is shown in Figure 2.40, with the new sampling skimmer shown in Figure 2.41. The same gate configuration as in the near field case was used.

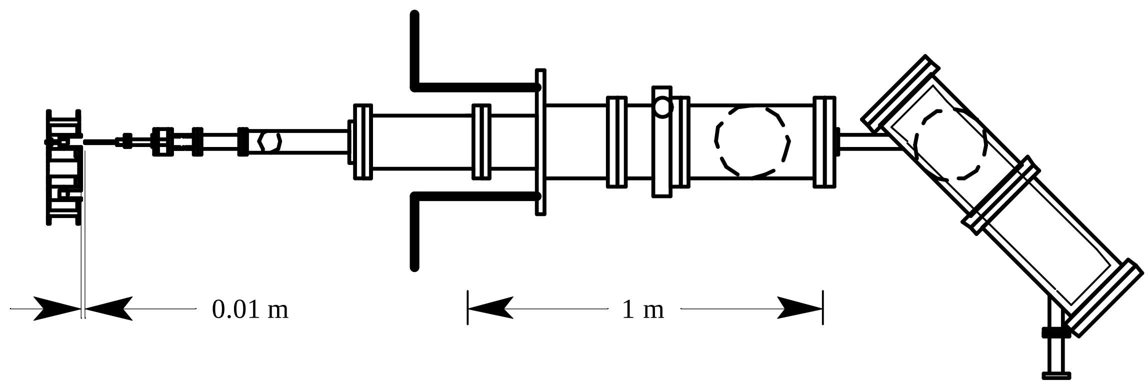

Figure 2.40. Very Near Field Configuration Schematic (Top View)

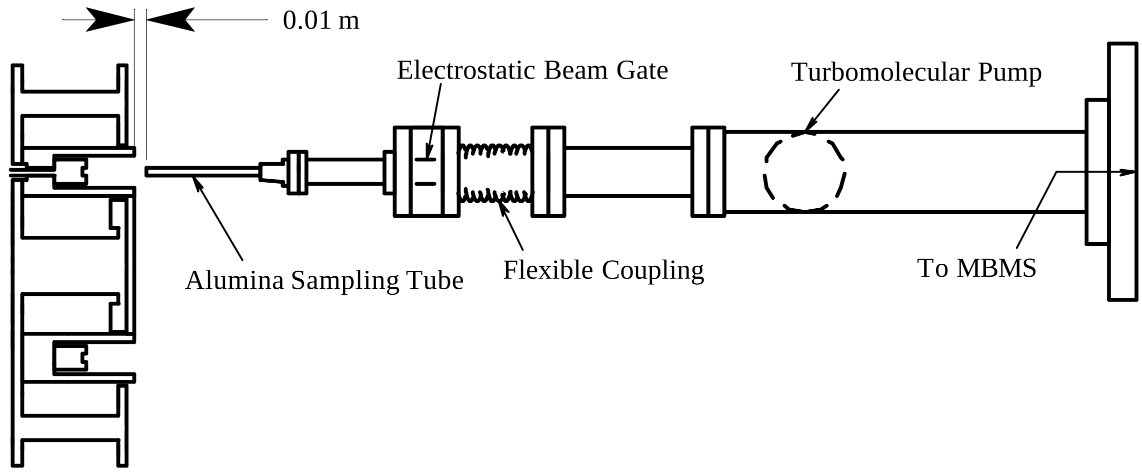

Figure 2.41. Sampling Skimmer for Very Near Field Configuration (Top View)

CHAPTER III

FAR FIELD MEASUREMENTS

Far field measurements were taken on the P5 using the system described in Section 2.3.3.

3.1. Ion Energy Measurements

Far field ion energy measurements were taken 75 cm from the thruster at three operating conditions (See Table 2.2). The thruster was mounted on a New England Affiliated Technologies (NEAT) model RT-6-SM rotary positioning table to allow it to be rotated from 0° until loss of signal (typically ~105°) as shown in Figure 3.1. This table had an angular accuracy of 0.05° and a repeatability of 0.007°. The center of rotation for far field measurements was the center of the thruster exit plane (Figure 3.1). Measurements were taken in 5° increments. The 45-degree pass voltage was swept from 0 to 1000 V in 1 V increments which, with a spectrometer constant of 0.549, gives a sweep of ion energy of 0 to 1800 V in 1.8 V increments.

The sampling orifice was aligned to the 45 degree energy analyzer entrance slit by passing a laser through the entrance slit such that it was parallel to the ion beam path. The orifice was then aligned to that beam. The thruster angle was set such that the laser was parallel to the face of the thruster when it was oriented at 90°. This alignment system improved positional accuracy to ± 0.5° (compared to the line-of-sight method used for the probe measurements described in Section 2.2). Other uncertainties arise from the test and measurement equipment. Values of Ion Energy/Unit Charge have an uncertainty of ± 0.4% due to the resolution of the 45-degree energy analyzer and

± 0.012% in the value of the pass voltage supplied by the Keithley sourcemeter. Values of the ion current have an uncertainty arising from the resolution of the Keithley picoammeter, which varies with the range used: ± 0.3% at 2 nA, ± 0.2% at 20 nA, and ± 0.15% at 200 nA and 2 μA.

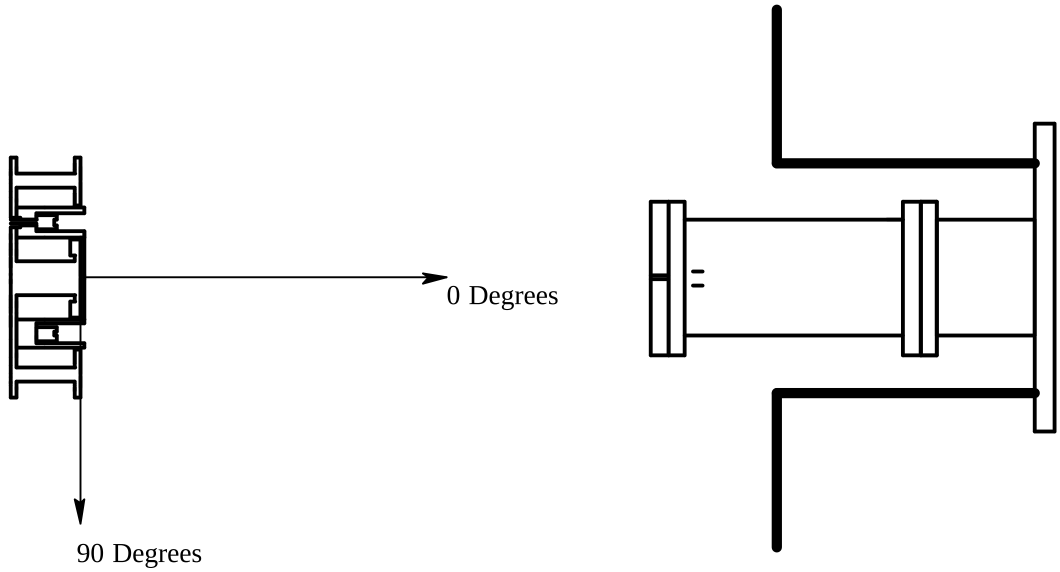

Figure 3.1. Far Field Rotational Configuration

Far field ion energy sweeps performed at Condition 1 are presented in Figure 3.2 through Figure 3.27. For this case, the thruster discharge voltage was 300 V, the discharge current was 5.2 A, the anode mass flow rate was 58 sccm, and the cathode flow rate was 6 sccm. The horizontal scale was decreased from 1800 V to 800 V and selected plots are also shown in semi-log scale to increase resolution.

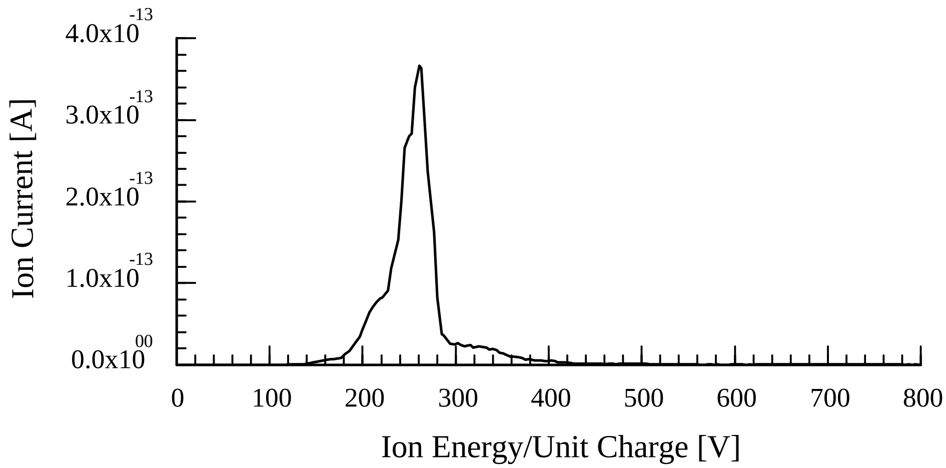

Figure 3.2. Far Field - Condition 1, 0 Degrees

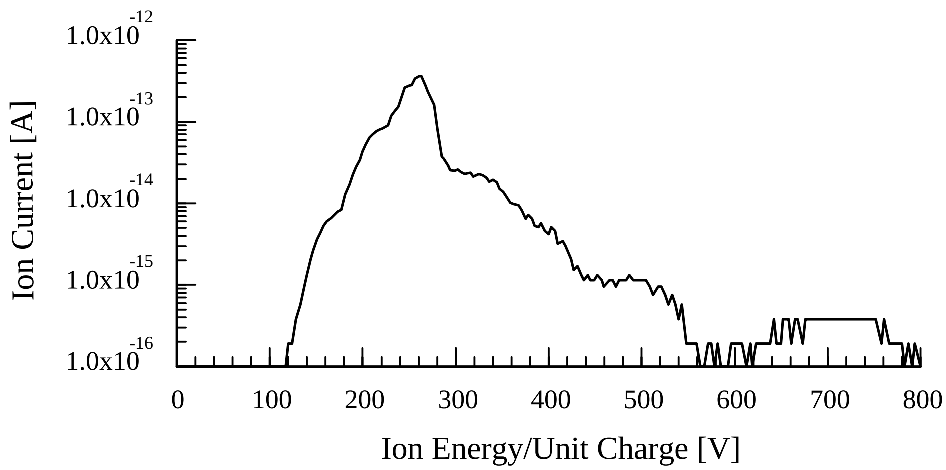

Figure 3.3. Far Field - Condition 1, 0 Degrees [Semi-log]

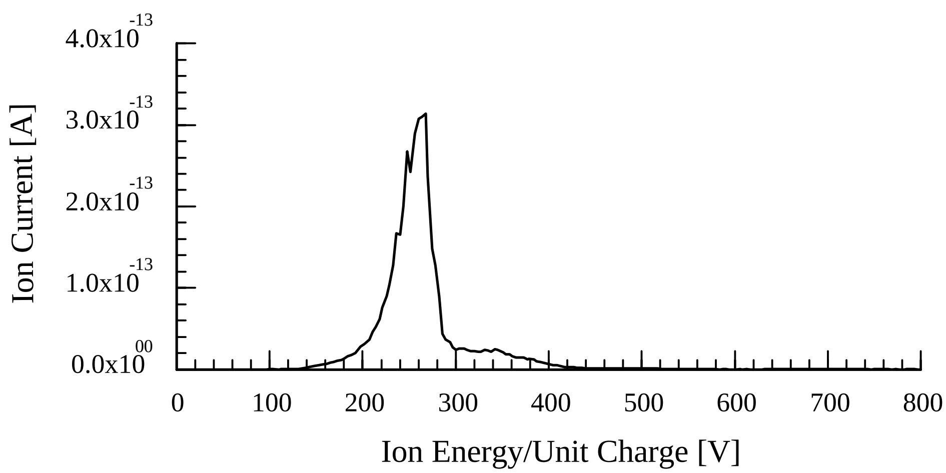

Figure 3.4. Far Field - Condition 1, 5 Degrees

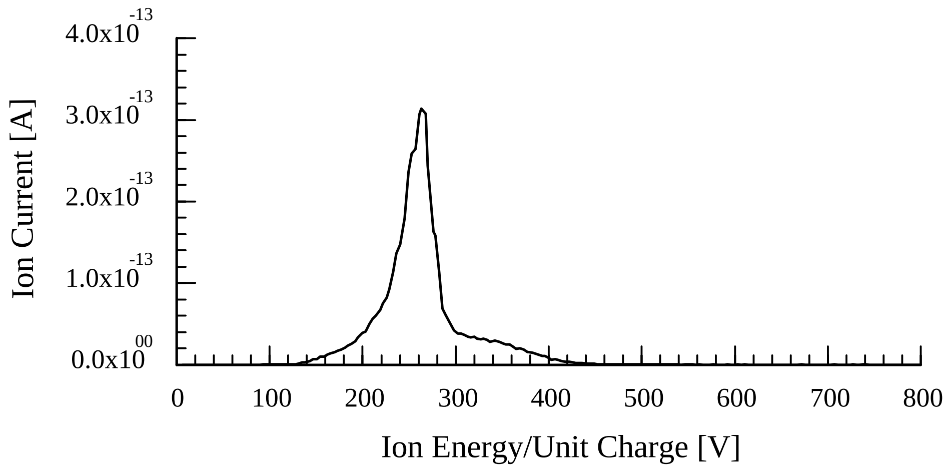

Figure 3.5. Far Field - Condition 1, 10 Degrees

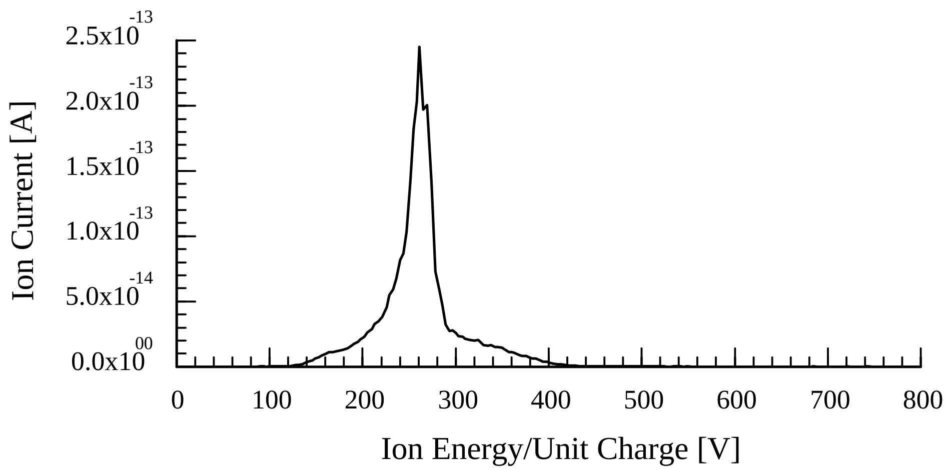

Figure 3.6. Far Field - Condition 1, 15 Degrees

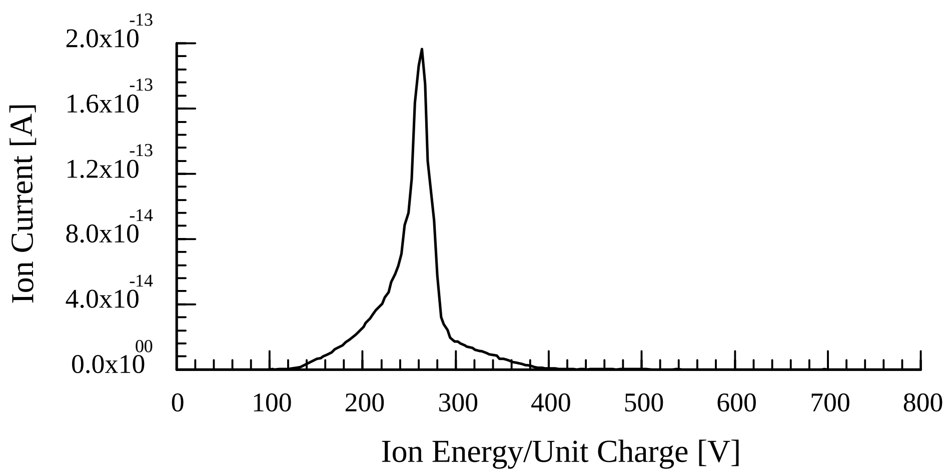

Figure 3.7. Far Field - Condition 1, 20 Degrees

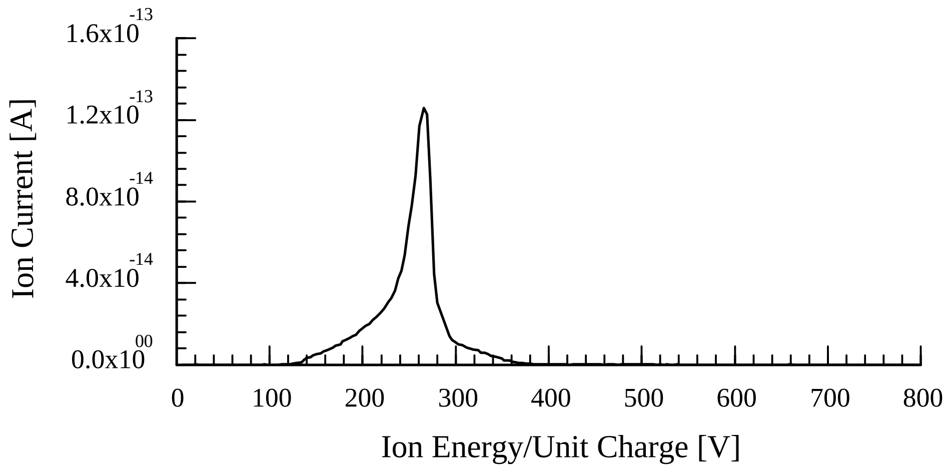

Figure 3.8. Far Field - Condition 1, 25 Degrees

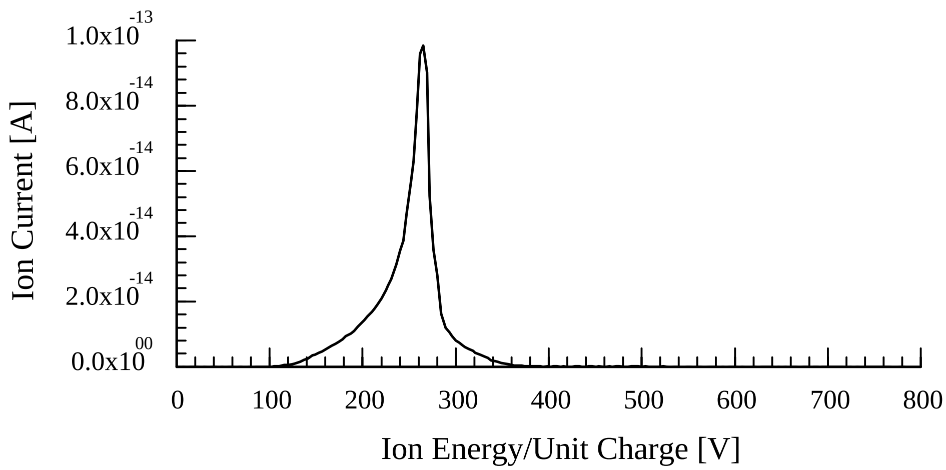

Figure 3.9. Far Field - Condition 1, 30 Degrees

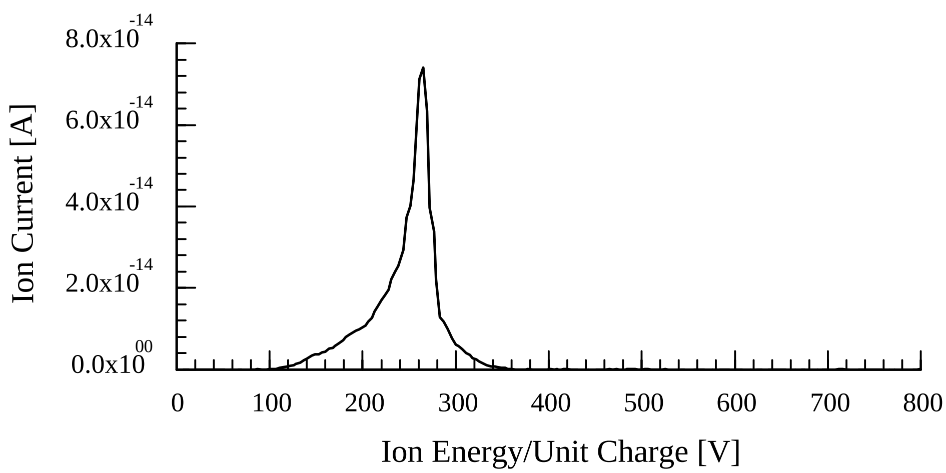

Figure 3.10. Far Field - Condition 1, 35 Degrees

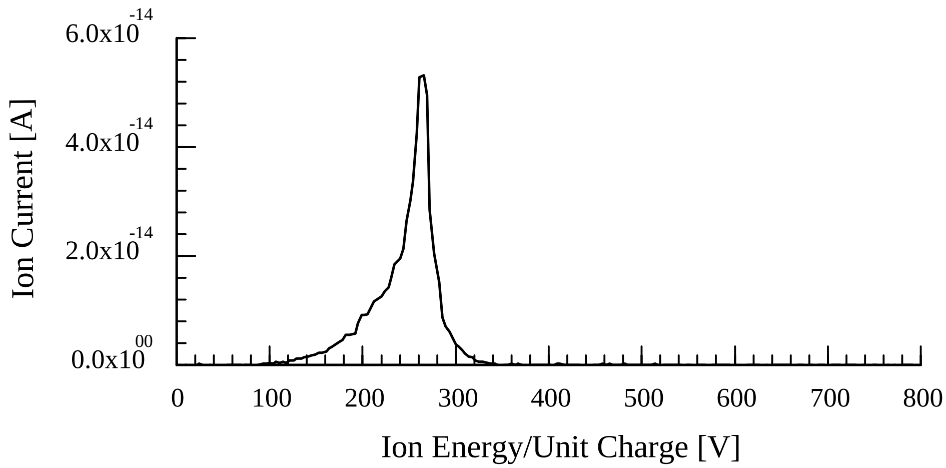

Figure 3.11. Far Field - Condition 1, 40 Degrees

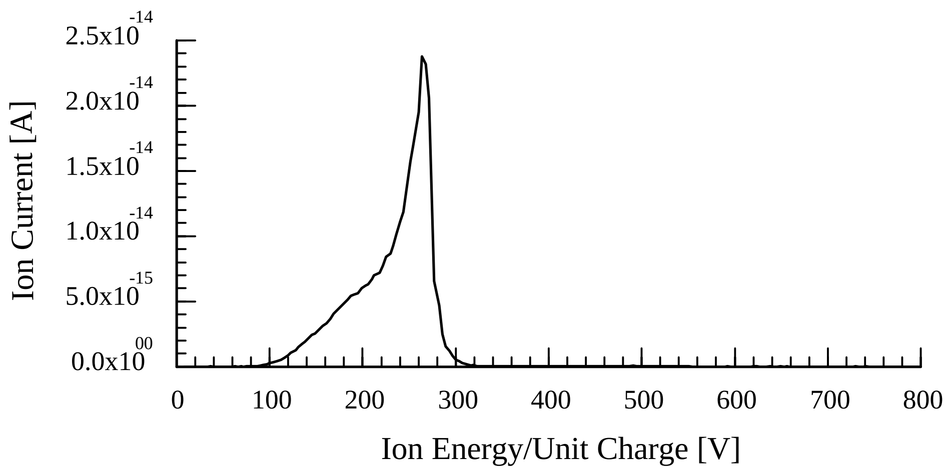

Figure 3.12. Far Field - Condition 1, 45 Degrees

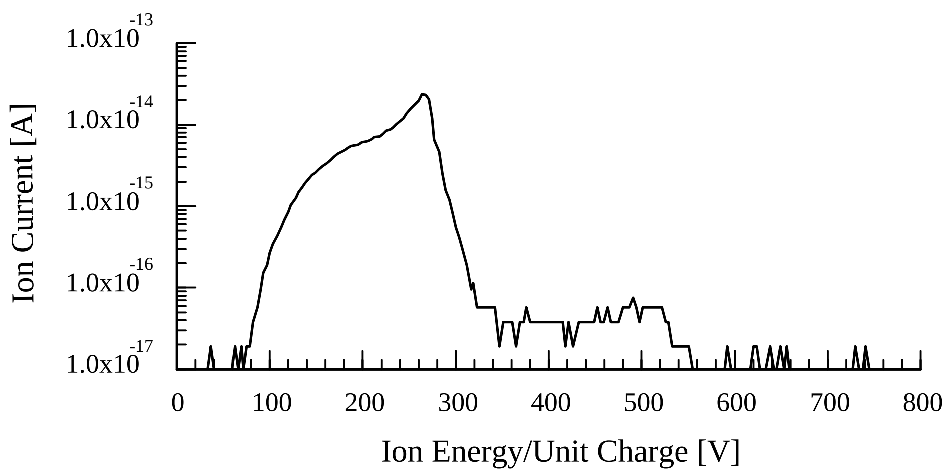

Figure 3.13. Far Field - Condition 1, 45 Degrees [Semi-log]

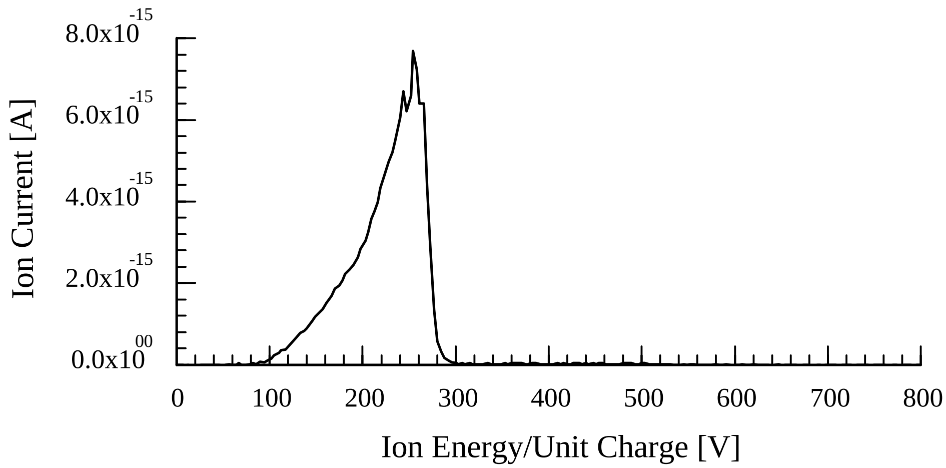

Figure 3.14. Far Field - Condition 1, 50 Degrees

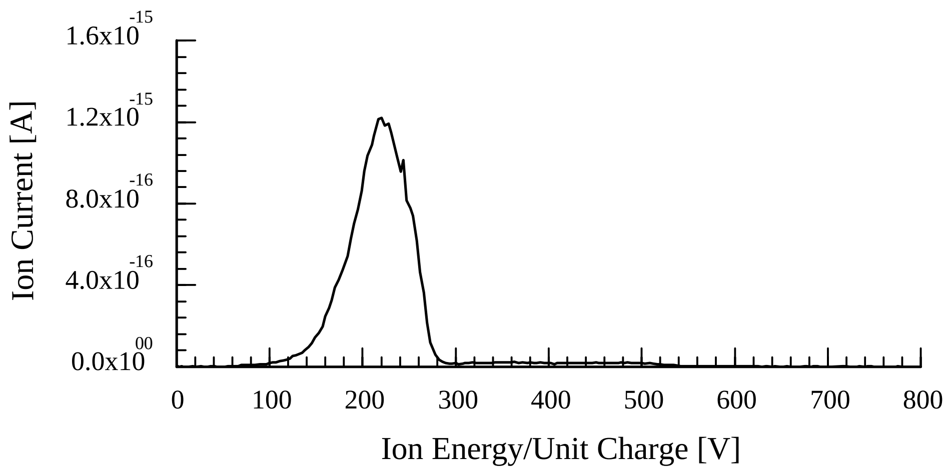

Figure 3.15. Far Field - Condition 1, 55 Degrees

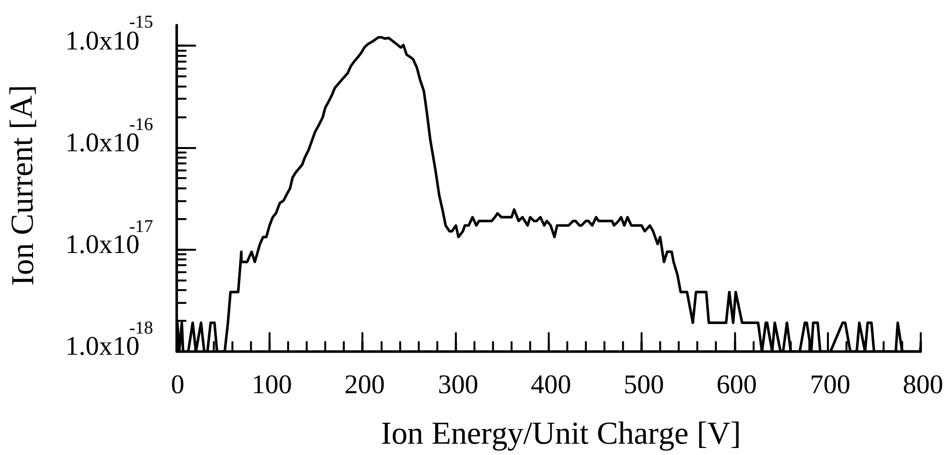

Figure 3.16. Far Field - Condition 1, 55 Degrees [Semi-log]

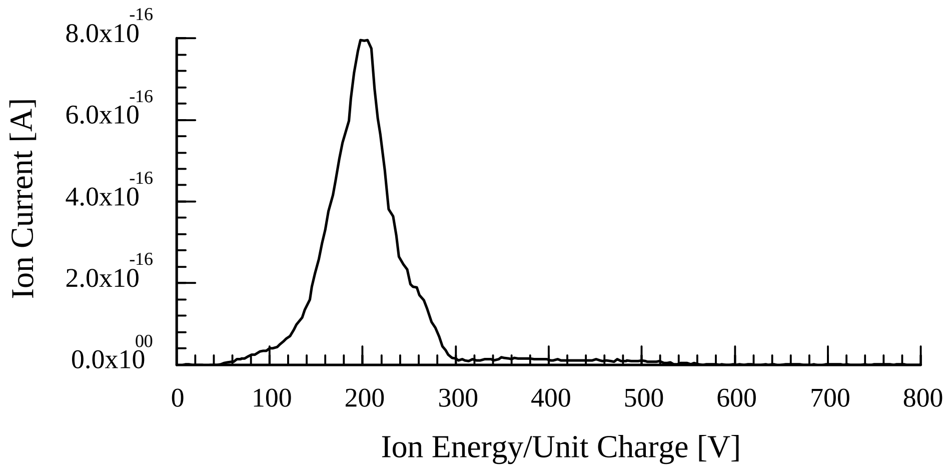

Figure 3.17. Far Field - Condition 1, 60 Degrees

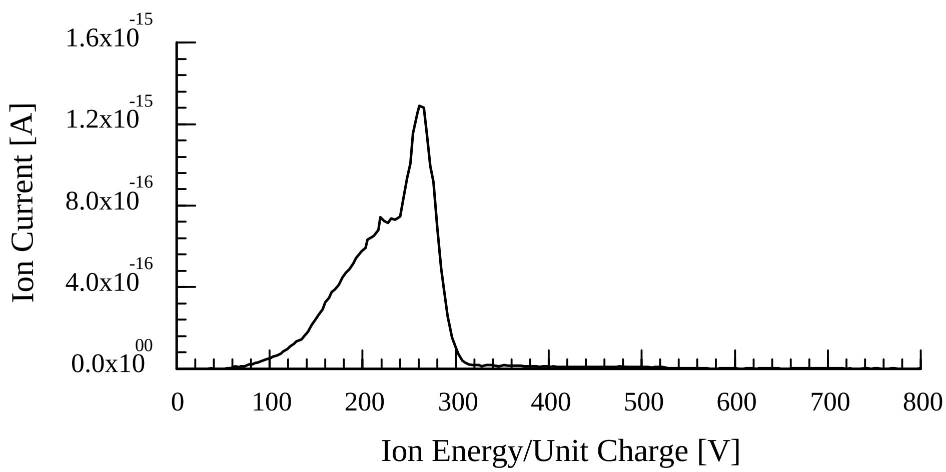

Figure 3.18. Far Field - Condition 1, 65 Degrees

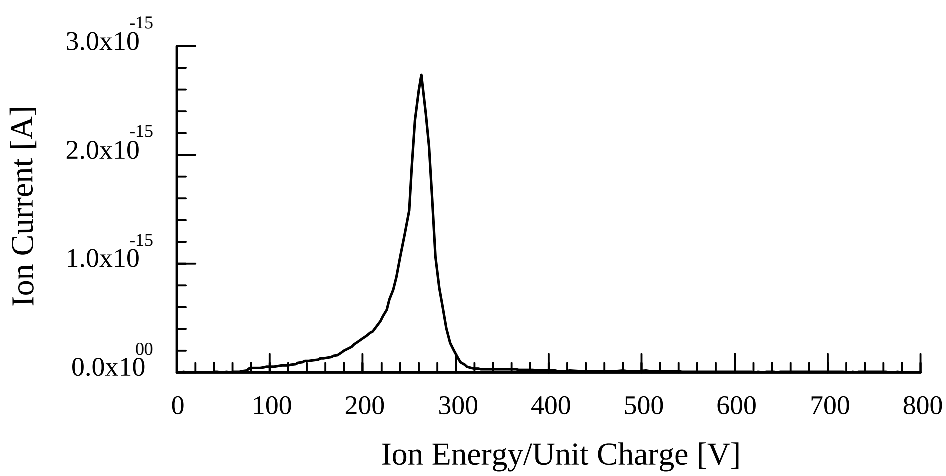

Figure 3.19. Far Field - Condition 1, 70 Degrees

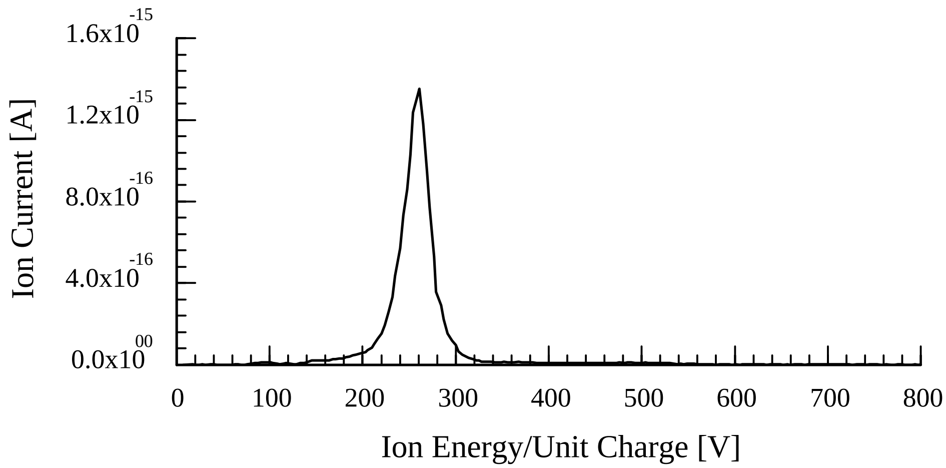

Figure 3.20. Far Field - Condition 1, 75 Degrees

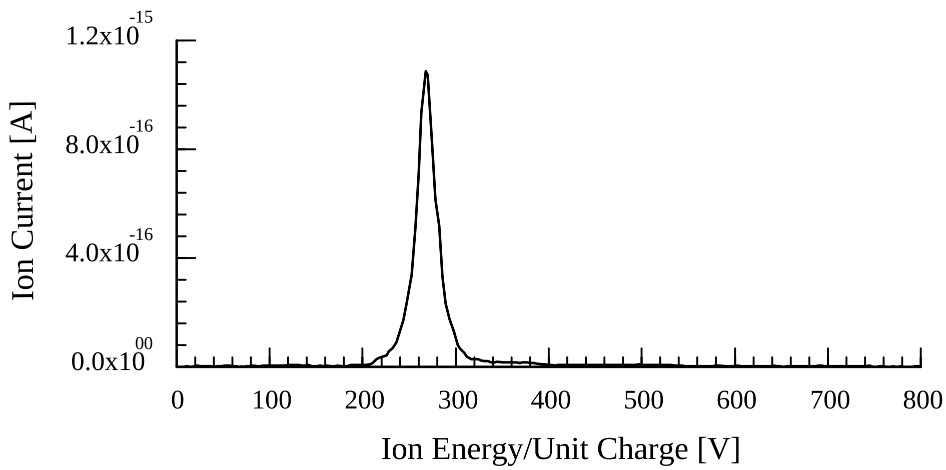

Figure 3.21. Far Field - Condition 1, 80 Degrees

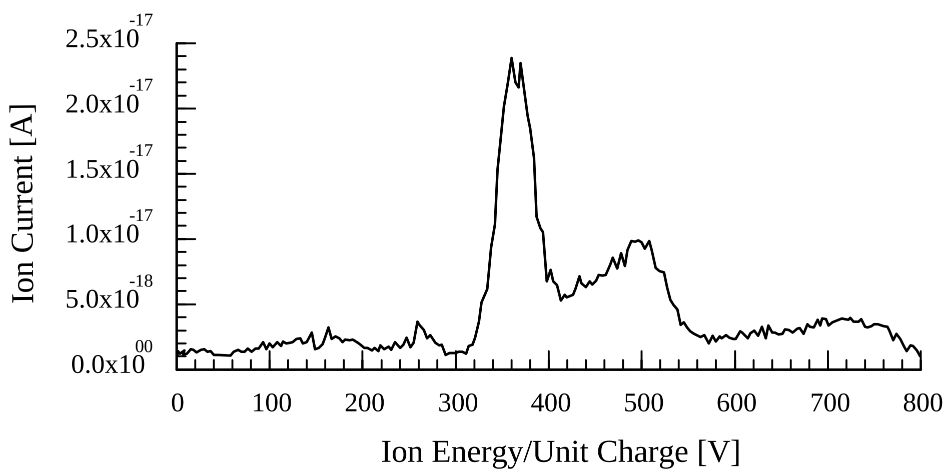

Figure 3.22. Far Field - Condition 1, 85 Degrees

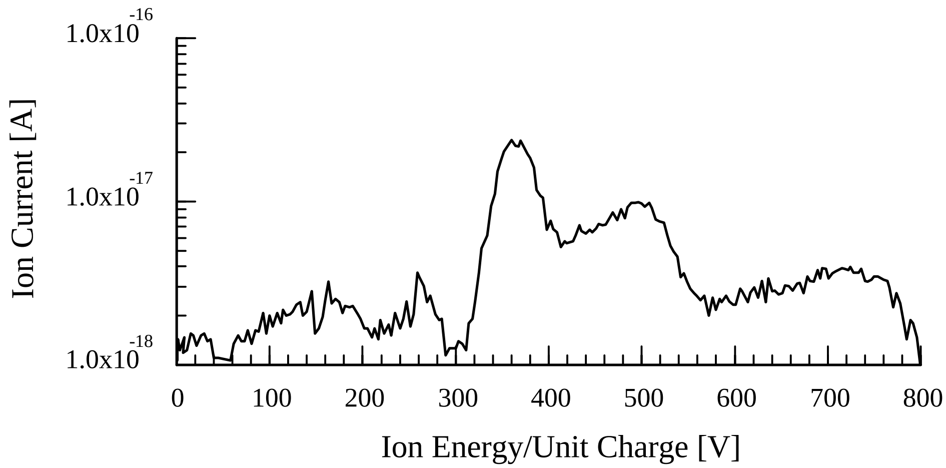

Figure 3.23. Far Field - Condition 1, 85 Degrees [Semi-log]

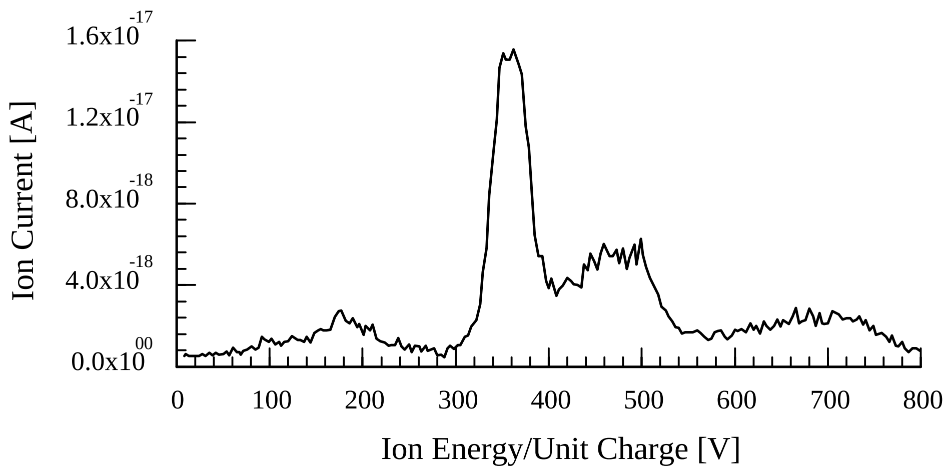

Figure 3.24. Far Field - Condition 1, 90 Degrees

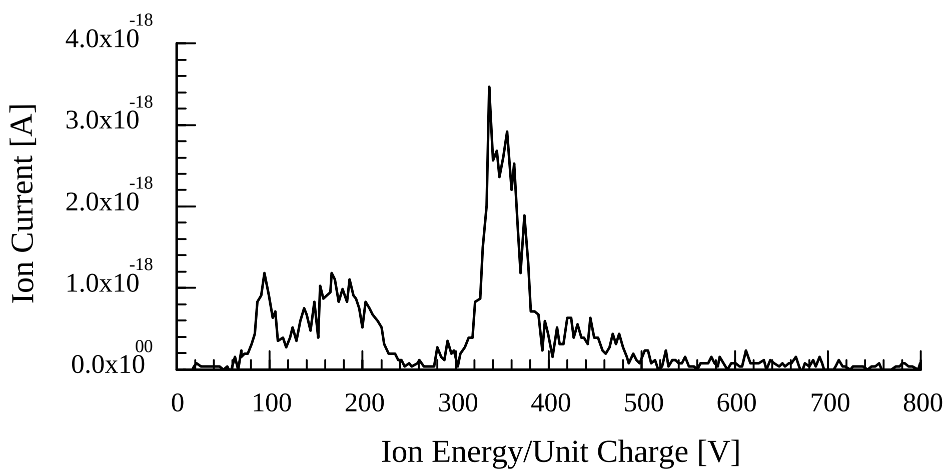

Figure 3.25. Far Field - Condition 1, 95 Degrees

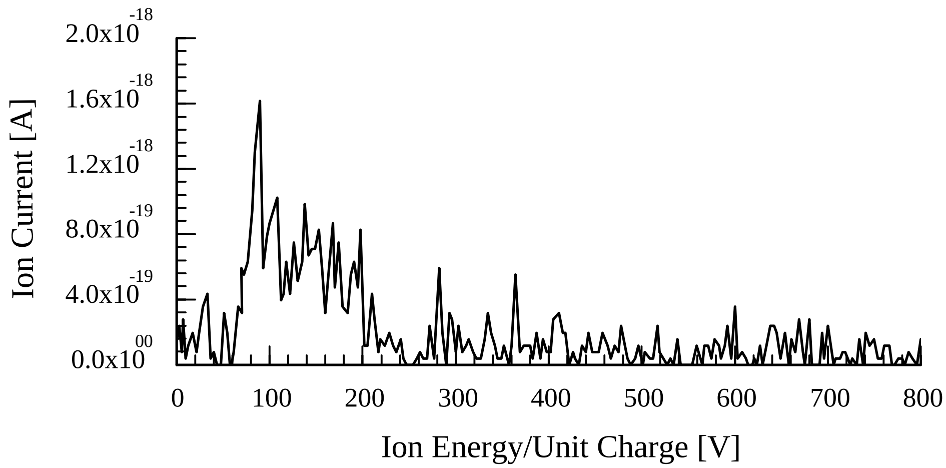

Figure 3.26. Far Field - Condition 1, 100 Degrees

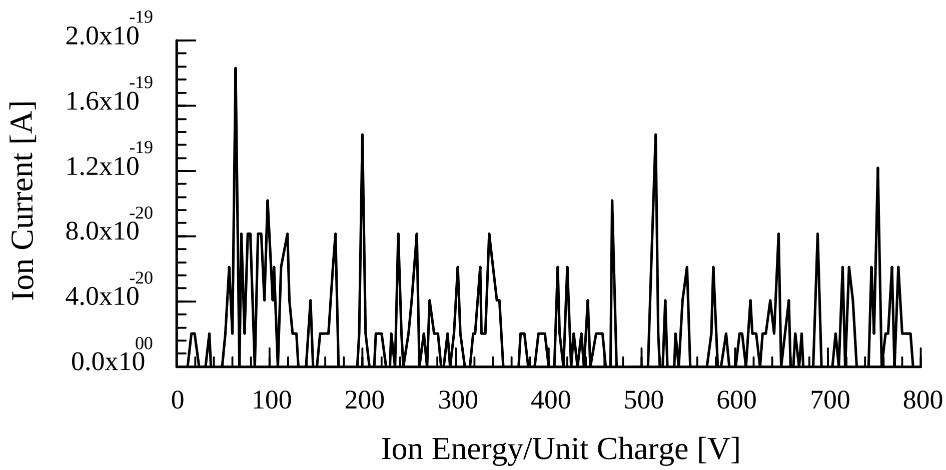

Figure 3.27. Far Field - Condition 1, 105 Degrees - Loss of Signal

Far field ion energy sweeps performed at Condition 2 are presented in Figure 3.28 through Figure 3.51. For this case, the thruster discharge voltage was 500 V, the discharge current was 5.3 A, the anode mass flow rate was 58 sccm, and the cathode flow rate was 6 sccm. The horizontal scale was decreased from 1800 V to 1500 V and selected plots are also shown in semi-log scale to increase resolution.

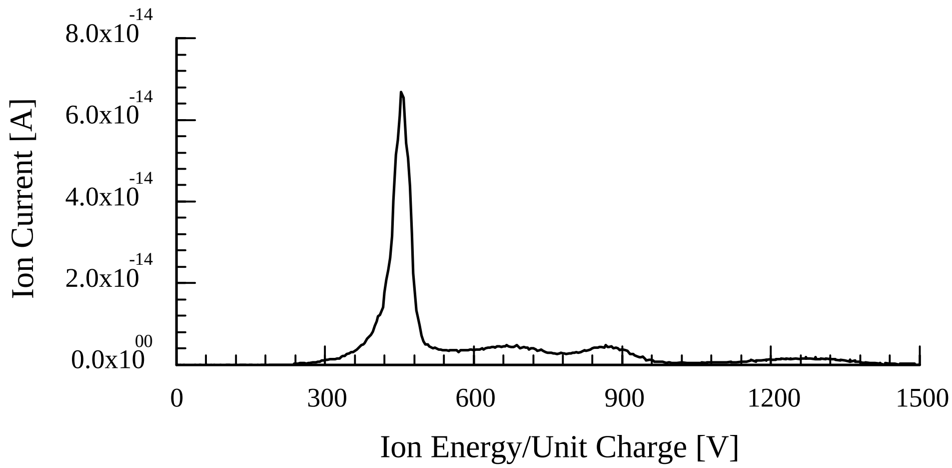

Figure 3.28. Far Field - Condition 2, 0 Degrees

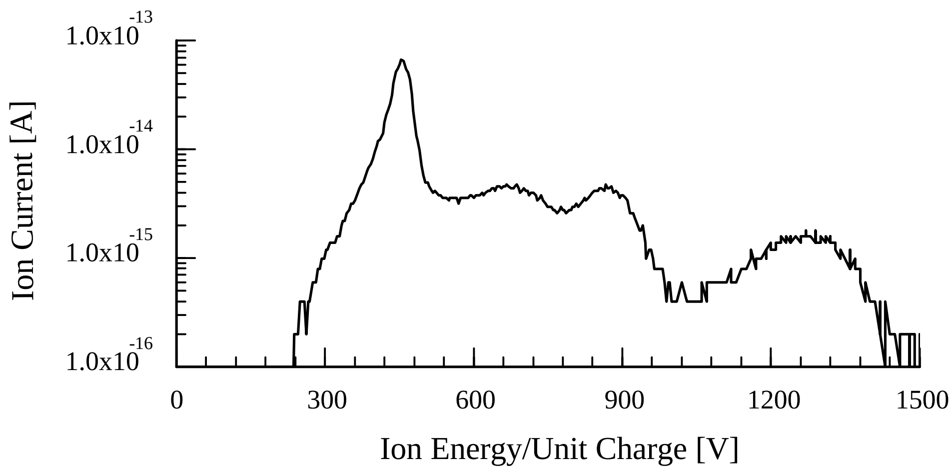

Figure 3.29. Far Field - Condition 2, 0 Degrees [Semi-log]

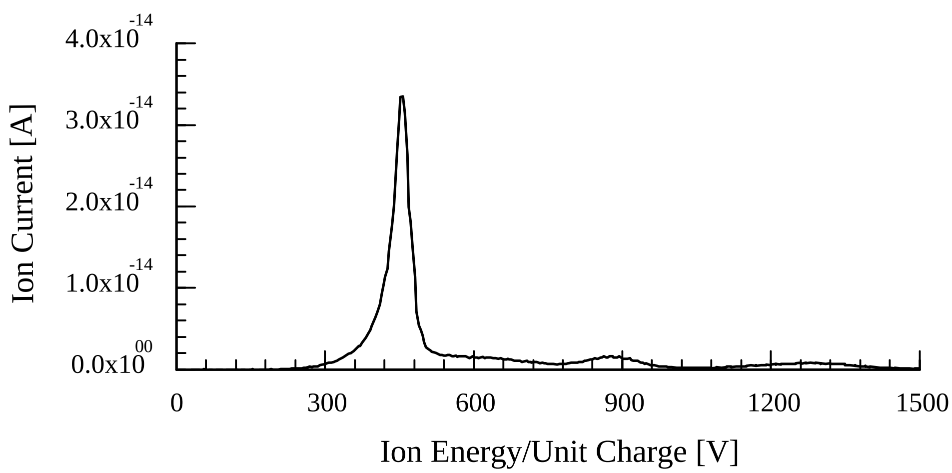

Figure 3.30. Far Field - Condition 2, 5 Degrees

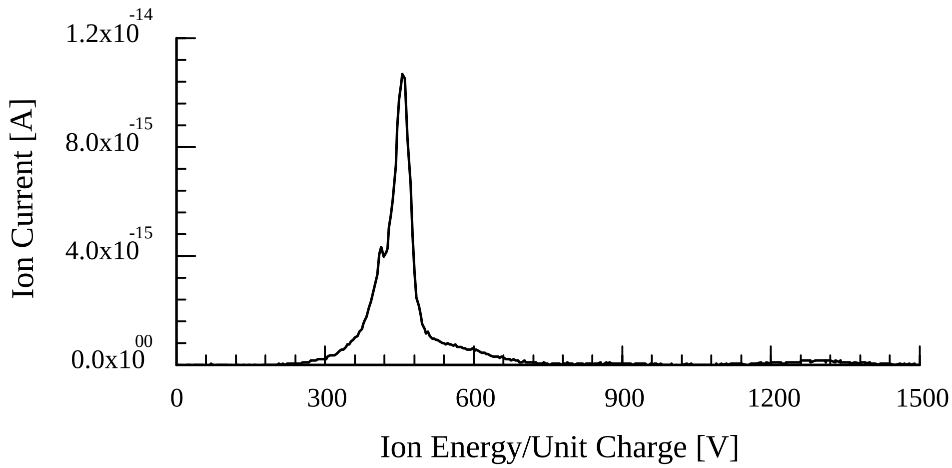

Figure 3.31. Far Field - Condition 2, 10 Degrees

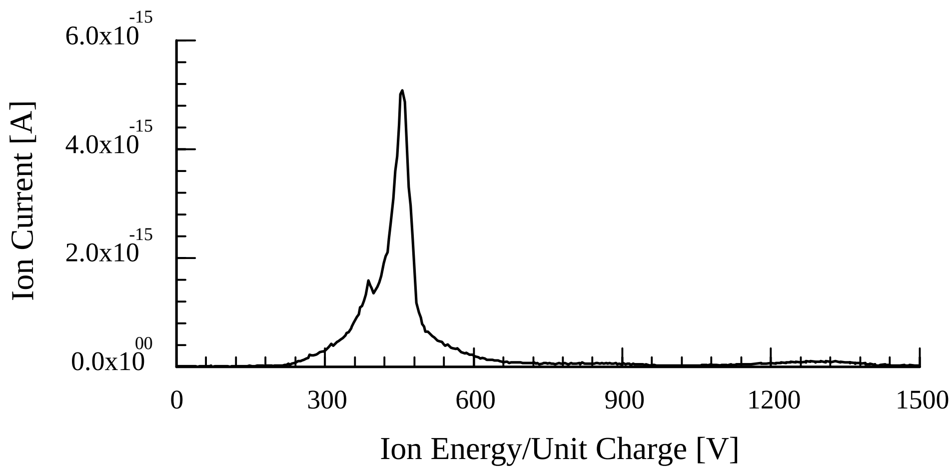

Figure 3.32. Far Field - Condition 2, 15 Degrees

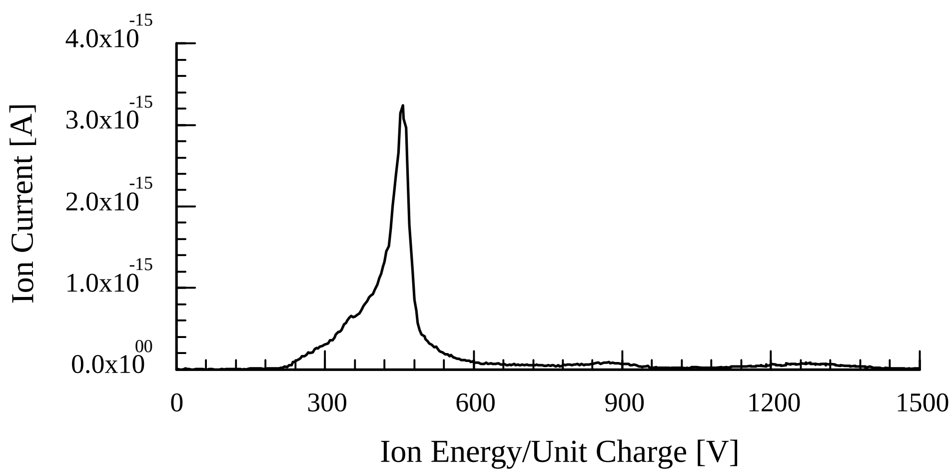

Figure 3.33. Far Field - Condition 2, 20 Degrees

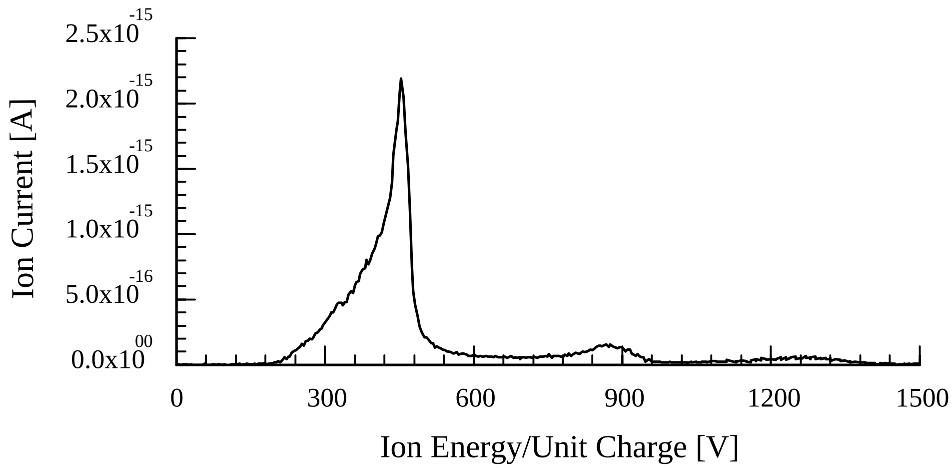

Figure 3.34. Far Field - Condition 2, 25 Degrees

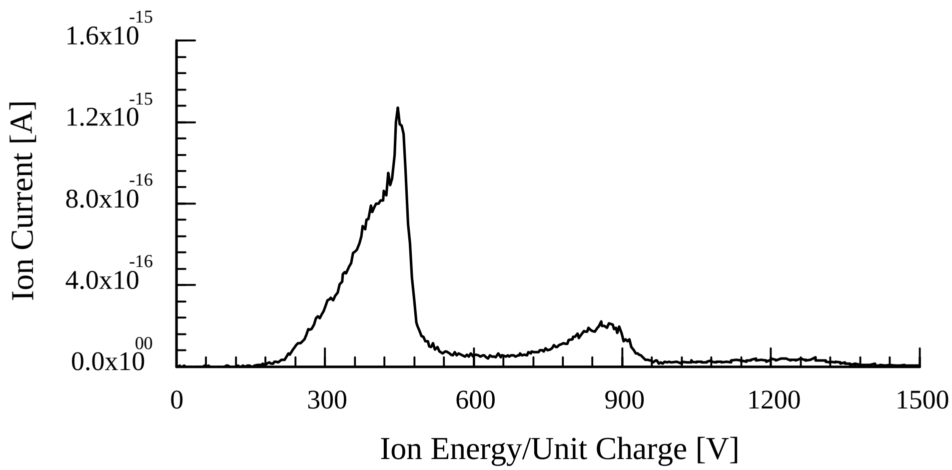

Figure 3.35. Far Field - Condition 2, 30 Degrees

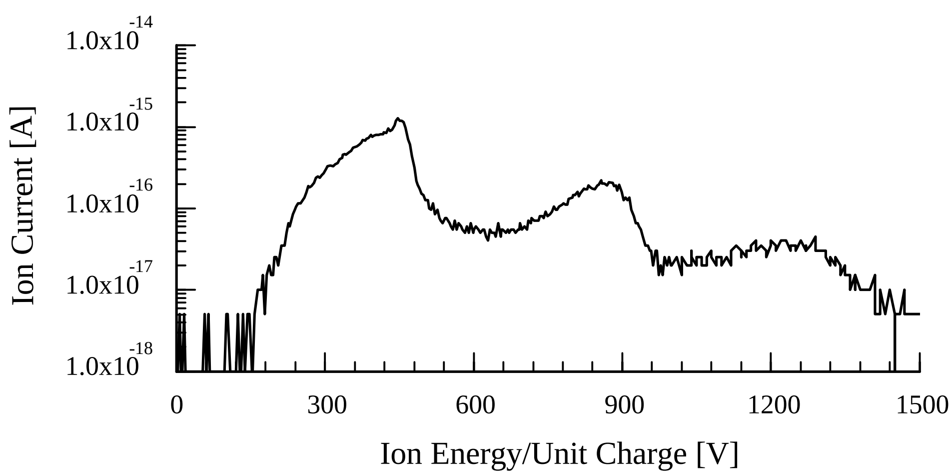

Figure 3.36. Far Field - Condition 2, 30 Degrees [Semi-log]

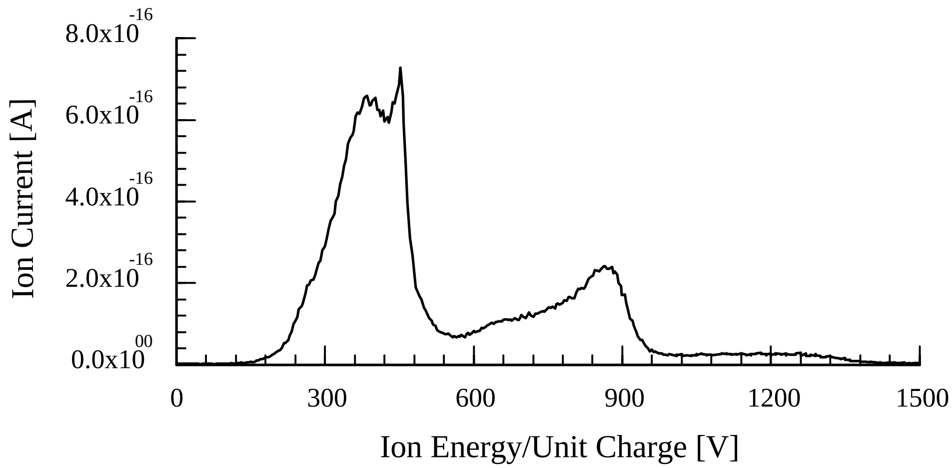

Figure 3.37. Far Field - Condition 2, 35 Degrees

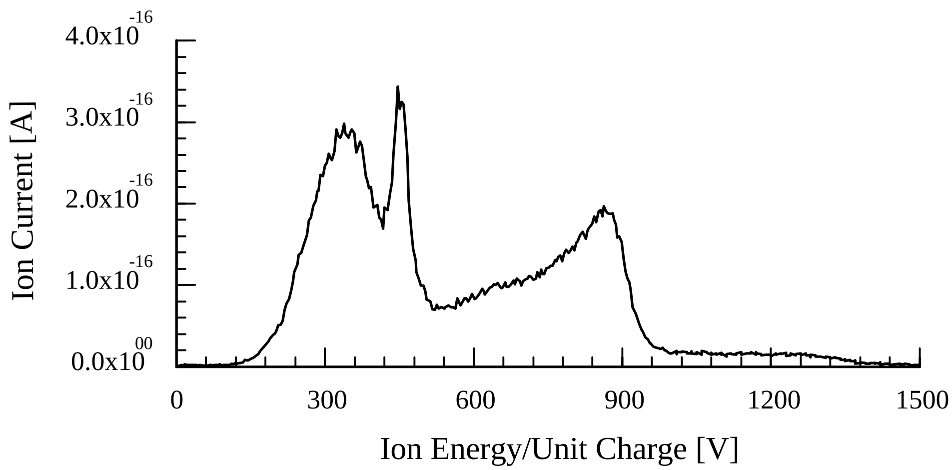

Figure 3.38. Far Field - Condition 2, 40 Degrees

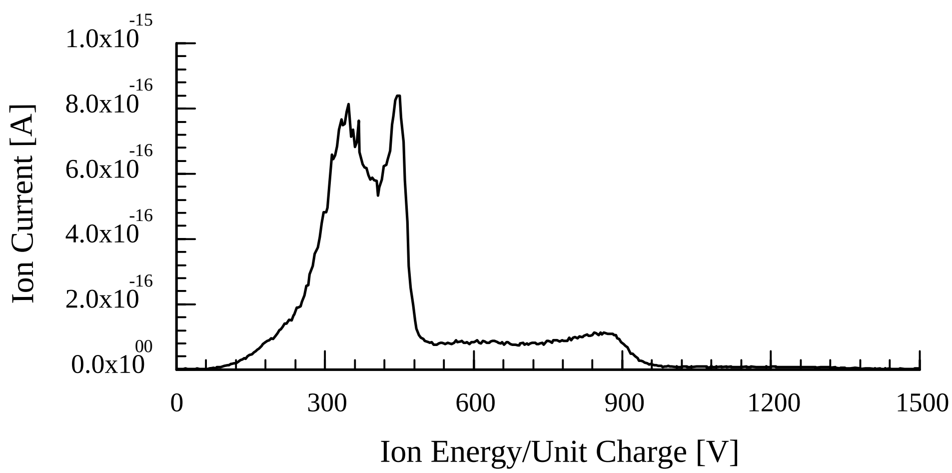

Figure 3.39. Far Field - Condition 2, 45 Degrees

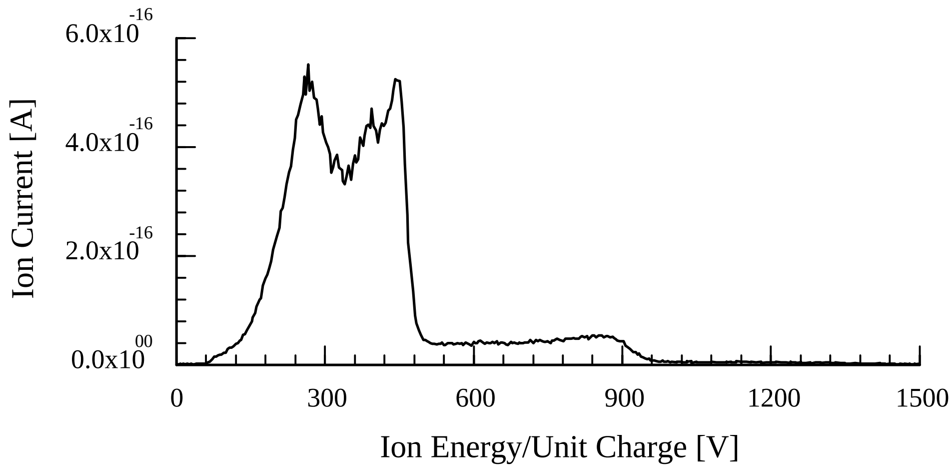

Figure 3.40. Far Field - Condition 2, 50 Degrees

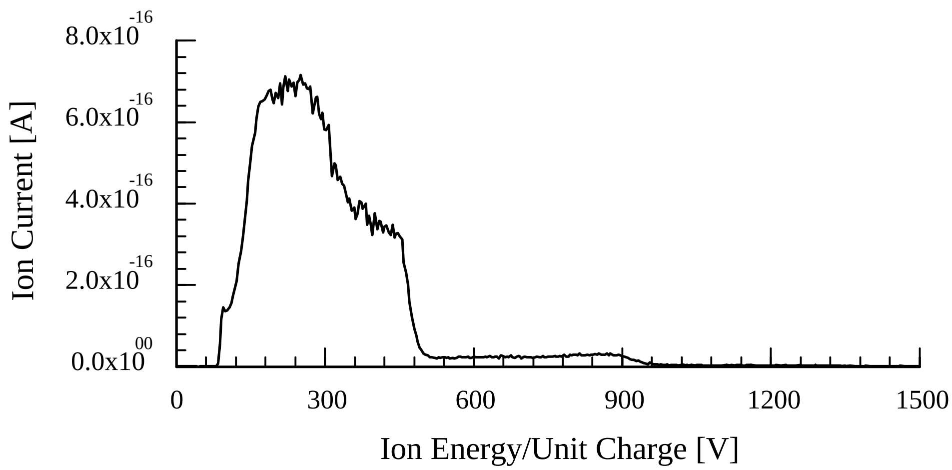

Figure 3.41. Far Field - Condition 2, 55 Degrees

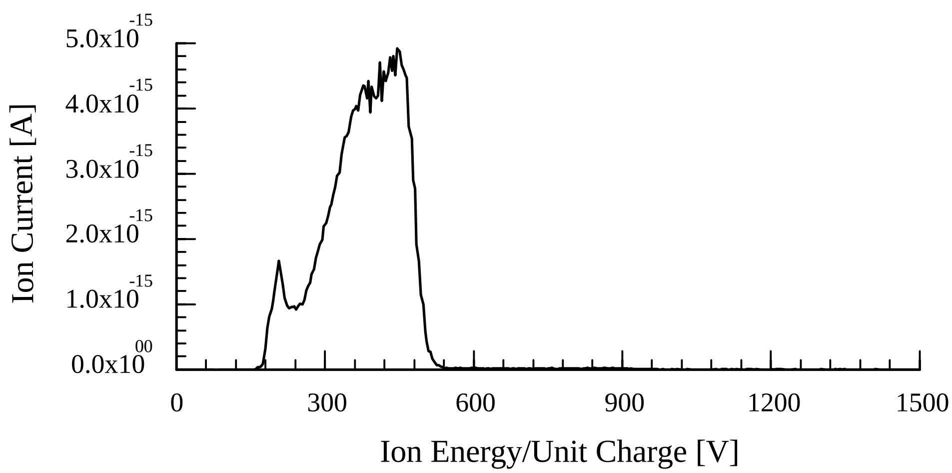

Figure 3.42. Far Field - Condition 2, 60 Degrees

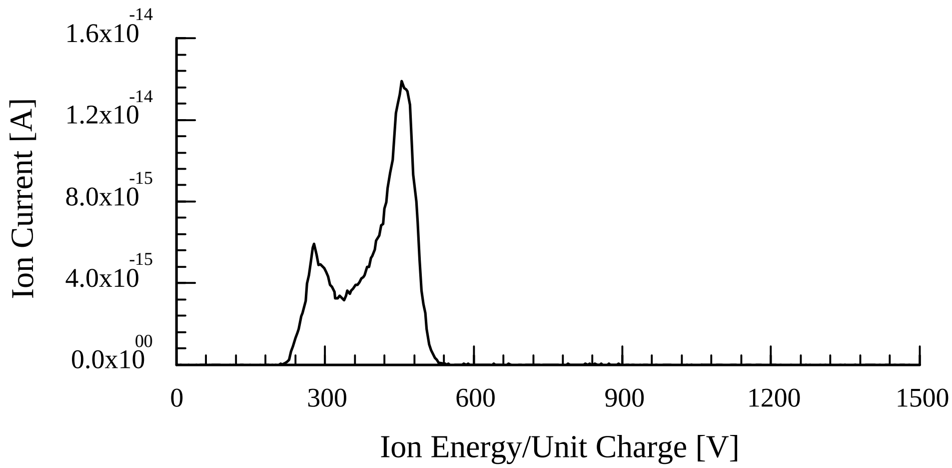

Figure 3.43. Far Field - Condition 2, 65 Degrees

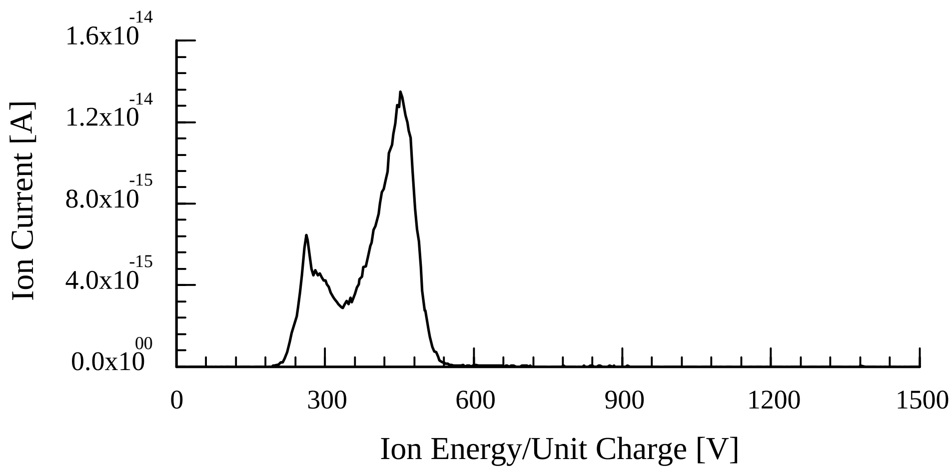

Figure 3.44. Far Field - Condition 2, 70 Degrees

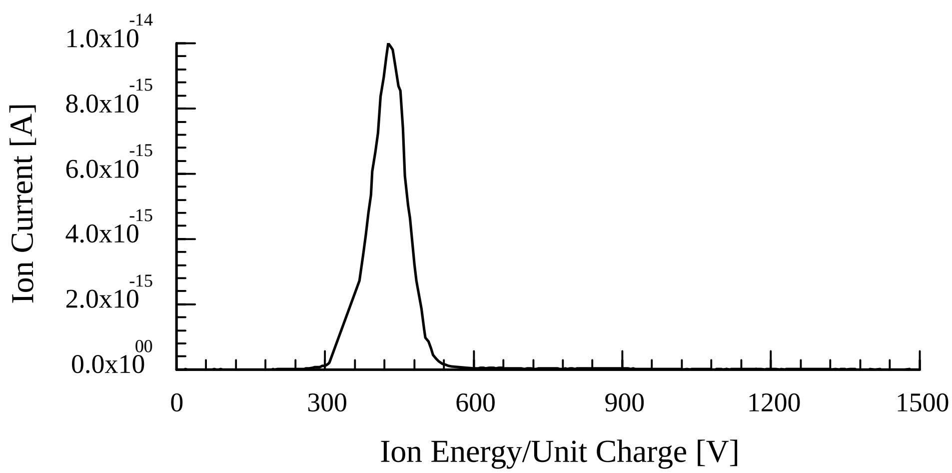

Figure 3.45. Far Field - Condition 2, 75 Degrees

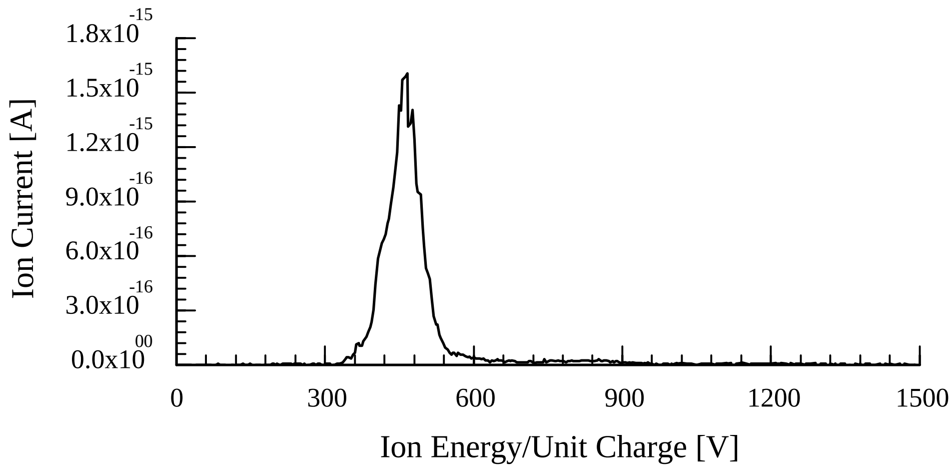

Figure 3.46. Far Field - Condition 2, 80 Degrees

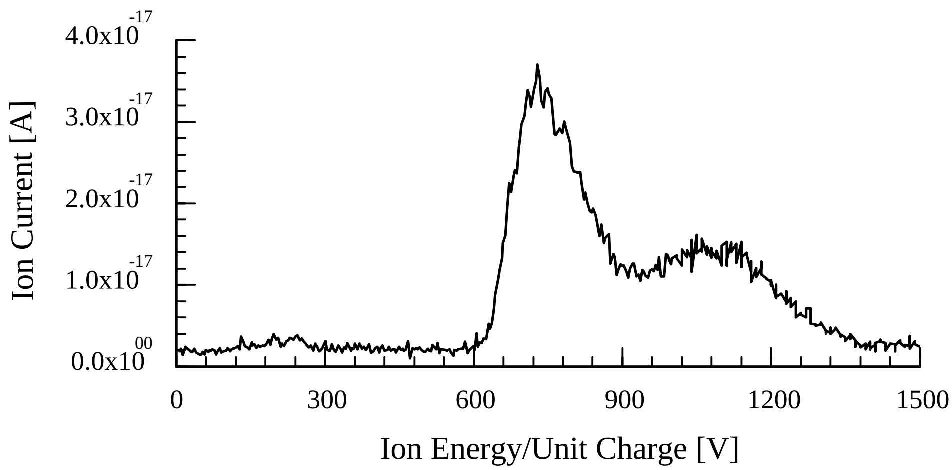

Figure 3.47. Far Field - Condition 2, 85 Degrees

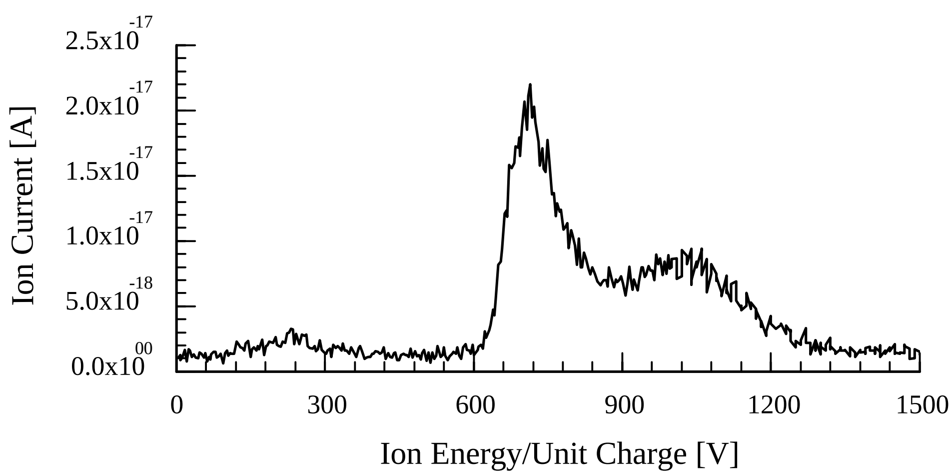

Figure 3.48. Far Field - Condition 2, 90 Degrees

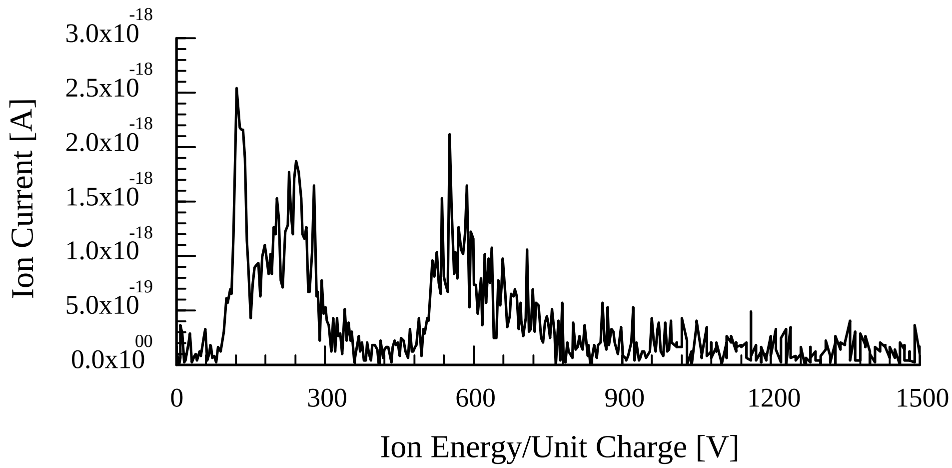

Figure 3.49. Far Field - Condition 2, 95 Degrees

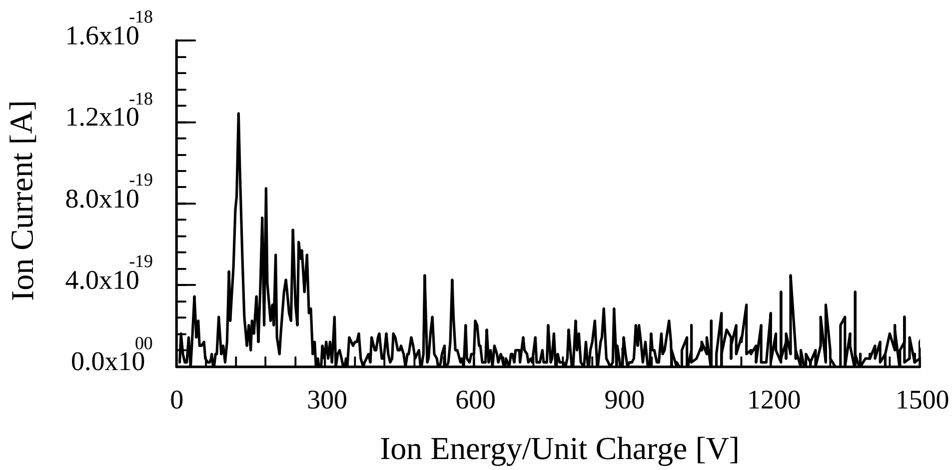

Figure 3.50. Far Field - Condition 2, 100 Degrees

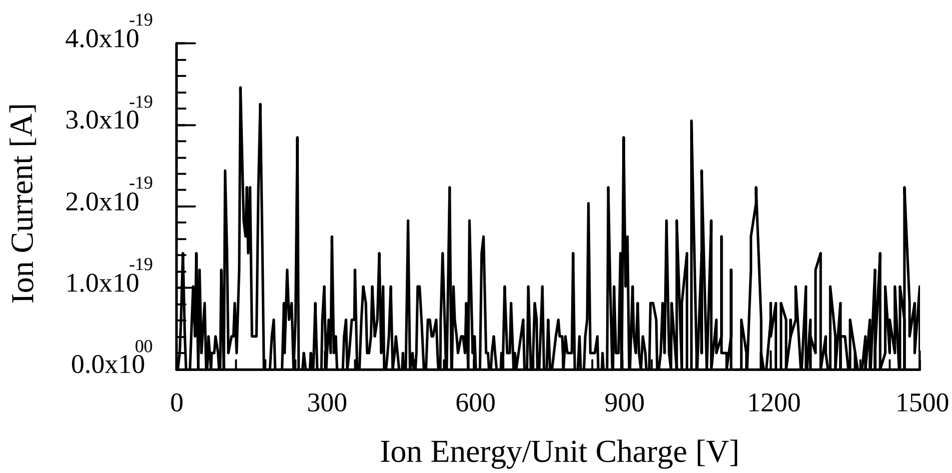

Figure 3.51. Far Field - Condition 2, 105 Degrees - Loss of Signal

Far field ion energy sweeps performed at Condition 3 are presented in Figure 3.52 through Figure 3.74. For this case, the thruster discharge voltage was 500 V, the discharge current was 10.0 A, the anode mass flow rate was 105 sccm, and the cathode flow rate was 6 sccm. The horizontal scale was decreased from 1800 V to 1500 V and selected plots are also shown in semi-log scale to increase resolution.

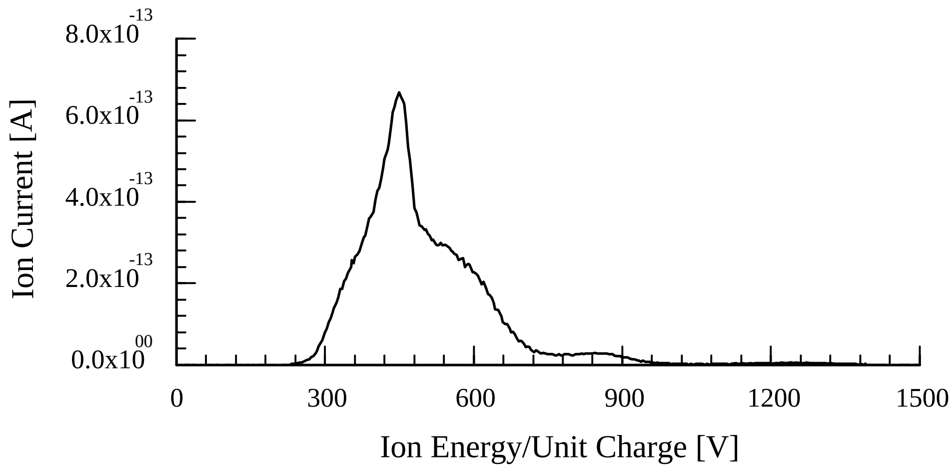

Figure 3.52. Far Field - Condition 3, 0 Degrees

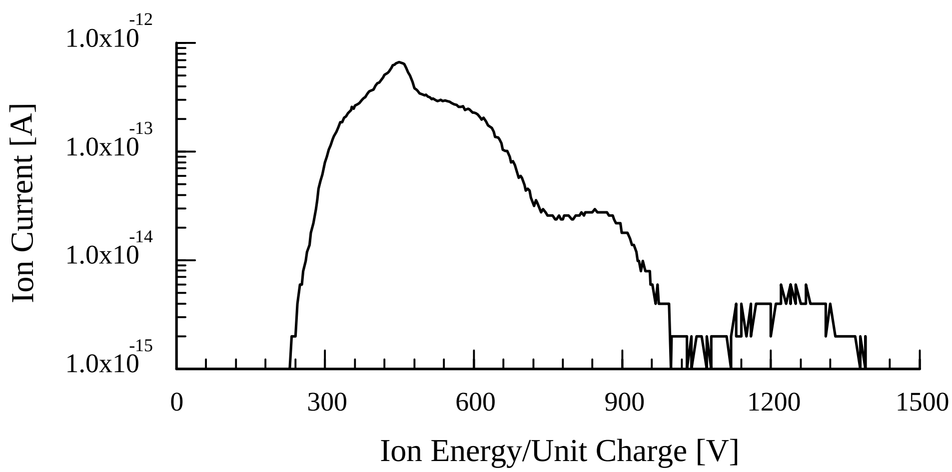

Figure 3.53. Far Field - Condition 3, 0 Degrees [Semi-log]

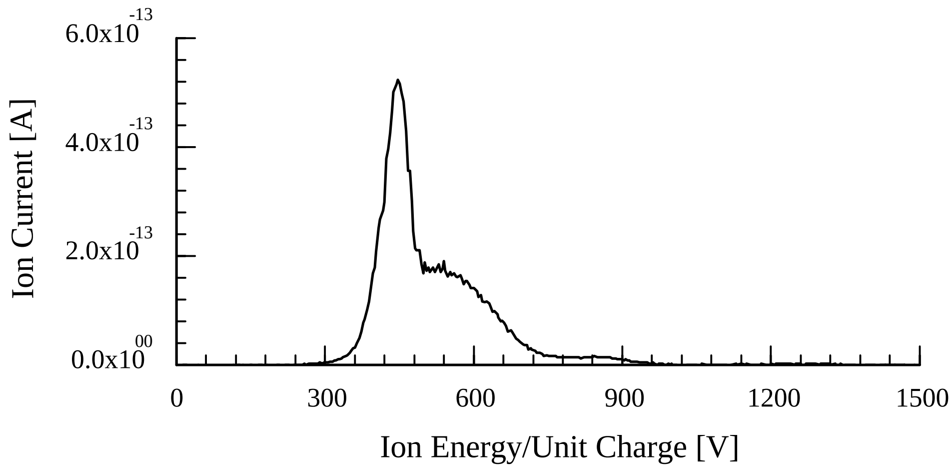

Figure 3.54. Far Field - Condition 3, 5 Degrees

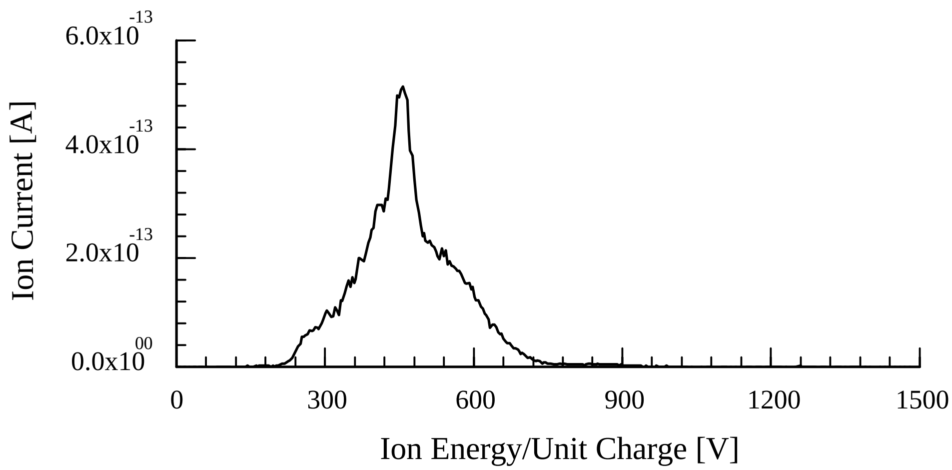

Figure 3.55. Far Field - Condition 3, 10 Degrees

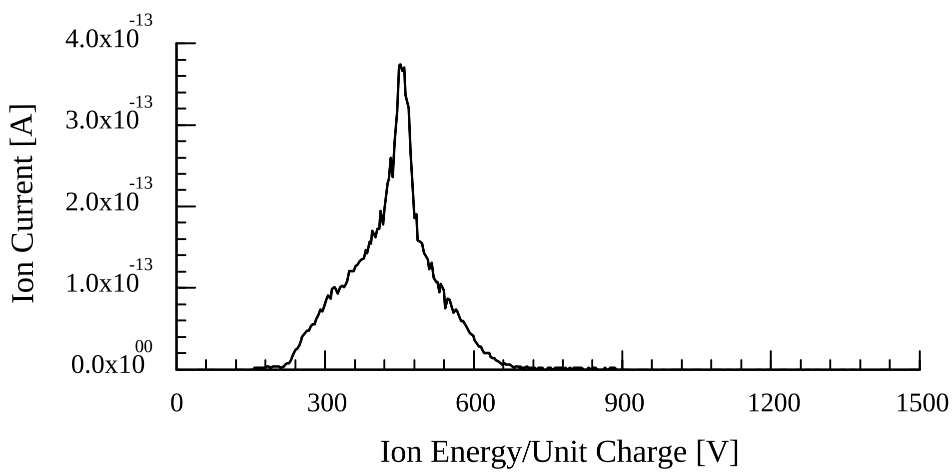

Figure 3.56. Far Field - Condition 3, 15 Degrees

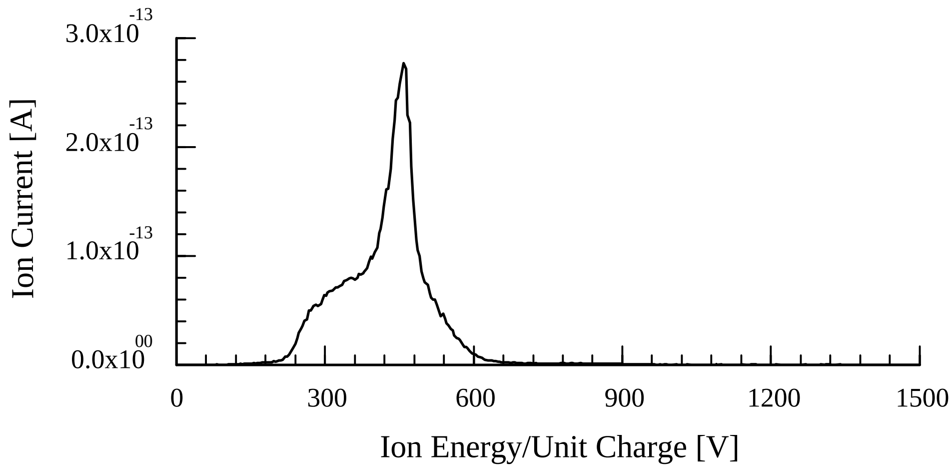

Figure 3.57. Far Field - Condition 3, 20 Degrees

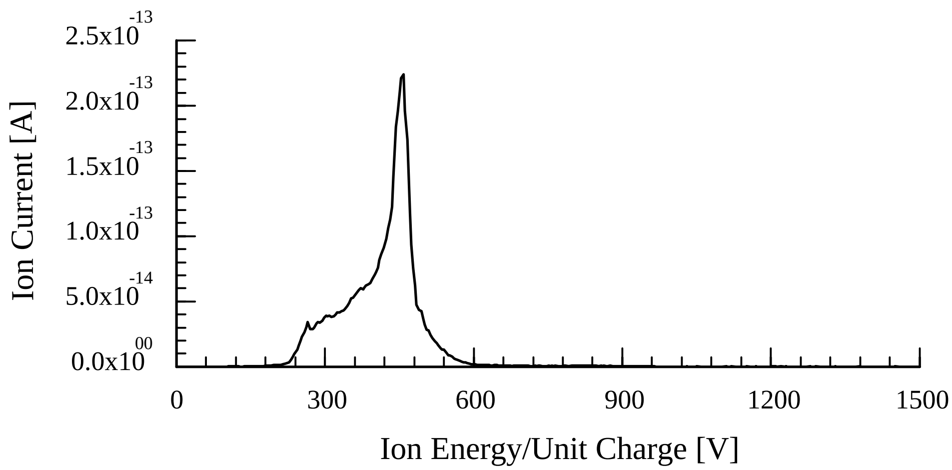

Figure 3.58. Far Field - Condition 3, 25 Degrees

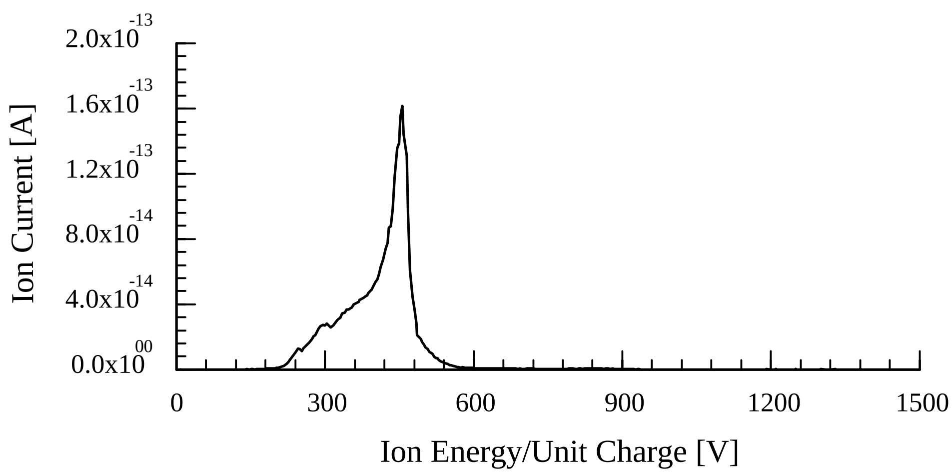

Figure 3.59. Far Field - Condition 3, 30 Degrees

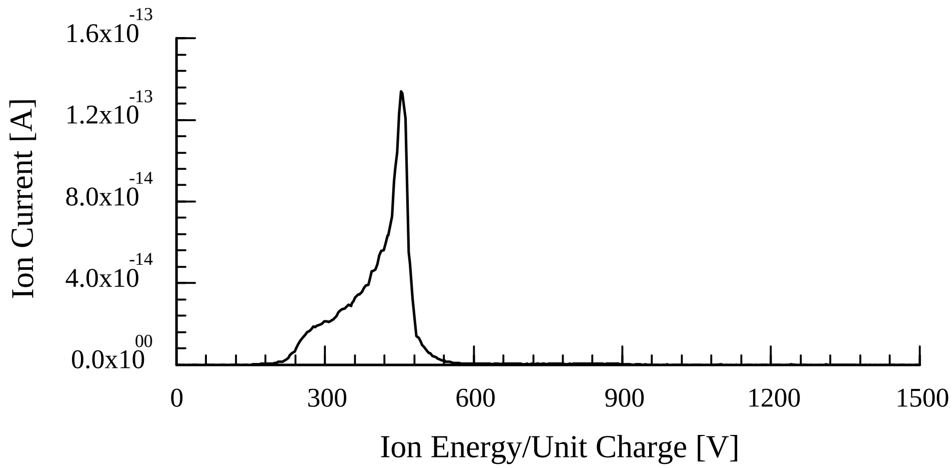

Figure 3.60. Far Field - Condition 3, 35 Degrees

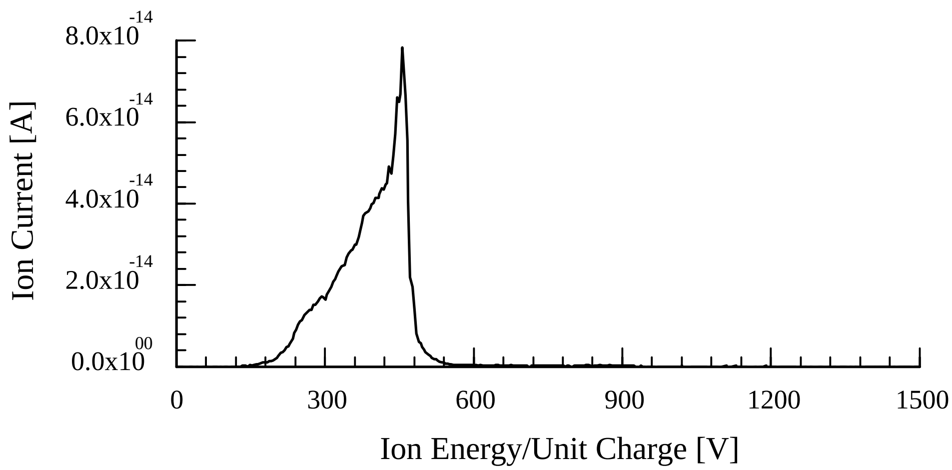

Figure 3.61. Far Field - Condition 3, 40 Degrees

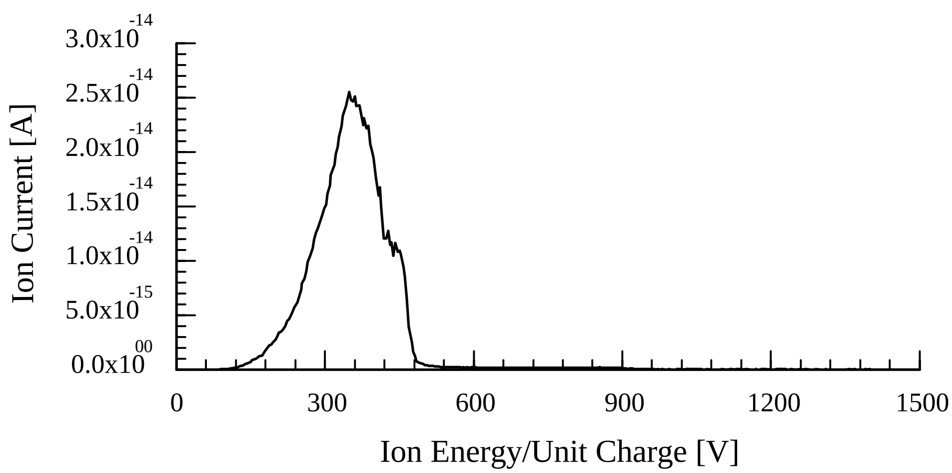

Figure 3.62. Far Field - Condition 3, 45 Degrees

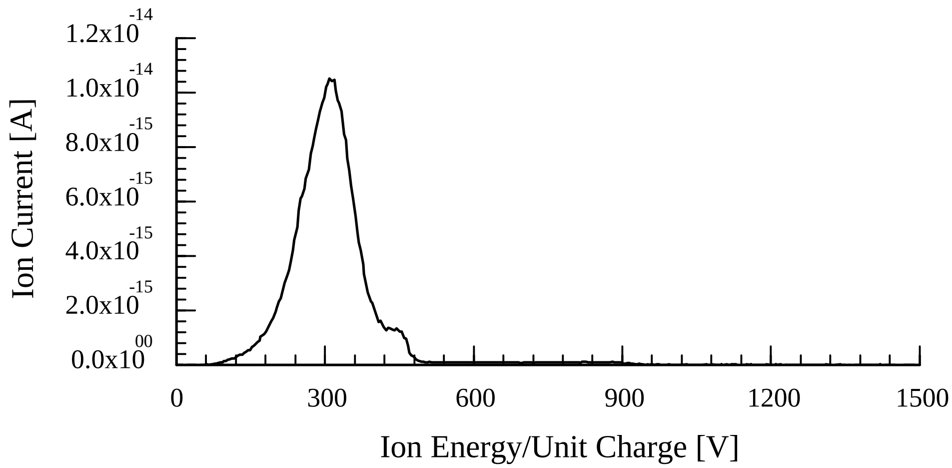

Figure 3.63. Far Field - Condition 3, 50 Degrees

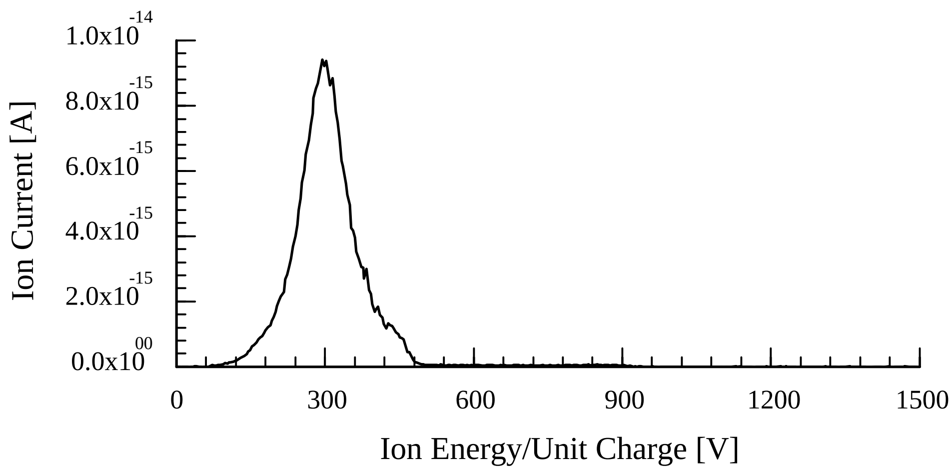

Figure 3.64. Far Field - Condition 3, 55 Degrees

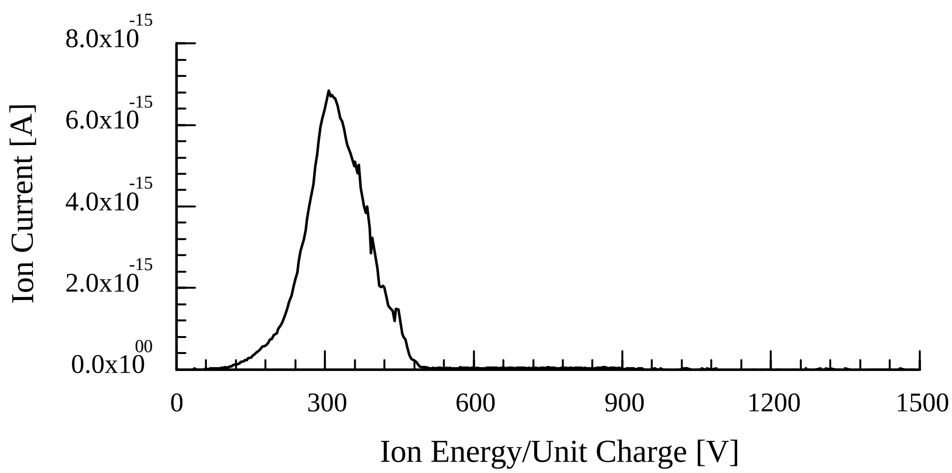

Figure 3.65. Far Field - Condition 3, 60 Degrees

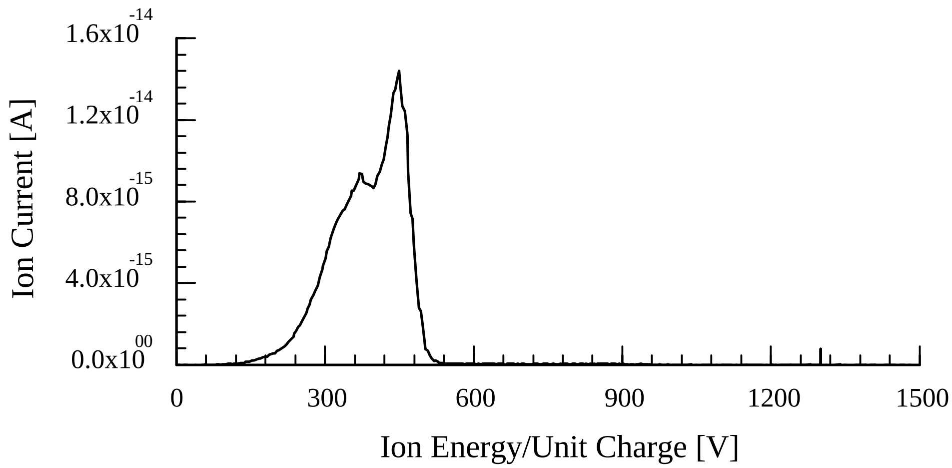

Figure 3.66. Far Field - Condition 3, 65 Degrees

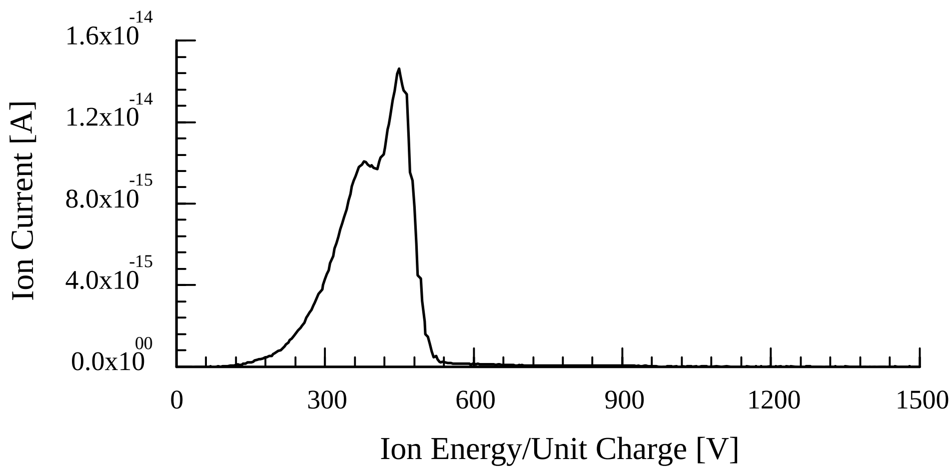

Figure 3.67. Far Field - Condition 3, 70 Degrees

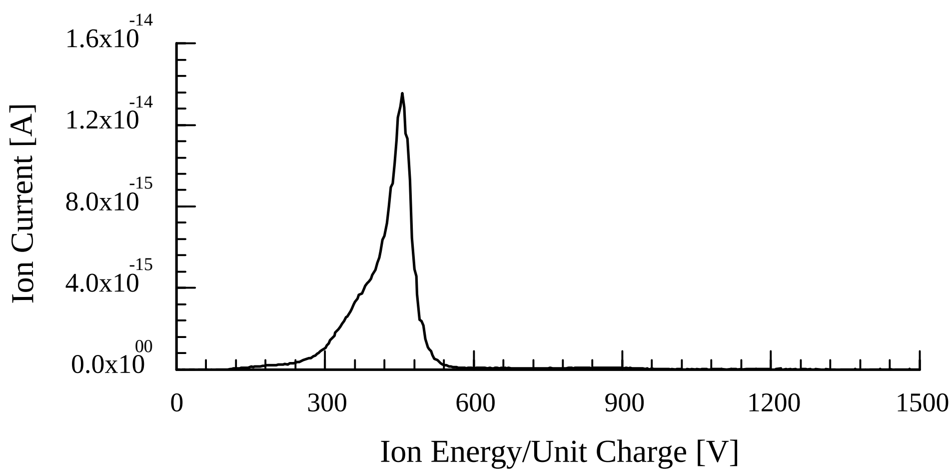

Figure 3.68. Far Field - Condition 3, 75 Degrees

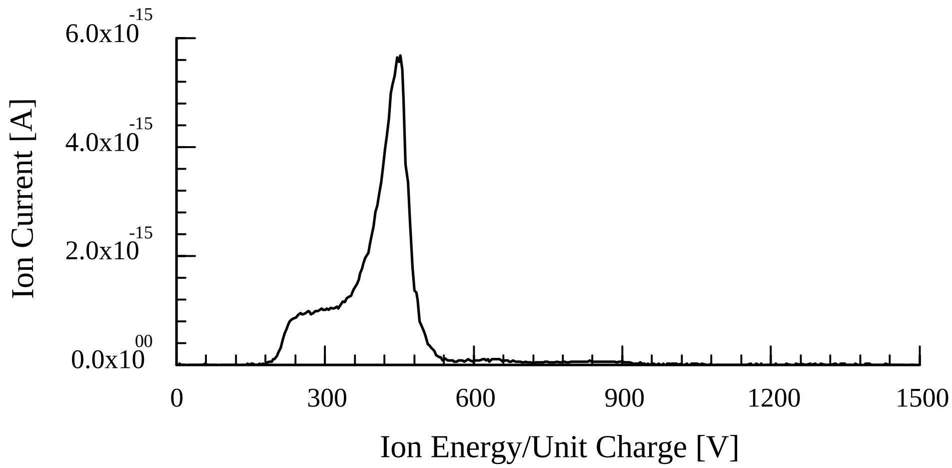

Figure 3.69. Far Field - Condition 3, 80 Degrees

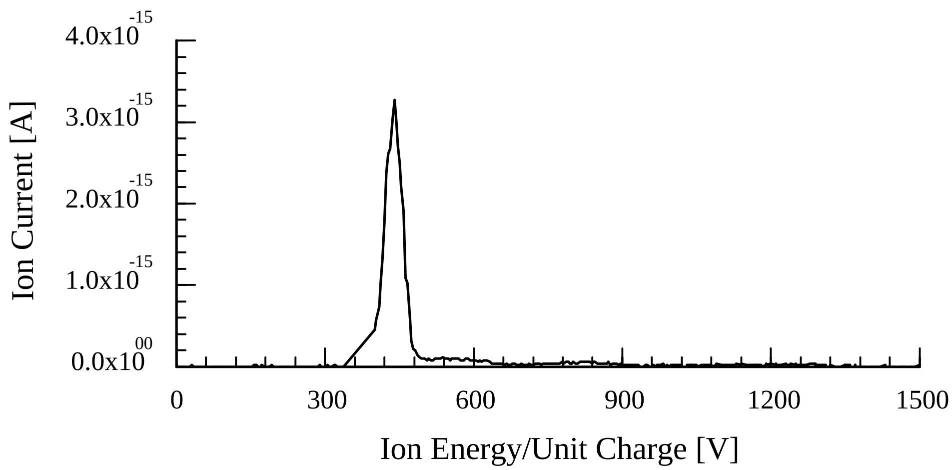

Figure 3.70. Far Field - Condition 3, 85 Degrees

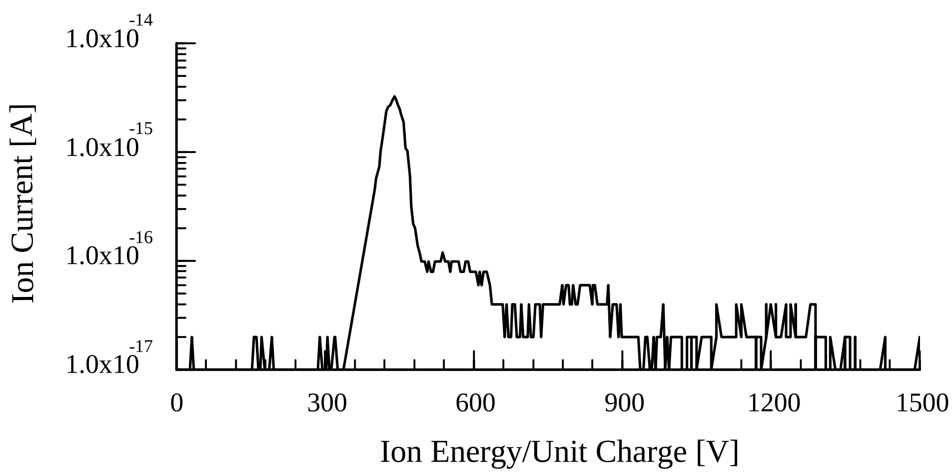

Figure 3.71. Far Field - Condition 3, 85 Degrees [Semi-log]

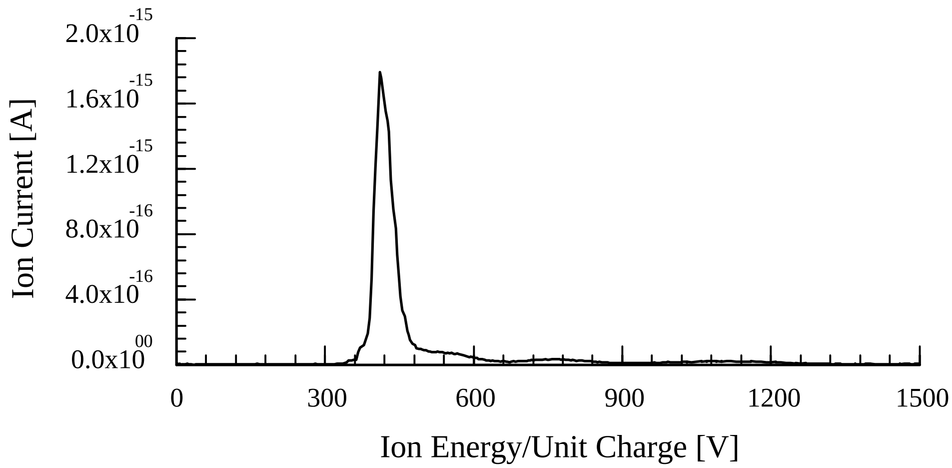

Figure 3.72. Far Field - Condition 3, 90 Degrees

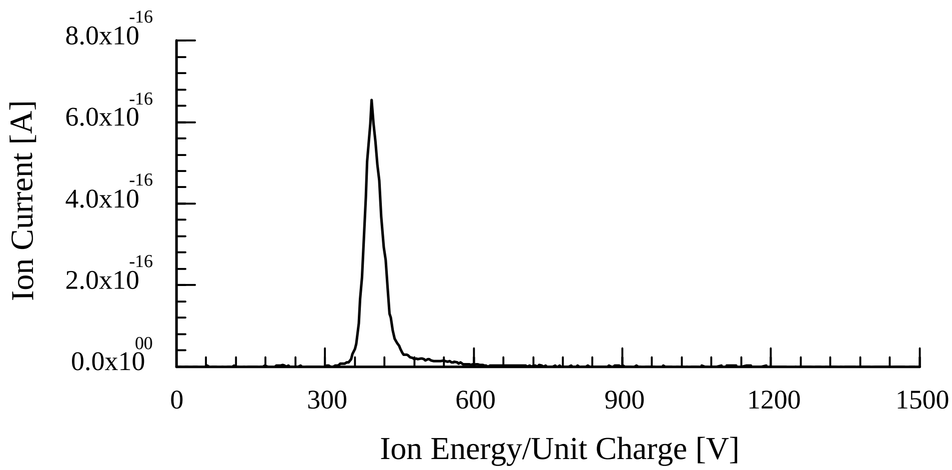

Figure 3.73. Far Field - Condition 3, 95 Degrees

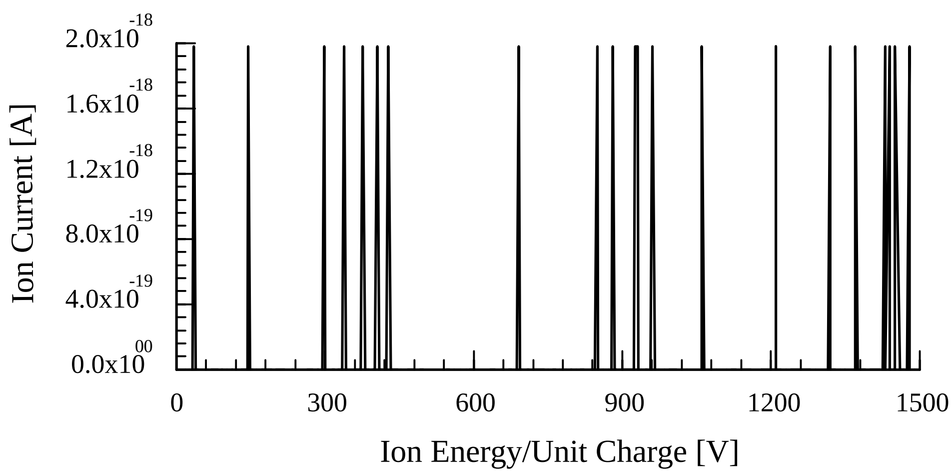

Figure 3.74. Far Field - Condition 3, 100 Degrees - Loss of Signal

3.2. Time-of-flight Mass Measurements

For species composition, measurements were taken at the primary ion energy, as determined by finding the maximum ion current for the 0 degree ion energy distributions, and in 20 V increments above and below that voltage. The time-of-flight path length was 2.34 m. Complete species composition traces were taken at Condition 1 and Condition 2. For far-field species measurements at Condition 3, an experimental failure interrupted the test. As will be shown later, based on the data that were collected, it was decided that the experiment did not require completion.

Figure 3.75 through Figure 3.80 show traces obtained in time-of-flight measurements at the primary ion energy for the three conditions and at several off-peak voltages. Since it is difficult to identify peaks corresponding to higher charge states in most cases, several plots are presented in both linear and semi-log formats for clarity. It should be noted that the point of arrival of a species in terms of ion mass/unit charge corresponds to the beginning of the rise of a peak, not its maximum. The signal dropout seen following the Xe^+ peak in several of these traces (e.g., Figure 3.75) results from ringing in the time-of-flight amplifier circuitry.

Uncertainties in the time-of-flight measurements arise from several of the same sources as for the ion energy measurements. The rotational position of the P5 was known to within ± 0.5°. The 45-degree energy analyzer pass voltage was known to within its resolution (± 0.4%) and the uncertainty in the voltage provided by the Keithley sourcemeter (± 0.012%). Data were recorded using a Tektronix TDS-540 digitizing oscilloscope that had a horizontal resolution of 0.4 μs and a vertical resolution of 0.3125 mV.

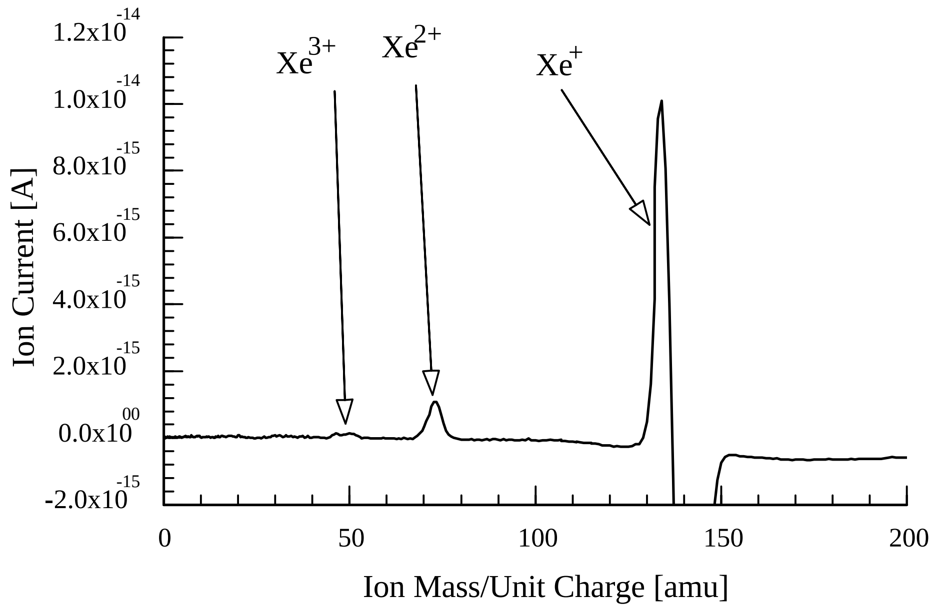

Figure 3.75. Far Field Time-of-flight, Condition 1 - Primary Voltage (263 V)

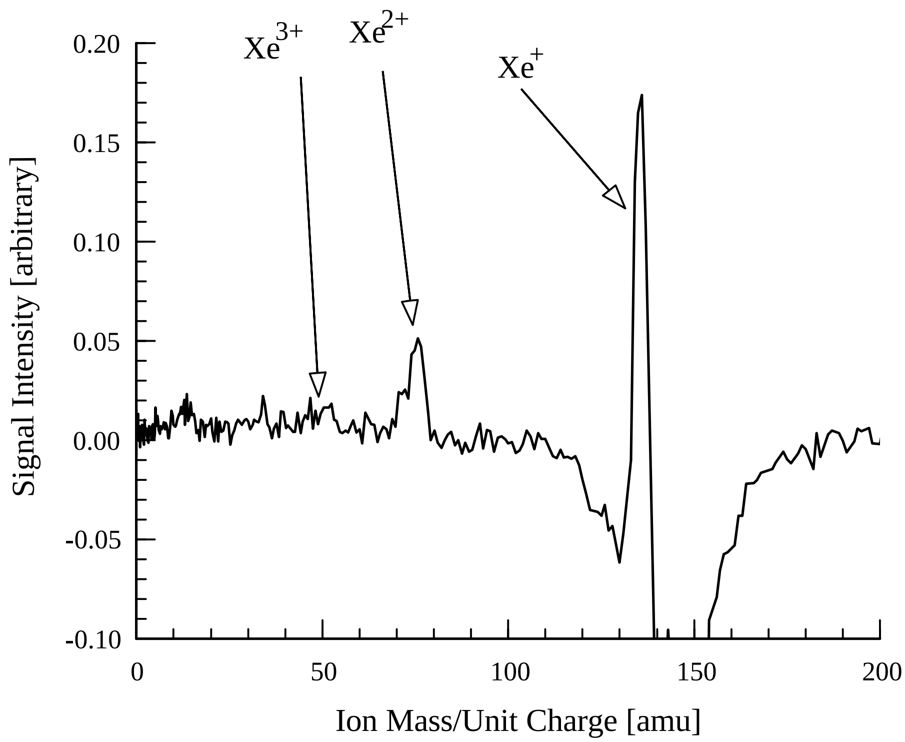

Figure 3.76. Far Field Time-of-flight, Condition 2 - Primary Voltage (454 V)

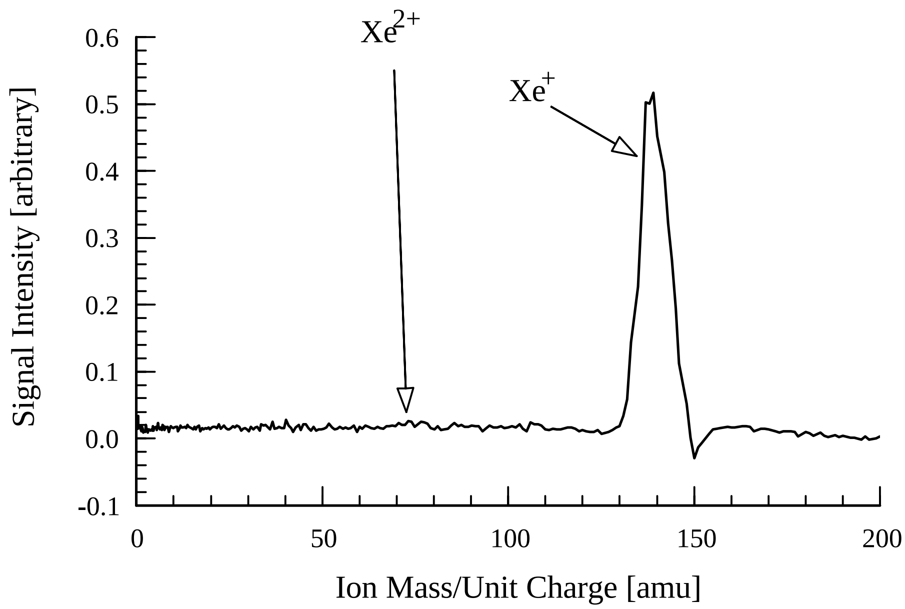

Figure 3.77. Far Field Time-of-flight, Condition 3 - Primary Voltage (449 V)

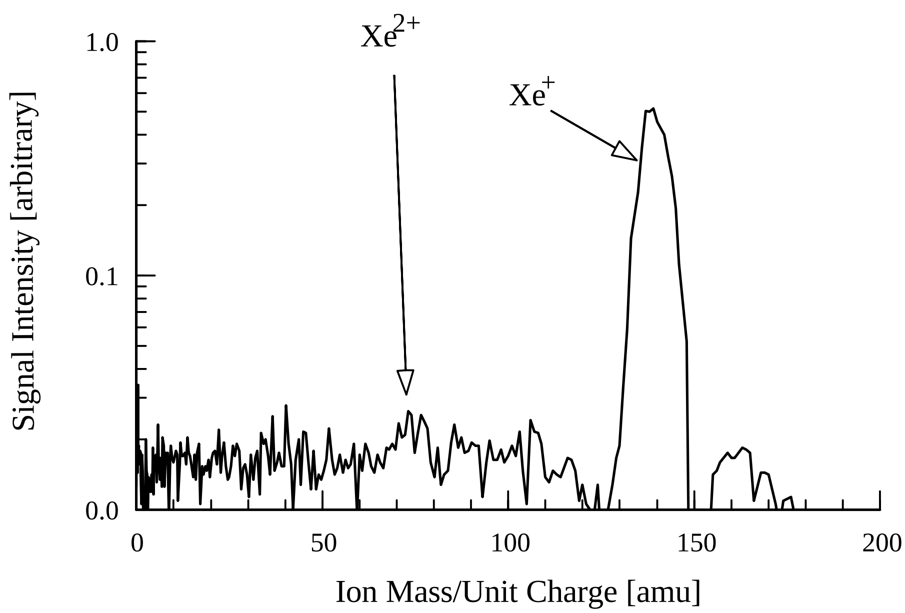

Figure 3.78. Far Field Time-of-flight, Condition 3 - Primary Voltage (449 V) [Semi-log]

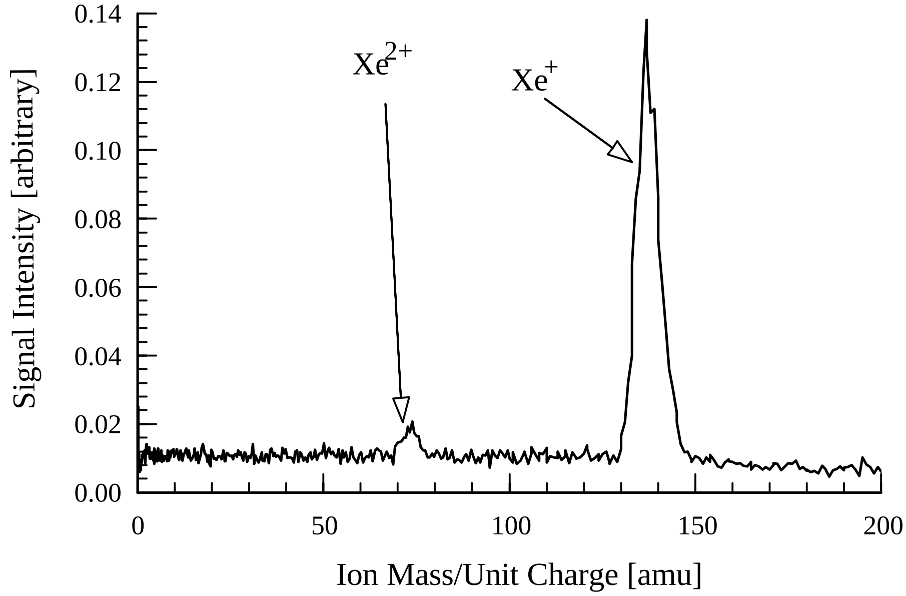

Figure 3.79. Far Field Time-of-flight, Condition 1 - 203 V

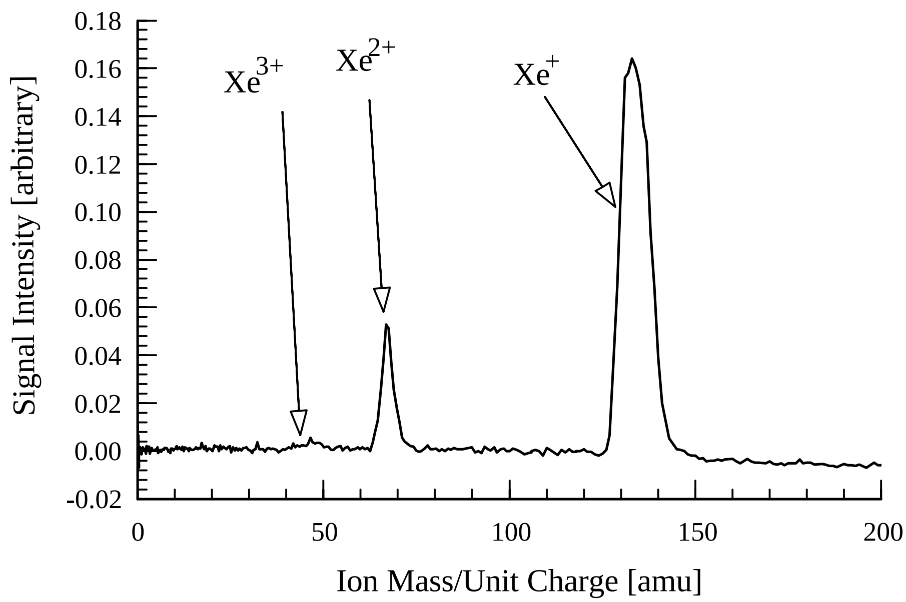

Figure 3.80. Far Field Time-of-flight, Condition 1 - 343 V

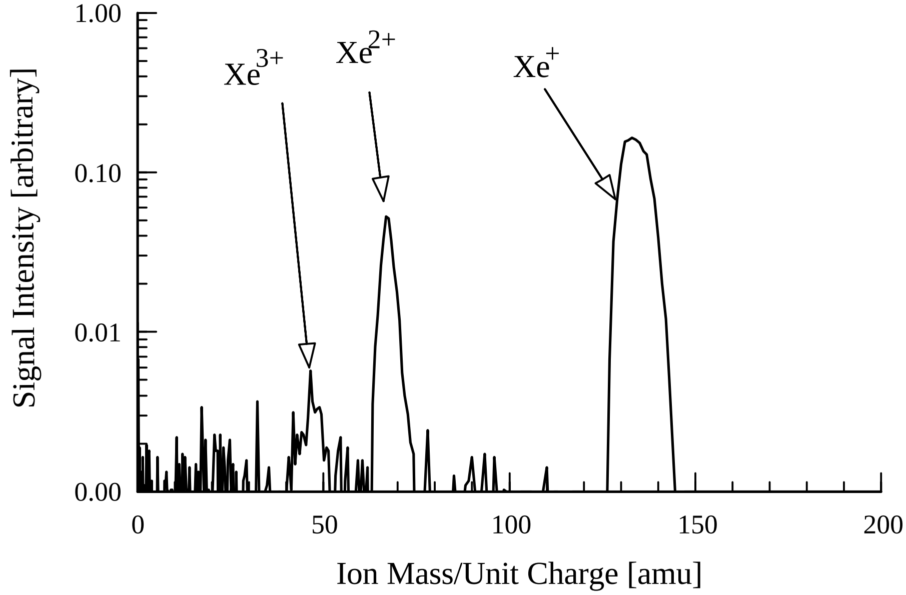

Figure 3.81. Far Field Time-of-flight, Condition 1 - 343 V [Semi-log]

The results of the far-field ion energy distribution and time-of-flight measurements will be discussed in Chapter 6.

CHAPTER IV

NEAR FIELD MEASUREMENTS

Near field measurements were taken on the P5 using the system described in Section 2.3.4.

4.1. Ion Energy Measurements

Near field ion energy measurements were taken 10 cm from the thruster at three operating conditions (See Table 2.2). The thruster was rotated from 0° until loss of signal (typically ~95°) as shown in Figure 4.1. For these measurements, however, the center of rotation was the center of the annular discharge chamber. This was done so that the ion energy contributions of one side of the discharge chamber could be examined independently of the other. Measurements were taken in 5° increments. The 45-degree pass voltage was swept from 0 to 1000 V in 1 V increments which, with a spectrometer constant of 0.549, gives a sweep of ion energy of 0 to 1800 V in 1.8 V increments.

The sampling orifice was aligned to the 45 degree energy analyzer entrance slit by passing a laser through the entrance slit such that it was parallel to the ion beam path. The orifice was then aligned to that beam. The thruster angle was set such that the laser was parallel to the face of the thruster when it was oriented at 90°. The uncertainty factors were the same as in the far field.

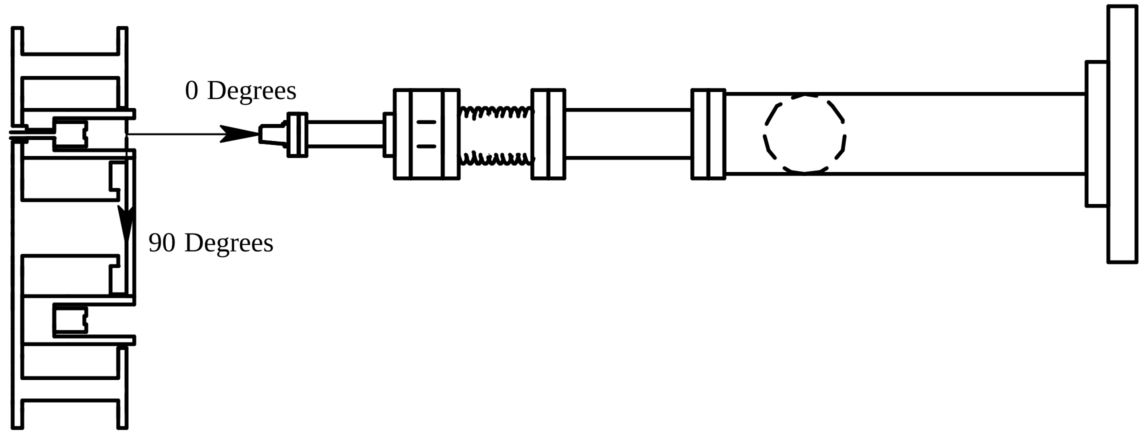

Figure 4.1. Near Field Rotational Configuration

Near field ion energy sweeps performed at Condition 1 are presented in Figure 4.2 through Figure 4.25. For this case, the thruster discharge voltage was 300 V, the discharge current was 5.2 A, the anode mass flow rate was 58 sccm, and the cathode flow rate was 6 sccm. The horizontal scale was decreased from 1800 V to 1200 V and selected plots are also shown in semi-log scale to increase resolution.

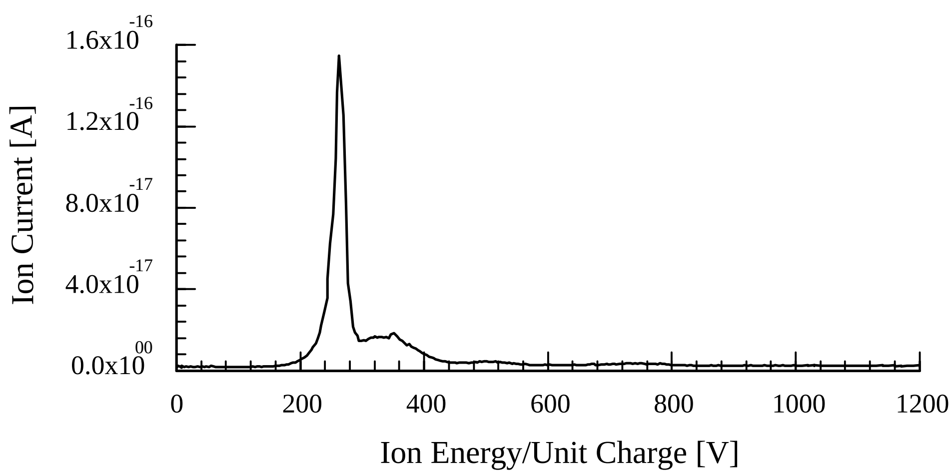

Figure 4.2. Near Field - Condition 1, 0 Degrees

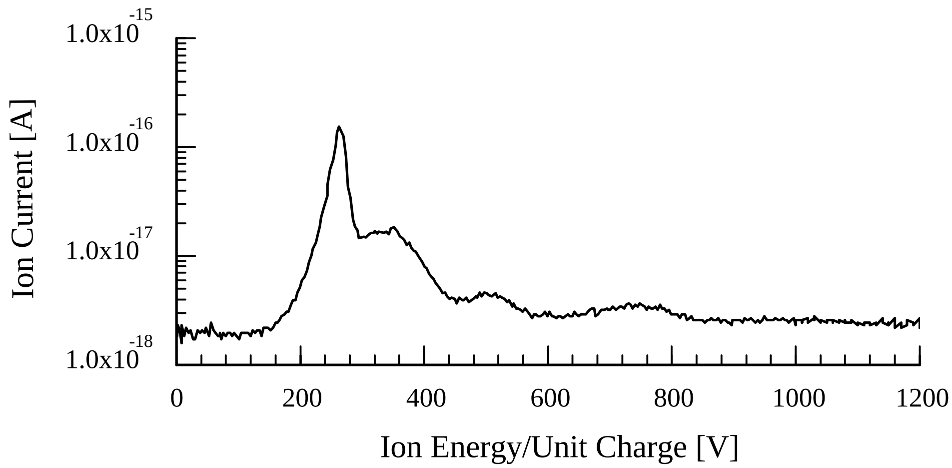

Figure 4.3. Near Field - Condition 1, 0 Degrees [Semi-log]

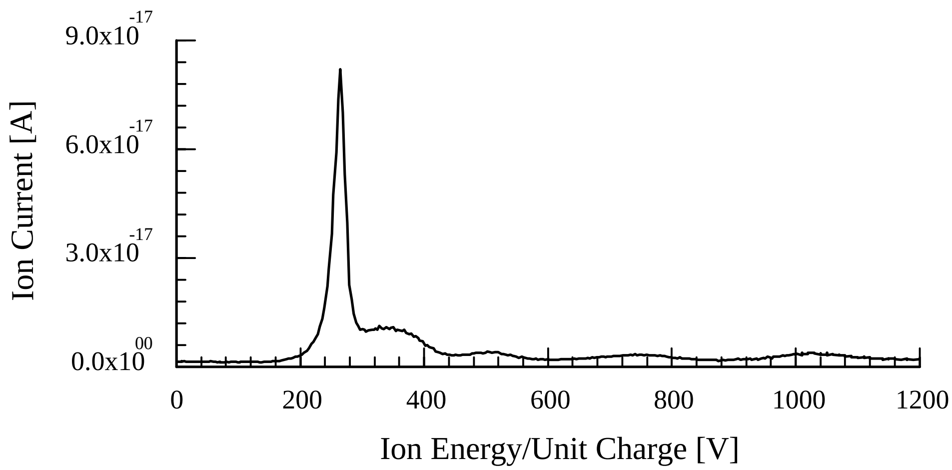

Figure 4.4. Near Field - Condition 1, 5 Degrees

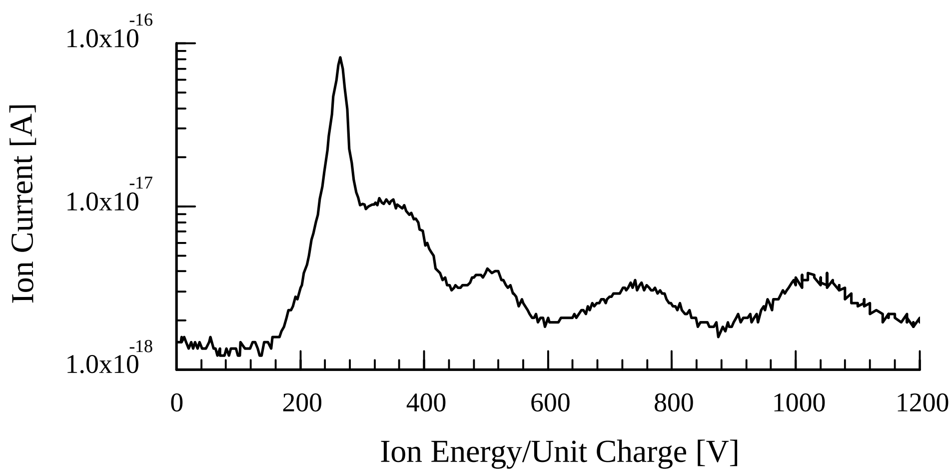

Figure 4.5. Near Field - Condition 1, 5 Degrees [Semi-log]

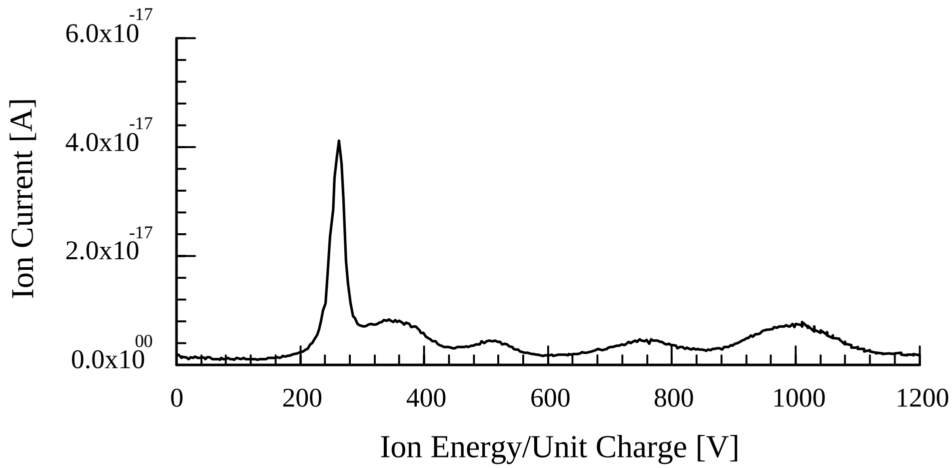

Figure 4.6. Near Field - Condition 1, 10 Degrees

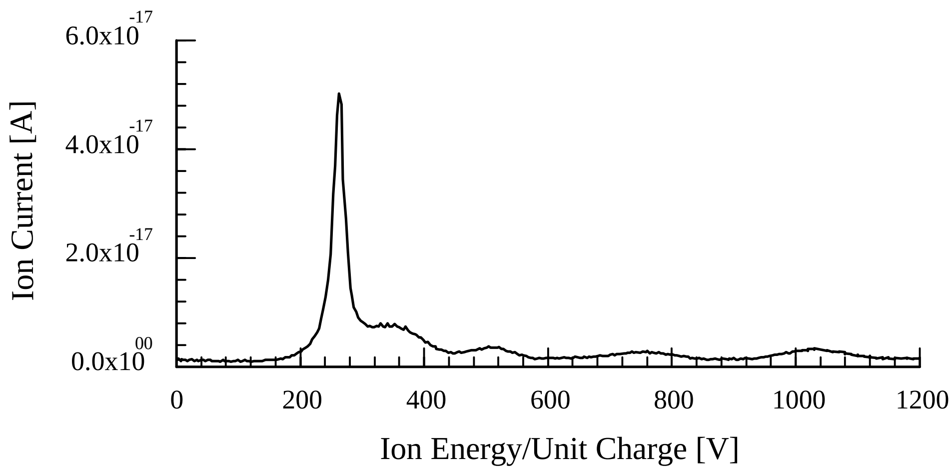

Figure 4.7. Near Field - Condition 1, 15 Degrees

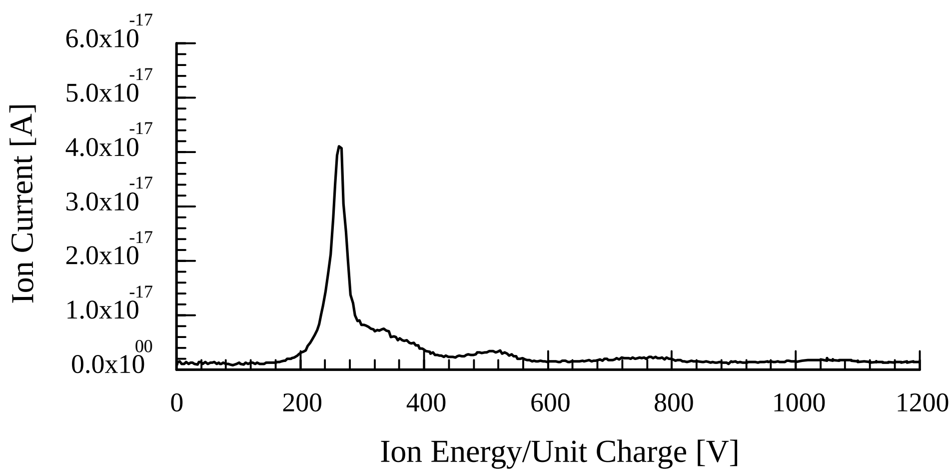

Figure 4.8. Near Field - Condition 1, 20 Degrees

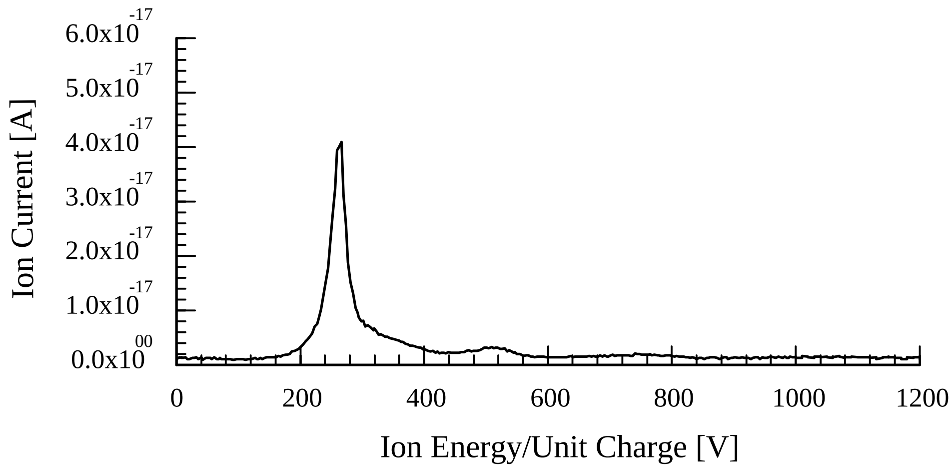

Figure 4.9. Near Field - Condition 1, 25 Degrees

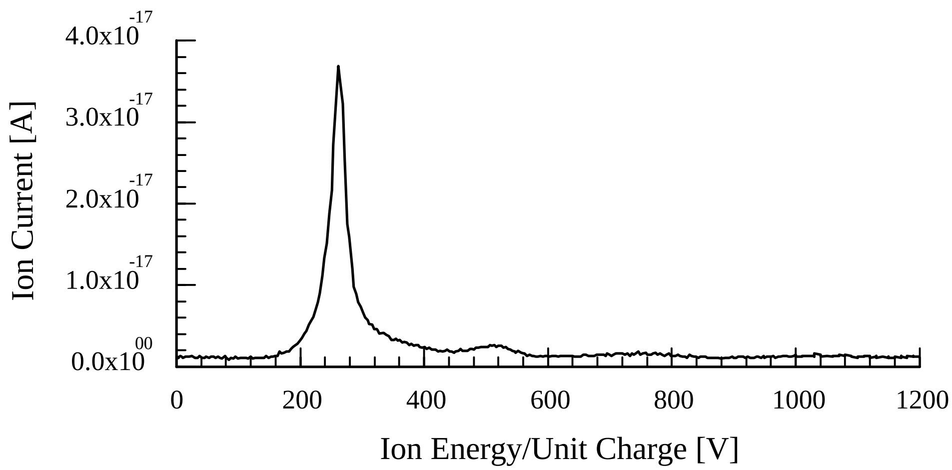

Figure 4.10. Near Field - Condition 1, 30 Degrees

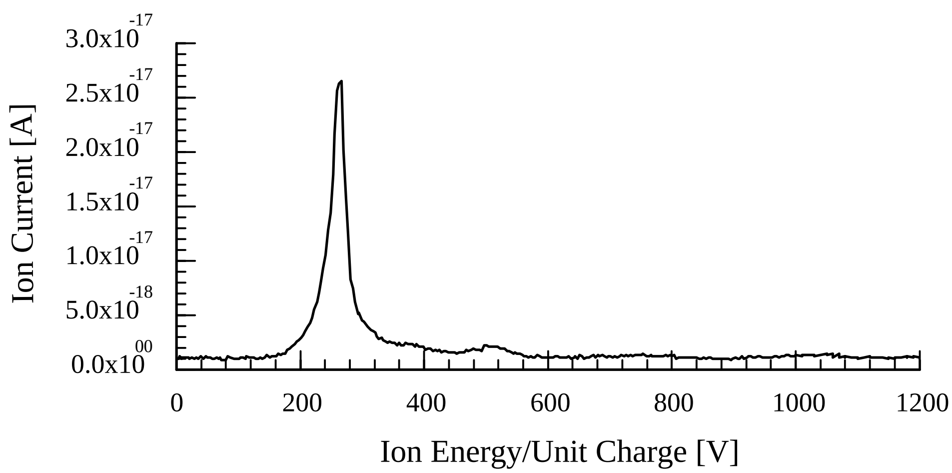

Figure 4.11. Near Field - Condition 1, 35 Degrees

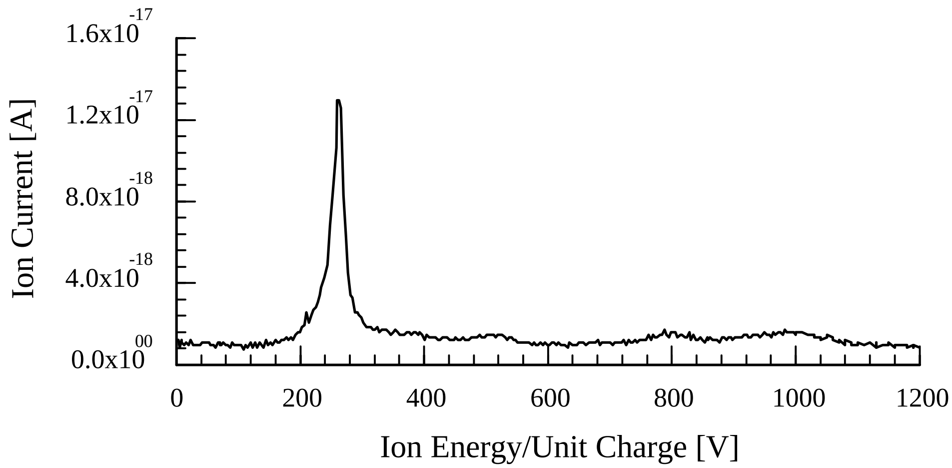

Figure 4.12. Near Field - Condition 1, 40 Degrees

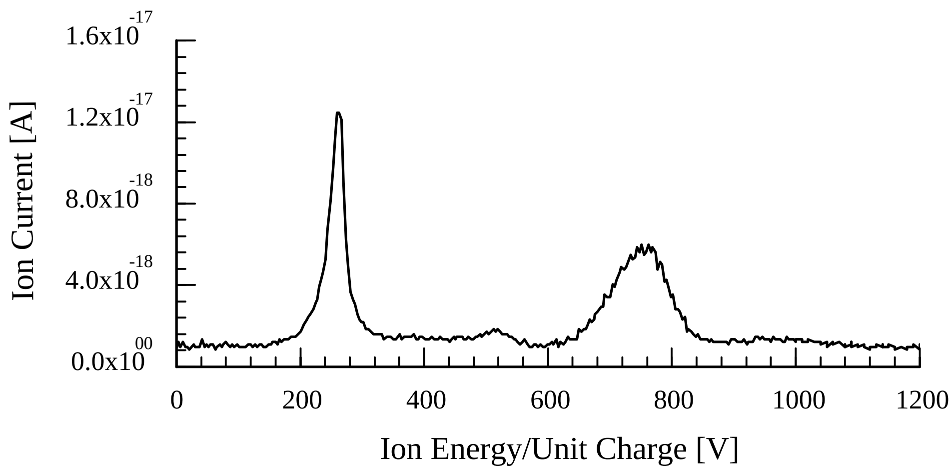

Figure 4.13. Near Field - Condition 1, 45 Degrees

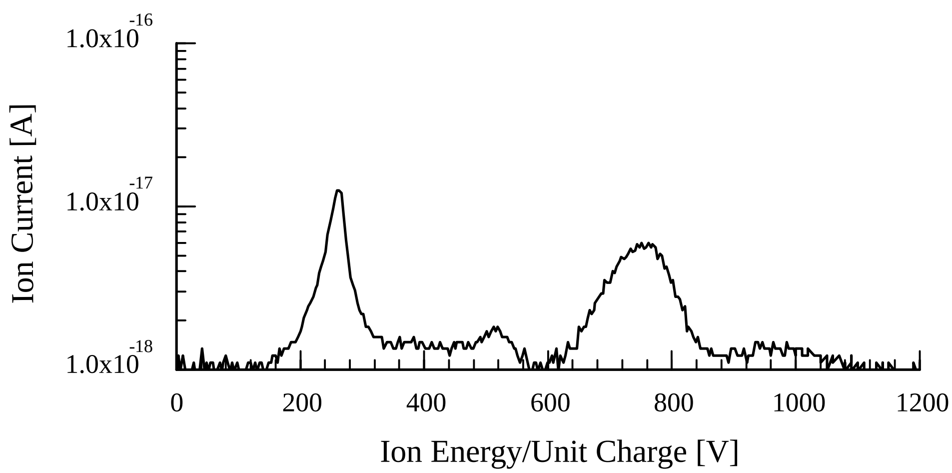

Figure 4.14. Near Field - Condition 1, 45 Degrees [Semi-log]

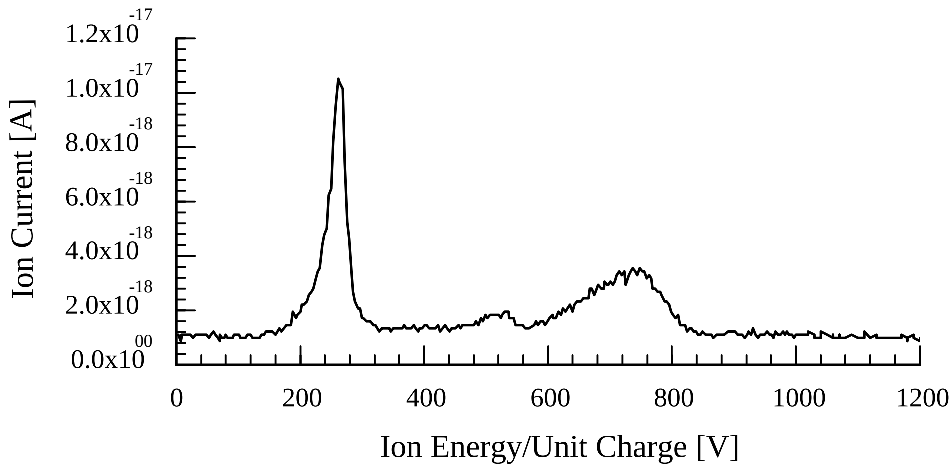

Figure 4.15. Near Field - Condition 1, 50 Degrees

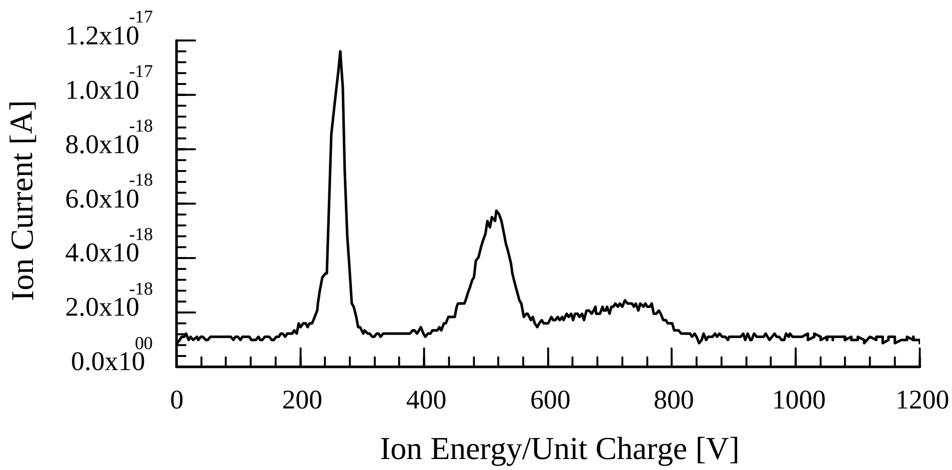

Figure 4.16. Near Field - Condition 1, 55 Degrees

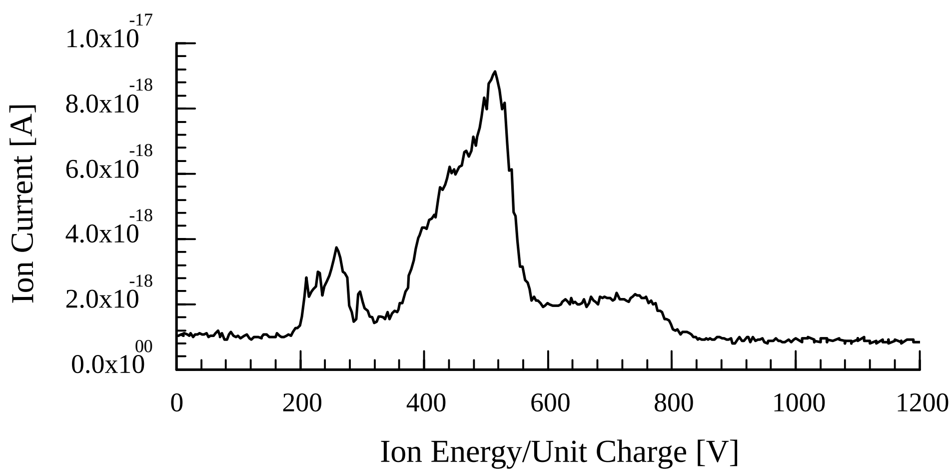

Figure 4.17. Near Field - Condition 1, 60 Degrees

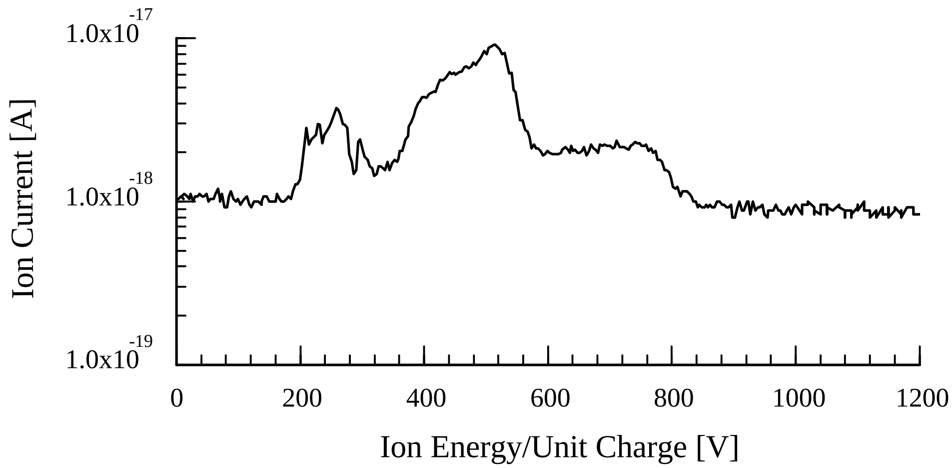

Figure 4.18. Near Field - Condition 1, 60 Degrees [Semi-log]

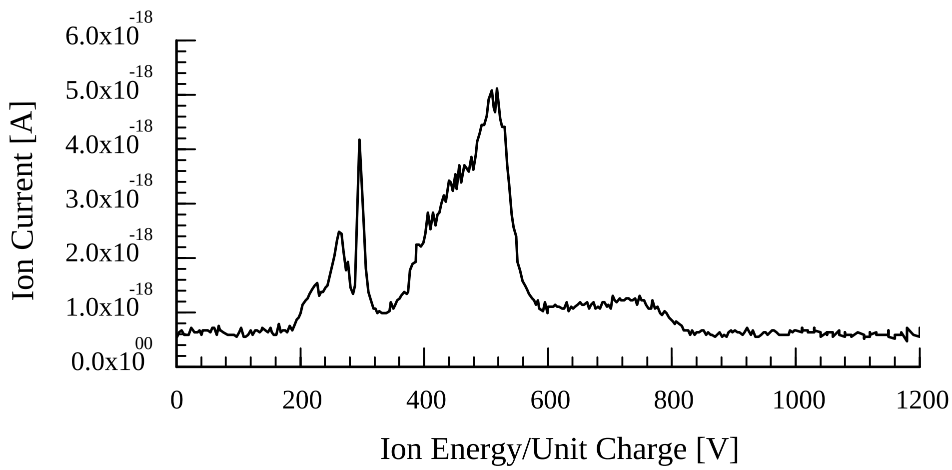

Figure 4.19. Near Field - Condition 1, 65 Degrees

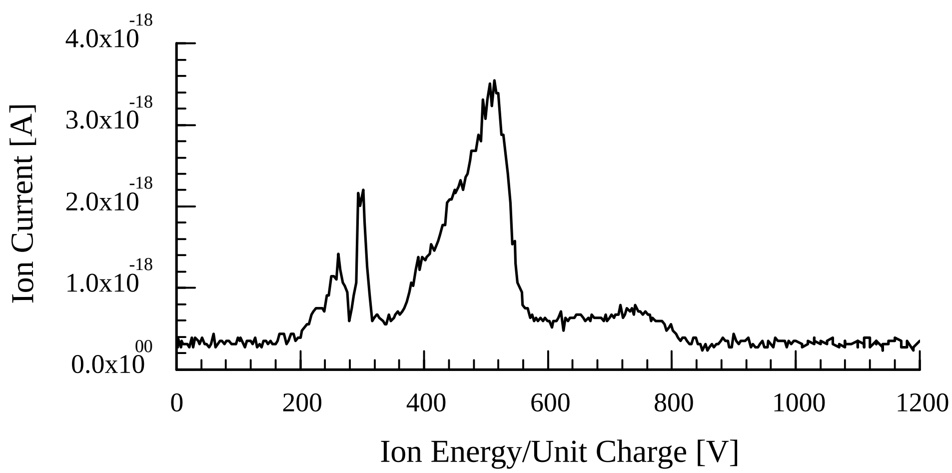

Figure 4.20. Near Field - Condition 1, 70 Degrees

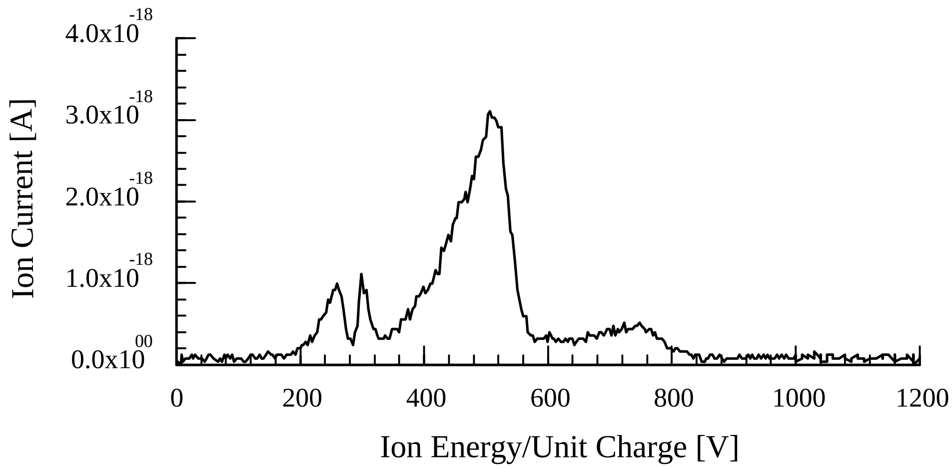

Figure 4.21. Near Field - Condition 1, 75 Degrees

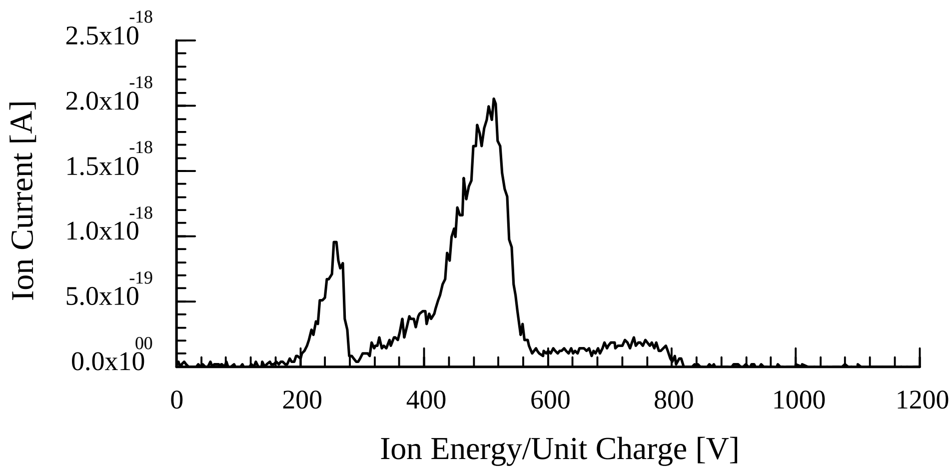

Figure 4.22. Near Field - Condition 1, 80 Degrees

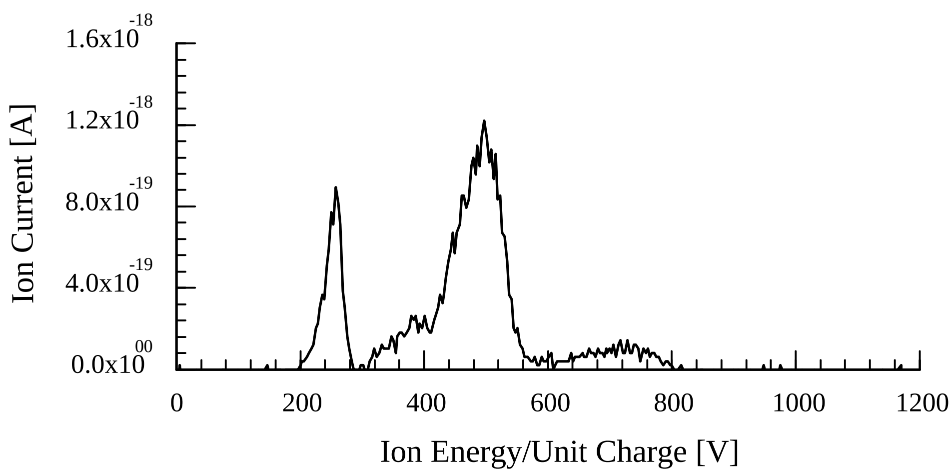

Figure 4.23. Near Field - Condition 1, 85 Degrees

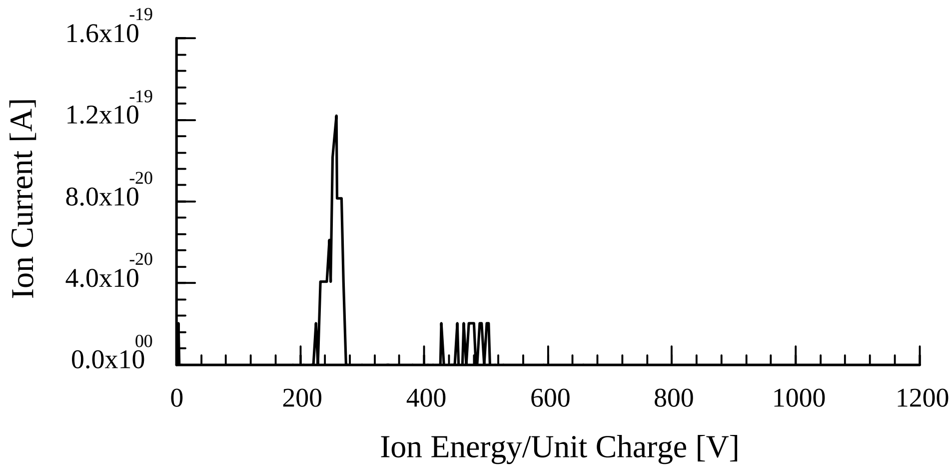

Figure 4.24. Near Field - Condition 1, 90 Degrees

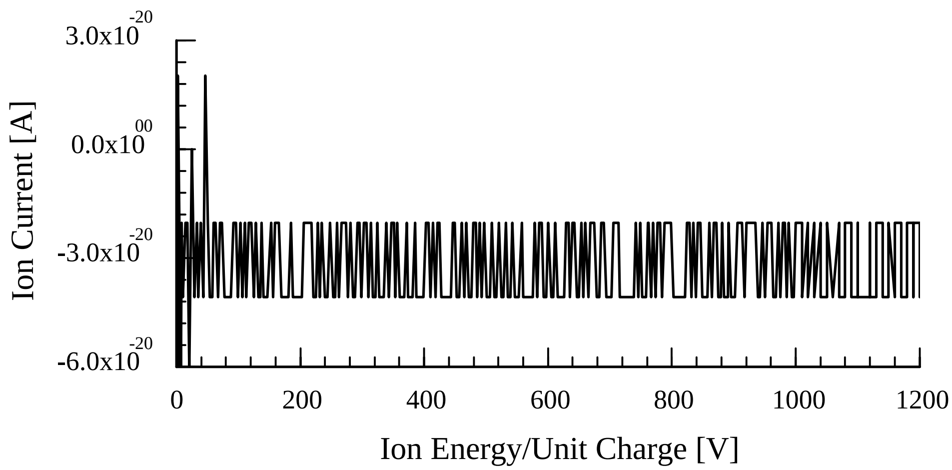

Figure 4.25. Near Field - Condition 1, 95 Degrees - Loss of Signal

Near field ion energy sweeps performed at Condition 2 are presented in Figure 4.26 through Figure 4.47. For this case, the thruster discharge voltage was 500 V, the discharge current was 5.4 A, the anode mass flow rate was 58 sccm, and the cathode flow rate was 6 sccm. Selected plots are also shown in semi-log scale to increase resolution.

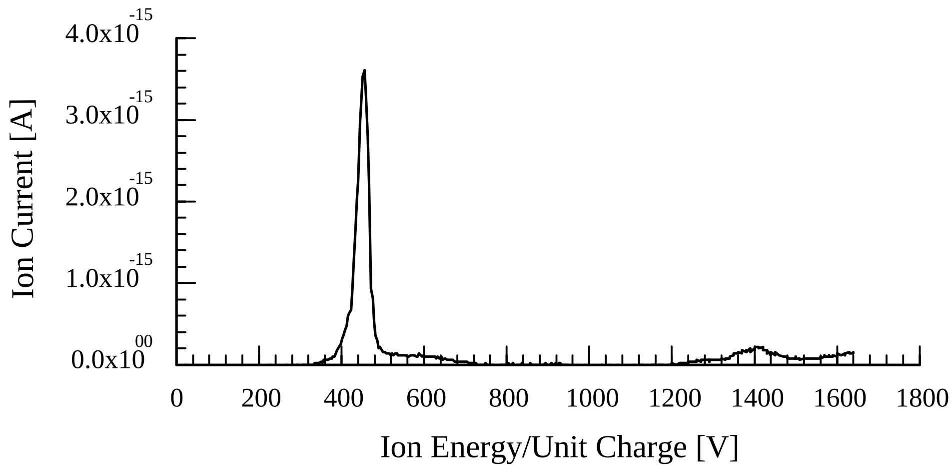

Figure 4.26. Near Field - Condition 2, 0 Degrees

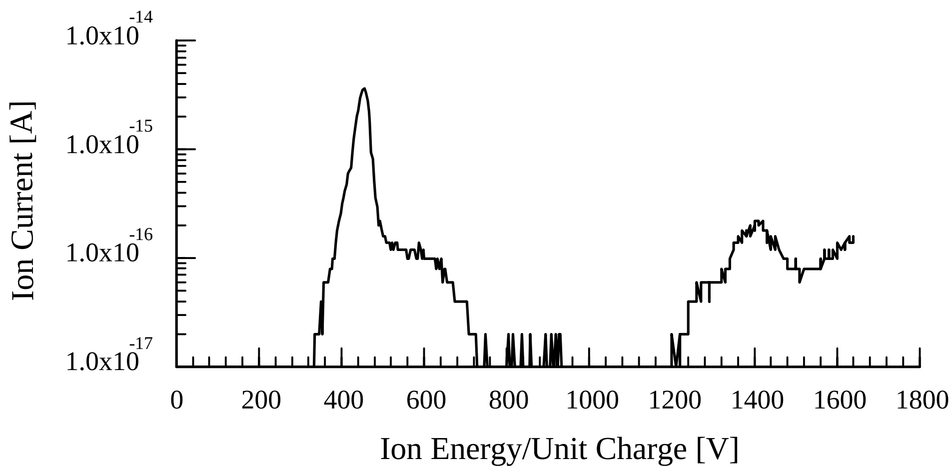

Figure 4.27. Near Field - Condition 2, 0 Degrees [Semi-log]

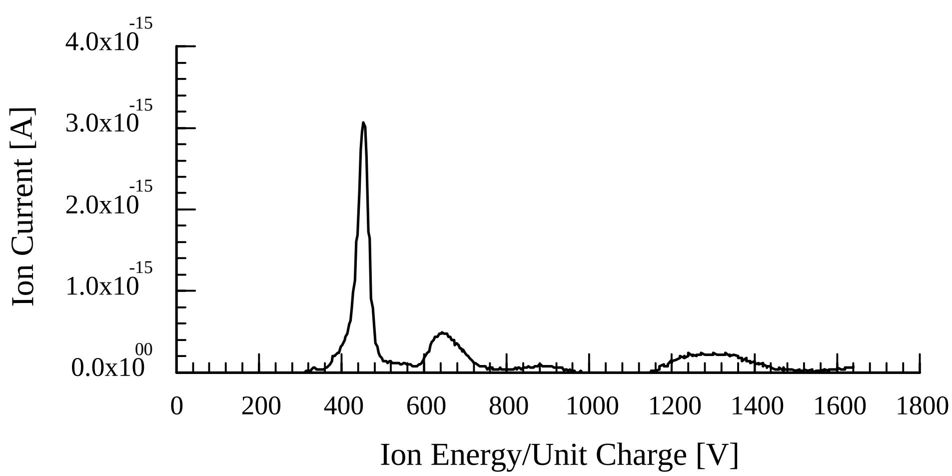

Figure 4.28. Near Field - Condition 2, 5 Degrees

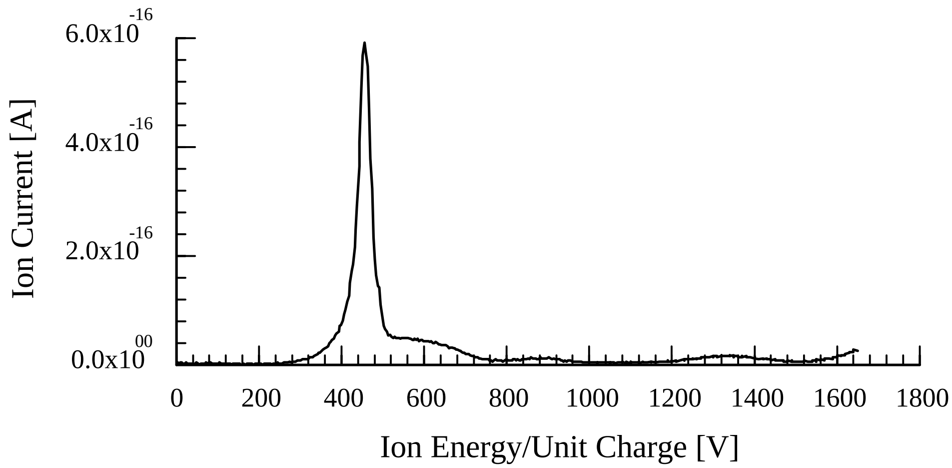

Figure 4.29. Near Field - Condition 2, 10 Degrees

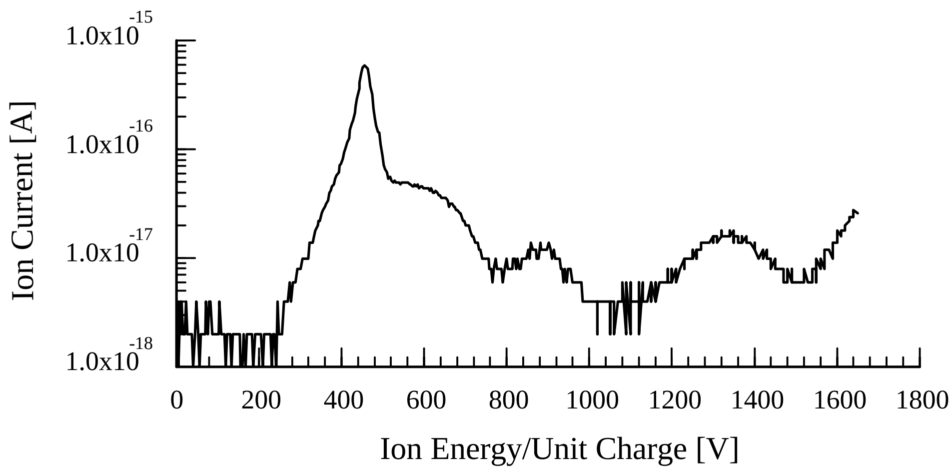

Figure 4.30. Near Field - Condition 2, 10 Degrees [Semi-log]

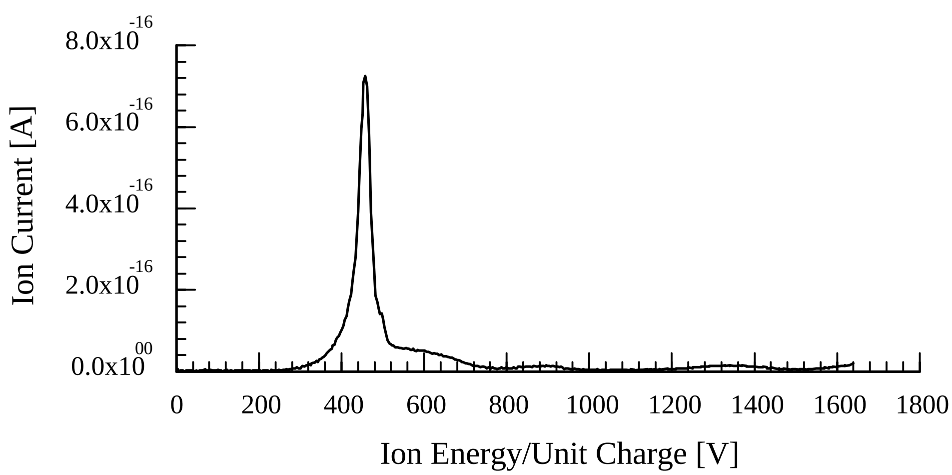

Figure 4.31. Near Field - Condition 2, 15 Degrees

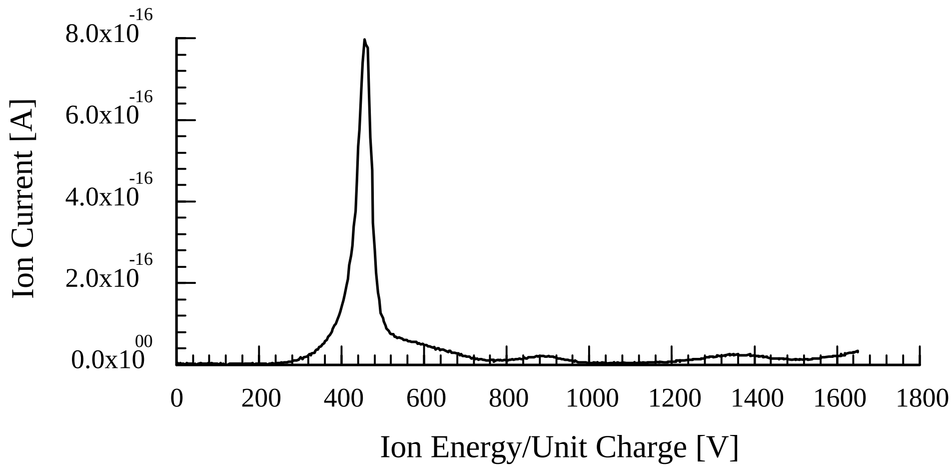

Figure 4.32. Near Field - Condition 2, 20 Degrees

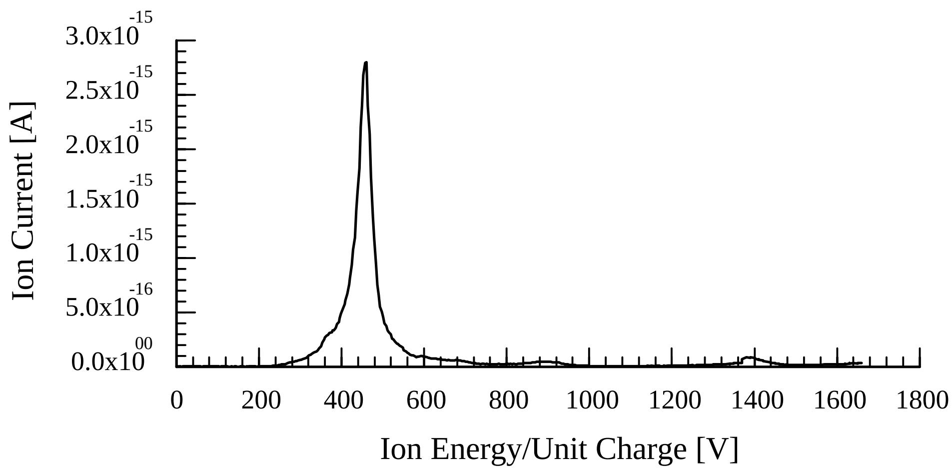

Figure 4.33. Near Field - Condition 2, 25 Degrees

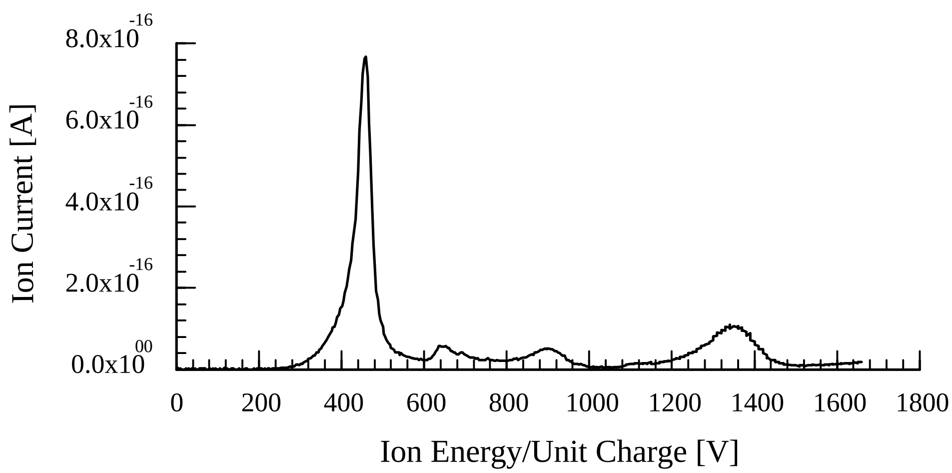

Figure 4.34. Near Field - Condition 2, 30 Degrees

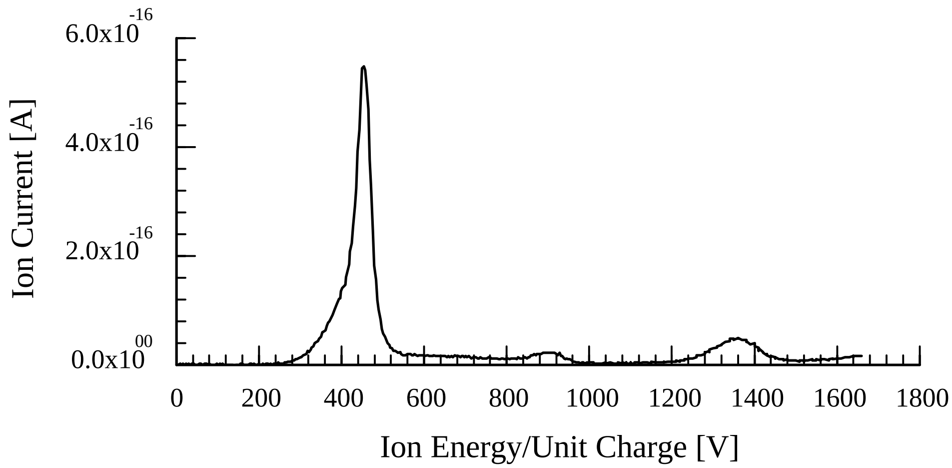

Figure 4.35. Near Field - Condition 2, 35 Degrees

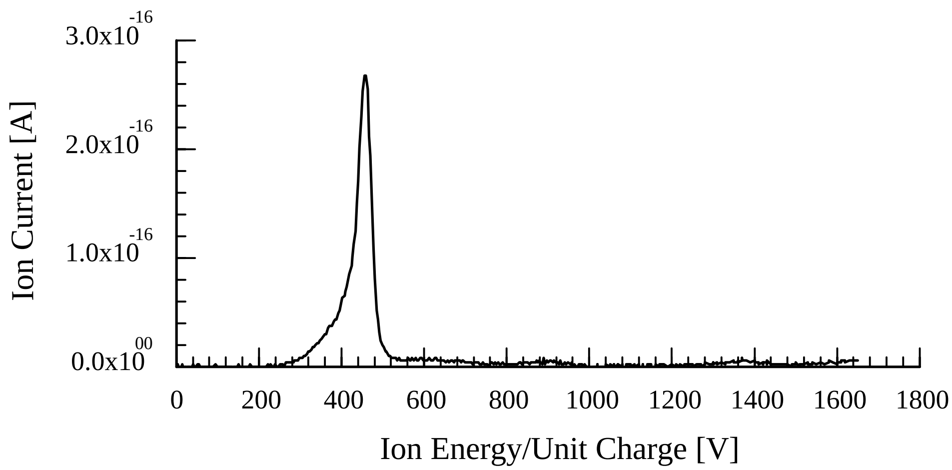

Figure 4.36. Near Field - Condition 2, 40 Degrees

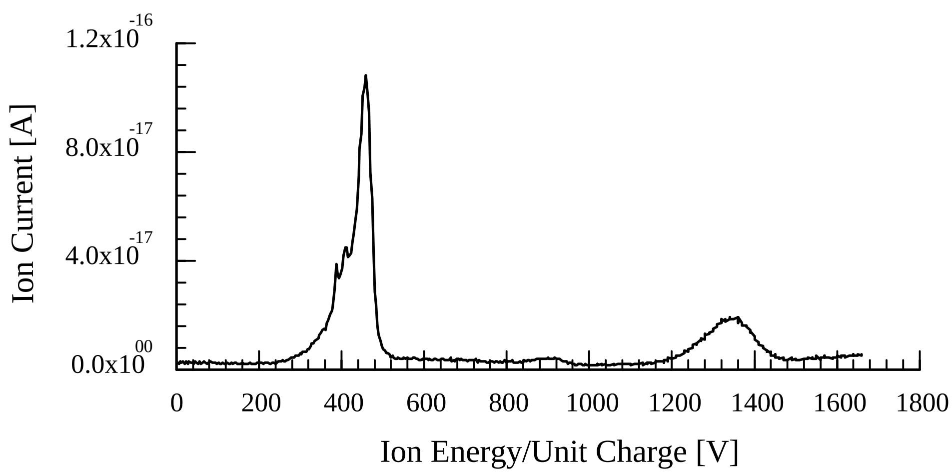

Figure 4.37. Near Field - Condition 2, 45 Degrees

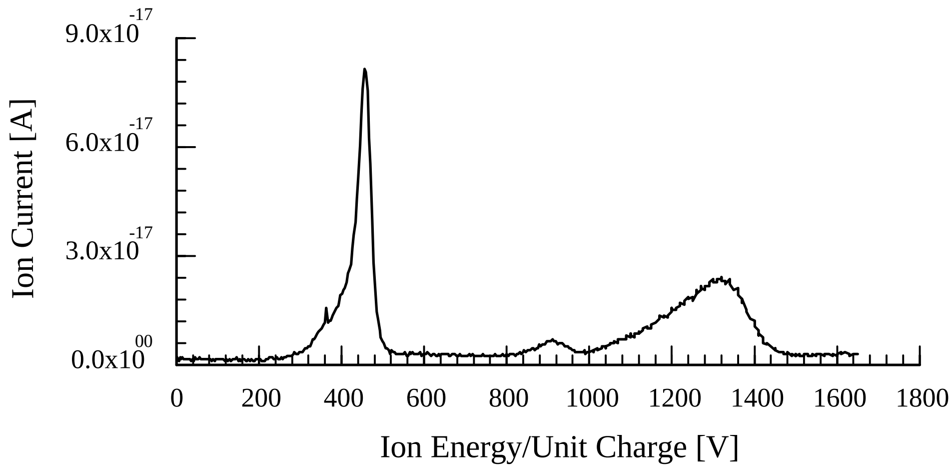

Figure 4.38. Near Field - Condition 2, 50 Degrees

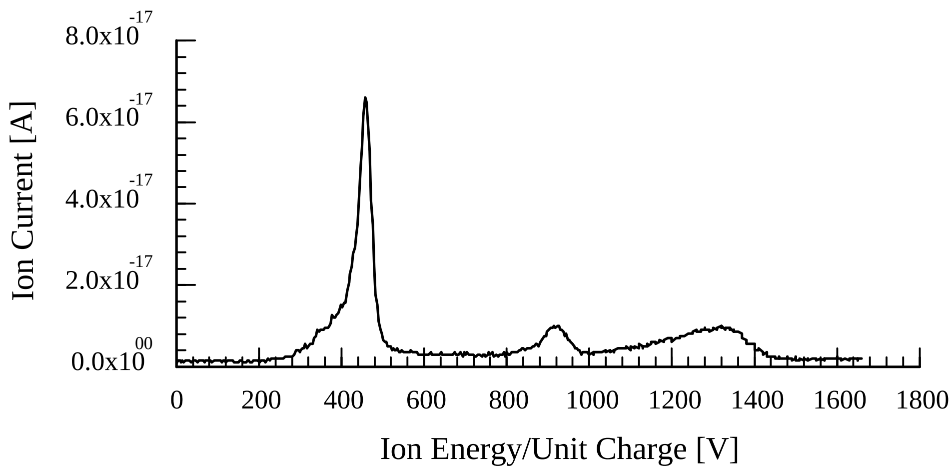

Figure 4.39. Near Field - Condition 2, 55 Degrees

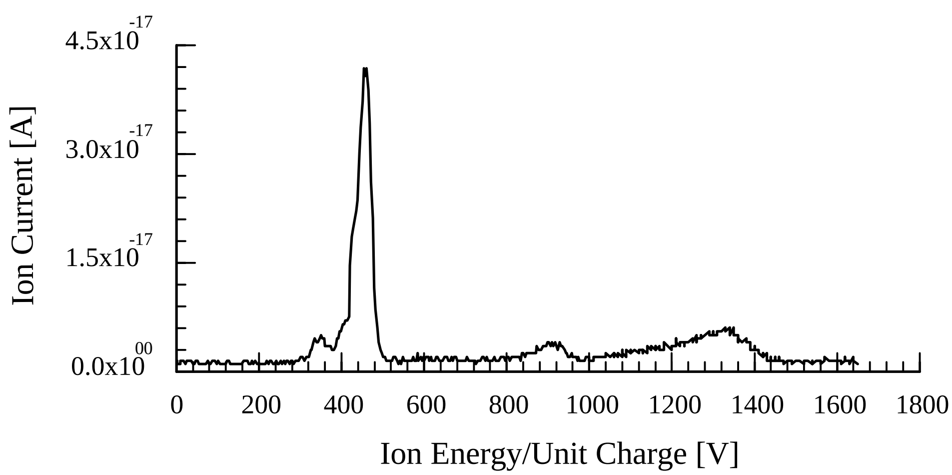

Figure 4.40. Near Field - Condition 2, 60 Degrees

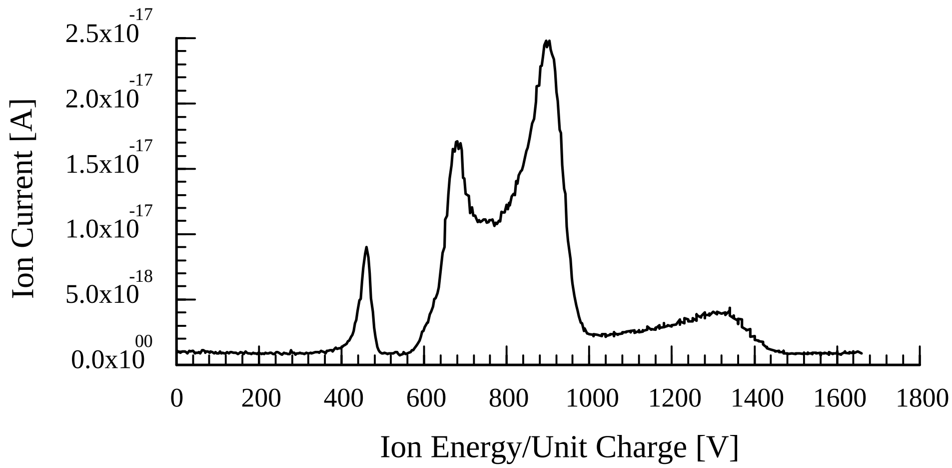

Figure 4.41. Near Field - Condition 2, 65 Degrees

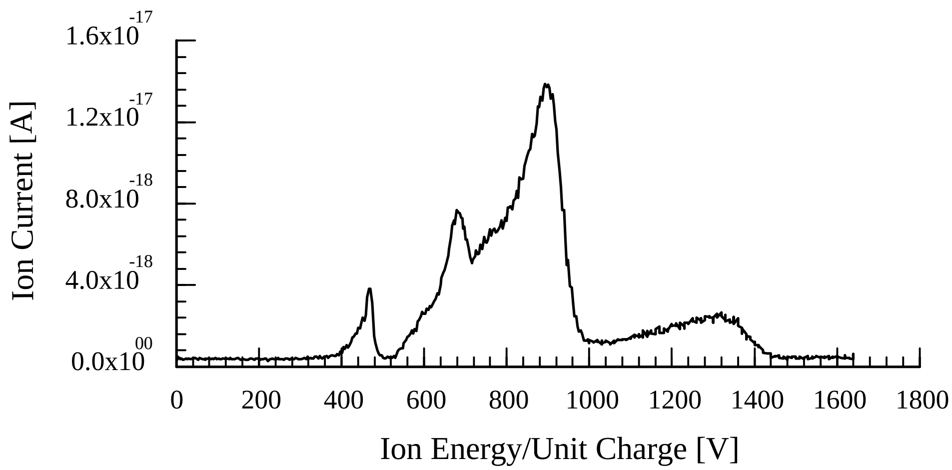

Figure 4.42. Near Field - Condition 2, 70 Degrees

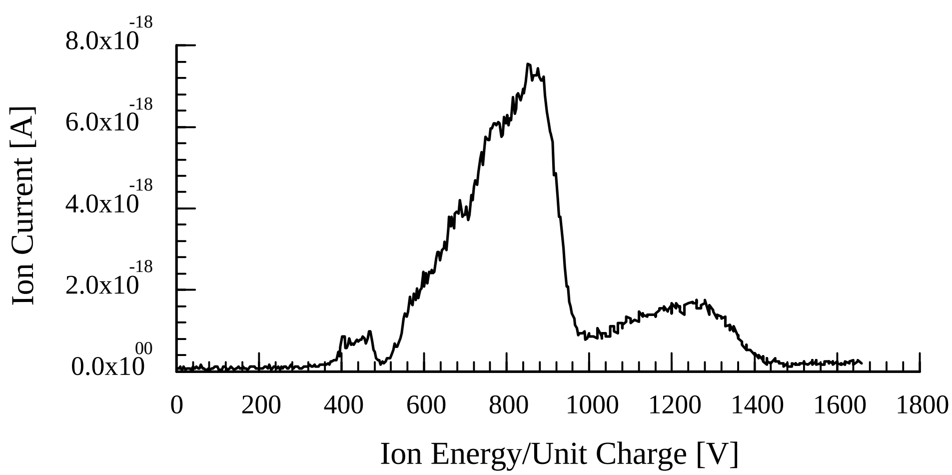

Figure 4.43. Near Field - Condition 2, 75 Degrees

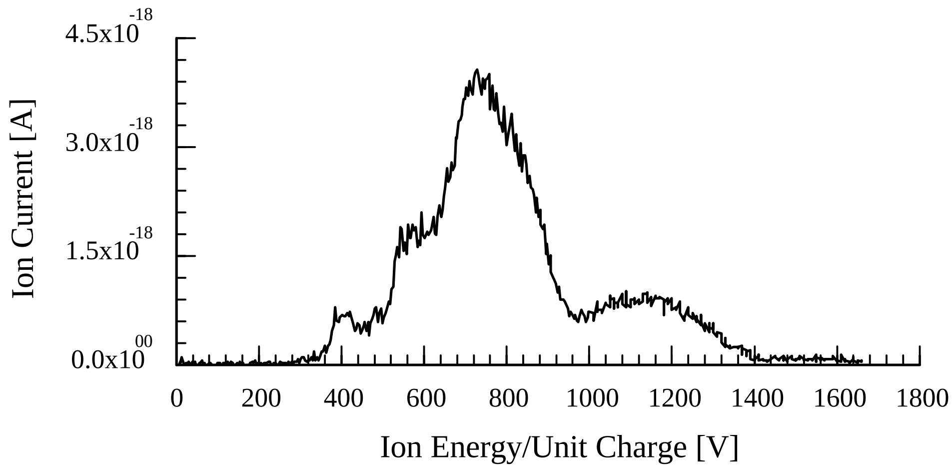

Figure 4.44. Near Field - Condition 2, 80 Degrees

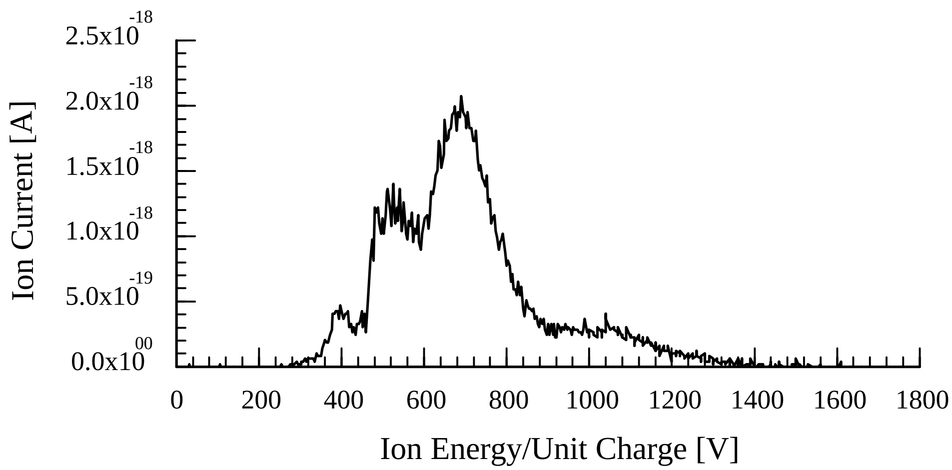

Figure 4.45. Near Field - Condition 2, 85 Degrees

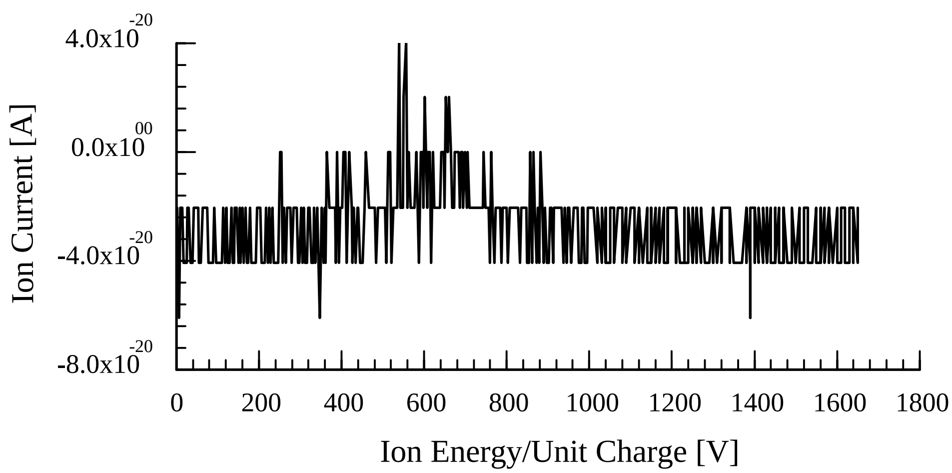

Figure 4.46. Near Field - Condition 2, 90 Degrees

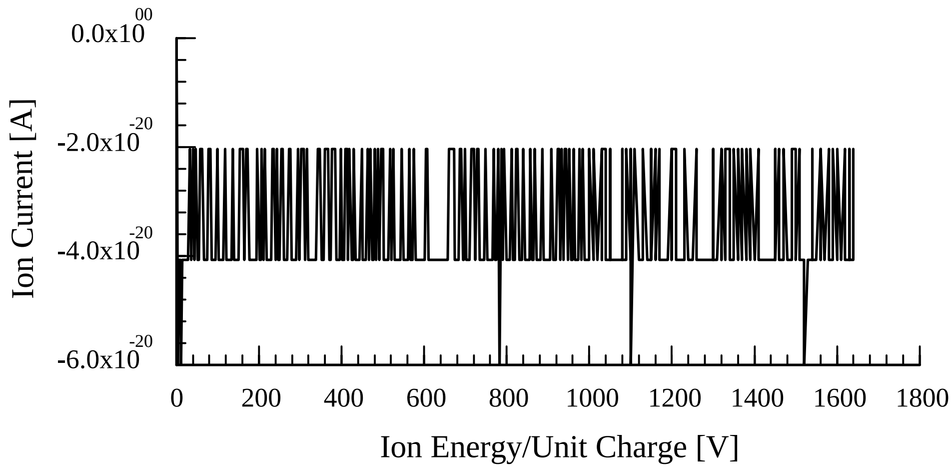

Figure 4.47. Near Field - Condition 2, 95 Degrees - Loss of Signal

Near field ion energy sweeps performed at Condition 3 are presented in Figure 4.48 through Figure 4.68. For this case, the thruster discharge voltage was 500 V, the discharge current was 10.2 A, the anode mass flow rate was 105 sccm, and the cathode flow rate was 6 sccm. Selected plots are shown in semi-log scale to increase resolution.

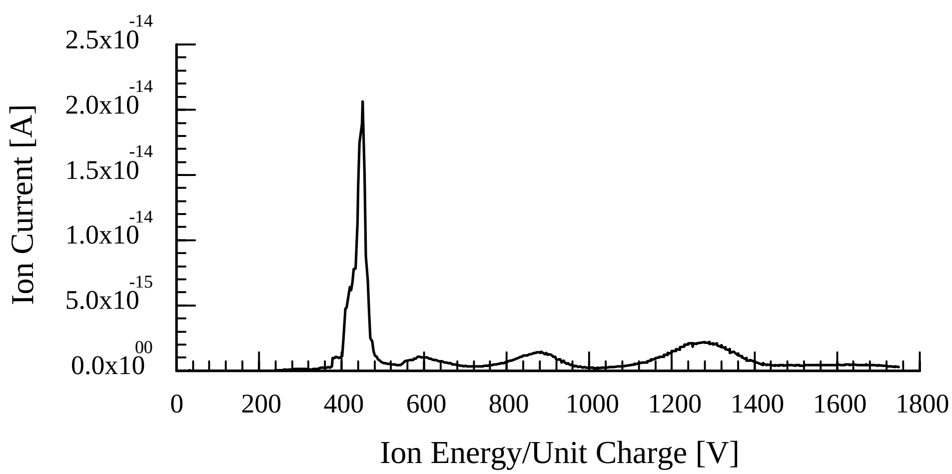

Figure 4.48. Near Field - Condition 3, 0 Degrees

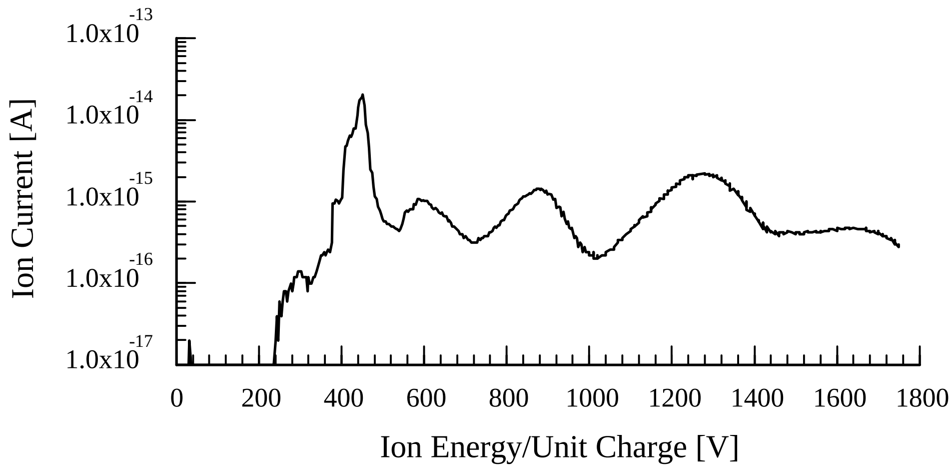

Figure 4.49. Near Field - Condition 3, 0 Degrees [Semi-log]

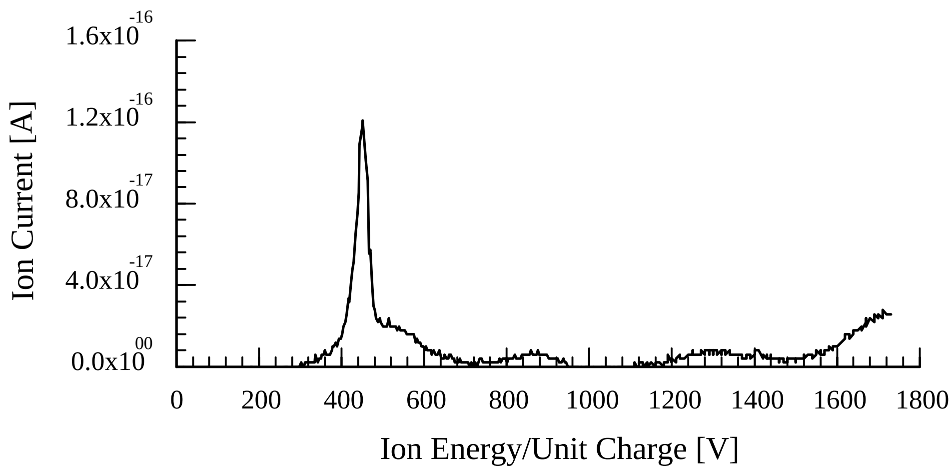

Figure 4.50. Near Field - Condition 3, 5 Degrees

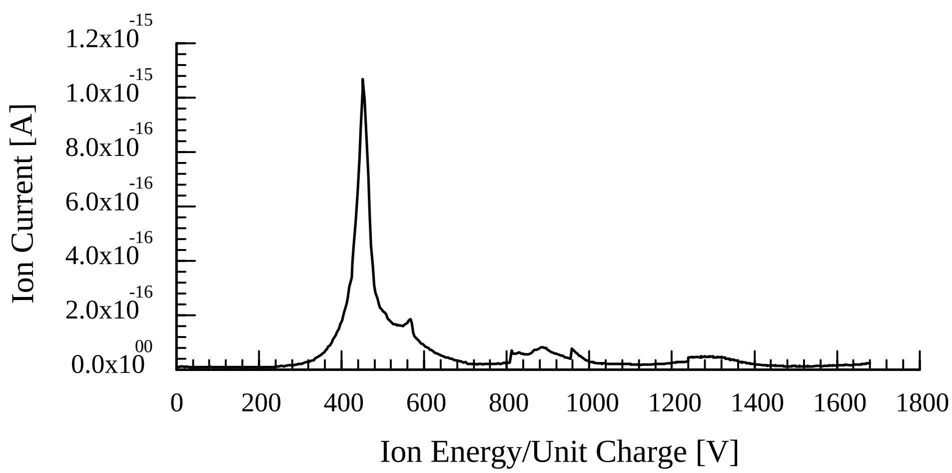

Figure 4.51. Near Field - Condition 3, 10 Degrees

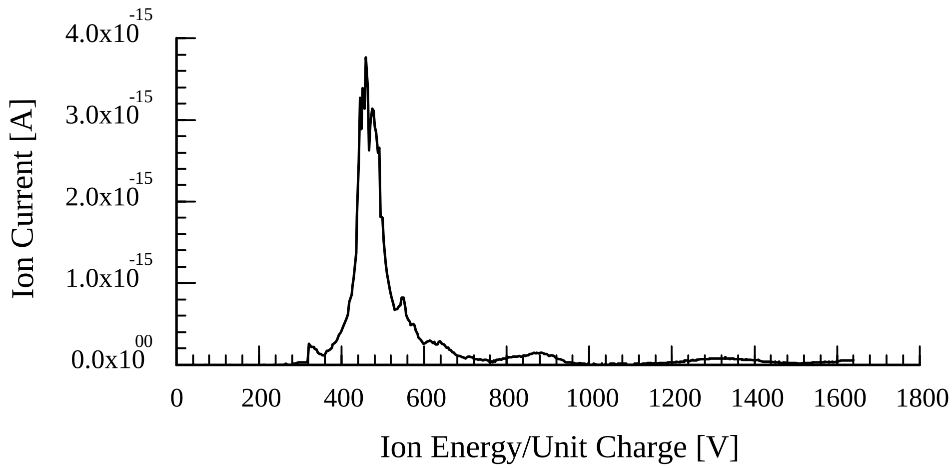

Figure 4.52. Near Field - Condition 3, 15 Degrees

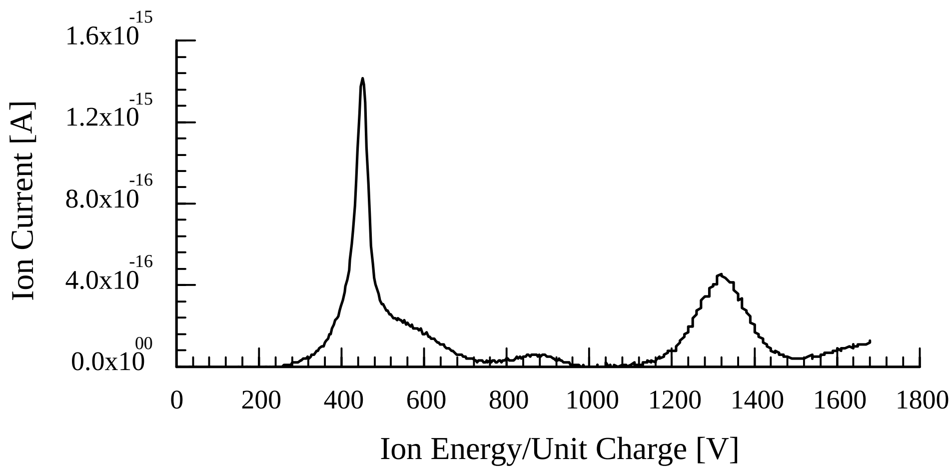

Figure 4.53. Near Field - Condition 3, 20 Degrees

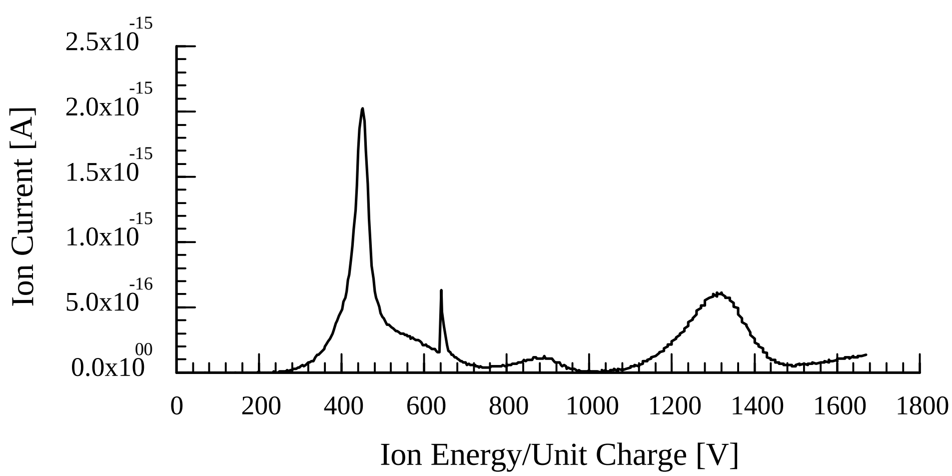

Figure 4.54. Near Field - Condition 3, 25 Degrees

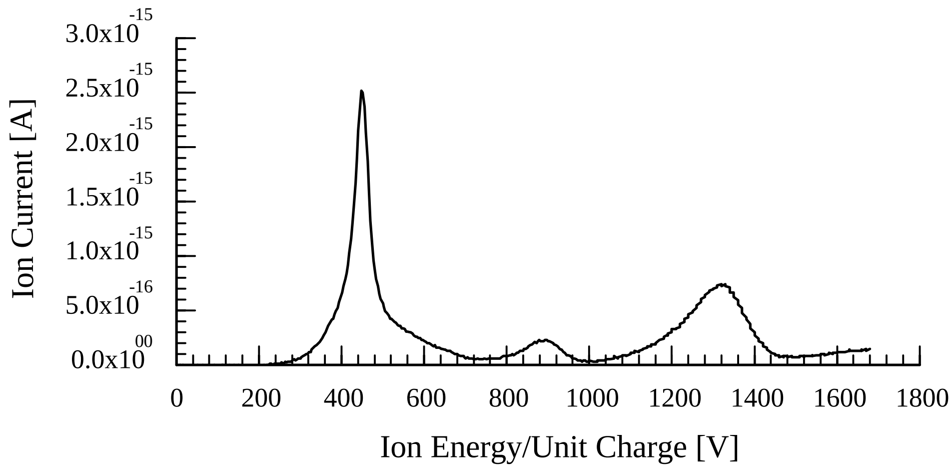

Figure 4.55. Near Field - Condition 3, 30 Degrees

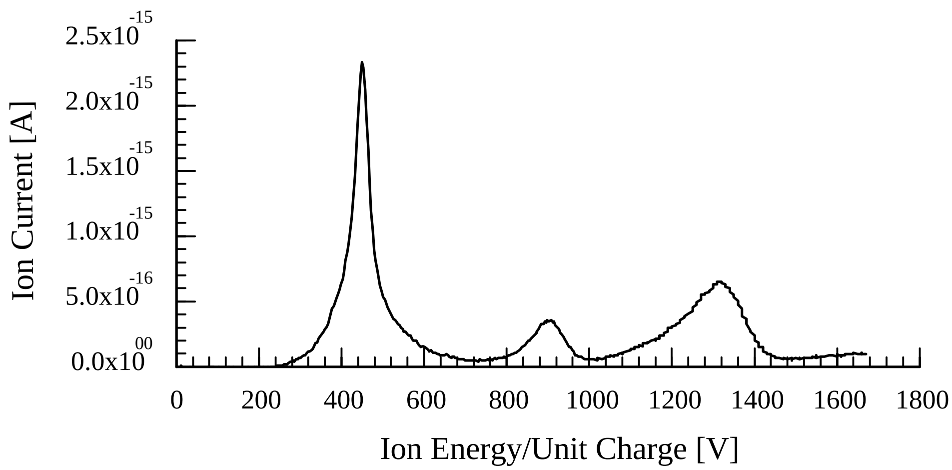

Figure 4.56. Near Field - Condition 3, 35 Degrees

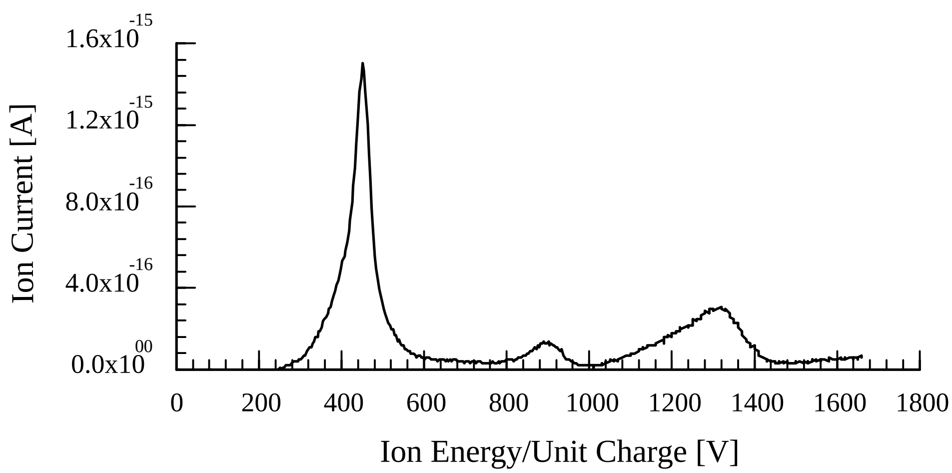

Figure 4.57. Near Field - Condition 3, 40 Degrees

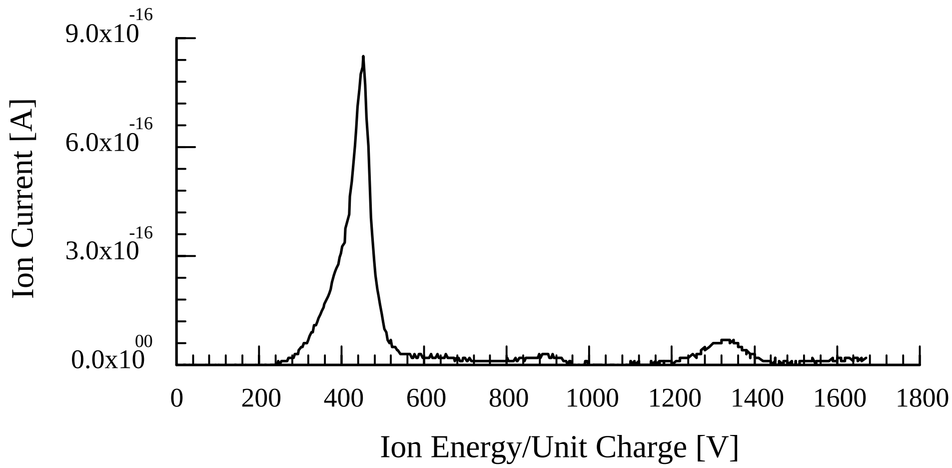

Figure 4.58. Near Field - Condition 3, 45 Degrees

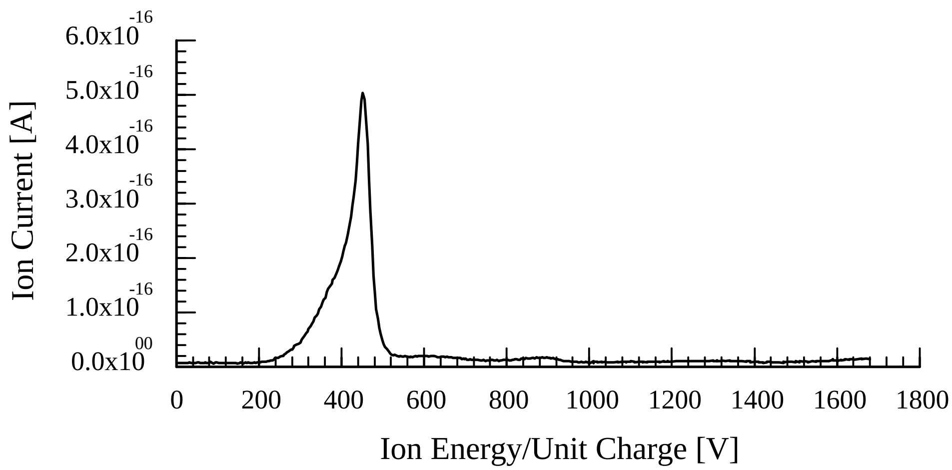

Figure 4.59. Near Field - Condition 3, 50 Degrees

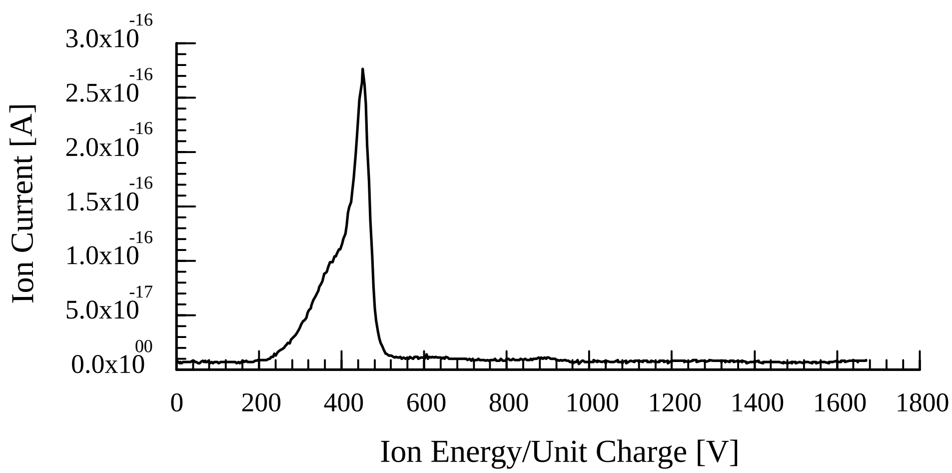

Figure 4.60. Near Field - Condition 3, 55 Degrees

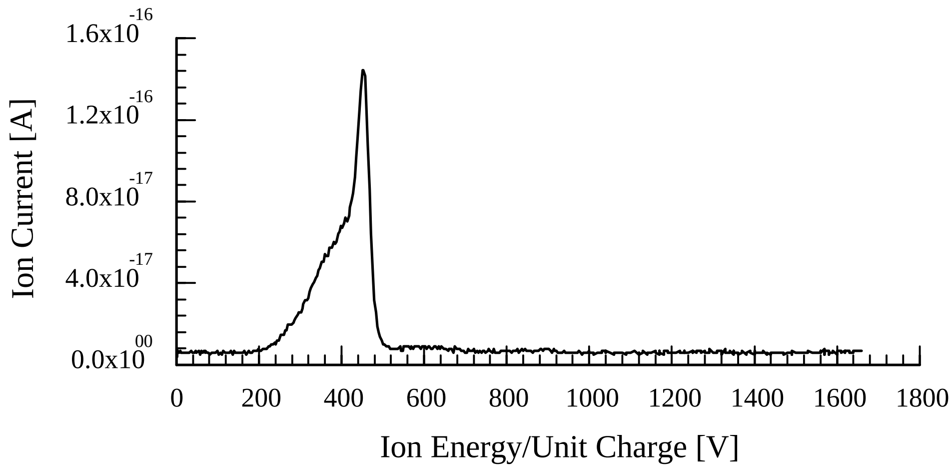

Figure 4.61. Near Field - Condition 3, 60 Degrees

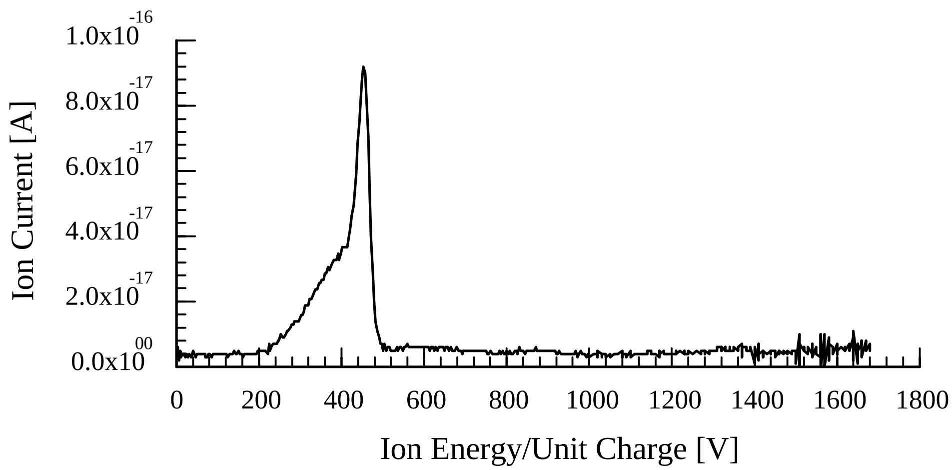

Figure 4.62. Near Field - Condition 3, 65 Degrees

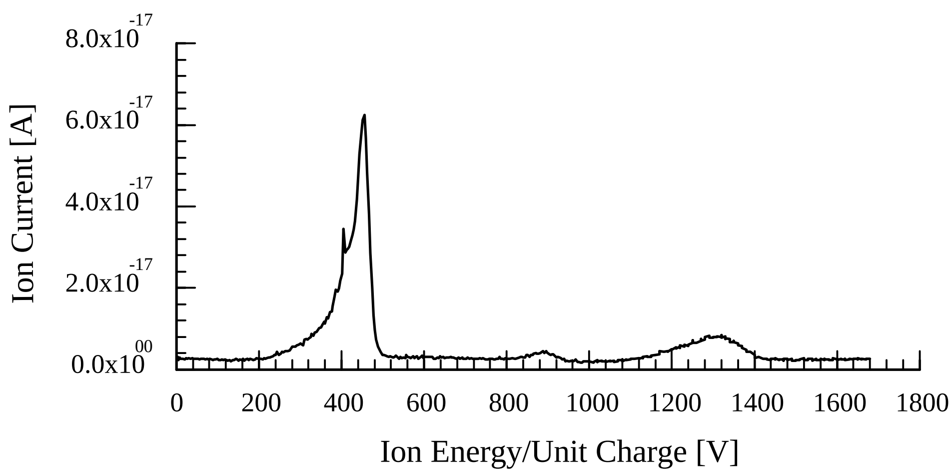

Figure 4.63. Near Field - Condition 3, 70 Degrees

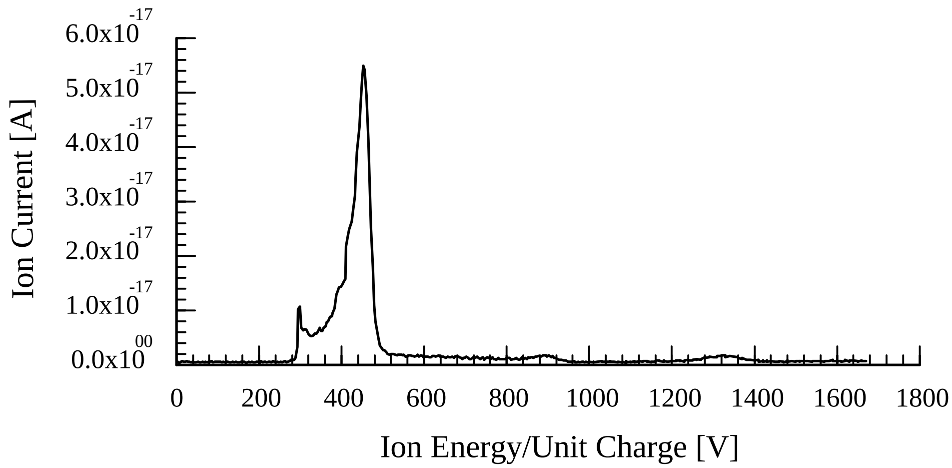

Figure 4.64. Near Field - Condition 3, 75 Degrees

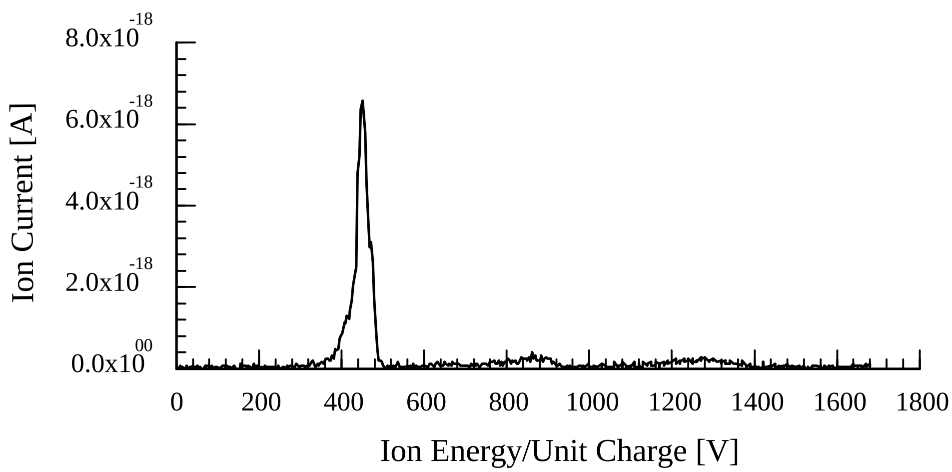

Figure 4.65. Near Field - Condition 3, 80 Degrees

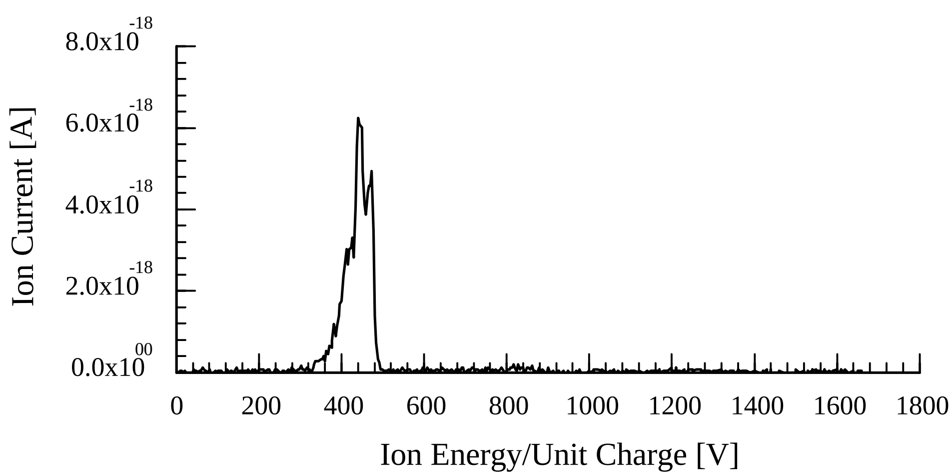

Figure 4.66. Near Field - Condition 3, 85 Degrees

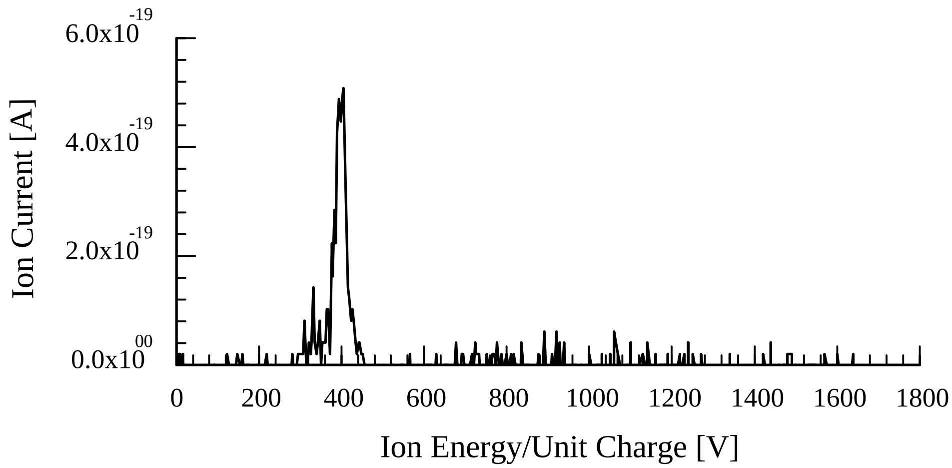

Figure 4.67. Near Field - Condition 3, 90 Degrees

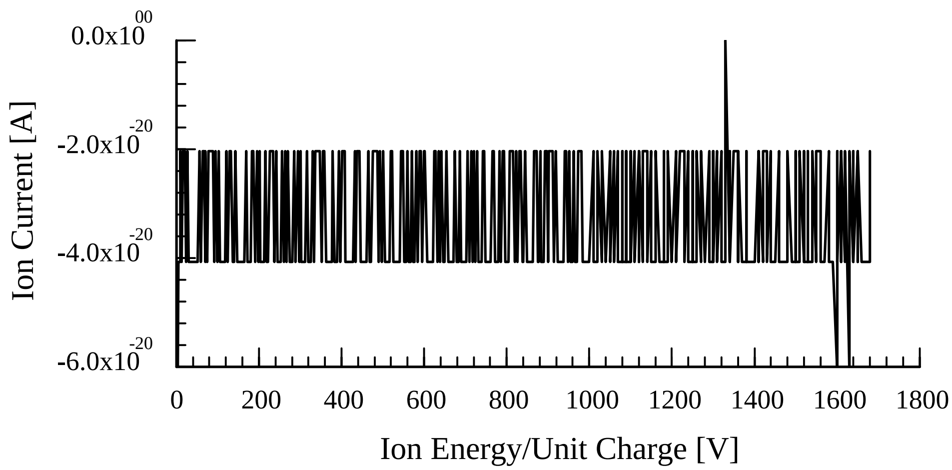

Figure 4.68. Near Field - Condition 3, 95 Degrees - Loss of Signal

4.2. Time-of-flight Mass Measurements

For the near-field measurements, the time-of-flight distance was increased to 2.92 m due to the use of the miniaturized gate near the sampling skimmer. Species composition traces were taken at Condition 1 and Condition 2. Measurements were not taken for Condition 3 because operating the thruster at the high anode mass flow rates needed for a 10 A discharge in close proximity to the sampling skimmer resulted in neutralized propellant backstreaming into the discharge chamber. When this occurred, the thruster responded as if the anode mass flow rate had been increased - with an increase in current. Thus, the thruster was being forced to operate at an off-nominal condition. This was not a problem during the ion energy measurements because scans took far less time to complete.

Figure 4.69 through Figure 4.71 show traces obtained in time-of-flight measurements at the primary ion energy for the two conditions and at off-peak voltages. Again, the point of arrival of a species in terms of ion mass/unit charge corresponds to the beginning of the rise of a peak, not its maximum. The signal dropout seen following the Xe^{+} peak in several of these figures (e.g., Figure 4.69) results from ringing in the time-of-flight amplifier circuitry.

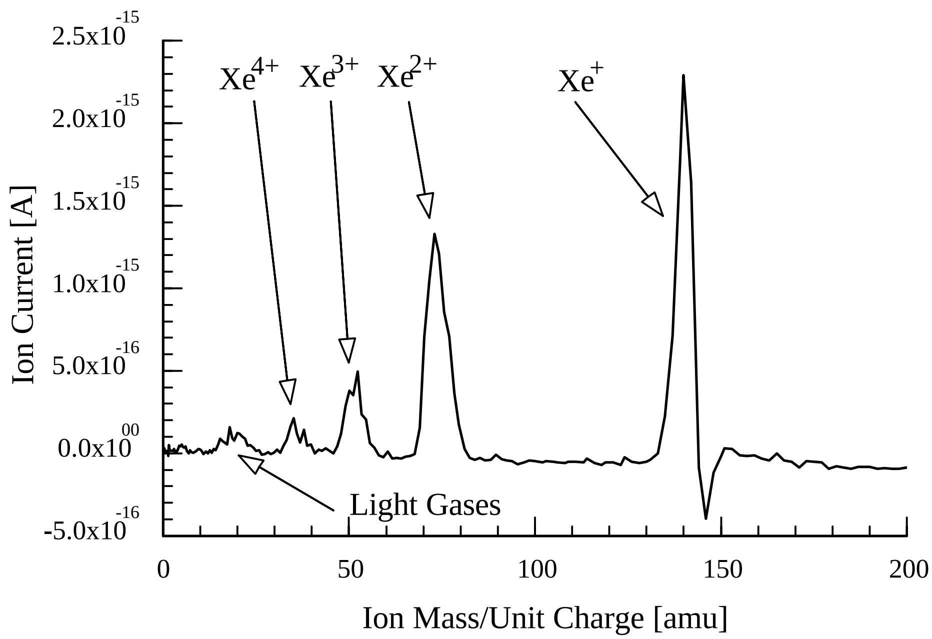

Figure 4.69. Near Field Time-of-flight, Condition 1 - Primary Voltage (263 V)

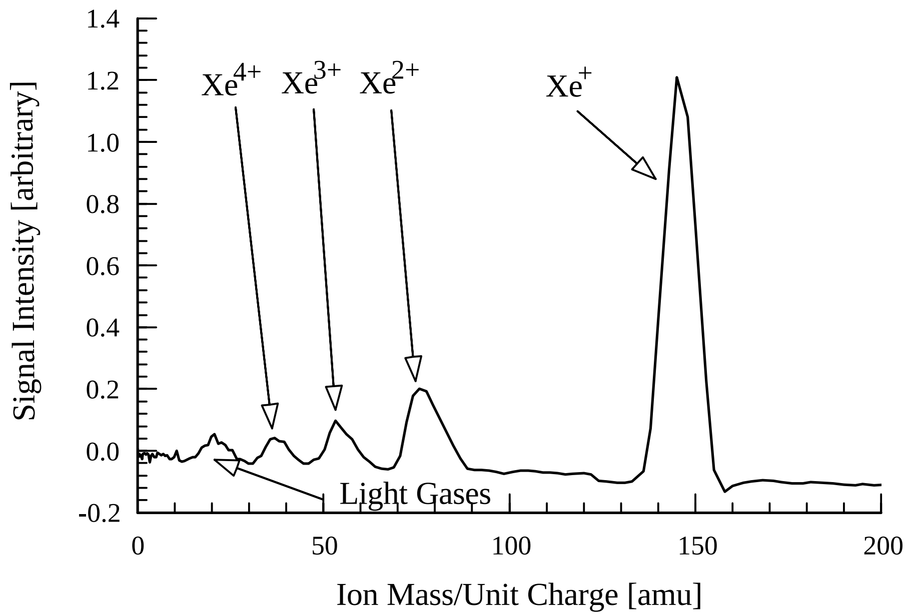

Figure 4.70. Near Field Time-of-flight, Condition 2 - Primary Voltage (456 V)

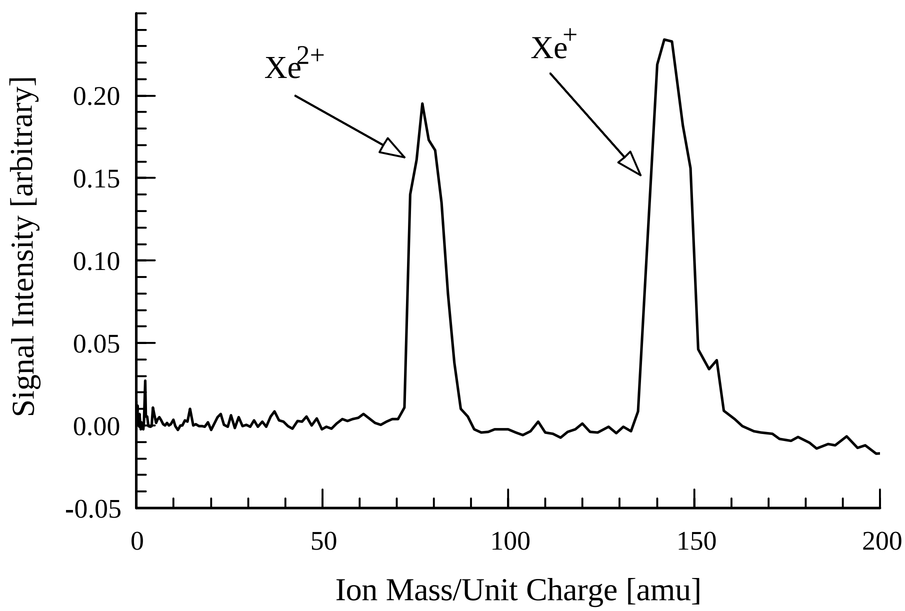

Figure 4.71. Near Field Time-of-flight, Condition 1 - 403 V

The results of the near-field ion energy distribution and time-of-flight measurements will be discussed in Chapter 6.

CHAPTER V

VERY NEAR FIELD MEASUREMENTS

Attempts were made to take very near field measurements on the P5 using the system described in Section 2.3.5.

5.1. Ion Energy Measurements

Attempts were made to obtain very near field ion energy measurements 1 cm from the thruster discharge chamber. The thruster was placed on an Aerotech, Inc. model ATS-62150 linear translation stage. This was done so that the thruster could be translated in front of the sampling orifice as shown in Figure 5.1. This table had a resolution of 5.0 μm, an accuracy better than ± 1 μm/25 mm, and a repeatability better than ± 1 μm. Measurements were taken in 5 mm increments from -10 to +10 mm (0 mm = center of discharge chamber). The 45-degree pass voltage was swept from 0 to 1000 V in 2 V increments which, with a spectrometer constant of 0.549, gives a sweep of ion energy of 0 to 1800 V in 3.6 V increments.

The sampling orifice was aligned to the 45 degree energy analyzer entrance slit by passing a laser through the entrance slit such that it was parallel to the ion beam path. The orifice was then aligned to that beam.

Unfortunately, there were difficulties making these measurements. When the thruster was translated in front of the sampling orifice, there was an unacceptable level of interference with thruster operation that led to a marked increase in thruster current. Very near field Langmuir probe measurements taken by Haas[43] indicate that the potential field for this thruster extends beyond 1 cm downstream of the exit of the discharge chamber. Therefore, when the thruster was brought in front of the orifice, the sampling skimmer interfered with its acceleration processes. However, the data do show the proper form, and are therefore presented so their qualitative trends can be investigated.

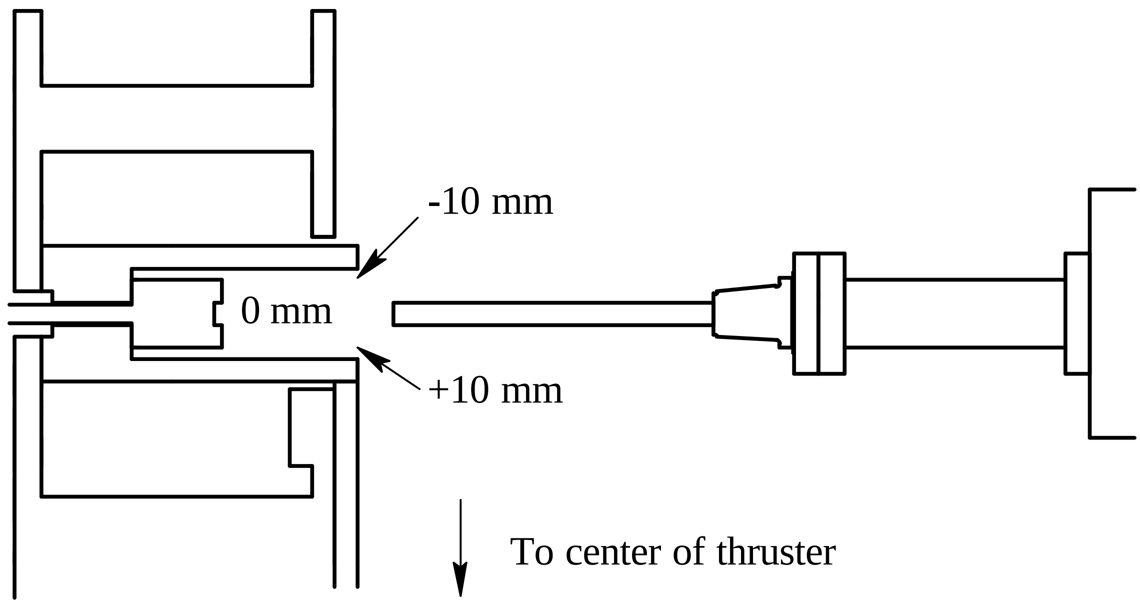

Figure 5.1. Very Near Field Translational Configuration

Very near field ion energy sweeps performed at Condition 1 are presented in Figure 5.2 through Figure 5.9. For this case, the thruster discharge voltage was 300 V, the discharge current increased to approximately 7 A from the nominal value of 5.3 A, the anode mass flow rate was 58 sccm, and the cathode flow rate was 6 sccm. The horizontal scale was decreased from 1800 V to 800 V and selected plots are also shown in semi-log scale to increase resolution.

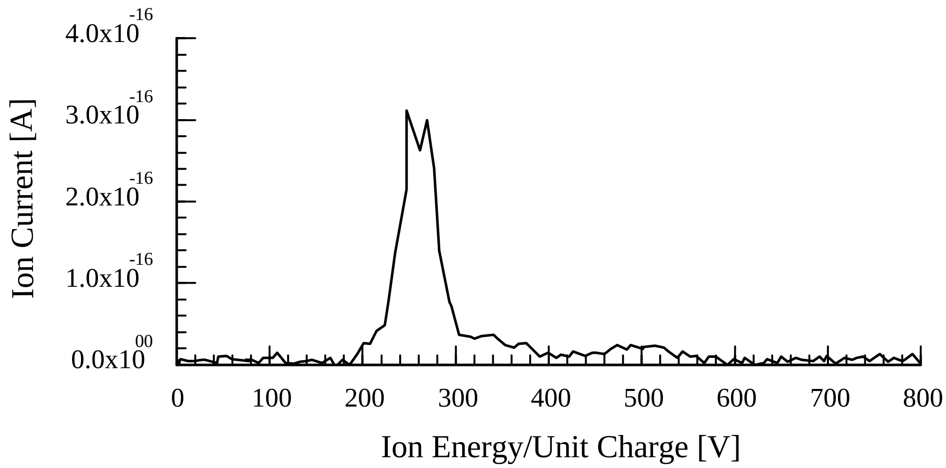

Figure 5.2. Very Near Field - Condition 1, - 10 mm

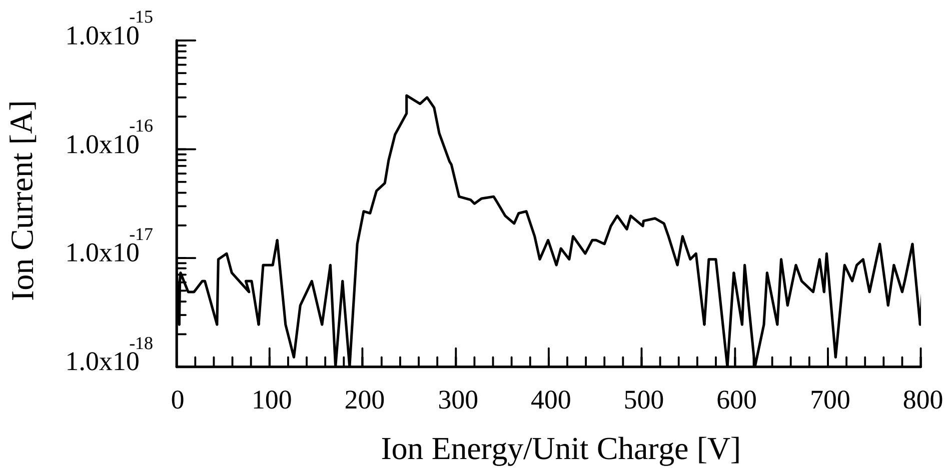

Figure 5.3. Very Near Field - Condition 1, -10 mm [Semi-log]

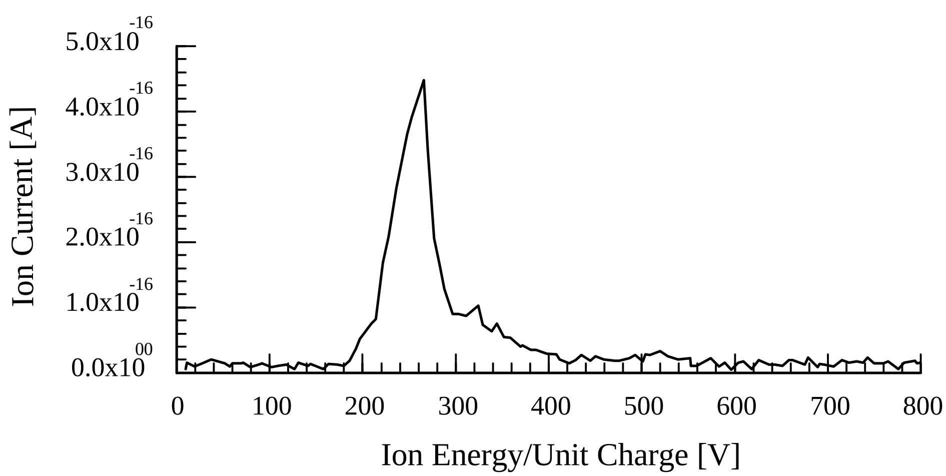

Figure 5.4. Very Near Field - Condition 1, - 5 mm

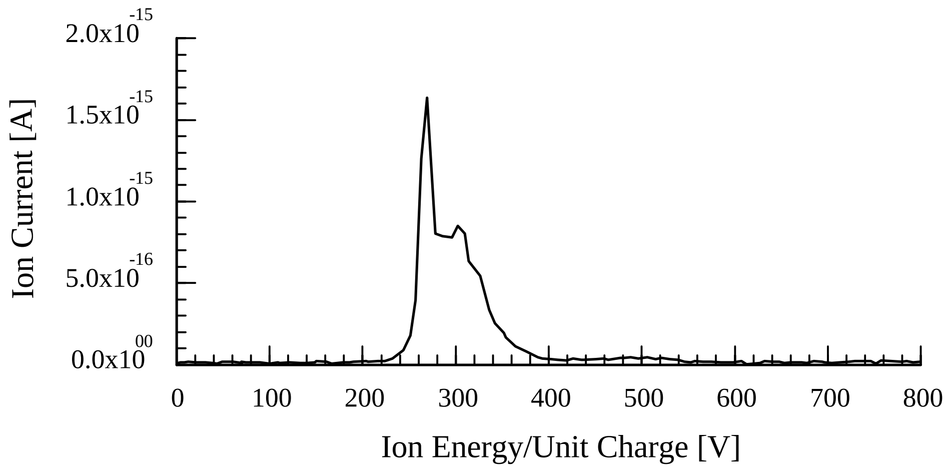

Figure 5.5. Very Near Field - Condition 1, 0 mm

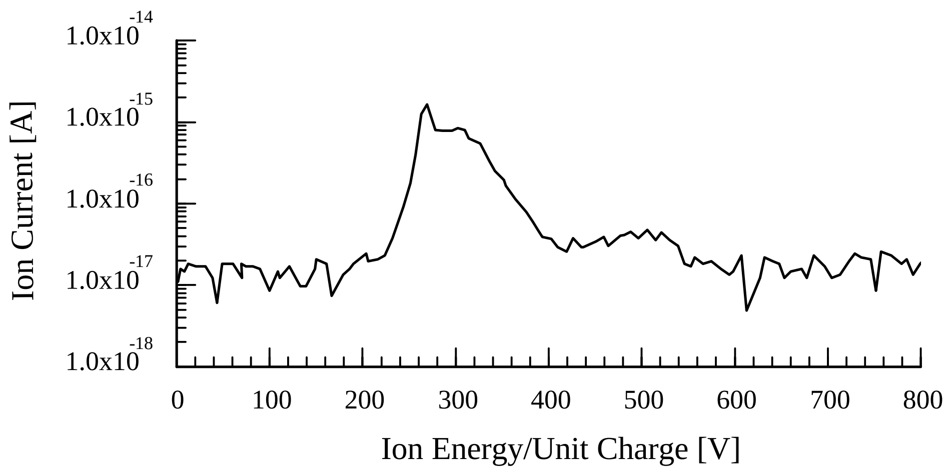

Figure 5.6. Very Near Field - Condition 1, 0 mm [Semi-log]

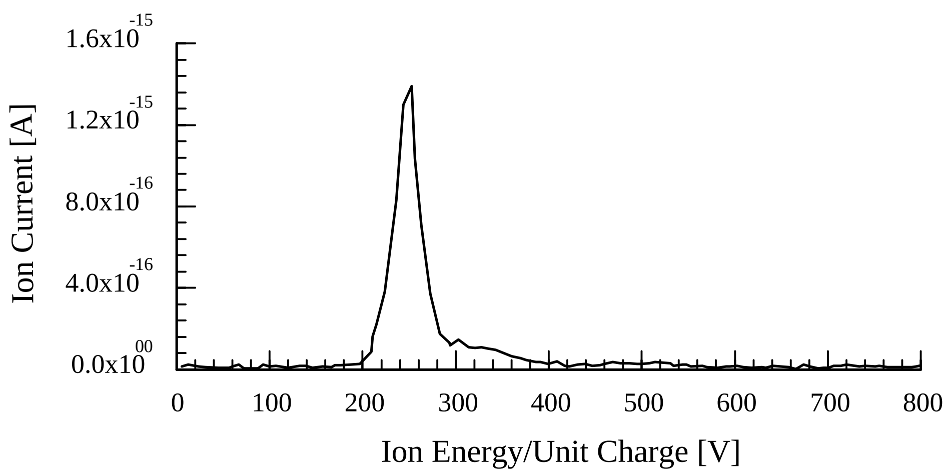

Figure 5.7. Very Near Field - Condition 1, +5 mm

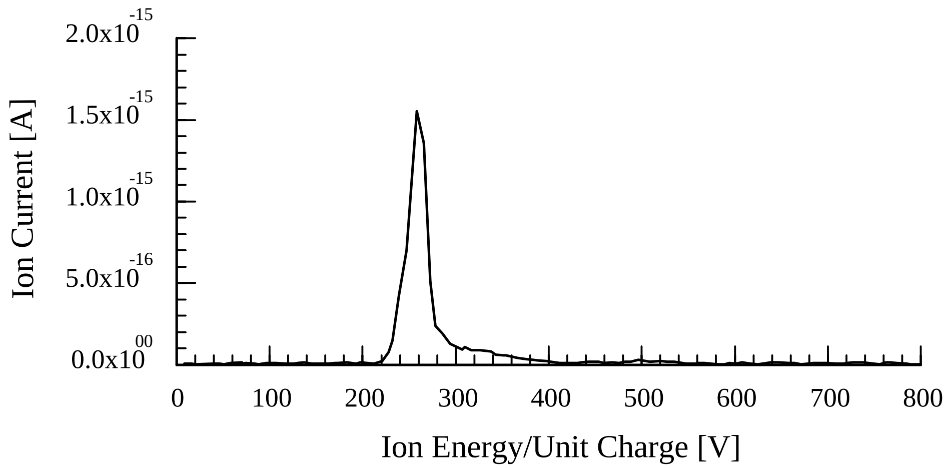

Figure 5.8. Very Near Field - Condition 1, +10 mm

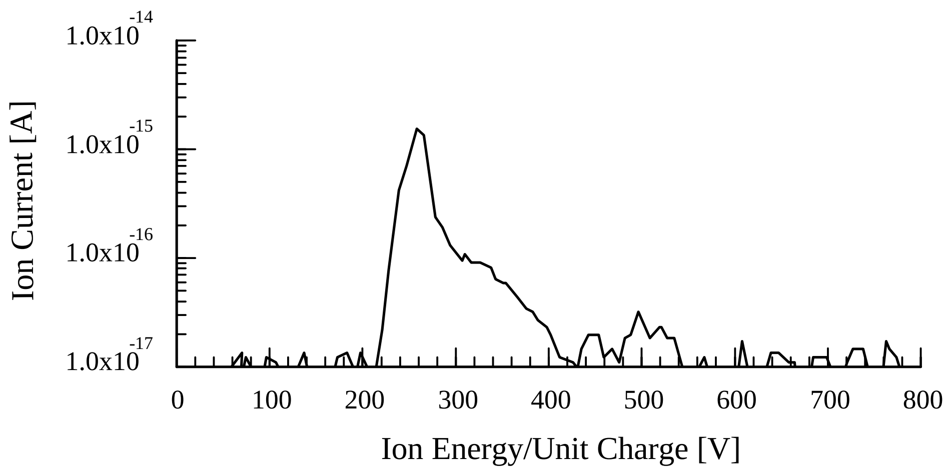

Figure 5.9. Very Near Field - Condition 1, +10 mm [Semi-log]

5.2. Time-of-flight Mass Measurements

Due to the difficulties encountered taking ion energy measurements and concerns regarding damage to the thruster, time-of-flight measurements were not attempted in the very near field.

The results of the very near-field ion energy distribution measurements will be discussed in Chapter 6.

CHAPTER VI

DATA ANALYSIS

The key to analyzing the ion energy distributions measured in these experiments is an understanding of the collisional processes involving ionized and neutral particles occurring within the plume of the Hall thruster. Unfortunately, the cross sections necessary for a complete quantitative analysis of these collisions have not been determined experimentally for xenon at impact energies on the order of those found in the Hall thruster (300 to 500 eV). However, by qualitatively examining the effects that collisions have on ion energy distributions, an understanding of these processes can be obtained that allows for a meaningful dissection of the data via simple observation.[34] A summary of this method will be presented here for simplicity.

There are three types of collisions that can occur in a plasma that involve heavy particles (ions and neutrals):

- Elastic collisions, where there is a transfer of momentum, but total kinetic energy is conserved
- Inelastic collisions, where some kinetic energy is lost
- Charge exchange collisions, where an electron is transferred quantum mechanically from one particle to another with no appreciable transfer of momentum

The inelastic collisions that could have a significant effect on the ion energy distributions in the Hall thruster plume are impact ionizations. In impact ionizing collisions, an electron is ejected from one of the collisional reactants due to the impact of another. For interactions involving two atoms, impact ionization is most probable when the difference in energy between the particles involved is high. However, charge exchange collisions are more likely to occur the longer the particles are in close proximity, thus they are most probable when the interparticle energy is low. This is illustrated in Figure 6.1,[44] which shows the collisional cross section as a function of interparticle energy. In the plume of the Hall thruster, interparticle energies are on the order of 1 eV (for ion-ion collisions) to 10^2 eV (for ion-neutral collisions). Thus, charge exchange collisions are far more likely than impact ionization collisions.

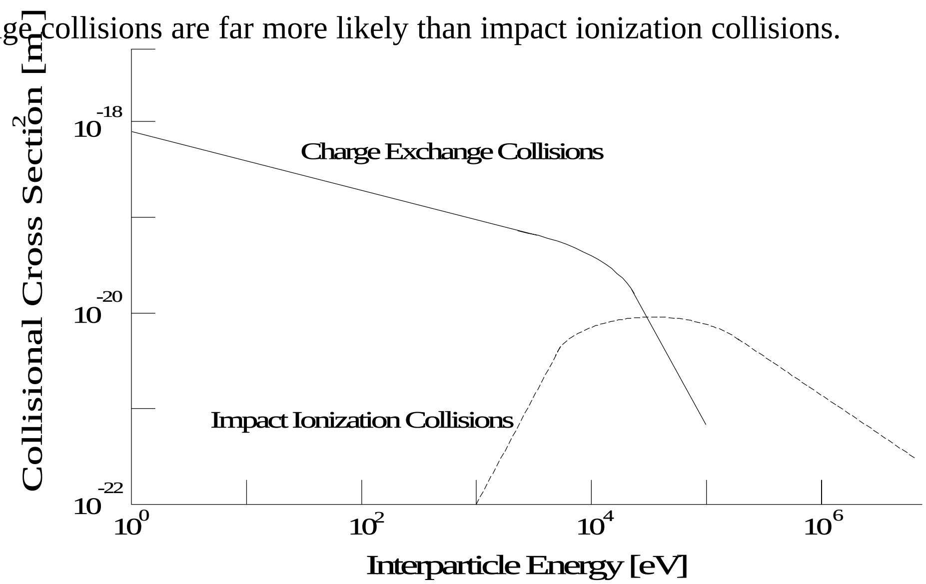

Figure 6.1. Collisional Cross Sections at Various Interparticle Energies for Charge Exchange and Impact Ionization Collisions[44]

Additional measurements show that the probability of a charge exchange collision is approximately an order of magnitude greater than an elastic collision. This is shown in Figure 6.2, which shows the collision probability at various interparticle energies.[45] Thus, the dominant collisional mechanism that is expected in the plume of the Hall thruster is charge exchange, with elastic collisions appearing as a secondary mechanism. Due to the nature of the MBMS, only certain collisional products will be "detectable." Ions with zero kinetic energy will not be detectable since they will not traverse the flight path into the detector. Neutrals of any energy will not be detectable because they cannot pass through the 45-degree energy analyzer.

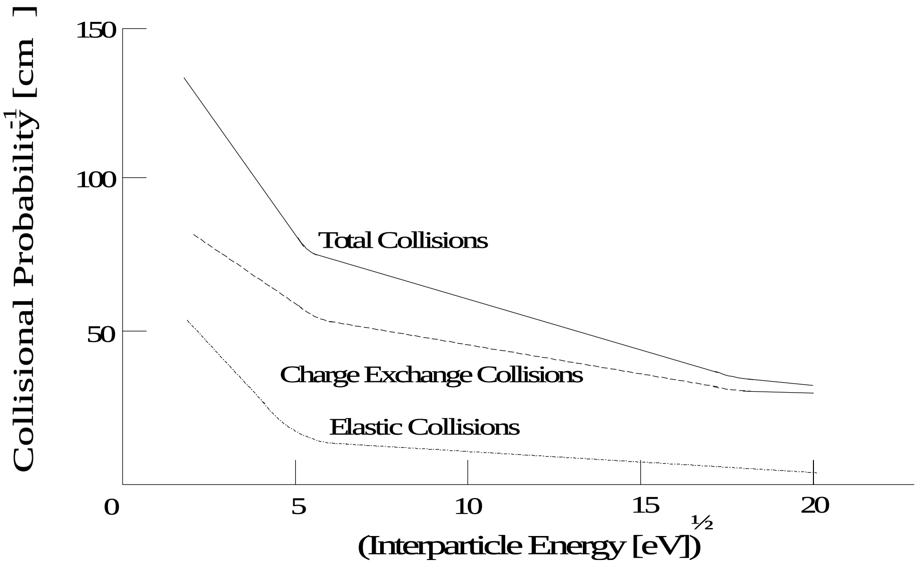

Figure 6.2. Collisional Probabilities at Various Interparticle Energies for Charge Exchange and Elastic Collisions[45]

Each type of collision results in a distinctive perturbation of the ion energy distribution of the species involved as measured by the MBMS. It is important to note that though the distributions occur as a physical spread in energy, the MBMS makes measurements in terms of energy/charge (which is equivalent to an acceleration voltage- see EQN 2.7). Collisions are observed based on the following characteristics:

Elastic Collisions (between an ion of charge q=1 and an ion of charge q=n):

- A high voltage "tail" on the singly charged ion energy/charge distribution that decays to zero at an energy/charge equal to n times the maximum pre-collision energy/charge of the ion with charge n
- A low voltage "tail" on the energy/charge distribution of the ion with charge n that decays to zero at an energy/charge equal to 1/n times the minimum energy/charge of the singly charged ion
- These "tails" decay monotonically without any local maxima

Since all ions experience the same accelerating voltage, the maximum energy/charge will be the same and will be very close to, but less than, the thruster discharge voltage. Thus, for n=2, the high voltage “tail” will decay to zero at approximately twice the discharge voltage. The minimum energy/charge is more difficult to define as it depends on how far the accelerating potential drops within the ionization zone of the thruster. The peaks of both voltage distributions will occur at the same value of energy/charge. Examples of the pre-collision and post-collision energy and energy/charge profiles are given in Figure 6.3 and Figure 6.4, respectively, for an elastic collision between a singly and a doubly charged ion. The vertical scale is arbitrary intensity of signal and the relative magnitude of the species distribution heights is also arbitrary. The distribution measured by the MBMS will be the sum of the q = 1 and q = 2 distributions in terms of Energy/Unit Charge shown in Figure 6.4.

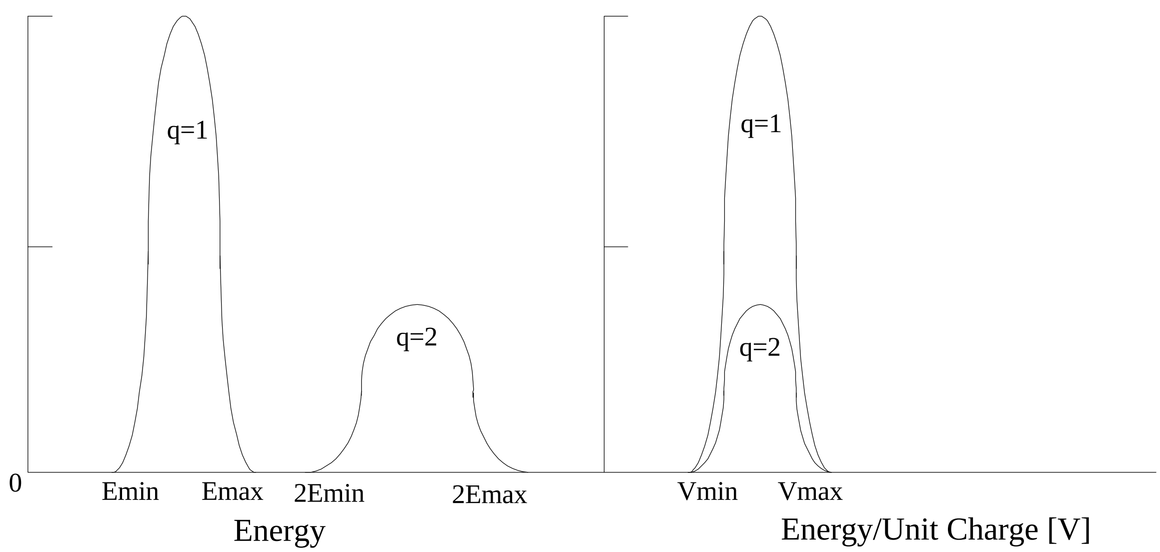

Figure 6.3. Pre-Collision Distributions

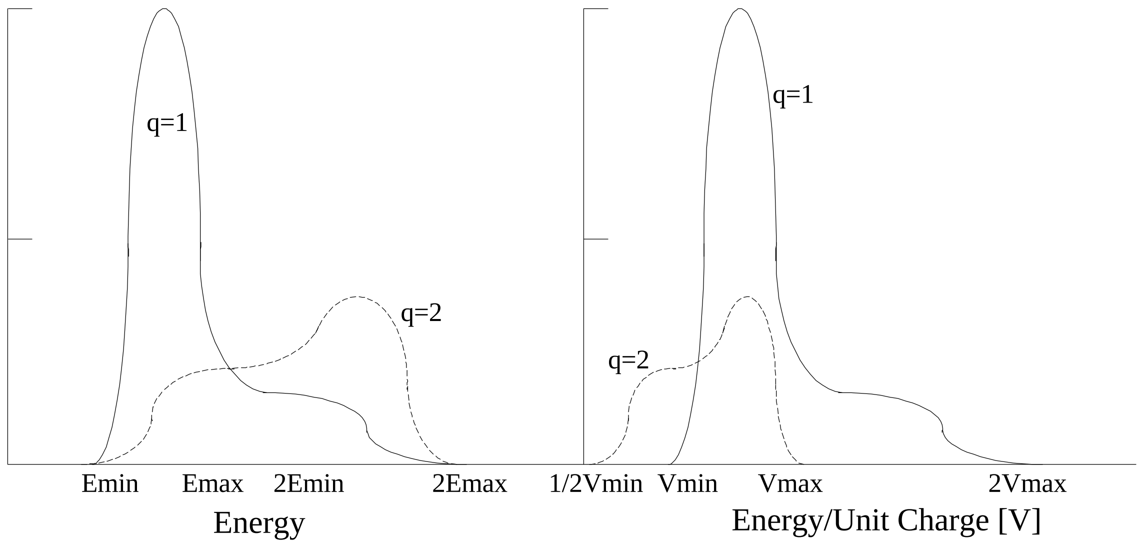

Figure 6.4. Elastic Collision Post-Collision Distributions

Charge Exchange Collisions

- Charge exchange collisions produce appendages to the main distribution that do not decay monotonically as in the case of elastic collisions
- These appendages exhibit local maxima corresponding to the energy distribution of the colliding species
- Charge exchange collisions conserve the shape of the original distribution
- Ion-Neutral charge exchange collisions only produce detectable ions at energy/charge ratios greater than the original ion
- Ion-Ion charge exchange collisions can produce detectable ions at energy/charge ratios above and below the original ions

For example, if a doubly charged ion, accelerated by a potential V_i (thus energy, $E_i \sim 2V_i$, since $E_i = q_i e V_i$), undergoes a charge exchange collision with a neutral atom (with zero velocity), there are two possible outcomes. In the first, there could be two electrons transferred from the neutral atom to the ion, neutralizing it. However, this would result in a doubly charged ion with zero velocity – which will not travel to the detector, and a neutral atom with E_i ~ $2V_i$ – but since neutrals do not pass through the 45-degree energy analyzer, it will not be detected. Thus, the first outcome cannot be observed. The second outcome, however, can be observed. If one electron is transferred to the doubly charged ion (E_i ~ $2V_i$, E_i/q_i ~ V_i), the resulting singly charged ion would have twice the energy of a normally produced singly charged ion (E_i ~ $2V_i$, E_i/q_i ~ $2V_i$). Thus, in the energy/charge domain of the MBMS measurements, it will appear as a maximum at twice the most probable voltage found in the main distribution. The detectable products for ion-neutral charge exchange collisions are given in Table 6.1, for collisions between single, double, triple, and quadruple ions accelerated by a potential V with zero velocity background neutral xenon.

Reaction	Detectable Products	Electrons Transferred
Xe^{+} + Xe	NONE	1
Xe^{2+} + Xe	Xe^{+} at $E_i/q_i = 2\ V_i$	1
Xe^{3+} + Xe	Xe^{2+} at $E_i/q_i = 3/2\ V_i$	1
Xe^{3+} + Xe	Xe^{+} at $E_i/q_i = 3\ V_i$	2
Xe^{4+} + Xe	Xe^{3+} at $E_i/q_i = 4/3\ V_i$	1
Xe^{4+} + Xe	Xe^{2+} at $E_i/q_i = 2\ V_i$	2
Xe^{4+} + Xe	Xe^{+} at $E_i/q_i = 4\ V_i$	3

Table 6.1. Ion-Neutral Charge Exchange Collision Products

For an ion-ion charge exchange collision between singly (E_i ~ V_i) and doubly (E_i ~ $2V_i$) charged ions, there are three detectable outcomes. In the first, there is a single electron transferred from the single ion to the double ion, resulting in a single ion with E_i/q_i ~ $2V_i$ and a double ion with E_i/q_i ~ $1/2V_i$. Both of these ions can be detected by the MBMS, and the resulting post-collision distribution is shown in Figure 6.5 (the pre-collision distributions will be the same as for the elastic collision, shown in Figure 6.3).

The second outcome will result in a single electron transferred from the double ion to the single ion, resulting in a triple ion with $E_i/q_i \sim 2/3V_i$ and an undetectable neutral. The final possibility has two electrons transferred from the single ion to the double ion, resulting in a triple ion with $E_i/q_i \sim 1/3V_i$ and an undetectable neutral. The detectable products for ion-ion charge exchange collisions are given in Table 6.2, for collisions involving single, double, triple, and quadruple ions.

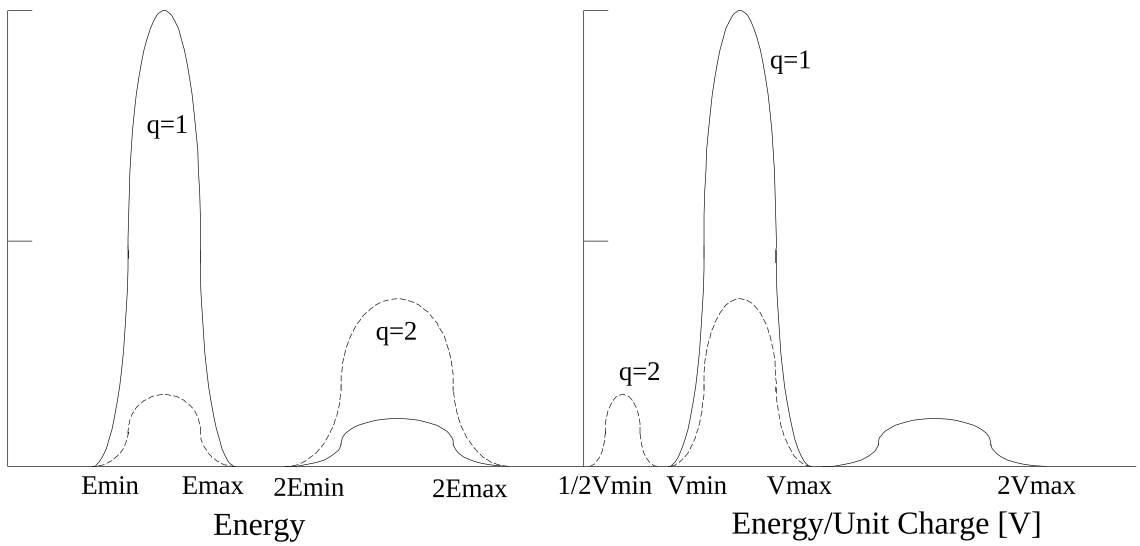

Figure 6.5. Charge Exchange Collision Post-Collision Distributions

Reaction	Detectable Products	Electrons Transferred
$Xe^{2+} + Xe^{+}$	Xe^{+} at $E_i/q_i = 2\ V_i$ and Xe^{2+} at $E_i/q_i = 1/2\ V_i$	1
$Xe^{2+} + Xe^{+}$	Xe^{3+} at $E_i/q_i = 2/3\ V_i$	1
$Xe^{2+} + Xe^{+}$	Xe^{3+} at $E_i/q_i = 1/3\ V_i$	2
$Xe^{3+} + Xe^{+}$	Xe^{2+} at $E_i/q_i = 3/2\ V_i$ and Xe^{2+} at $E_i/q_i = 1/2\ V_i$	1
$Xe^{3+} + Xe^{+}$	Xe^{4+} at $E_i/q_i = 3/4\ V_i$	1
$Xe^{3+} + Xe^{+}$	Xe^{+} at $E_i/q_i = 3\ V_i$ and Xe^{3+} at $E_i/q_i = 1/3\ V_i$	2
$Xe^{3+} + Xe^{+}$	Xe^{4+} at $E_i/q_i = 1/4\ V_i$	3
$Xe^{3+} + Xe^{2+}$	Xe^{2+} at $E_i/q_i = 3/2\ V_i$ and Xe^{3+} at $E_i/q_i = 2/3\ V_i$	1
$Xe^{3+} + Xe^{2+}$	Xe^{+} at $E_i/q_i = 2\ V_i$ and Xe^{4+} at $E_i/q_i = 3/4\ V_i$	1
$Xe^{3+} + Xe^{2+}$	Xe^{+} at $E_i/q_i = 3\ V_i$ and Xe^{4+} at $E_i/q_i = 1/2\ V_i$	2
$Xe^{3+} + Xe^{2+}$	Xe^{5+} at $E_i/q_i = 3/5\ V_i$	2
$Xe^{3+} + Xe^{2+}$	Xe^{5+} at $E_i/q_i = 2/5\ V_i$	3
$Xe^{4+} + Xe^{+}$	Xe^{3+} at $E_i/q_i = 4/3\ V_i$ and Xe^{2+} at $E_i/q_i = 1/2\ V_i$	1
$Xe^{4+} + Xe^{+}$	Xe^{5+} at $E_i/q_i = 4/5\ V_i$	1
$Xe^{4+} + Xe^{+}$	Xe^{2+} at $E_i/q_i = 2\ V_i$ and Xe^{3+} at $E_i/q_i = 1/3\ V_i$	2
$Xe^{4+} + Xe^{+}$	Xe^{+} at $E_i/q_i = 4\ V_i$ and Xe^{4+} at $E_i/q_i = 1/4\ V_i$	3
$Xe^{4+} + Xe^{+}$	Xe^{5+} at $E_i/q_i = 1/5\ V_i$	4
$Xe^{4+} + Xe^{2+}$	Xe^{3+} at $E_i/q_i = 4/3\ V_i$ and Xe^{3+} at $E_i/q_i = 2/3\ V_i$	1
$Xe^{4+} + Xe^{2+}$	Xe^{+} at $E_i/q_i = 2\ V_i$ and Xe^{5+} at $E_i/q_i = 4/5\ V_i$	1
$Xe^{4+} + Xe^{2+}$	Xe^{2+} at $E_i/q_i = 2\ V_i$ and Xe^{4+} at $E_i/q_i = 1/2\ V_i$	2
$Xe^{4+} + Xe^{2+}$	Xe^{6+} at $E_i/q_i = 2/3\ V_i$	2
$Xe^{4+} + Xe^{2+}$	Xe^{+} at $E_i/q_i = 4\ V_i$ and Xe^{5+} at $E_i/q_i = 2/5\ V_i$	3
$Xe^{4+} + Xe^{2+}$	Xe^{6+} at $E_i/q_i = 1/3\ V_i$	4
$Xe^{4+} + Xe^{3+}$	Xe^{3+} at $E_i/q_i = 4/3\ V_i$ and Xe^{4+} at $E_i/q_i = 3/4\ V_i$	1
$Xe^{4+} + Xe^{3+}$	Xe^{2+} at $E_i/q_i = 3/2\ V_i$ and Xe^{5+} at $E_i/q_i = 4/5\ V_i$	1
$Xe^{4+} + Xe^{3+}$	Xe^{2+} at $E_i/q_i = 2\ V_i$ and Xe^{5+} at $E_i/q_i = 3/5\ V_i$	2
$Xe^{4+} + Xe^{3+}$	Xe^{+} at $E_i/q_i = 3\ V_i$ and Xe^{6+} at $E_i/q_i = 2/3\ V_i$	2
$Xe^{4+} + Xe^{3+}$	Xe^{+} at $E_i/q_i = 4\ V_i$ and Xe^{6+} at $E_i/q_i = 1/2\ V_i$	3
$Xe^{4+} + Xe^{3+}$	Xe^{7+} at $E_i/q_i = 4/7\ V_i$	3
$Xe^{4+} + Xe^{3+}$	Xe^{7+} at $E_i/q_i = 3/7\ V_i$	4

Table 6.2. Ion-Ion Charge Exchange Collision Products

As stated previously, there is very little data regarding experimentally determined collisional cross sections for xenon at energies relevant to Hall thruster studies. A search of the literature yielded only two cross sections: Xe^{+} + Xe (as shown in Section 2.3) and Xe^{2+} + Xe.[46] These share the same functional form, given in EQN 2.2, with different constants, K_1 and K_2. The relative velocity for the Xe^{2+} + Xe collision increases by the square root of two from EQN 1.3. The resulting collisional parameters are given in Table 6.3.

Reaction	K_1	K_2	Collisional Cross Section [m^2]	Mean Free Path [m]
Xe^{+} + Xe	-0.8821	15.1262	$4.38*10^{-19}$	9.1
Xe^{2+} + Xe	-2.7038	34.069	$4.98*10^{-19}$	8.0

Table 6.3. Parameters for Ion-Neutral Charge Exchange Collisions

We see that the collisional cross section and mean free paths for these two reactions are approximately equivalent. Therefore, singly and doubly charged xenon will be depopulated at the same rate. However, whereas singly ionized charge exchange collisions create high energy neutrals and zero energy ions (neither of which are detectable), doubly ionized charge exchange collisions produce detectable singly charged ions – thereby partially repopulating singly charged xenon. Thus, at larger axial distances (or high density regions), where the collision probability is greater, the fraction of detectable singly charged ions will increase with respect to that of doubly charged ions.

6.1. Far Field

We begin our data analysis by examining the ion energy distributions taken in the far field, first looking at the 0 degree measurements, then examining the plume at higher angles.

In Figure 3.2, for Condition 1, the primary ion energy distribution has its peak at 263 V with respect to ground. For this condition, the plasma potential was approximately 7 to 8 V above ground (See Figure 2.20). The peak is at approximately 90% of the discharge voltage, which is what is expected for a well-developed Hall thruster.[47] In this distribution, we see strong evidence of elastic collisions between singly and doubly charged xenon ions, decaying at twice the discharge voltage. This behavior is very similar to that observed by King for the SPT-100. When this distribution is examined more closely on a semi-log plot as shown in Figure 3.3, small charge exchange collision peaks at 2X and 3X the primary peak are seen. Since there are no charge exchange peaks at voltages less than the primary peak, these peaks are the result of collisions by neutrals with doubly and triply ionized xenon that resulted in singly charged ions.

In Figure 3.28, for Condition 2, the primary distribution has its peak at 454 V with respect to ground and the plasma potential was approximately 7 to 8 V above ground (See Figure 2.20). Again, as expected, the peak is approximately 90% of the discharge voltage. In this distribution, there is some indication of elastic collisions. There are, however, very noticeable ion-neutral charge exchange collision peaks at 1.5X, 2X, and 3X the primary peak. The 2X and 3X peaks are the result of collisions by neutrals with doubly and triply ionized xenon that resulted in singly charged ions. The 1.5X peak results from a collision of triply ionized xenon with a neutral that produced a doubly charged ion.

In the case of Condition 3 (Figure 3.52), the total flow rate has almost doubled, going from 64 sccm to 111 sccm. The peak of the primary distribution is 449 V with respect to ground and the plasma potential is 10 V above ground (See Figure 2.22). As will be discussed in Section 7.3, the increase in flow rate leads to a large pressure build-up in front of the entrance orifice to the MBMS that increases the collision probability considerably. This is reflected in an ion energy distribution that shows significant elastic collision broadening. There are 2X and 3X peaks similar to those observed for Condition 2 evident in the semi-log plot (Figure 3.53), but any chance of observing the 1.5X peak is obscured by the broadening.

As the thruster is rotated to higher angles, similar trends were seen for all three conditions. For Condition 1, the profile changes very little from 0 to 40 degrees, maintaining the same shape seen in Figure 3.2. Then, as shown in Figure 3.12, at 45° the profile begins to broaden significantly toward the lower energy side of the distribution. This trend continues to approximately 50° (Figure 3.14) and then transitions into a shift of the primary peak location as seen at 60° (Figure 3.17) where the maximum of the primary peak is at 205 V. At angles where this broadening and shift are seen, the ion current intensity is significantly lower than in areas where the distribution has its peak at the same voltage as at 0°. Beginning at 65° (Figure 3.18), the profile shifts back to the same peak seen at centerline. The intensity of the signal also increases, though it is far less than at centerline. The next region begins at approximately 85° (Figure 3.22), where we see evidence of significant numbers of ion-ion charge exchange collisions and a highly attenuated peak at the centerline voltage. The last signal region occurs at 100° (Figure 3.26), where we see a low intensity distribution of low energy ions. Beyond this, the signal fades into the noise at 105° (Figure 3.27).

For Condition 2, the distributions retain the centerline shape of (Figure 3.28) out only to 10° (Figure 3.31). From 15° (Figure 3.32) to 30° (Figure 3.35), the low energy side of the distribution grows, and is accompanied by high energy charge exchange collision peaks at 2X and 3X the peak voltage. This then transitions into a peak shift, though it is slightly different than for Condition 1. From 35° (Figure 3.37) to 50° (Figure

3.40), the primary peak remains and is approximately the same intensity as the shifted peak. At these angles there is also a significant 2X charge exchange peak. Then, from 60° (Figure 3.42) to 70° (Figure 3.44), the primary peak regains dominance, though the shifted peak remains – in this range, there is no 2X charge exchange collision peak. The signal then shifts back toward the centerline shape before becoming dominated by high energy ion-ion charge exchange peaks at 85° (Figure 3.47). Again there is a low energy distribution at 100° (Figure 3.50) and the signal fades into the noise at 105° (Figure 3.51).

For Condition 3, the trends are qualitatively similar with subtle dissimilarities. The collision broadened centerline shape seen in Figure 3.52 remains out to 35° (Figure 3.60), with the broadening decreasing with angle, before increasing at 40° (Figure 3.61). Then from 45° (Figure 3.62) to 60° (Figure 3.65), we see the peak shift. The peak then shifts back to the centerline voltage at 65° (Figure 3.66). It remains there until 80° (Figure 3.69), then begins to decrease in voltage, falling to 394 V at 95° (Figure 3.73). However, this peak shift is different than that typically seen around 45° because it is not accompanied by the broadening that characterizes the lower angle shift. The signal fades into noise at 100° (Figure 3.74), without experiencing the charge exchange collision or low ion energy regions.

Next, we examine the results for species measurements obtained using the time-of-flight configuration of the instrument. As detailed in Section 2.3.2 we look at the traces obtained as the ion beam is gated, allowing ions to separate based on their charge state. The peaks are measured on an oscilloscope versus time, then converted to a horizontal scale in terms of their mass-to-charge ratio, using EQN 2.12. An example of such a plot is shown in Figure 3.75 for Condition 1 at the primary discharge voltage (263 V with respect to ground).

In this trace, singly, doubly, and triply ionized xenon were observed at 131, 65.5, and 44 AMU, respectively. The point of arrival of a species corresponds to the beginning of the rise of a peak. The width of the peak relates to the length of time that the gate is left open. If the gate is left open for a sufficient amount of time such that the peak is not clipped by the closing of the gate, the intensity is related to the density of a particular species. For a particular accelerating potential, the individual species fraction, f_i, can be determined using the following equation, where I_i is the species ion current.

EQN 6.1
$$f_i(V_i) = \frac{I_i / \sqrt{q_i}}{\sum_i \left(I_i / \sqrt{q_i} \right)}.$$

By repeating this process at accelerating voltages above and below the primary voltage in 20 V increments, species fraction distributions were determined for all three operating conditions. These are presented in Figure 6.6 through Figure 6.8, along with a normalized ion energy trace taken at 0 degrees for reference. They show local maxima of double and triple ion fraction that correspond closely to bumps in the ion energy distribution, thus confirming their role as collisional products

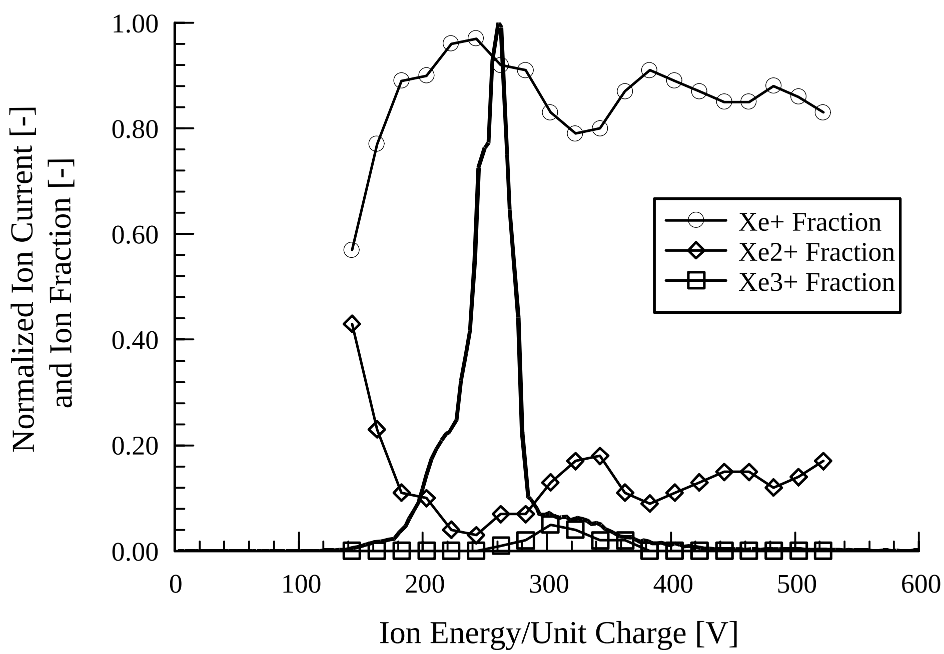

Figure 6.6. Far Field Ion Fractions at Condition 1, 0 Degrees, with Normalized Ion Energy Trace for Reference

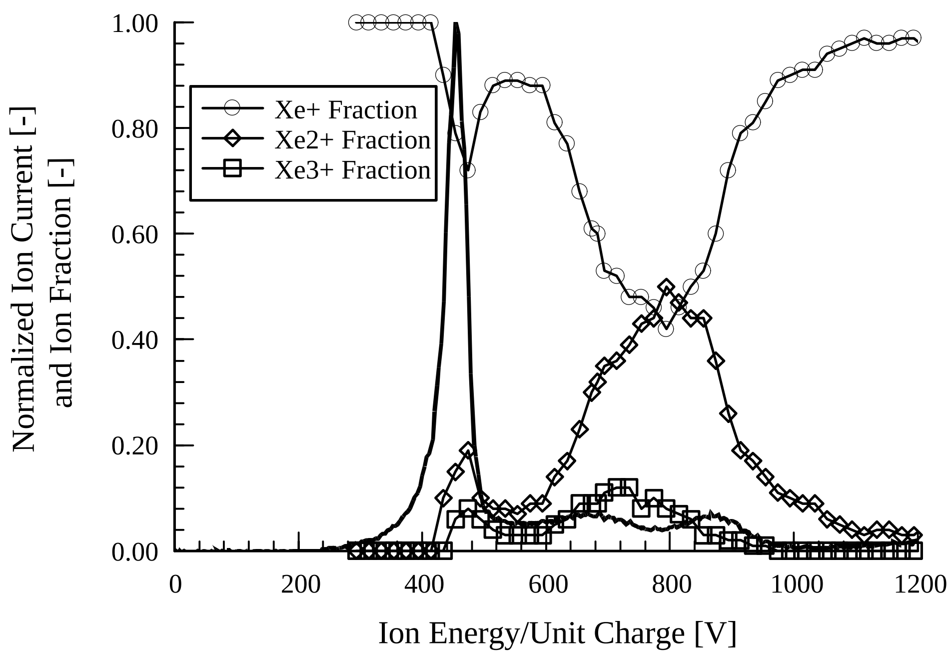

Figure 6.7. Far Field Ion Fractions at Condition 2, 0 Degrees, with Normalized Ion Energy Trace for Reference

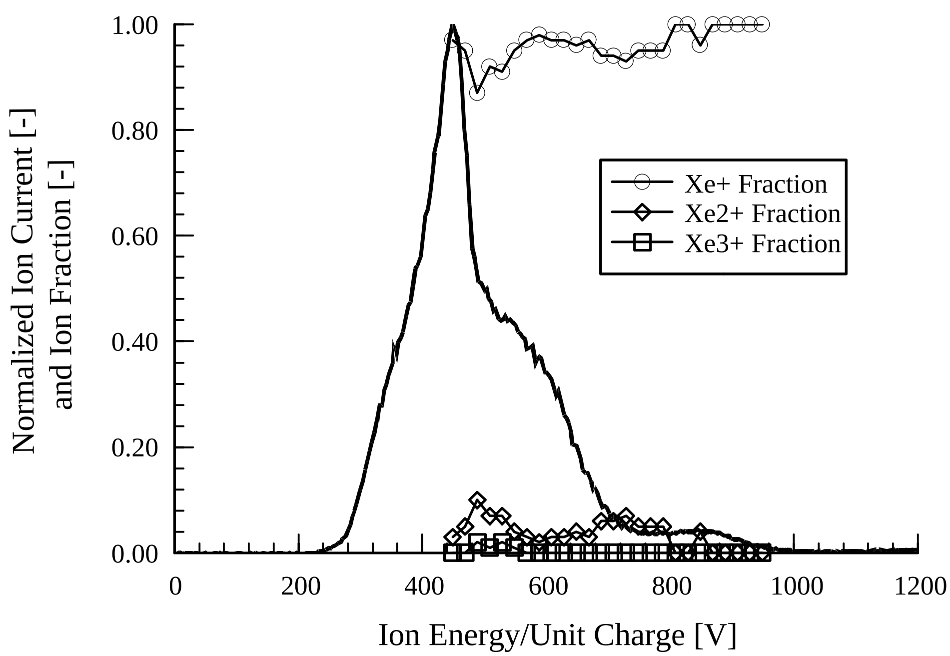

Figure 6.8. Far Field Ion Fractions at Condition 3, 0 Degrees, with Normalized Ion Energy Trace for Reference

The readings taken at Condition 3 were cut short by an experimental failure. Examining Figure 6.8, we see that the species fractions are dominated by singly ionized xenon. It is believed that the large anode mass flow rate required for operating the thruster at 10 A results in a highly collisional zone in front of the sampling orifice. Previous measurements of Hall thruster plumes have shown that approximately 90% of the plume is singly ionized xenon.[33,34] In a high collision area, beam ions will undergo ion-neutral charge exchange collisions that lower the plasma's overall total charge state. Collisions between neutrals and double or triple ions will depopulate these charge states in favor of singly ionized xenon. However, when singly ionized xenon undergoes a charge exchange collision, it is neutralized and removed from the total beam ion population (the total number of ions remains constant, but the number of beam ions - those that reach the detector - is reduced). Therefore, collisions reduce the total number of beam ions but increase the fraction of singly charged ions. This has shown that under high flow rate conditions, facility effects can artificially reduce species fractions. For this reason, along with the large amount of sputtering that occurs when the thruster is operated at 10 A, these tests were not continued.

In addition to the experimental uncertainties in the time-of-flight measurements discussed in Section 3.2, there is additional uncertainty in obtaining the species fractions. The noise level of the time-of-flight signal was approximately ± 0.005 V. When the signal level approached the noise at the extremes of the Ion Energy/Unit Charge range, it became increasingly difficult to distinguish between the signal and noise. Thus, the fractions at the high and low end of the range should be viewed with caution.

To obtain an overall fraction for each species, we perform a signal intensity weighted integration of the species fraction for each accelerating potential, $f_i(V_i)$:

EQN 6.2

$$F_i = \frac{\int_0^\infty f_i(V_i) I_i(V_i) dV_i}{\int_0^\infty I_i(V_i) dV_i}.$$

The overall fractions for the three species identified in the far field are given in Table 6.4.

Species	Condition 1	Condition 2	Condition 3
Xe^{+}	0.925	0.790	0.947
Xe^{2+}	0.068	0.164	0.047
Xe^{3+}	0.007	0.046	0.006

Table 6.4. Overall Far Field Species Fractions

For Condition 1, the fractions of the P5 compare reasonably well with those calculated for the SPT-100 using the MBMS[34] and emission spectroscopy,[33] confirming that when the P5 operates at Condition 1, it behaves very similarly to a 1.5 kW class commercial Hall thruster. For Condition 2, we see a dramatic increase in the fractions of the multiply charged ions. By forcing the ions (and electrons) to fall through a larger potential, we increase the probability of the occurrence of multiple ionization. The fractions for Condition 3 reflect the depopulation of the higher charge states discussed previously.

6.2. Near Field

We continue our data analysis by examining the ion energy distributions taken in the near field, again looking first at the 0 degree measurements, then examining the plume at higher angles.

In Figure 4.2, for Condition 1, the primary peak again has its maximum at 263 V. In the near field, the profile is charge exchange collision dominated. Upon closer examination, we see peaks at 1.33X, 2X, and 3X the discharge voltage. A peak at 1.33X indicates a charge exchange collision between a quadruply charged xenon ion and a neutral xenon atom with one electron exchanged. Peaks at 1.5X for triply charged xenon becoming doubly charged and at 4X for quadruply charged xenon are not seen at 0°, but are seen from 5° to 15° (Figure 4.4 - Figure 4.7).

In Figure 4.26 at Condition 2, the primary peak has a maximum at 456 V. Close examination shows that the profiles are again dominated by charge exchange collisions. Peaks are observed at 1.33X, 1.5X, 2X, and 3X the primary peak (due to their proximity, the 1.33X and 1.5X peaks tend to blend together into a single “bump” with two maxima). For many of the sweeps at Conditions 2 and 3, we observe an increase in intensity at the end of the scanning range. It is hypothesized that this is the beginning of the peak at 4X the primary peak (~1800 V). Unfortunately, the scanning range of the sourcemeter is not sufficient to encompass this peak in its entirety.

The results for Condition 3 (Figure 4.48) are very similar to Condition 2, and do not suffer the broadening seen for the far-field measurements. It was, however, very difficult to take measurements at this condition, and many sweeps showed unusual amounts of noise and other detrimental effects.

As was seen for far-field measurements, when the thruster is rotated to higher angles, similar trends are observed for all three conditions. For Condition 1 the centerline profile, seen in Figure 4.2, is maintained to 40° off centerline (Figure 4.12). Then from 45° (Figure 4.13) to 55° (Figure 4.16), there are strong 2X and 3X charge exchange peaks. From 60° (Figure 4.17) to 85° (Figure 4.23), the charge exchange peaks remain, but the primary peak at 263 V is attenuated. The primary peak briefly regains dominance at 90° (Figure 4.24), before the signal fades into the noise at 95°(Figure 4.25).

For Condition 2, the trends are almost identical. The only differences were that the primary peak at 456 V did not attenuate until an angle of 65° (Figure 4.41), instead of 60°, and the signal fades into the noise at 90° (Figure 4.46), before the primary peak has an opportunity to reappear.

Once again, Condition 3 is somewhat different. The centerline structure remains to an angle of 15° (Figure 4.52) with a maximum at 451 V. We then see significant charge exchange collision peaks from 20° (Figure 4.53) to 40° (Figure 4.57). From 45° (Figure 4.58) to 80° (Figure 4.65), these peaks fade, and the signal returns to a profile similar to centerline, though with significant collisional broadening on the low energy side. At 85° (Figure 4.66), the peak voltage begins to shift downward, similar to the far-field case, reaching 405 V at 90° (Figure 4.67) before the signal fades into noise at 95° (Figure 4.68).

For near-field time-of-flight measurements, we again present a trace of the species peaks versus mass for Condition 1 at the maximum of the ion energy distribution (263 V) in Figure 4.69. Longer gate times were necessary for these measurements to obtain a clear, non-clipped signal. The gate time is short enough, however, to allow for species differentiation. In addition to the singly, doubly, and triply ionized xenon that was detected in the far field, we detect the presence of a peak at 32 AMU. This could correspond to two different species: quadruply ionized xenon or ionized oxygen molecules. However, in our near-field ion energy measurements we detected charge exchange peaks at 1.33X and 4X the primary discharge peak, which correspond to quadruply ionized xenon. Additionally, O_2^+ is expected to be very uncommon since it would have to survive being ingested, ionized, and accelerated by the thruster without dissociating. Thus, there are two measurements that act as independent confirmation of the presence of Xe^{4+} in the plume. Collisions that remove quadruply ionized xenon from the system are greater in number (See Table 6.1 and Table 6.2) and probability than those that produce it. Therefore, by the time a sample is taken 75 cm from the thruster, almost all of the quadruply charged xenon has been converted to a lower charge state ion or neutral, increasing the fraction of these other ions in the process. Figure 6.9 and Figure 6.10 provide the near-field ion fractions for a range of acceleration voltages at Condition 1 and Condition 2, respectively (as stated previously, measurements were not taken at

Condition 3 due to interference with thruster operation). Again, peaks in the multiply charged species closely correspond to ion collision peaks.

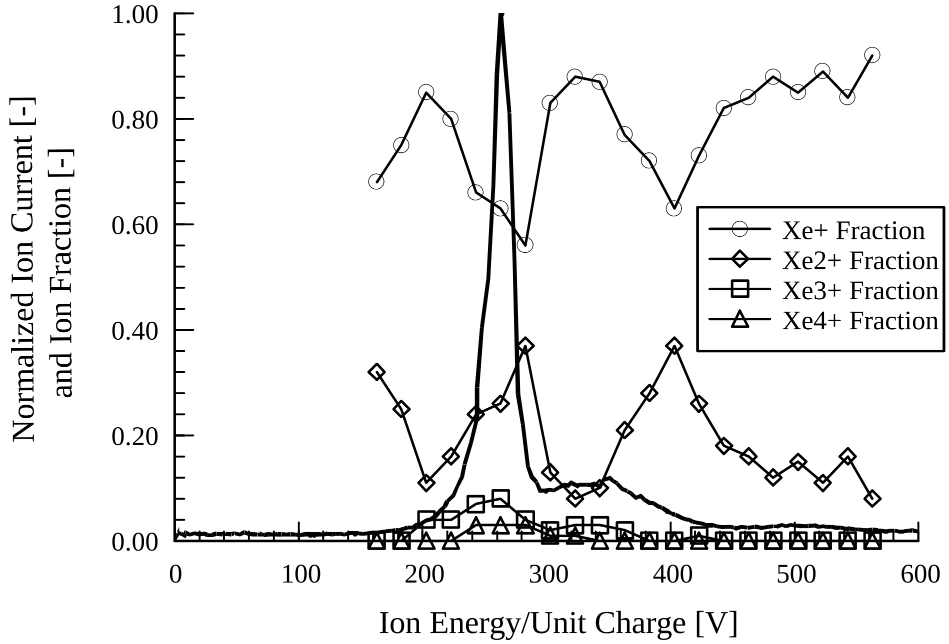

Figure 6.9. Near Field Ion Fractions at Condition 1, 0 Degrees, with Ion Energy Trace for Reference

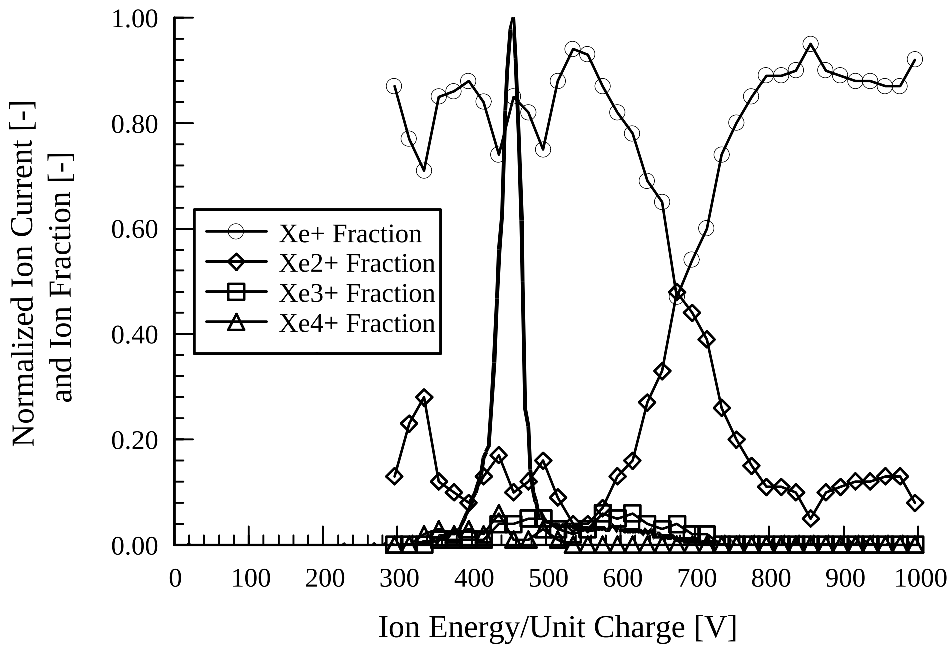

Figure 6.10. Near Field Ion Fractions at Condition 2, 0 Degrees, with Ion Energy Trace for Reference

The overall near field species fractions calculated from EQN 6.2 are given in Table 6.5.

Species	Condition 1	Condition 2
Xe^{+}	0.698	0.812
Xe^{2+}	0.231	0.128
Xe^{3+}	0.052	0.036
Xe^{4+}	0.019	0.024

Table 6.5. Overall Near Field Species Fractions

Comparing the near field fractions for Condition 1 with the far field, we see that the fraction of multiply charged ions is higher in the near field. This is as expected since collisions will preferentially depopulate higher charge states, and the probability of these collisions increases with downstream distance. For Condition 2, the near field fractions are fairly equivalent to the far field, with Xe^{2+} and Xe^{3+} being depopulated in favor of Xe^{+} and Xe^{4+}. It is not clear why the fraction of singly ionized xenon would be greater in the near field.

6.3. Very Near Field

Examining the very near field data presented in Figure 5.2 through Figure 5.9 we see several trends worth noting. However, due to the interference with thruster operation experienced when sampling in the very near field, only the most general conclusions will be made. First, the shape of the distributions is consistent with those measured at 0 degrees in the near field (see Figure 4.2). Second, the width of the distributions is the same as measured in the near field (full width at half maximum = 22 V at 0° - profile width will be discussed in detail in Section 7.3). Finally, there is a qualitative increase in signal intensity, and therefore ion density, on the inner portion of the discharge chamber.

6.4. Comparison with Laser Induced Fluorescence

The University of Michigan LIF system was used to investigate the ion energy profile of the P5.[48] The centerpiece of this system is an argon-ion pumped Coherent model 899-29 dye laser. Operating on Rhodamine-6G dye, this laser typically generates 0.25 W at a wavelength of 605 nm. It was operated in a 3-beam multiplexing scheme that allowed for measurement of all three velocity components simultaneously. Because of the low pressure and large dimensions of the LVTF, the plume could be investigated much farther downstream from the thruster than in other LIF investigations.[30,31,32] Measurements were taken at Condition 1, 10 cm downstream of the exit plane. At the center of the discharge chamber, the axial velocity was measured to be 16700 m/s. This is approximately 87% of the velocity – 19250 m/s – calculated based on the peak ion energy distribution at the same location (see Figure 4.2), corrected for plasma potential.

The axial ion temperature at this point was 0.75 eV, while the full width at half-maximum spread in ion energy measured by the MBMS was 21 V. The discrepancies between LIF and MBMS measurements will be discussed in Section 7.5.

CHAPTER VII

CONCLUSIONS

There are three primary variables examined in ion energy measurements: power, angle, and sampling location. The effects of changes in these variables will now be discussed.

7.1. Thruster Operating Condition

Examining the changes between the thruster operating conditions, we see very similar trends between Condition 1 and Condition 2, the two cases at 5.5 A (total flow of 64 sccm). The changes in structure with angle are nearly identical. For Condition 3, at 10 A (111 sccm), the distributions are much broader in the far field. Since there is more propellant, the background pressure of neutral xenon in front of the thruster will be higher, thus increasing the amount of collisional broadening. However, the overall variation with angle is still fairly consistent with the lower discharge current conditions. The primary driving force in altering these distributions is change to the thruster's magnetic field. When the operating condition of this thruster is changed, the electromagnet coil currents are also changed. The values used for the electromagnet currents were determined during performance measurements, and were set to minimize discharge current (thereby maximizing efficiency). It is presumed that altering the intensity of the magnetic field in this way also results in an alteration of its shape. Thus, unlike a commercial thruster, the P5 has not undergone magnetic field optimization for the plume shape.

7.2. Thruster Angle

In presenting the changes in ion energy distribution with angle, an attempt to divide the plume into several zones was made. Of course, these zones do not have finite boundaries, and the characteristics seen in them often overlap, thus the zones are created for the purpose of clarity. The angular boundaries of these zones are different for the different operating conditions.

In the far field, the first zone is the primary discharge region near 0 degrees, as seen in Figure 3.2. The ions accelerated in this manner are those created by collisions with electrons trapped by radial or near-radial magnetic field lines in close proximity to the end of the discharge chamber as shown in Figure 7.1. This figure shows electric field lines based on plasma potential measurements taken using a high speed reciprocating Langmuir probe.[43] The ions near 0 degrees are the ones that are desired in a Hall thruster, and which create a majority of the useful thrust. The intensity of peaks in this zone are the highest, thus a majority of propellant ions are concentrated in this zone.

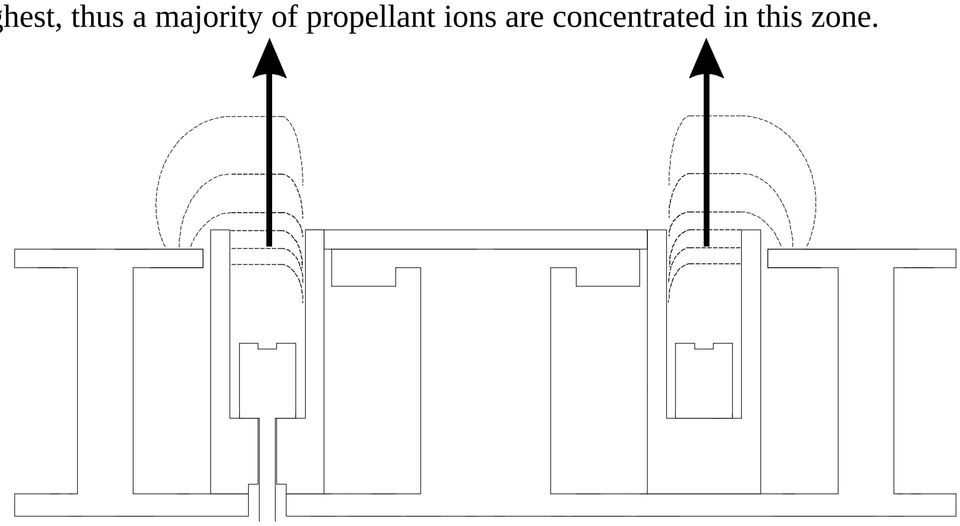

Figure 7.1. Far Field Centerline Accelerating Structure

Next in the far field is a low energy region, typically extending from 40 to 70 degrees, with ions that have energy/charge ratios less than the primary peak (for example, Figure 3.17). They do not, however, have voltages or other characteristics that correspond to charge exchange collisions. It is conjectured that these ions are accelerated outside of the discharge chamber, in a region where the magnetic field lines have a significantly greater curvature than those in the primary discharge region, as shown in Figure 7.2. Magnetic field lines in a Hall thruster serve essentially as lines of equipotential, with electrons being preferentially trapped by the strongest magnetic field lines. In a properly designed Hall thruster, these lines are radial and are where the primary discharge region ions are created and accelerated. Progressing outward from the discharge chamber, the electric potential drops and the magnetic field lines obtain greater curvature. The electric fields at this point are weaker and spread over a wider range of angles. Thus, they accelerate ions at off-centerline angles with voltages significantly less than the discharge voltage (the distribution of ions accelerated near 0° from these field lines is overwhelmed in the measurements by ions from the primary discharge region). As will be explained in the near-field section, it is thought that these ions originate from the far side of the discharge chamber and are accelerated inward, across centerline. When these crossover ions encounter regions of higher plume density, we see large numbers of charge exchange collisions. These lead to significant broadening of the ion energy profile at high angles, which is shown in Figure 7.8 through Figure 7.10.

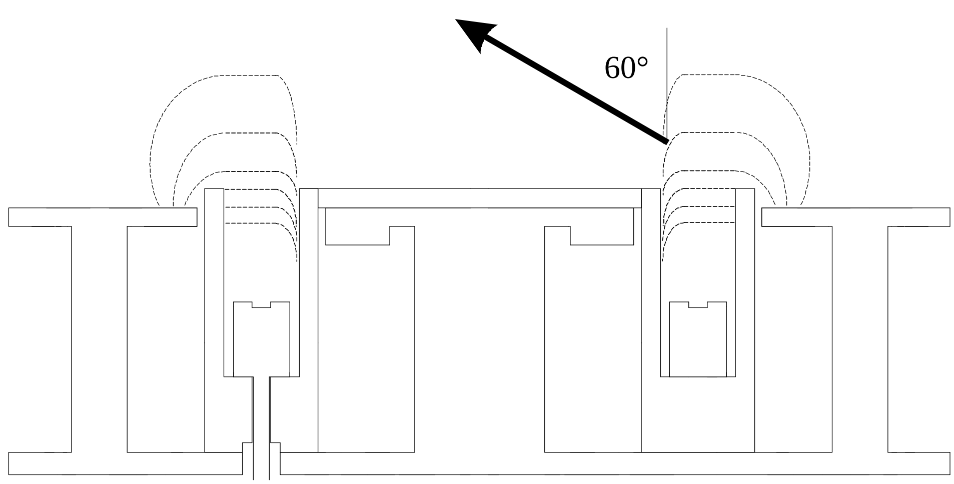

Figure 7.2. Far Field Low Energy Crossover Accelerating Structure

The next two regions, where the profile returns to a centerline-like shape followed by a charge exchange region, are the most puzzling. In both these regions ions are accelerated by the same potential that the primary discharge regions ions see, but at a large angle. It is theorized that the field lines that produce the primary discharge ions are not completely linear, but instead have a sharp curvature on the inward side of the discharge chamber. Ions created in this region are accelerated normal to the field lines, thus creating ions that experience the same accelerating potentials as centerline ions but are directed in the range of 60 to 80 degrees with respect to centerline (Figure 3.18). As the angle is increased toward 90 degrees (Figure 3.22), these ions encounter the acceleration region on the opposite side of the discharge chamber, undergoing large numbers of charge exchange collisions. The accelerating structure is shown in Figure 7.3

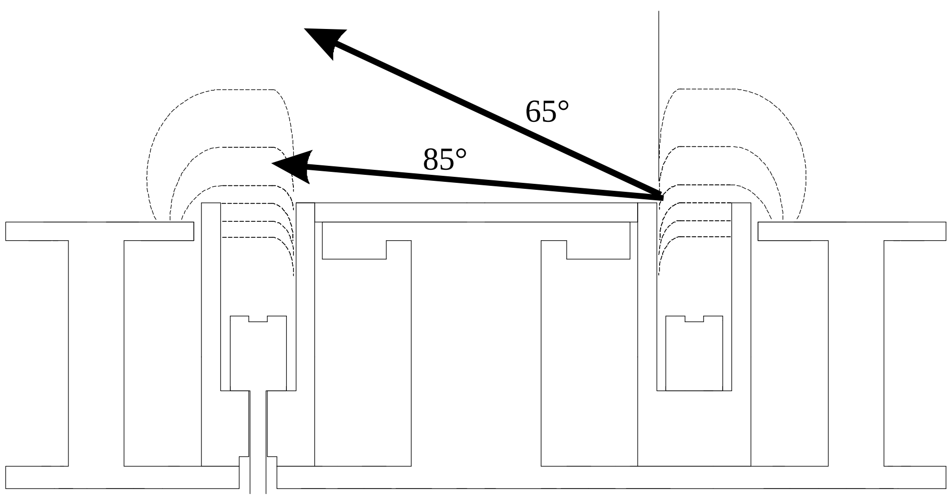

Figure 7.3. Far Field High Curvature Accelerating Structure

Beyond 90 degrees, we see a small region of low energy ions (Figure 3.26). These are created along magnetic field lines with very large radii, such that they curve beyond 90 degrees and accelerate the ions backwards with respect to the desired thrust vector. The energy of these ions is low, since they were created along a field line relatively far outside the discharge chamber as shown in Figure 7.4.

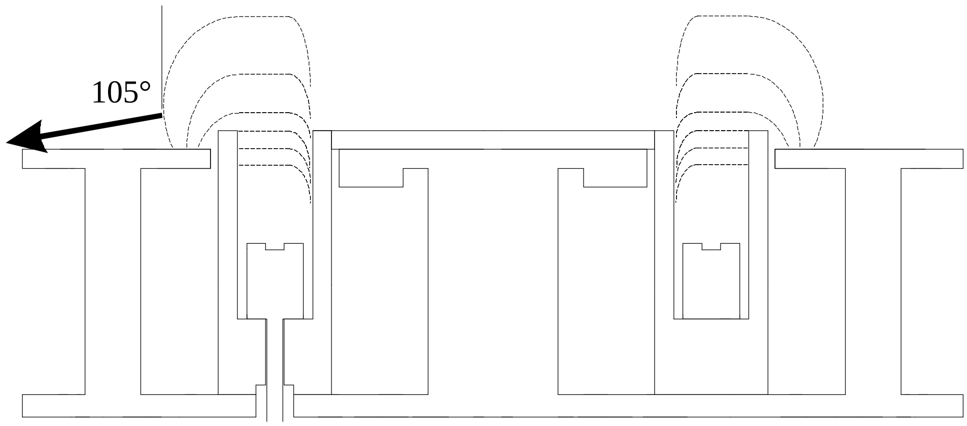

Figure 7.4. Far Field High Angle Low Energy Accelerating Structure

One of the surprising results of this study was that there did not appear to be any ions at angles significantly beyond 90 degrees. Measurements taken on the SPT-100 found ions at 180 degrees (i.e., directly behind the thruster).[34] However, examining the SPT-100 (Figure 1.2), we note that the magnetic pole pieces are designed to minimize mass and thus are – wherever possible – narrower than the magnetic cores. The P5 was designed with extra wide pole pieces (see Figure 2.7 and Figure 2.8) to minimize magnetic field leaking. These pole pieces act as a shield that prevents ions from flowing backward

In the near field we see, as expected, the primary discharge region near centerline (see Figure 4.2) with an accelerating structure shown in Figure 7.5. Going outward in the plume, we do not see the low energy region that was seen in the near field. Instead, we encounter a charge exchange region at approximately 45° (Figure 4.13), before the primary peak attenuates at around 60° (Figure 4.17). Looking at the thruster orientation, we realize that with the sampling orifice centered on one side (the “near” side) of the annular discharge chamber (see Figure 4.1), ions from the other (“far”) side cannot enter the orifice and still reach the entrance slit of the energy analyzer at low angles. Only ions that exit the “far” side at angles greater than or equal to approximately 80° (with respect to the “far” side annulus) can reach the analyzer. However, whereas these ions would be detected at approximately 80° in the far field, due to the orientation the MBMS detects them at a near field angle of approximately 50° with respect to the “near” side annulus. Thus, at around 45° (Figure 4.13) we start to see crossover ions that leave the “far” side at 75° (with respect to the center of “far” side of the annulus) that are shown in Figure 3.20. These ions cause considerable numbers of ion-neutral charge exchange collisions. At higher angles, around 60° (Figure 4.17) we see the effect of ions that leave the “far” side at approximately 85° and encounter the acceleration region on the “near” side (Figure 3.22), causing ion-ion charge exchange collisions. This behavior continues to dominate all the way out to loss of signal. The accelerating structure is shown in Figure 7.6.

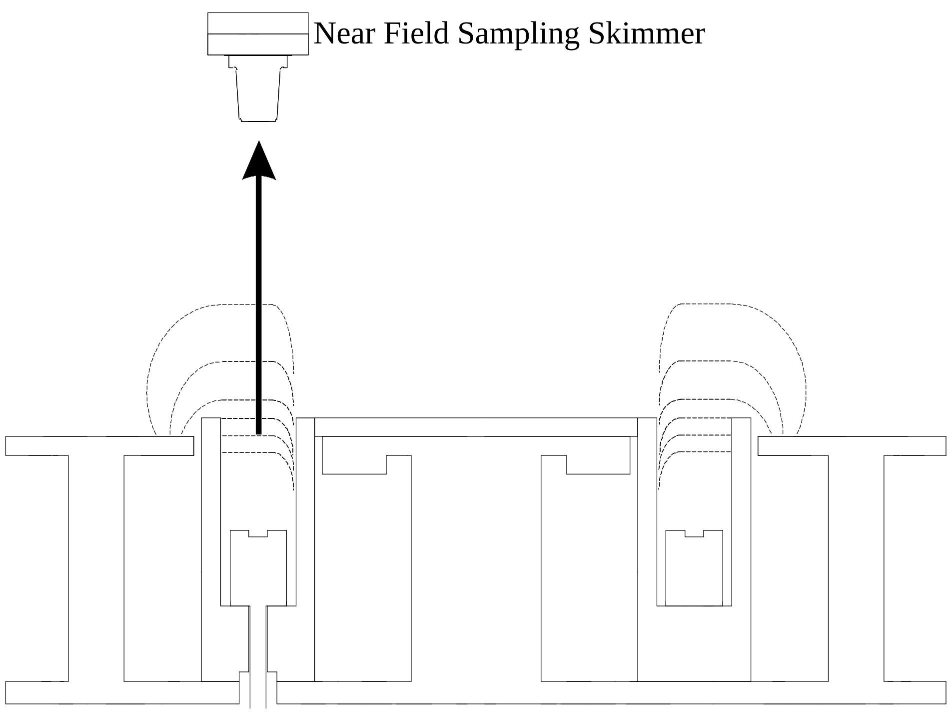

Figure 7.5. Near Field Centerline Accelerating Structure

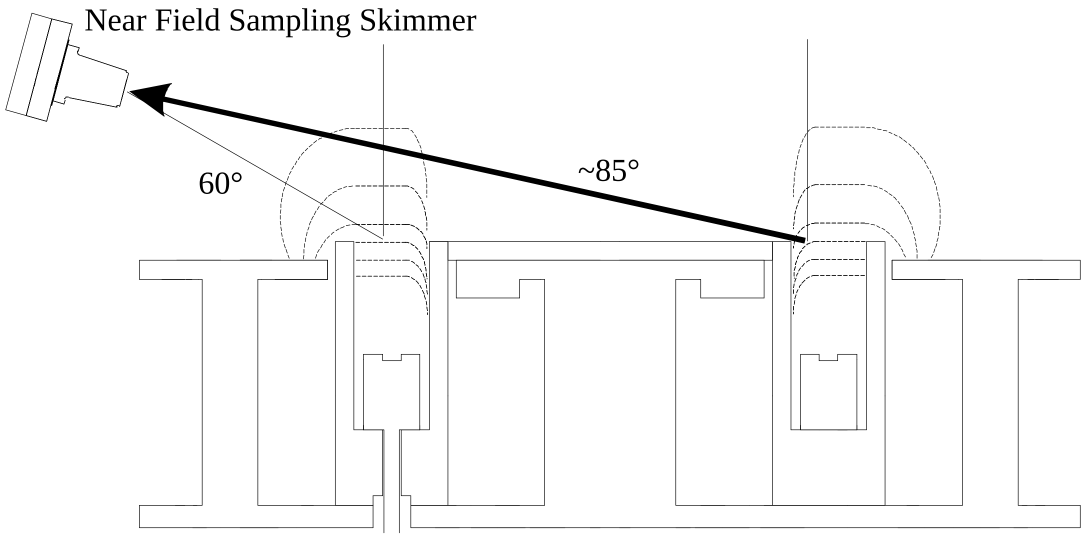

Figure 7.6. Near Field High Angle Accelerating Structure

If the ion energy distributions observed at angles outside the primary discharge region were the result of ions travelling radially outward from the discharge chamber, then there should be very little variation in their shape, since at all angles the plasma would be undergoing charge exchange collisions with the uniform background neutral gas. However, if the ions are travelling radially inward, we expect much greater variation since the plasma would be encountering ions and neutrals from the other side of the annulus, the density of which will increase with angle (i.e., as the beam path moves closer to the exit plane of the discharge chamber). This appears to be what was observed in this investigation. For this to be correct, however, the density must be high enough that the mean free path for ion-neutral charge exchange collisions is on the order of (or less than) the diameter of the discharge chamber (~ 15 cm). Measurements taken inside of a D-55 TAL[49] indicate pressures on the order of 1 mTorr for equivalent flow rates. Calculations for the P5 also indicate a neutral pressure of approximately 1 mTorr based on a neutral temperature of 1000 K and a neutral velocity of 300 m/s. At these pressures, the ion-neutral charge exchange collision mean free path was determined to be 5 cm from EQN 2.1 and EQN 2.2. Thus, the density is high enough to support this conclusion. Therefore, as a consequence of this analysis, it appears that most of the ions produced by this thruster are either accelerated axially along the thrust vector or have an inwardly directed radial component, toward thruster centerline. This conclusion is supported by the Langmuir probe measurements taken inside the discharge chamber by Haas using a high speed reciprocating probe.[43] As illustrated in Figure 7.1 through Figure 7.6, these measurements show plasma equipotential lines that curve back toward the anode in the inner portion of the discharge chamber; and ions are accelerated perpendicular to equipotential lines. An additional piece of evidence that supports inward acceleration was that visual inspection of the thruster while firing shows a plume with a single central core. This differs from other thrusters, such as the SPT-100, which demonstrate a double peaked core, corresponding to the annular nature of the thruster discharge chamber. Since, to a first approximation, equipotential lines follow magnetic field lines, these facts seem to confirm that the magnetic field structure of the P5 is such that the plume is focused inward.

As discussed in Section 5.1, an attempt was made to obtain ion energy measurements in the very near field, 1 cm from the exit of the discharge chamber. Measurements were made, but operating the thruster in such close proximity to an obstruction led to unacceptable interference with thruster operation with a marked increase in thruster current. Therefore, the effort was abandoned. However, as discussed in Section 6.3, the plots that were taken in 5 mm increments across the face of the discharge chamber do show a repeatable qualitative trend toward higher intensity on the inner half of the discharge chamber than on the outer. Assuming that the initial propellant distribution is uniform, this indicates that most of the ionization is occurring near the inner wall of the discharge chamber, where the ions encounter electric potentials that accelerate them directly downstream or inward. Ionization structures such as this were seen by Bishaev and Kim for the SPT-100.[50]

7.3. Axial Location

When we compare individual near field ion energy traces to those taken in the far field, we see a number of differences. Figure 7.7 shows the 0 degree ion energy profiles for Condition 1 in the near field and far field. They have been normalized and overlaid for comparative purposes.

The first thing that we notice is that the trace taken at 10 cm is significantly narrower than that taken at 75 cm. The full width at half maximum in the near field was 22 V, as compared to 35 V in the far field. The increased width appears as low energy elastic collisions. We also see that the 1.33X charge exchange collision observed at 10 cm has disappeared by 75 cm. In general, elastic collisions are far more prevalent in the far field than in the near field, obscuring charge exchange collisions in some cases. This is as expected, since for ions of the energy range found in the Hall thruster,[45] charge exchange collisions are approximately an order of magnitude more likely than elastic collisions. Thus, by sampling close to the thruster, the plume is interrogated before it has had an opportunity to undergo a significant number of elastic collisions that would obscure some charge exchange peaks.

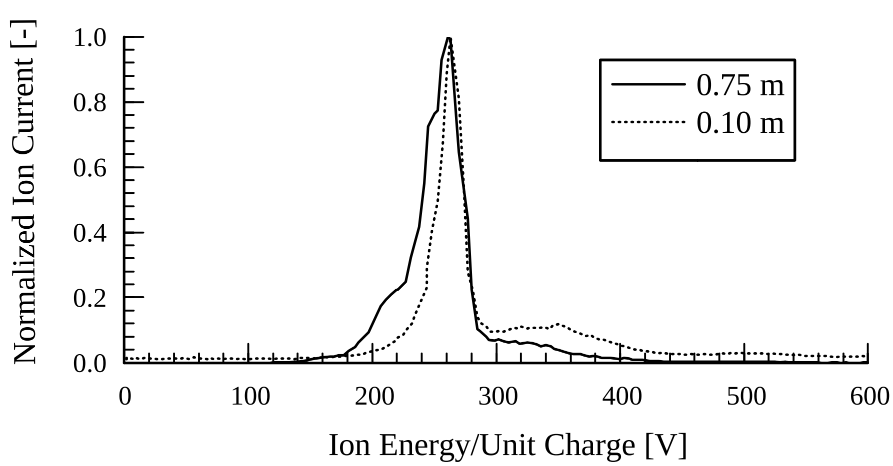

Figure 7.7. Normalized Ion Energy Profiles - 0 Degrees

Figure 7.8 through Figure 7.10 show the full width at half maximum measured at near and far field for the three conditions studied. In addition, since it is a very similar operating point, Condition 1 is compared to SPT-100 data taken by King[34] in Figure 7.8. The narrowing of these ion energy profiles compared to those taken on the SPT-100 is a result of the improvements made to the chamber pumping capacity through the installation of cryopumps. With lower background pressure, the frequency of pressure broadening causing collisions is reduced and thus the profiles are narrower at low angles.

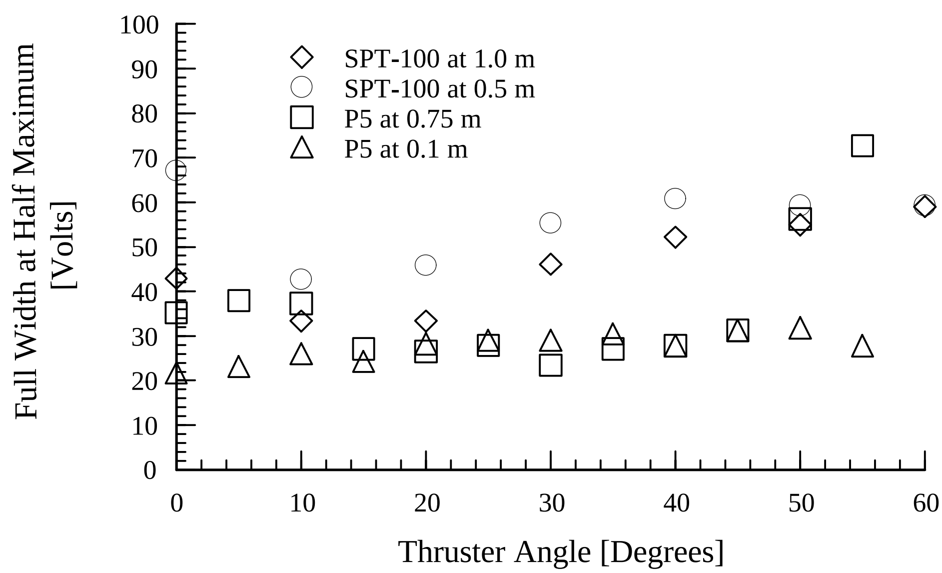

Figure 7.8. Full Width at Half Maximum - Condition 1 and SPT-100

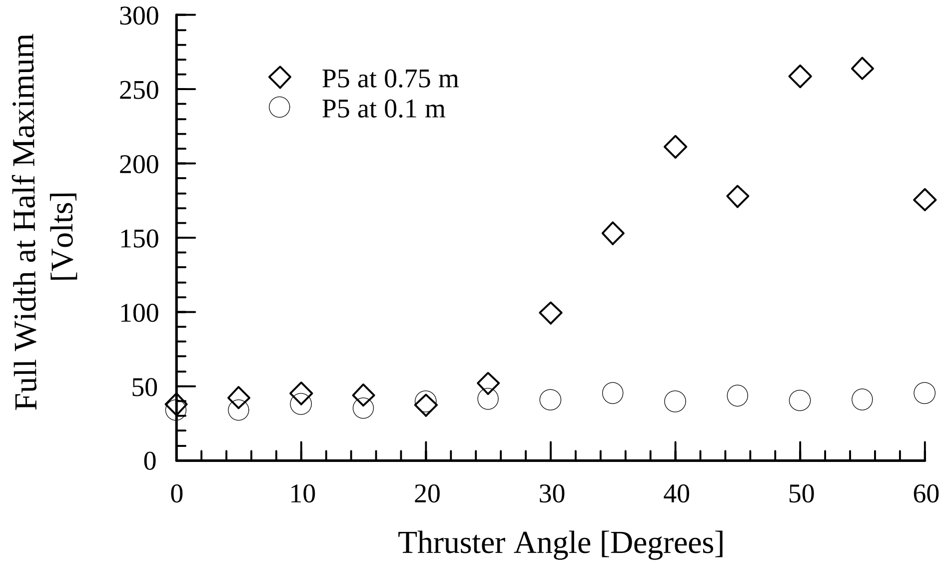

Figure 7.9. Full Width at Half Maximum - Condition 2

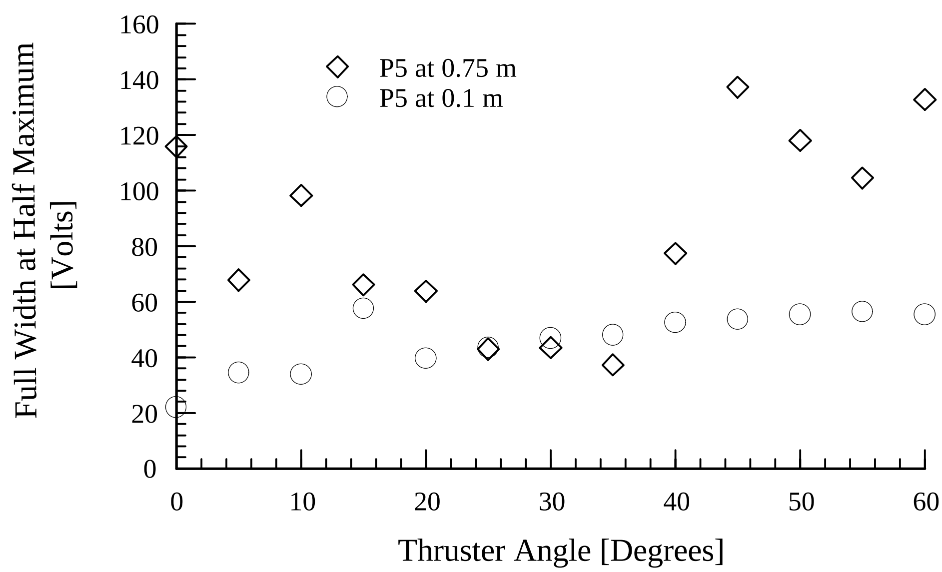

Figure 7.10. Full Width at Half Maximum - Condition 3

In Figure 7.8 through Figure 7.10, we see that the full width at half maximum is broadened in the far field at high and low angles. As discussed previously, at high angles inwardly directed low energy ions crossover the centerline and collide with the flow from the other side of the discharge chamber. These collisions result in broadening of the ion energy distribution. At low angles, the conjecture was that when the thruster was firing directly toward the sampling skimmer, plasma from the thruster that does not enter the orifice impacts on the surrounding flange and is neutralized. This would represent a localized area of higher pressure neutral xenon that would cause collisions and broaden the profile. This hypothesis was checked by placing a neutral particle flux probe[51,52] just below the sampling orifice, perpendicular to the flow. The NPF grids were charged to repel all ions and electrons, and an uncalibrated ion gauge was used to obtain pressure changes relative to the background pressure measured by a calibrated ion gauge as the thruster was rotated inward. Figure 7.11 shows the change in pressure with thruster angle for Condition 1 and Condition 3 along with the background pressure for each condition (determined as an average of two ion gauges and corrected for xenon). We see a notable increase in pressure within 20 degrees of centerline, the same region where the far-field full width at half maximum measurements show broadening. This explains the very broad profiles obtained for Condition 3 in the far field near 0 degrees as seen in Figure 3.52

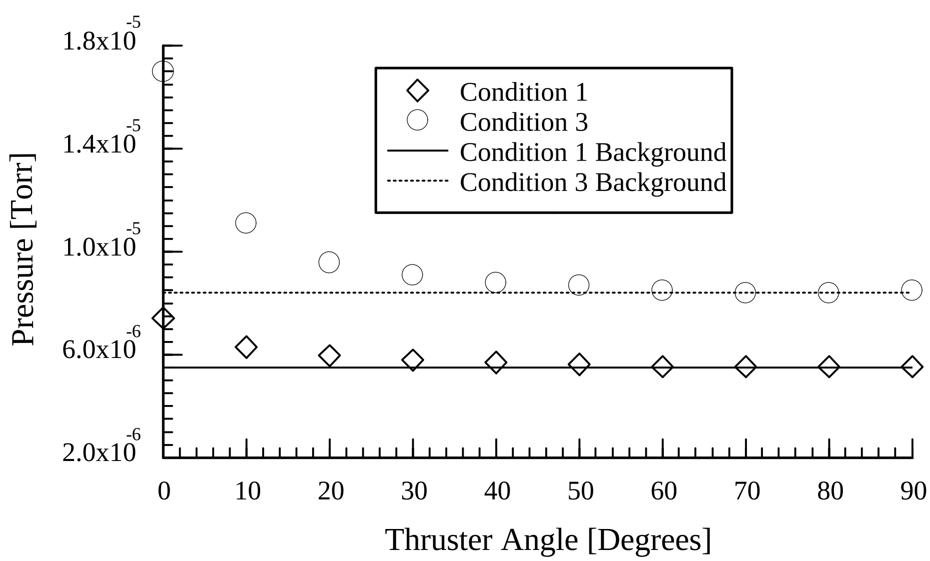

Figure 7.11. Pressure in Front of Far-field Sampling Orifice with Chamber Background Pressures

The mean free paths and charge exchange collision probabilities can be determined based on these pressure readings, and are summarized in Table 7.1.

	Pressure [Torr]	Mean Free Path [m]	0.75 m Collision Probability
Condition 1: Background	$5.5*10^{-6}$	9.1	7.9%
Condition 1: 0°	$7.4*10^{-6}$	6.6	10.5%
Condition 3: Background	$8.5*10^{-6}$	6.0	10.8%
Condition 3: 0°	$1.7*10^{-5}$	3.3	20.4%

Table 7.1. Comparison of Collisions in Background and at 0 Degrees

Therefore, based on these results, we believe that the low angle broadening in the full width at half maximum is primarily a facility effect. This effect can be minimized by reducing pressure build-up through the use of a near field skimmer with a small cross section in place of the larger cross section flange used in the far field. Measurements taken in the very near field did not show reduced broadening, indicating that the near field distributions display a minimum measurable profile width. The high angle broadening is the result of collisions caused by crossover flow.

7.4. Effect of Multiply Charged Ions on Thruster Performance

The creation of multiply charged ions affects the performance of the thruster. The measurements of species ion current obtained using time-of-flight mass spectroscopy can be used to obtain overall species ion currents for each condition. Then, calculations presented by Kim[53] are used to determine the effect of multiply charged ions on thrust, efficiency, and specific impulse.

The sum of the species ion currents is the beam current:

EQN 7.1 $$I_{BEAM} = \sum_i I_i \ .$$

This relationship can then be used to split the anode mass flow among the charged species:

EQN 7.2 $$\dot{m}_a = \frac{m_i}{e} \sum_i \frac{I_i}{q_i} \ .$$

Using EQN 1.13 to combine the anode mass flow rate with the ion velocity (EQN 1.3) gives the thrust for a multispecies plasma:

EQN 7.3 $$T = \sqrt{\frac{2 m_i V_i}{e}} \sum_i \frac{I_i}{\sqrt{q_i}} \ .$$

This is the true thrust measured using a thrust stand as described in Section 2.2. However, if the plume were comprised solely of singly charged ions the thrust would be:

EQN 7.4 $$T^{1+} = \sqrt{\frac{2 m_i V_i}{e}} \sum_i I_i \ .$$

Thus, the presence of multiply charged ions decreases the thrust by the ratio:

EQN 7.5 $$\frac{T}{T^{1+}} = \frac{\sum_i \frac{I_i}{\sqrt{q_i}}}{\sum_i I_i} \ .$$

Using the relationships between efficiency, thrust, specific impulse and anode mass flow rate given in EQN 1.2, similar relationships can be derived for the efficiency and specific impulse:

EQN 7.6 $$\frac{h}{h^{1+}} = \frac{\left(\sum_i \frac{I_i}{\sqrt{q_i}} \right)^2 \Big/ \sum_i \frac{I_i}{q_i}}{\sum_i I_i}$$

EQN 7.7

$$\frac{I_{sp}}{I_{sp}^{1+}} = \frac{\sum_i \frac{I_i}{\sqrt{q_i}}}{\sum_i \frac{I_i}{q_i}}.$$

From EQN 7.6, we see that the efficiency also decreases because of the presence of multiply charged ions. However, EQN 7.7 shows that the specific impulse increases, as expected from EQN 1.12.

Using the overall species ion currents, these ratios can be calculated for centerline (0°) performance and are presented in Table 7.2. Near-field species ion currents were used for Conditions 1 and 2, since these have undergone less collisional perturbation. However, since near field time-of-flight measurements could not be obtained for Condition 3, far field data were used.

	$\frac{T}{T^{1+}}$	$\frac{h}{h^{1+}}$	$\frac{I_{sp}}{I_{sp}^{1+}}$
Condition 1	0.870	0.964	1.108
Condition 2	0.907	0.969	1.068
Condition 3 (Far Field)	0.977	0.993	1.016

Table 7.2. Performance Fractions Due to the Presence of Multiply Charged Ions

Based on these results, we see that the creation of multiply charged ions is an energy loss mechanism for the thruster.

7.5. Discrepancies Between MBMS and LIF Energy Profiles

Discrepancies were found between the ion energy profiles measured using the MBMS and those calculated from LIF data. Possible explanations are presented here.

For Condition 1, the bulk ion velocity calculated form LIF was 16700 m/s, which is only 87% of that measured using the MBMS (19250 m/s). However, LIF measurements taken over an axial range from 0.1 cm to 10 cm showed a steady increase in axial velocity. This seems to indicate that the acceleration zone of the thruster extends at least 10 cm beyond the end of the discharge chamber. It is entirely possible that the acceleration zone extends beyond 10 cm, and that if LIF measurements were taken further downstream the velocity would show greater agreement with MBMS data. If the acceleration zone does, in fact, extend beyond 10 cm, the effect of a sampling skimmer at 10 cm would be to shorten the zone axially because the mounting structure for the skimmer was grounded. However, given the fact that the primary acceleration voltage at 10 cm agrees with that measured at 75 cm, it appears that if the near-field sampling skimmer is within the acceleration zone it is not perturbing the ion energy distributions in an appreciable manner.

The discrepancies between the widths of the distributions measured using the MBMS and LIF are far more significant. Again for Condition 1, at 0 degrees, the near field MBMS measurements show a full width at half-maximum spread in ion energy of 21 V (see Figure 7.8), whereas LIF calculates an ion temperature of 0.75 eV. Based on recent calculations, it appears that this discrepancy results from a difference in terminology. LIF measurements on a hollow cathode indicated an ion temperature of 1.3 eV.[54] However, by deconvolving these data, shifting and summing the deconvolved functions, and converting to energy space, a full width at half maximum of 12.5 eV was determined for a 14 V discharge. Similar methods show that velocity distributions can be deconvolved from simulated Hall thruster LIF data using inverse Fourier transforms of the LIF signal and the atomic line structure.[55] Thus, it appears that it is possible to extract an ion energy spread from LIF using the proper analysis technique.

It is also possible to determine an "ion temperature" for singly charged xenon based on the MBMS data. To determine this ion temperature, the ion energy distribution is assumed to fit a drifting Maxwellian. Beginning with a drifting Maxwellian in terms of ion velocity:

EQN 7.8
$$f(v_i) = \sqrt{\frac{b}{p}} \exp\left(-b\left(v_i - v_{drift}\right)^2\right)$$

where $b = m_i/2k_BT_i$, $v_i = (2E_i/m_i)^{1/2}$, and v_{drift} is the drift velocity. The drift velocity is related to the energy where the energy distribution is maximum, E_{peak}, by first defining the Maxwellian energy distribution:

EQN 7.9
$$f(E_i) = \frac{dv_i}{dE_i} f(v_i) = \frac{1}{\sqrt{2m_iE_i}} f\left(\sqrt{\frac{2E_i}{m_i}}\right).$$

The value of the Maxwellian distribution, $f(E_i)$, is merely the ion current measured in the ion energy distributions. Next, the drift velocity can be determined in terms of the peak of the energy distribution by setting $df(E_i)/dEi = 0$ at $E_i = E_{peak}$ and solving for v_{drift}:

EQN 7.10
$$v_{drift} = \sqrt{\frac{2E_{peak}}{m_i}} + \frac{1}{2b}\sqrt{\frac{m_i}{2E_{peak}}}.$$

This result can be substituted into EQN 7.9 to give the drifting Maxwellian energy distribution:

EQN 7.11
$$f(E_i) = \sqrt{\frac{b}{2pm_iE_i}} \exp\left(-b\left(\sqrt{\frac{2E_i}{m_i}} - \sqrt{\frac{2E_{peak}}{m_i}} - \frac{1}{2b}\sqrt{\frac{m_i}{2E_{peak}}}\right)^2\right).$$

The ion temperature is defined as the half width of the Maxwellian distribution at the energy, E_t, where the value of the ion current is equal to e^{-1} times the value at the peak, or mathematically, $f(E_t) = e^{-1}f(E_{peak})$. We substitute this relation into EQN 7.11 and solve for the ion temperature (by solving for b) to give:

EQN 7.12 $$T_i = \frac{\left(\sqrt{\frac{E_t}{E_{peak}}}-1\right)^2}{\sqrt{\frac{E_t}{E_{peak}}}-\ln\sqrt{\frac{E_t}{E_{peak}}}}\frac{E_{peak}}{e} = \frac{\left(\sqrt{\frac{V_t}{V_{peak}}}-1\right)^2}{\sqrt{\frac{V_t}{V_{peak}}}-\ln\sqrt{\frac{V_t}{V_{peak}}}}V_{peak}\ [\mathrm{eV}]$$

V_{peak} and V_t are the ion energy/unit charge of the peak in ion current and the point where the ion current is equal to e^{-1} times the peak value, respectively since $E_i = eV_i\,(q_i = 1)$. The ion temperature determined from EQN 7.12 is in electron volts.

Using this relationship, we can determine an "ion temperature" for singly ionized xenon the near field Condition 1 at 0 degrees (Figure 4.2) where the full width at half maximum was 21 V. The peak voltage, V_{peak} = 263 V and the ion current at the peak voltage, $f(V_{peak}) = 1.55 \times 10^{-16}$ A. Thus, $f(V_t) = 5.70 \times 10^{-17}$ A and linear interpolation gives V_t = 276 V. This gives an "ion temperature" of 0.16 eV, which is of the same order as the ion temperature computed from LIF and agrees well with previous measurements in the plume of a 1.5 kW class Hall thruster.[56]

Therefore, it appears that the commonly reported discrepancy between LIF and other ion energy measurements stems from the fact that they are reporting different, but related, ion energy quantities. LIF measurements report the random spread in ion energy, the "ion temperature", while MBMS measurements give the spread in ion energy resulting from ion acceleration over a potential spread. These measurements are interchangeable given the proper analysis technique.

7.6. Summary and Future Work

A number of conclusions regarding the ion energy and species composition of the P5 Hall thruster have been determined in this work. They are summarized here for convenience:

- Though improvements have been made to the pumping capacity of the LVTF, the nature and location of the MBMS are such that there are still significant numbers of elastic and charge exchange collisions. However, these collisions can act as a valuable diagnostic in their own right, allowing for the qualitative identification of multiply charged species in the plasma.

- By examining the variation of the ion energy distributions with thruster angle, an overall profile of the thruster's ion acceleration structure can be determined. For the P5, this examination indicated a structure that tends to preferentially accelerate the ions inward.
- The acceleration structures were similar, with subtle dissimilarities, at the different thruster operating conditions. The differences stem from changes in the magnetic field for each operating condition of the P5. However, the similarities indicate that if a thruster can be operated without damaging the satellite it is mounted on at one operating condition, it should also be able to do so at other operating conditions.
- Time-of-flight mass spectroscopy can be used to quantitatively determine the species composition of the thruster's plume. Charged species up to quadruply ionized xenon were identified. Collisions with background gases tend to depopulate higher charge states when compared to singly charged xenon.
- By moving the sampling skimmer closer to the thruster, the effects of collisions on measurements can be reduced. This is seen in ion energy distributions that have reduces widths and species composition measurements that show higher fractions of multiply charged ions.
- Comparisons of MBMS measurements with LIF data indicate that both are providing accurate data. The nature of these measurements is such that each produces a different quantity for the spread in ion energy. These quantities are different, but related. The data from each measurement can be manipulated to give the quantity from the other, producing results that agree fairly well.

While this work has greatly expanded the scope of MBMS work, it has also indicated future directions for research:

- The major signal loss source is beam expansion. This is especially detrimental for the Hall thruster because it has a low velocity, high density plasma (in comparison to other mass spectrometer investigations). A set of electrostatic beam optics to focus and steer the beam could be used to maximize signal. This would be especially critical to any attempts to measure erosion products or other light ions using time-of-flight mass spectroscopy.
- Excellent ion energy distribution and time-of-flight mass spectroscopy measurements were taken at Condition 2 (500 V, 5.3 A). This was the high velocity (with respect to Condition 1), low density (with respect to Condition 3) case. Thus, at this condition, beam expansion should be minimized. Based on this, it appears that an ion engine, with its high discharge voltage and low ion density would be an excellent candidate for an MBMS investigation.
- For MBMS measurements, the P5 was operated very close to the end cap of the LVTF (See Figure 2.1). This configuration can lead to unacceptable levels of material sputtering, interference with thruster operation, and modification of data profiles at high thruster power levels. The near field sampling skimmer was somewhat successful in minimizing these problems. However, as long as the thruster is operated near the end cap, they will persist. Thus, development has begun on the Miniaturized Ion Energy Analyzer (MIEA), a small version of the 45-degree parallel-plate energy analyzer that can be mounted in the center of the chamber.[57] It is expected that this device will further minimize the effect that collisions have on the ion energy distributions. However, in doing so it may omit valuable information on plume species composition that results from charge exchange collisions.

APPENDICIES

APPENDIX A

ANALYSIS OF HALL EFFECT THRUSTERS AND ION ENGINES FOR ORBIT TRANSFER MISSIONS**

ABSTRACT

Analytical methods were combined with actual thruster data to create a model used to predict the performance of systems based on two types of electric propulsion thrusters, Hall-effect thrusters and ion engines, for several orbit transfer missions. Two missions were trip time constrained: a LEO-GEO transfer and a LEO constellation transfer. Hall thrusters were able to deliver greater payload due to their higher overall specific power. For the power limited orbit-topping mission, the choice of thruster is dependent on the user's need. Ion engines can deliver the greatest payload due to their higher specific impulse, but they do so at the cost of higher trip time. Study of reusable electric propulsion orbit transfer vehicle systems indicates that they can offer payload mass gains over chemical systems, but that these gains are less than those offered by other electric propulsion transfer scenarios due to the necessity of carrying propellant for return trips. Additionally, solar array degradation leads to increased trip time for subsequent reusable transfers.

** Originally presented as American Institute of Aeronautics and Astronautics paper number 96-2973 at the 32nd Joint Propulsion Conference, July 1996. Co-author, Ronald A. Spores: United States Air Force Research Laboratory, Electric Propulsion Laboratory, Edwards AFB, CA 93524.

INTRODUCTION

The US Air Force has recently completed several studies to investigate the potential advantages of advanced space propulsion for several orbit transfer scenarios. The first study investigated advanced propulsion concepts for expendable orbit transfer vehicles[58] and concluded that the potential for launch vehicle downsizing that resulted from the use of high specific impulse thrusters provided significant cost savings over baseline chemical launch vehicle/upper stage systems. The second study looked at reusable advanced upper stages[59] and preliminary indications are that while there remains the potential for launch vehicle downsizing, it is significantly reduced compared to expendable systems. This difference was largely due to the added propellant required to perform the round trip mission from low-earth orbit to geostationary orbit. Both studies pointed out advantages for advanced electric propulsion systems based on xenon propellant. The objective of this paper is to analyze the trade-off between Hall-effect thrusters and ion engines as a high power propulsion system for orbit transfer missions.

Both the Hall-effect thruster and the gridded ion engine are classified as electrostatic thrusters and operate on heavy noble gases, primarily xenon. These electric propulsion devices are capable of specific impulses ranging from approximately 1500 to 4000 seconds, compared to chemical systems that typically operate in the range of 300 to 400 seconds.

Electric propulsion is a type of rocket propulsion for space vehicles and satellites which utilizes electric and/or magnetic processes to accelerate a propellant at a much higher specific impulse than attainable using classical chemical propulsion. The concomitant reduction in required propellant mass results in increased payload mass capability.

The method of analysis used in this study is based on the model developed by Messerole.[16] It has been modified to reflect the most current information on thruster development levels and to allow for greater flexibility in system component variation.

There are four missions examined in this study. They are a low earth orbit to geosynchronous earth orbit (LEO-GEO) transfer, a LEO to intermediate orbit transfer for constellations of satellites, a geostationary orbit insertion with partial chemical propulsion, and a reusable orbit transfer vehicle concept. These missions are representative of the range of orbit transfer scenarios that the Air Force presently envisions for an electric propulsion upper stage, and are among those likely to be attempted over the next 10 to 20 years.

ORBIT TRANSFER HARDWARE

The essential components of an electric propulsion orbit transfer vehicle are the thrusters and the power generation sub-system. In this study, two types of thrusters are examined: the Hall thruster and the ion engine. Power is generated by a concentrator solar array.

Hall-effect thrusters are a type of electrostatic thruster in which ions are generated by electron bombardment. The ions are then accelerated by an electron cloud, which is held in place by a magnetic field perpendicular to the direction of acceleration. The electron cloud is generated by an external cathode.

Initial work on Hall-effect thrusters began in the 1960’s in the United States and the former Soviet Union. Due to difficulties achieving the same levels of efficiency reached by the gridded ion engine, work ceased in the United States around 1970.[5] In the Soviet Union, research into the ion acceleration mechanism led to improvements in efficiency and further research and development. Two basic types of Hall thrusters were developed: the stationary plasma thruster (SPT) developed under the leadership of A.I. Morozov at the Kurchatov Institute and the thruster with anode layer (TAL) developed under the leadership of A.V. Zharinov at TSNIIMASH.[7] The primary differences between the two types are that the acceleration region of the SPT is within the thruster itself while for the TAL it is in front of the thruster and the lack of an acceleration chamber insulator in the TAL. This study does not distinguish between the various types of Hall thruster concepts with regards to performance.

Over sixty-four SPT-50 and SPT-70 units have flown aboard Russian spacecraft, beginning with the Meteor satellite in 1972[60] (the numerical designation in the name of a stationary plasma thruster is the outer diameter of the discharge chamber in millimeters). The first SPT-100s flew in 1994 on the GALS spacecraft. Larger thrusters; such as the SPT-140, SPT-200, and SPT-290; have undergone various levels of laboratory development. With the end of the Cold War, this technology became available for evaluation and use in the West. Work in the United States to further quantify stationary plasma thruster performance and flight qualify them for western spacecraft has been done primarily at the NASA Lewis Research Center[8] and the Jet Propulsion Laboratory.[9] Space Systems Loral has developed power processing units for the SPT-100 and is working to develop higher capacity power processing unit.

By examining a range of thruster sizes and operating conditions,[12,13,14] we are able to make modeling predictions. One of the most important parameters for this study is the curve of thruster power in terms of the specific impulse (I_{sp}). As specific impulse increases, the discharge voltage will increase as well. The Hall thruster power is modeled using a polynomial fit. This relation is shown in Figure A.1.

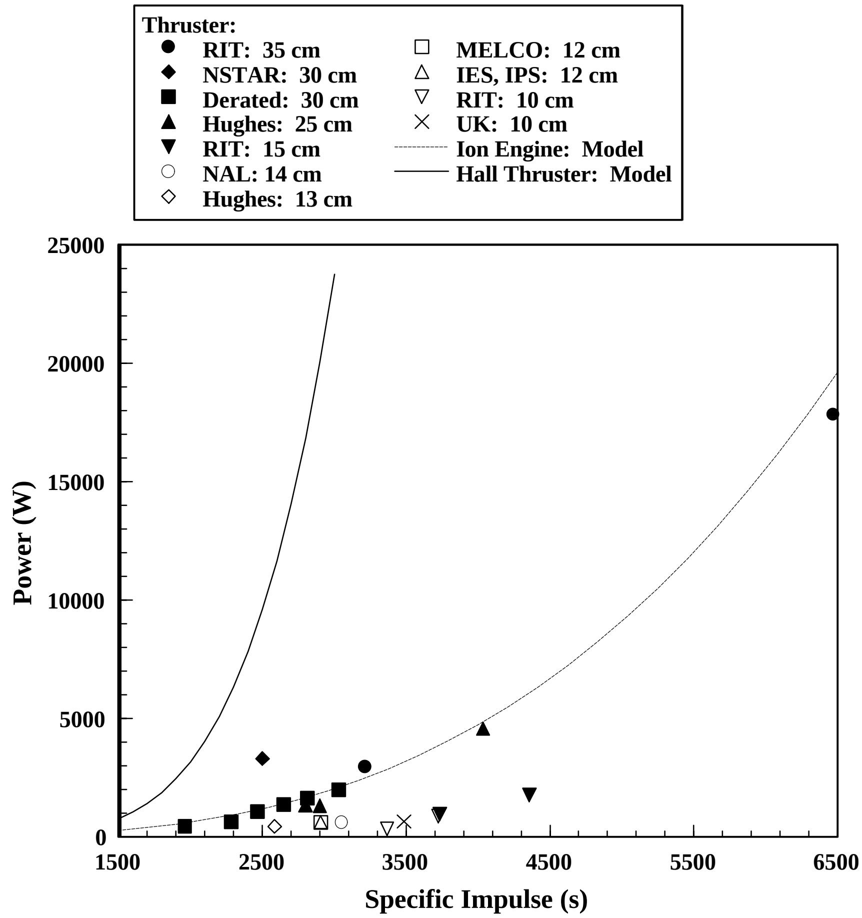

Figure A.1. Thruster Power versus Specific Impulse

The thruster efficiency is modeled using the relationship:

EQN A.1

$$h = \frac{a}{1 + \frac{b}{\left(g_o I_{sp}\right)^2}}$$

which is based on the ion thruster efficiency equation developed by Brophy.[17] This efficiency model is shown in Figure A.2.

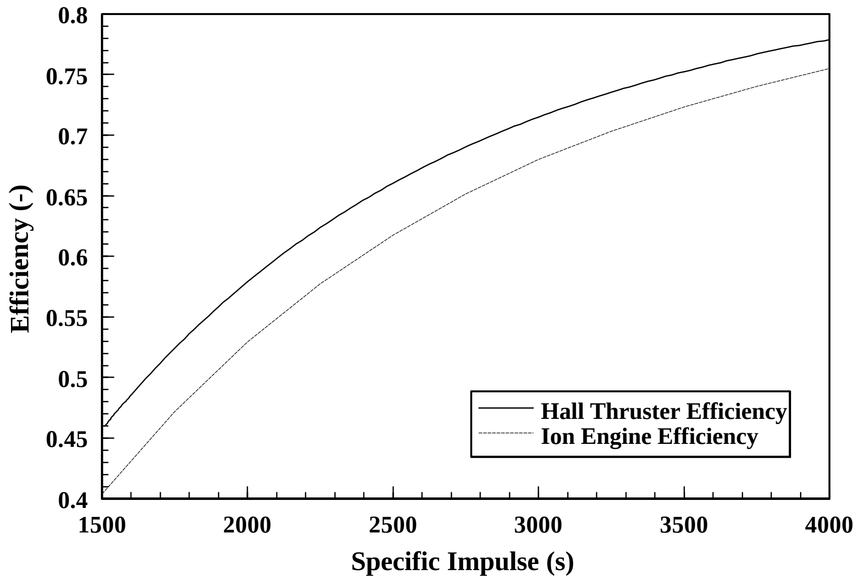

Figure A.2. Thruster Efficiency versus Specific Impulse

In the gridded ion engine, propellant is injected into an ionization chamber and ionized by electron bombardment. The propellant is then electrostatically accelerated through a series of biased grids. Traditionally, these grids have been molybdenum, though recent work has been done to develop carbon-carbon composite grids.

In the United States, ion engines were developed at NASA's Lewis Research Center in the late 1950's under the guidance of Dr. Harold Kaufman.[3] The original models used primarily mercury or cesium for propellants. Thruster development has continued at various levels, using thrusters with diameters ranging from 2.5 to 150 centimeters and power levels ranging from 50 W to 200 kW. Flight experiments have included SNAPSHOT, a US Air Force satellite that flew a cesium ion engine in 1965; SERT-2, a NASA satellite that flew a mercury ion engine in 1970; and ETS-3, a Japanese satellite that also flew a mercury ion engine in 1982.[61] In the 1980's, emphasis shifted to xenon and other noble gases because of concern over spacecraft contamination and environmental issues during ground testing. As part of its New Millennium program, NASA has been developing NASA's Solar Electric Propulsion Technology Application Readiness (NSTAR) engine for use on the first New Millennium mission, Deep Space 1, which includes an asteroid and comet fly-by.[4] Other nations including the United Kingdom, Germany, and Japan are also currently developing ion engine technologies.[62] Hughes Space and Communication Co. has undertaken an extensive development effort and has baselined ion engines for North-South Station-keeping on it's next generation of communications satellites.[63]

In determining the thruster power curve, Figure A.1, we took data from a wide range of ion engines.[62,63,64,65,66,67,68,69] Figure A.1 shows two distinctly different trends for the ion engines depending on the diameter of the thruster. Thrusters larger than 20 cm follow a steeper power versus specific impulse curve than those smaller than 20 cm. These smaller thrusters are intended primarily for station-keeping missions. Therefore, since this study is concerned with orbit transfer missions, data from thrusters smaller than 20 cm is omitted.

Ion engine efficiency was modeled using the same form as the Hall thruster, and is shown in Figure A.2.

One of the main concerns about both Hall thruster and ion engines for orbit transfer is lifetime. Lifetimes of up to 7400 hours (308 days) for the Hall thruster (SPT-100)[60] and 4350 hours (181 days) for the xenon ion engine[68] have been demonstrated, with an 8000 hour (333 days) test set to begin on the NSTAR ion engine.[65] The primary concern is thruster erosion (wall erosion for the SPT, guard ring erosion for the TAL, and grid erosion for the ion engine) which will become even more of an issue with higher power thrusters.

Of paramount importance for any solar electric propulsion vehicle is solar panel technology. For orbit transfer missions, concentrator arrays offer several advantages over conventional planar arrays.[61] Concentrator arrays use optics to focus solar radiation onto the solar cells, with concentration ratios up to 100:1. These optics provide inherent radiation shielding that reduces the need for a thick coverglass. This results in both greater radiation resistance and reduced cell area compared to conventional planar arrays. A concern of concentrator arrays is that they demand accurate 2-axis pointing, increasing the complexity of the orientation system.[70] Pointing accuracies of ± 3° are required as compared to ± 18° for planar arrays.[71] Projections for concentrator array systems indicate a specific power approaching 100 W/kg and a power to area ratio of well over 200 W/m^2, for technologies including gallium arsenide and multijunction arrays. Similar performance can be achieved with planar arrays, but with much greater radiation degradation.

MODEL

The centerpiece of the model is the payload mass fraction equation based on the method developed by Messerole.[16] This method is derived by starting with an initial mass breakdown:

EQN A.2 $m_o = m_{pl} + m_{pwr} + m_p + m_{tf} + m_{ps'} + m_{att} + m_{adap} + m_{ss'} + m_{cont} + m_{rp}$

where the terms are defined in Table A.1.

Term	Name	Explanation
m_o	Initial Mass	Total system mass at beginning of E.P. transfer
m_{pl}	Payload Mass	Useful on-station mass
m_{pwr}	Power Mass	Mass of power dependent components (thrusters, power processors, solar arrays, and radiators)
m_p	Propellant Mass	Mass of xenon used for transfer
m_{tf}	Tank and Feedsystem Mass	Mass of fuel tank and associated components
$m_{ps'}$	Primary Structure Mass	Mass of satellite's major structural components
m_{att}	Attitude Control Mass	Mass of attitude control system
m_{adap}	Adapter Mass	Mass of propulsion to satellite adapter
$m_{ss'}$	Secondary Structure Mass	Mass of power related system structures
m_{cont}	Contingency Mass	Contingency mass for power related systems
m_{rp}	Radiation Protection Mass	Mass of shielding to protect payload from radiation damage

Table A.1. Mass Breakdown

The masses are divided by the total initial system mass to obtain mass fractions. The propellant tank and feedsystem mass fraction is calculated by dividing by the mass of the fuel and is expressed as the tank and feedsystem fraction, f_{tf}. The primary structure mass, attitude control mass, and adapter mass are combined into one term, the primary structure fraction, f_{ps}. The secondary structure and contingency mass fractions are expressed in terms of the propulsion system dry mass (power mass plus tank and feedsystem mass) and are combined into the secondary structure fraction, f_{ss}. The radiation protection mass is expressed in terms of the payload mass using the radiation protection fraction, f_{rp}. Combining these terms, EQN A.2 can be rewritten to express the payload fraction as:

EQN A.3
$$\frac{m_{pl}}{m_o} = \frac{(1 - f_{ps}) - \left(1 + (1 + f_{ss})\left(\frac{m_{pwr}}{m_p} + f_{tf}\right)\right)\frac{m_p}{m_o}}{1 + f_{rp}}.$$

Other than the fractions, there are two terms in the payload fraction equation. The first term is the propellant mass fraction and the second is the power mass to propellant mass ratio. The propellant mass fraction is calculated from the rocket equation:[72]

EQN A.4
$$\frac{m_p}{m_o} = 1 - e^{-\Delta V_{Tot}/g_o I_{sp}}$$

where $\Delta V_{Tot} = (1 + f_{perf})\Delta V$ and f_{perf} is an orbit transfer performance factor designed to account for thrust vector misalignment, off nominal thruster performance, and other contingencies.

The power mass to propellant mass ratio, (m_{pwr}/m_p), is calculated using the propellant mass flow rate to obtain:

EQN A.5
$$\frac{m_{pwr}}{m_p} = \frac{m_{pwr}}{t_t \dot{m}_p}$$

where t_t is the thrusting time, equal to the trip time (t) multiplied by the non-occulated transit percentage. It is taken to be 86%, which is the case for a 180 day LEO to GEO mission, but is not adjusted for changes in trip time or mission. Using the definition of specific impulse and efficiency, we can then rewrite EQN A.5 as:

EQN A.6 $$\frac{m_{pwr}}{m_p} = \frac{(g_o I_{sp})^2}{2t_t h_{ppu} h_t f_{ave} a}.$$

The term f_{ave} is the mission average power fraction, which accounts for solar array degradation due to radiation damage. It is dependent on the solar array technology and trip time. For planar arrays, it is 0.70 for a 180 day transfer, for concentrator arrays, it is 0.97 for the same trip time.[16]

The overall specific power (for the power dependent components), a, is defined as:

EQN A.7 $$a = \frac{P_{B.O.L.}}{m_{pwr}} = \frac{P_{B.O.L.}}{m_a + m_{ppu} + m_t + m_{rad}}$$

where $P_{B.O.L.}$ is the power at the beginning of the orbit transfer vehicle's life. Then we determine the specific power by inversely summing the component specific powers:

EQN A.8 $$a = \left(a_a^{-1} + a_{ppu}^{-1} + a_t^{-1} + a_{rad}^{-1}\right)^{-1}.$$

Solar array specific power, a_a, is taken from data on concentrator array technologies to be 100 W/kg.[61]

For the thruster specific power, a_t, baseline conditions are taken from the SPT-100 and the NSTAR ion engine. It is then possible to show that if thruster mass is proportional to mass flow rate and mass flow rate is invariant with respect to input power, the specific power varies according to the relation:[16]

EQN A.9 $$a_t = a_{to} \frac{h_o}{h} \frac{I_{sp}^2}{I_{spo}^2} + a^*.$$

The constants a_o and a^* are determined by curve fitting actual thruster data as shown in Figure A.3. For the ion engine, only large (diameter ≥ 20 cm) ion engines are considered relevant. The optimal values found for these are summarized in Table A.2.

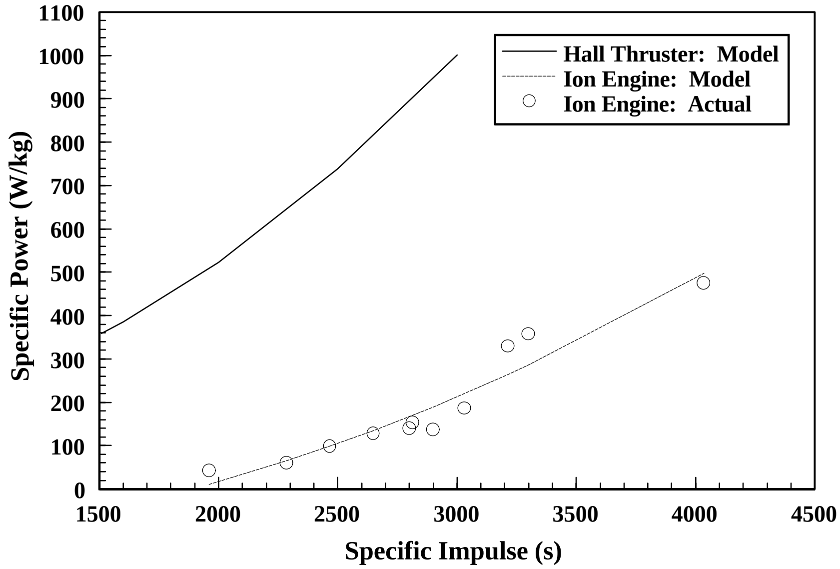

Figure A.3. Thruster Specific Power versus Specific Impulse

Thruster	a_o	a^*	I_{spo}	h_o
Hall Thruster	385.7	0.0	1600 s	0.49
Ion Engine	347.0	-243.0	2500 s	0.62

Table A.2. Thruster Specific Power Constants

For the power processing unit's specific power a_{ppu}, data was gathered from documented Hall thruster and ion engine power processing units.[60,65] Additionally, due to a lack of other high power (>3 kW) space qualified units for xenon propellant systems, data from the US Air Force's 26 kW arcjet Electric Propulsion Space Experiment's (ESEX) PPU is included.[73] The ESEX PPU is a 1991 design and is considered a conservative estimate of future power processing unit specific power performance. The resulting specific power versus power processing unit input power (shown in Figure A.4), was linearly curve fit with two straight lines. However, since power is an output quantity from this analysis, the recommended power per thruster is used to determine the power processing unit specific power by assuming one power processing unit per thruster.

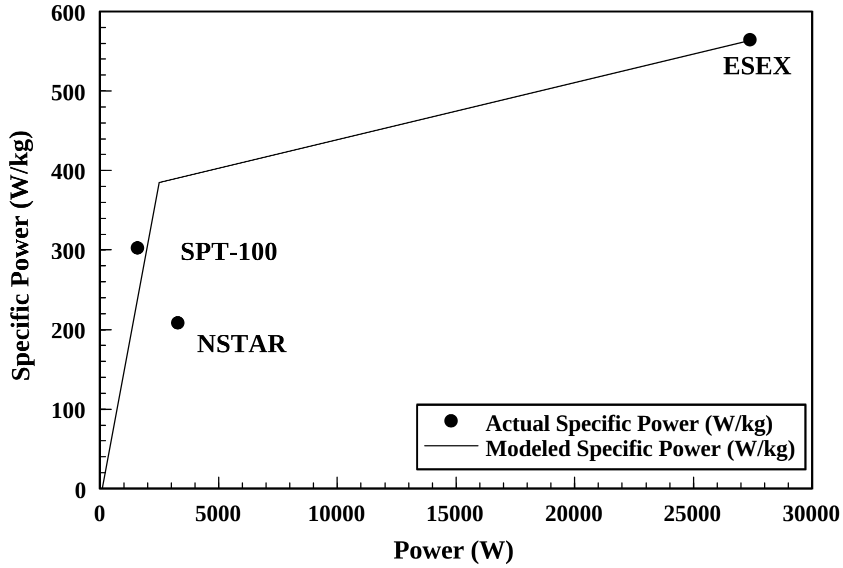

Figure A.4. PPU Specific Power versus Input Power

Based on documented power processing units, the efficiency was set to 93% for the Hall thruster[60] and 90% for the ion engine.[64] The lower efficiency of the ion engine power processing unit is due to its more complex power needs.

Finally, for the radiator specific power, a_{rad}, a value of 32 W/kg is assumed for a system with a power processing unit of 92% efficiency.[64]

The required beginning of life input power for a given thruster system can be determined from the overall specific power, the power mass to propellant mass ratio, the propellant mass fraction, and the initial mass:

EQN A.10
$$P_{B.O.L.} = m_o \frac{(g_o I_{sp})^2}{2 t_t \eta_{pcu} \eta_t f_{ave}} \left(1 - e^{-\Delta V_{Tot} / g_o I_{sp}}\right).$$

MISSIONS

Four orbit raising missions are considered in this paper:

- Low earth orbit (LEO) to geosynchronous earth orbit (GEO) all-electric propulsion transfer
- LEO to LEO (higher) orbit transfer for constellations of LEO satellites

- GEO insertion with partial chemical propulsion (orbit topping)
- Reusable Orbit Transfer Vehicle (ROTV) for LEO to GEO transfer

These missions represent a cross section of future orbit transfer missions for which electric propulsion is a viable option. High I_{sp} and DV missions involving interplanetary transit are not considered since they do not fall with the US Air Force's current mission parameters.

Though not a direct part of the orbit transfer mission, the launch vehicle makes a major impact on mission parameters, especially with regards to launch mass and payload faring size. The launch vehicles considered in this study were the McDonnell Douglas Delta II (7920), the General Dynamics Atlas IIAS, and the Lockheed Martin Titan IV with Hercules Solid Rocket Motor Upgrade (SRMU). Launches to LEO were not to the traditionally used 100 nautical mile (185 km), 28º circular orbit. This was because the large solar arrays necessary for electric propulsion orbit transfer vehicles coupled with their low thrust creating a thrust to drag ratio dangerously close to one. It was found, however, that by raising the launch altitude to 300 km, approximately 98% of the LEO mass could be retained while raising the thrust to drag ratio to almost ten. In all cases, the largest payload faring available was used with the booster to insure that maximum space was provided for large components such as solar arrays. With these considerations, the masses inserted into the 300 km LEO orbits are summarized in Table A.3.

Booster	Launch Mass
Delta II	4915 kg
Atlas IIAS	8300 kg
Titan IV	21150 kg

Table A.3. LEO Insertion Masses[74]

Thruster sizing is a major concern of satellite manufacturers. Due to the existence of a parametric series of Hall thrusters, it is possible to derive a sizing relation with respect to specific impulse based on the thrusters' characteristics. This relation is shown in Figure A.5 with existing and planned thrusters identified. However, the physical dimensions of the ion engine are not as sensitive to changes in specific impulse (and thus power) as the Hall thruster. Therefore, all ion thrusters are assumed to be 30 cm in this study. Thirty centimeters is the average size of the large ion engines considered in this study.

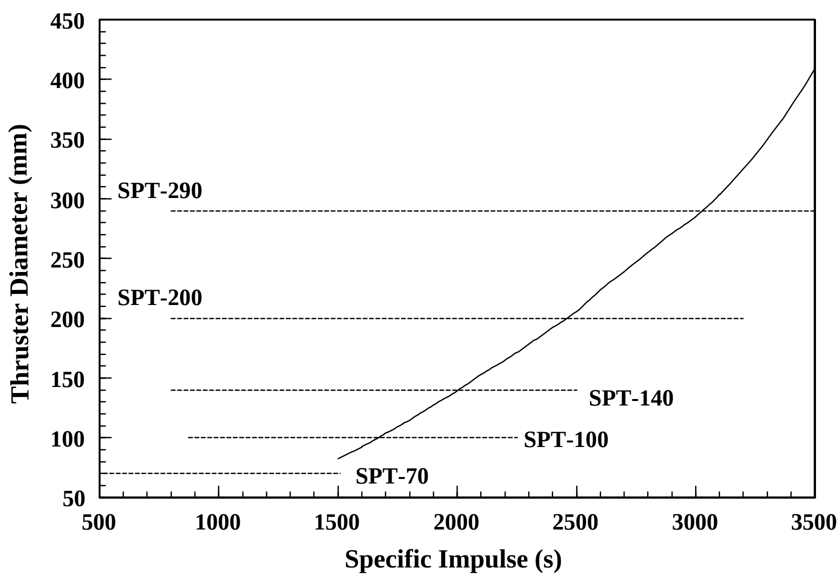

Figure A.5. Hall Thruster Diameter versus Specific Impulse

In this analysis, *DV* is calculated using the first order approximation:

EQN A.11 $$\Delta V = \sqrt{V_o^2 + V_f^2 - 2V_oV_f \cos j}$$

The effect of gravity on *DV*, due to the longer electric propulsion trip times is ignored in this analysis. In other cases, such as the orbit topping mission, *DV*s had previously been calculated using sophisticated orbit transfer codes like SECKSPOT[75] which include the gravity *DV*. These previously calculated *DV*s were manually entered for analysis. In no cases were the two *DV* methods mixed.

The mission parameters (*DV* and mass fractions) for the four missions examined are shown in Table A.4.

Parameter	LEO-GEO	Constellation	Orbit Topping	Reusable OTV
DV	5233 m/s	276.8 m/s	Varies	5233 m/s
f_{perf}	0.01	0.01	0.01	0.01
f_{ps}	0.06	0.06	0.06	0.20
f_{ss}	0.10	0.10	0.10	0.10
f_{tf}	0.12	0.12	0.12	0.12
f_{rp}	0.03(t/180)	0.20	0.03 (t/180)	0.03 (t/180)
f_{ave}	1-0.03(t/180)	0.97	1-0.03 (t/180): t ≥ 180 0.97: t < 180	$\prod_{i=1}^{n} f_{avei}$ n = transfer number
f_{avei}				1-0.03 (t/180)

Table A.4. Mission Parameters

LEO-GEO Transfer:

The first mission examined was a basic LEO-GEO orbit transfer. This mission is applicable not only to communications satellites, but also to proposed observation and reconnaissance missions. Transit times of 180, 270, and 360 days were examined for launches on all three launch vehicles. The values used in the payload fraction equations are shown in Table A.4.

Key parameters determined are the payload mass fraction, the array output power required, and the number of thrusters necessary. We note that payload mass fraction is independent of initial mass and thus invariant with launch vehicle. However, the power and number of thrusters is strongly dependent on the initial mass launched into LEO.

It is clear that no single parameter determines the best thruster configuration for any given mission. It must be a combination of critical factors including trip time, payload mass fraction, power required, and number of thrusters.

In Figure A.6 through Figure A.8 we see that for LEO-GEO transfers, Hall thrusters deliver a higher maximum payload fraction than ion engines. This is driven by the fact that ion engine systems have a lower overall specific power compared to Hall thruster systems. From EQN A.6, we see that this gives a higher power system mass to propellant mass ratio, resulting in a lower payload fraction from EQN A.3. The major factor driving the overall specific power differential is the lower specific power of the ion engine itself. This is clearly seen from Figure A.3. A secondary effect is the lower power per thruster for the ion engine (as seen from Figure A.1), resulting in ion engine power processing units having lower specific powers, from Figure A.4, for similar specific impulses. Comparing Figure A.6 through Figure A.8, we note that increasing trip time decreases the differential between Hall thrusters and ion engines. The decrease results from EQN A.6, where increasing trip time lessens the overall effect of specific power on payload fraction.

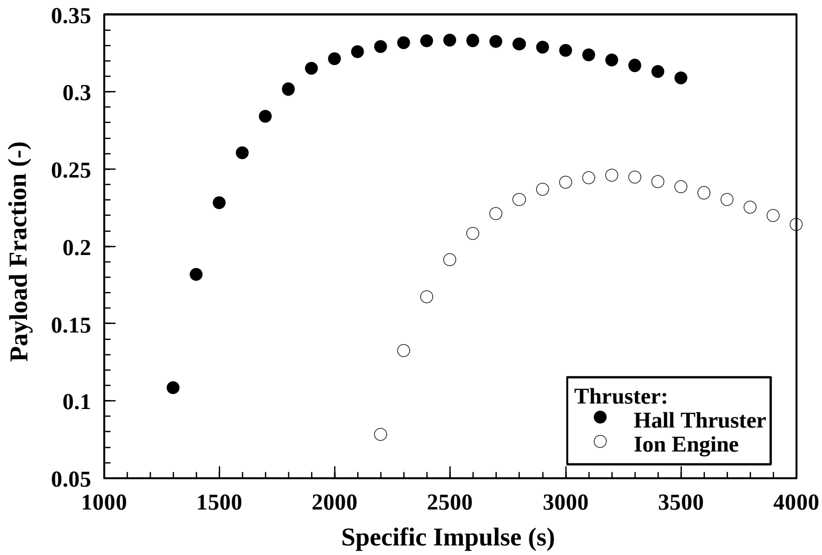

Figure A.6. Payload Mass Fraction versus Specific Impulse, Trip Time = 180 Days

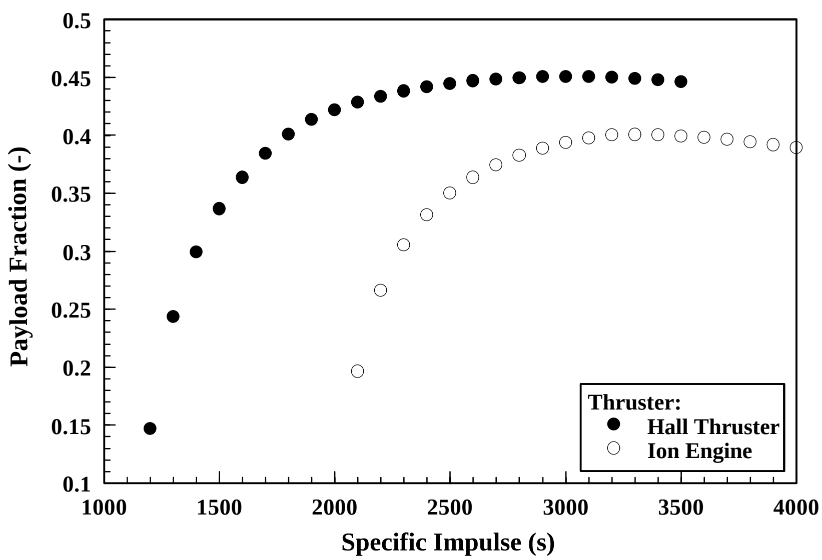

Figure A.7. Payload Mass Fraction versus Specific Impulse, Trip Time = 270 Days

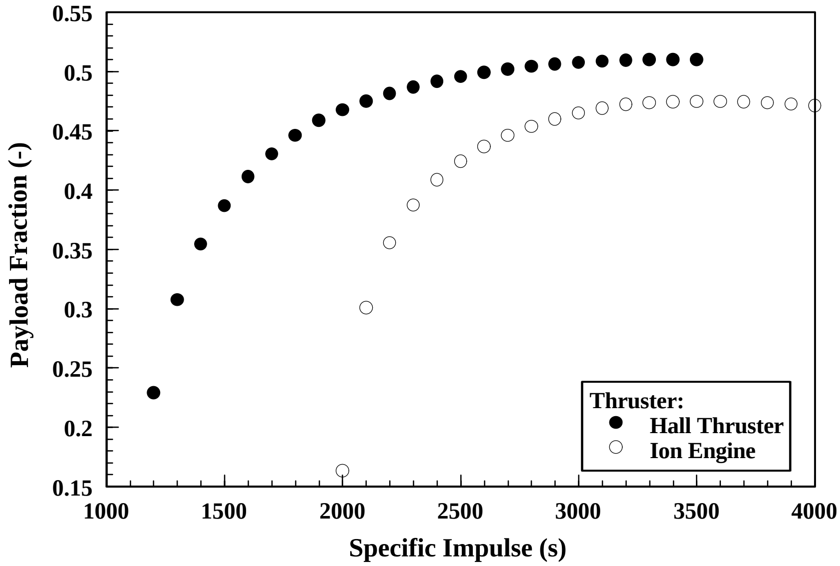

Figure A.8. Payload Mass Fraction versus Specific Impulse, Trip Time = 360 Days

Figure A.8 shows a peak in the payload fraction. This peak occurs for all trip times, but as trip time is increased, it occurs at progressively higher specific impulses. The peak can be explained as follows. As specific impulse is increased, we see from EQN A.4 that the propellant fraction decreases. Looking at the power mass/propellant mass term in EQN A.6, we see that the numerator increases with the square of the specific impulse. The terms in the denominator dependent on the specific impulse, the specific power and the thruster efficiency, also increase with specific impulse, but not as rapidly as the numerator (except at low specific impulses, where the efficiency term as seen in Figure A.2 increases rapidly). Thus, the power mass/propellant mass term increases with increasing specific impulse. As specific impulse is increased, the increasing power mass/propellant mass term is countered by the decreasing propellant mass fraction in EQN A.3, resulting in the initial rise in payload fraction versus specific impulse that we see in Figure A.6. However, we note from EQN A.4 that the rate of decrease of the propellant fraction slows with increasing specific impulse. Therefore, eventually the increase in power mass/propellant mass will overcome decreases in propellant fraction, resulting in the eventual decrease in payload fraction that is also observed in Figure A.6. To summarize, increases in power system mass fraction with increasing specific impulse begin to dominate the system, eliminating room for payload.

Next, we look at required power versus specific impulse as shown in Figure A.9 through Figure A.11.

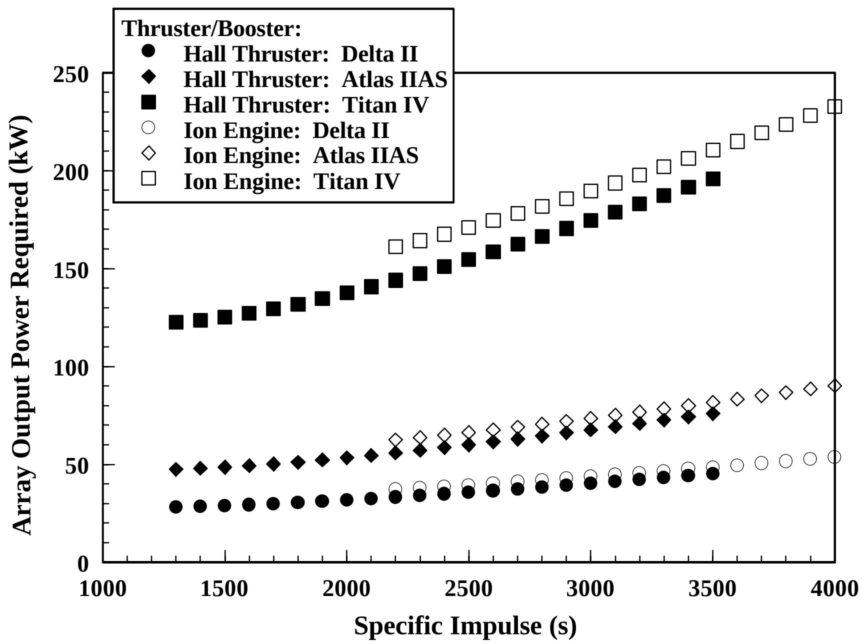

Figure A.9. Required Power versus Specific Impulse, Trip Time = 180 Days

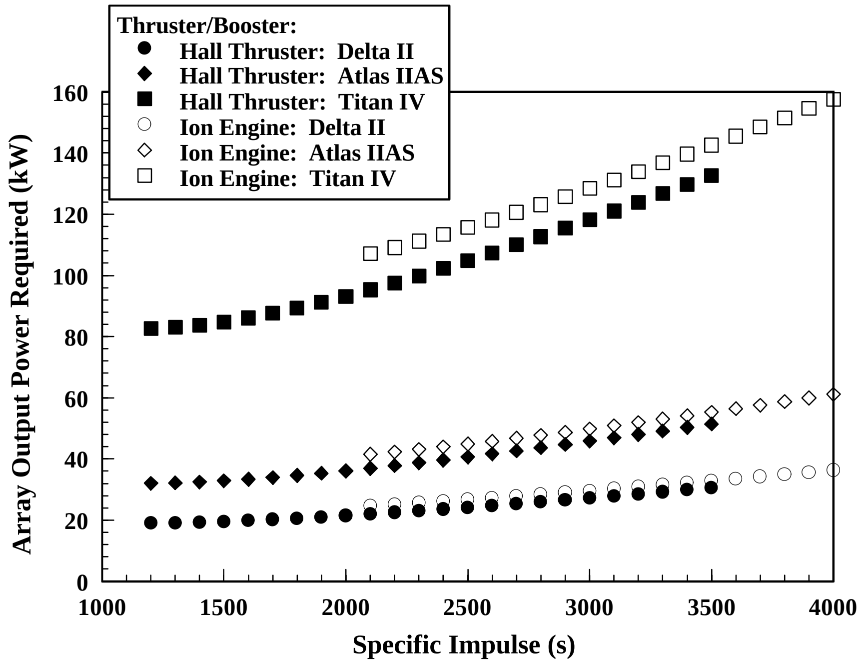

Figure A.10. Required Power versus Specific Impulse, Trip Time = 270 Days

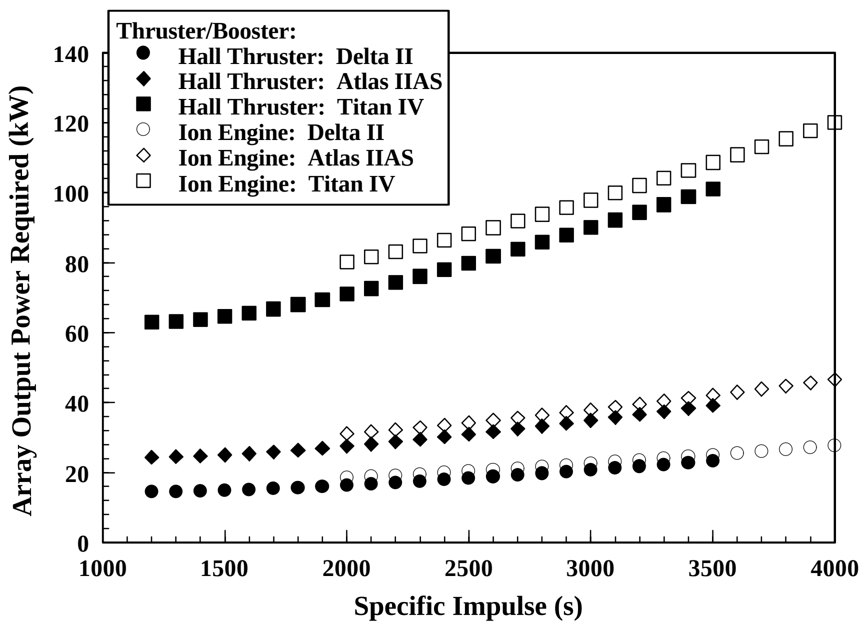

Figure A.11. Required Power versus Specific Impulse, Trip Time = 360 Days

For a given specific impulse, trip time, and payload the power levels are very similar between Hall thruster and ion engine systems, as expected from EQN A.10, since the only differences are the thruster and power processing unit efficiencies. However, when comparing power levels for equal payload fractions, Hall thruster systems require significantly lower power. Given projected trends in GEO satellite power levels, it appears from Figure A.9 through Figure A.11 that transfers of Delta II and Atlas IIAS payloads with trip times in the 270 to 360 day range should be feasible within the next 15 years. However, it appears that transfers of Titan IV class payloads will be impractical for some time to come.

Next, we look at the number of thrusters, operating at nominal conditions, necessary to accomplish the orbit transfer. From Figure A.9 through Figure A.11, we see that the total power for a mission goes up with increasing specific impulse. However, examining Figure A.1, we see that the power capacity per thruster also increases, and at a higher rate. Therefore, the number of thrusters, determined by dividing the total power by the power per thruster, decreases with increasing specific impulse. For redundancy purposes, we never consider fewer than two thrusters.

From Figure A.12 through Figure A.14, we note that at lower specific impulses an impractical number of thrusters is required. As specific impulse is increased, the number of Hall thrusters necessary drops to realistic levels (less than 10) in all cases. Ion engines, however, only reach the ten thruster cutoff for the 270 and 360 day Delta II missions and the 360 day Atlas IIAS missions. The Titan IV mission does not appear in Figure A.12 and Figure A.13 since the minimum number of ion engines is 50 and 32 respectively. Ion engine systems require higher power and, more importantly, ion engines increase in power capacity per thruster more slowly than Hall thrusters, as can be seen from Figure A.1.

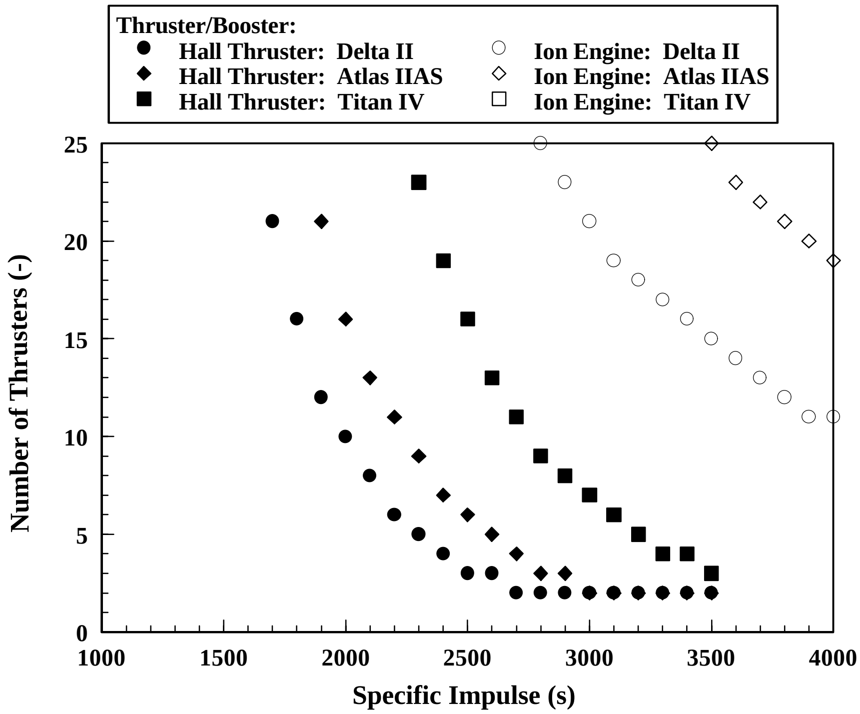

Figure A.12. Number of Thrusters versus Specific Impulse, Trip Time = 180 Days

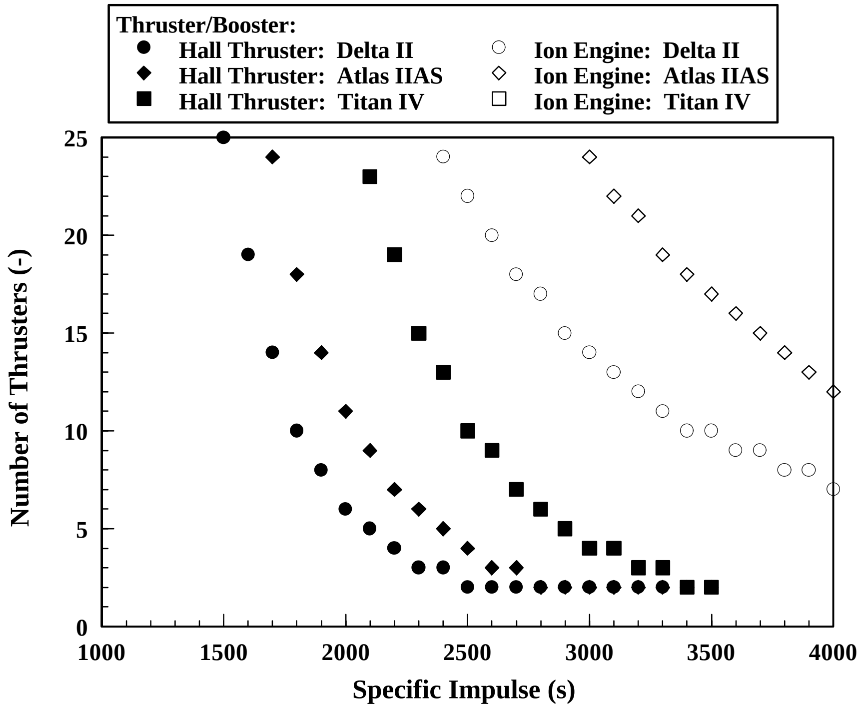

Figure A.13. Number of Thrusters versus Specific Impulse, Trip Time = 270 Days

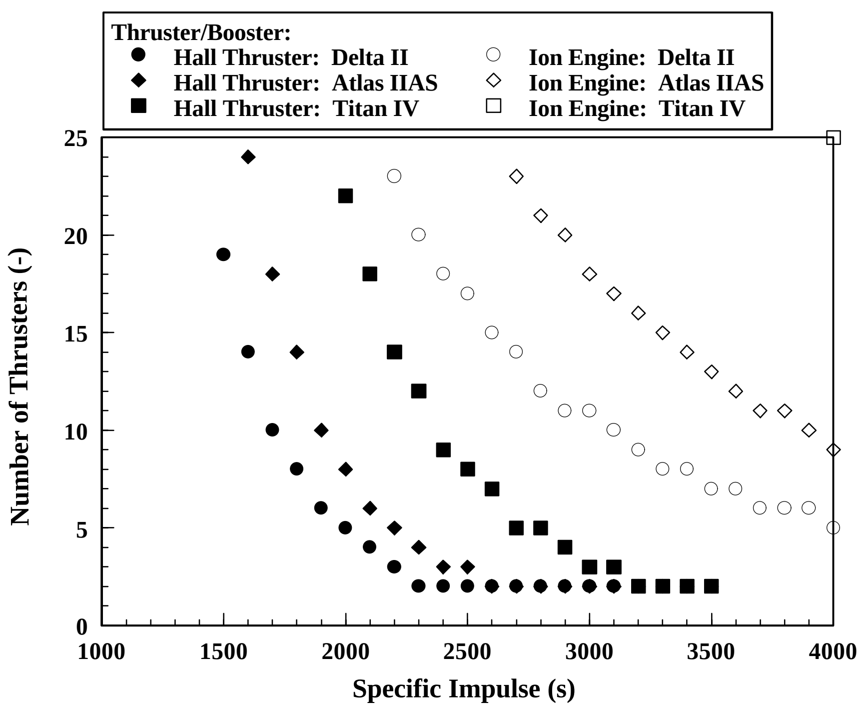

Figure A.14. Number of Thrusters versus Specific Impulse, Trip Time = 360 Days

Faring volumetric constraints of the propulsion system are anticipated to be another major concern of satellite manufacturers. LEO-GEO transfers require a large number of present generation thrusters. For example, a Delta II launch with an 180 day trip time delivers maximum payload using three 210 mm (approximate) Hall thrusters operating at 2500 s specific impulse and 35.6 kW of total power. This results in a total thruster area of approximately 0.26 m^2. By comparison, maximum payload for an ion engine system is obtained from eighteen thrusters (30 cm diameter), operating at 3200 s specific impulse and 45.5 kW total power. This is 3.16 m^2 of thruster area, or over twelve times the area of a Hall thruster system. A more practical system would probably have four larger ion thrusters, of approximately 64 cm each (the equivalent grid area of the eighteen smaller thrusters), however these larger thrusters may have significantly different operating conditions.

It appears in general that Hall thrusters are the best choice for LEO-GEO transfers. Ignoring Titan IV payloads, Hall thrusters in the specific impulse range of 2000 to 3000 s can deliver high payload fractions at power levels that are consistent with future trends for GEO satellites, and can do so with a realistic number of thrusters.

The true benefit of electric propulsion becomes even clearer when it is compared to chemical propulsion systems. Looking at the maximum payload deliverable to GEO and payload fraction for the Hall thruster cases examined and for all chemical systems in Table A.5, we see large increases in payload capacity. This increase in payload capacity gives three major benefits. First, and most obvious, it permits increases in useful payload delivered to orbit. This increased payload could result in increased satellite hardware or additional propellant for station-keeping to lengthen the life of the satellite. Second, increases in payload capacity will relax constraints on satellite design, allowing greater flexibility. Third, and perhaps most importantly, it allows for launch vehicle downsizing in some cases, as can be seen for 270 and 360 day transfers for the Delta II compared to the chemical Atlas IIAS. The obvious deterrent to these systems is the trip time required.

System	Delta II	Atlas IIAS	Titan IV
Chemical[74]	900 kg: 18.3%	2100 kg: 22.6%	4550 kg: 21.5%
180 Day EP: 33.3%	1637 kg	2766 kg	7047 kg
270 Day EP: 45.0%	2214 kg	3739 kg	9528 kg
360 Day EP: 51.0%	2506 kg	4232 kg	10784 kg

Table A.5. Chemical and Electric Propulsion GEO Masses, with Payload Fraction

LEO Constellations:

The second case is representative of transfers needed for LEO constellations. The particular case studied here is a space based observation system. It is based on the use of a large constellation (1148 satellites) in a Walker orbit at an altitude of 500 miles for theater level reconnaissance as discussed by Fiedler and Preiss.[76] Though this concept was not recommended in their study due to the cost of such a large number of satellites, the operating parameters nevertheless provide an excellent reference point for other potential LEO satellite constellations. For this case, we use a DV of 276.8 m/s, which is the DV from 162 to 500 miles. This mission DV does not include any inclination change or repositioning during the satellite's lifetime. Here, trip times of 180, 90, and 30 days are considered using each of the three launch vehicles.

There are two other parameter changes for this mission. The first is that since these satellites will be operating in a much more radiationally intense orbit than geosynchronous satellites, the radiation protection fraction, f_{rp} (the mass of the radiation shielding necessary to protect the payload, expressed in terms of the mass of the payload), is set to 0.20 as compared to 0.03 to 0.06 for the LEO-GEO case. Second, the average power fraction is maintained at the 180 day level, which is 0.97 for all missions. The parameters used are summarized in Table A.4.

In proceeding to the analysis of LEO constellations, we note that the same quantities are of interest as for the LEO-GEO transfer case.

Looking at Figure A.15, we see that for 180 day trip times, Hall thrusters and ion engines are nearly equal with regard to payload fraction. As trip time is decreases, we note from Figure A.16 and Figure A.17 that the Hall thruster delivers a higher payload fraction. The reasons for this behavior is the same as in the LEO to GEO case. The higher payload fractions compared to Figure A.6 result from reductions in propellant fraction at the lower *DV*. For Hall thrusters of higher than 1500 s specific impulse, payload fractions greater than 0.65 can be achieved at trip times as short as 30 days, assuming adequate power is available.

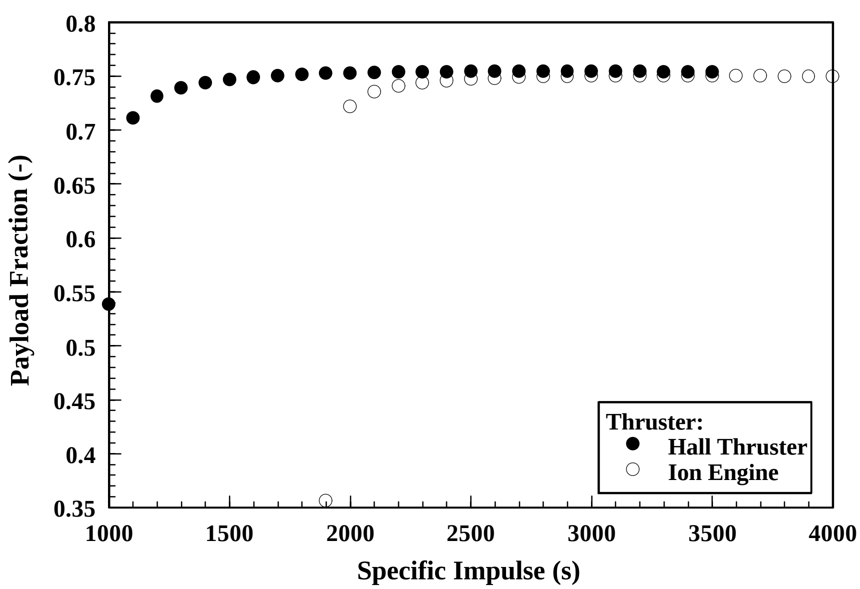

Figure A.15. Payload Mass Fraction versus Specific Impulse, Trip Time = 180 Days

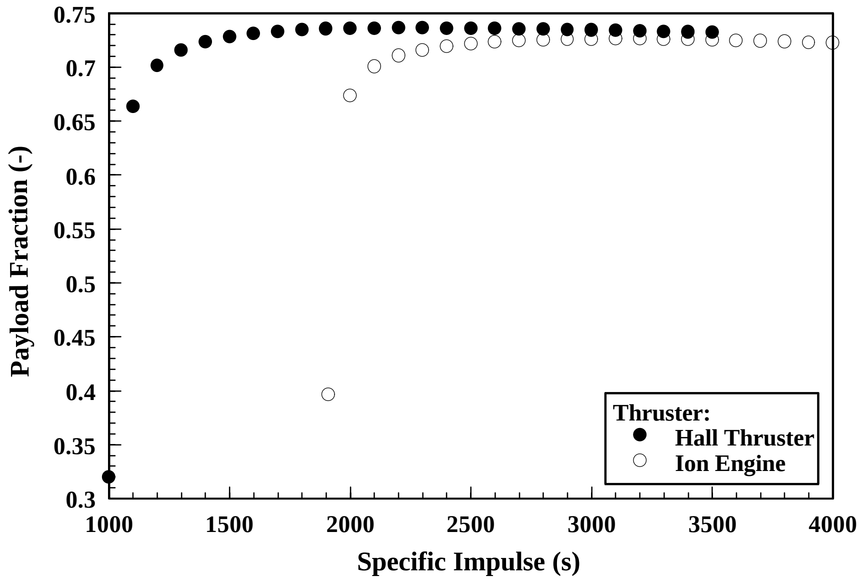

Figure A.16. Payload Mass Fraction versus Specific Impulse, Trip Time = 90 Days

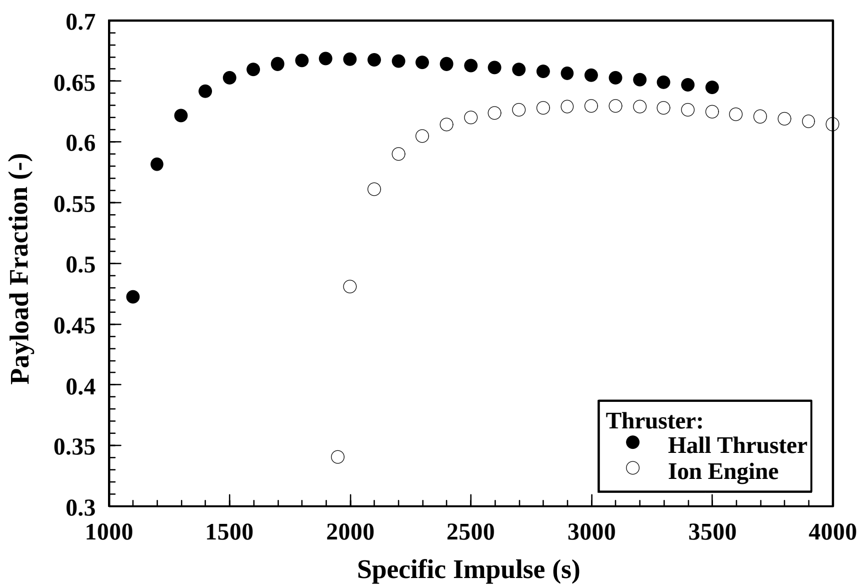

Figure A.17. Payload Mass Fraction versus Specific Impulse, Trip Time = 30 Days

Examining the power requirements for LEO constellation transit shown in Figure A.18 through Figure A.20, we see that they are much lower than those for LEO-GEO transfers with the same initial mass. However, given the lower power levels expected for LEO constellations, Atlas transfers of 30 days and Titan transfers of 90 days appear to be at the upper boundary of what is likely to be possible in the next 10 to 15 years.

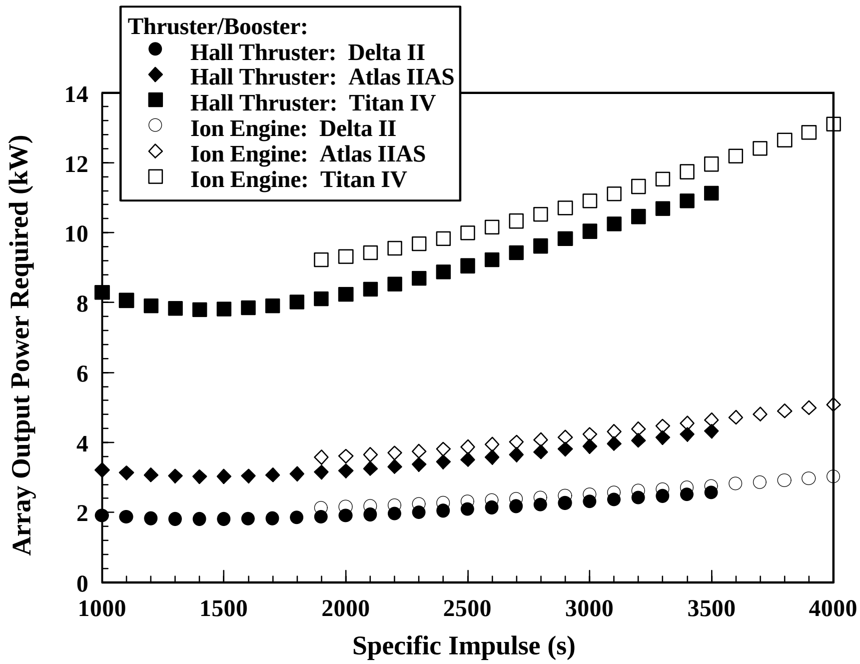

Figure A.18. Required Power versus Specific Impulse, Trip Time = 180 Days

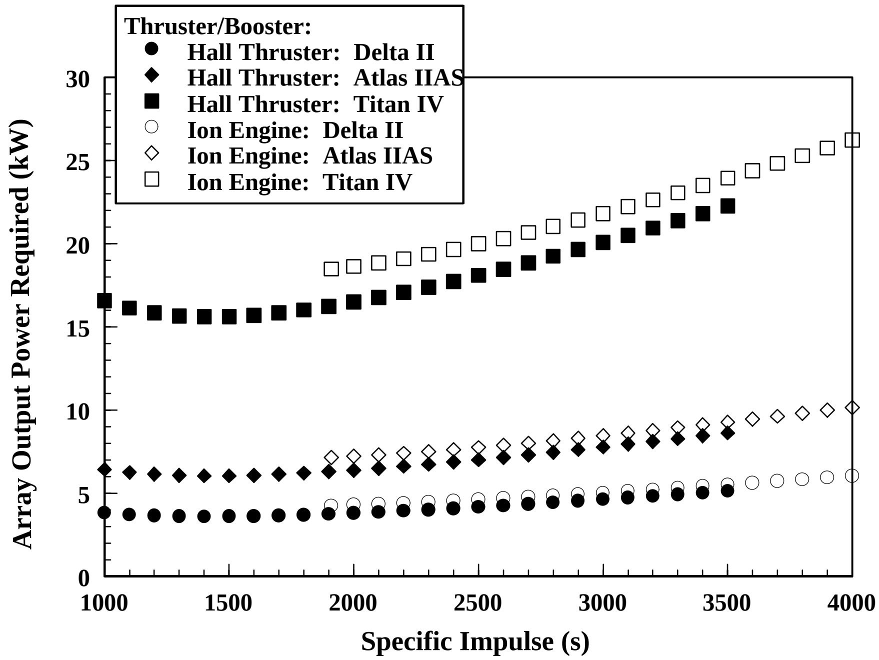

Figure A.19. Required Power versus Specific Impulse, Trip Time = 90 Days

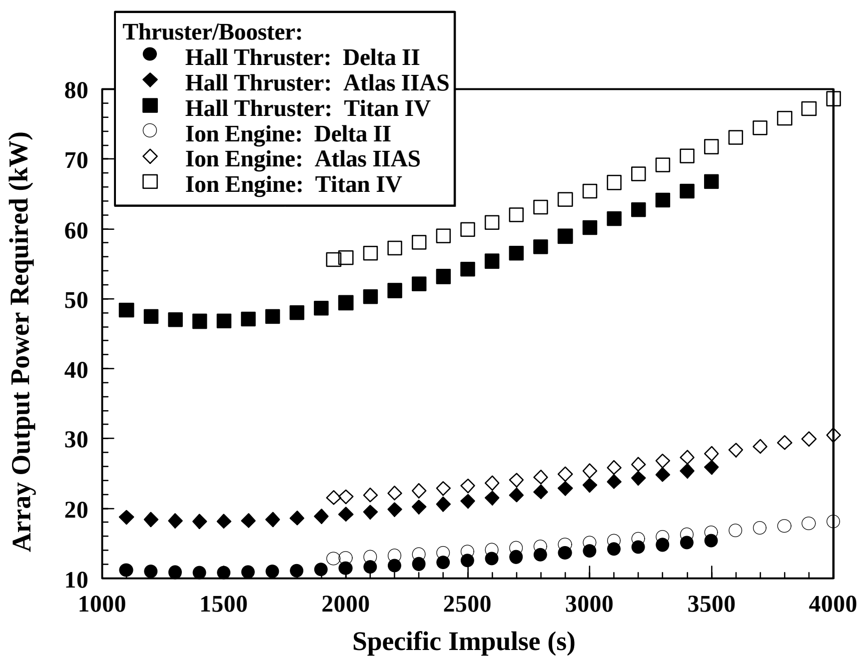

Figure A.20. Required Power versus Specific Impulse, Trip Time = 30 Days

The number of thrusters reduces similarly to the LEO-GEO case, but due to the smaller amount of thrust necessary, there are fewer needed. The only case where a system with fewer than 10 thrusters is not possible is the 30 day transfer of a Titan IV class payload using ion engines.

Orbit Topping:

One of the most intriguing applications of electric propulsion is orbit topping. Proposed by Free[77] and further studied by Oleson, et al.[75] and Spitzer,[78] the concept involves performing an initial portion of a LEO-GEO transfer using chemical propulsion, with the final GEO insertion done using electric propulsion. The primary advantage of this approach is that it allows a significant propellant mass savings over an all-chemical transfer without the long trip times of an all-electric transfer, which translates into a payload increase.

In the work of Oleson, et al., the SECKSPOT orbit transfer code was used to optimize a launch using an Atlas IIAS with a Centaur impulsive chemical stage. A combination of on-board chemical propulsion and electric propulsion is then used to insert the satellite into a geostationary orbit. In their study, the amount of on board chemical *DV* was decreased incrementally while the amount of electric propulsion *DV* was increased (the Centaur stage is the same in all cases). They considered several thrusters (arcjets, Hall thrusters, and ion engines) and two power levels, and found that the *DV*s for the transfer were approximately the same for all cases. The study indicated that the greatest mass gains could be made using an ion engine (2.5 kW NSTAR), with a stationary plasma thruster (1.5 kW SPT-100) coming in close behind. It was noted in Reference 75, however, that a more appropriately powered SPT (2.5 kW) may have increased benefits.

In our study, thrusters of equal power levels were compared against each other. Power levels up to 5 kW per thruster were studied here, compared to 1.5 kW Hall thrusters and 2.5 kW ion engines examined by Oleson, et al. The higher specific power devices investigated in this paper illustrate even greater advantages for electric propulsion orbit topping than those shown by Oleson, et al.

Using the electric propulsion starting conditions from the work of Oleson, et al., side-by-side comparisons of Hall thrusters and ion engines operating at 1.66, 2.5, and 5.0 kW were made for missions with 10 and 15 kW of total power. These total power levels determine the number of thrusters used for each case. Operating conditions were the same as the standard LEO-GEO transfer, with *DV* based on the SECKSPOT calculated orbits. The trip time and payload are calculated by decreasing trip time until the mission power level is reached. Array degradation was determined through the average power fraction, f_{ave} which was maintained at 0.97 for trip times of under 180 days and increased for trip times greater than 180 days using the same form as for LEO-GEO transfers. These fractions are summarized in Table A.4.

Since power and number of thrusters are a given for orbit topping, the only pertinent results are payload and cost. Data is presented in the same way as Oleson, et al., with final mass plotted versus trip time in Figure A.21 and Figure A.22. Final mass is defined as useful on-orbit mass including payload, power systems, structure, and attitude control. It also includes a mass penalty for array degradation (i.e., 1-f_{ave} multiplied by the mass of the array). Each data point represents an individual *DV* case.

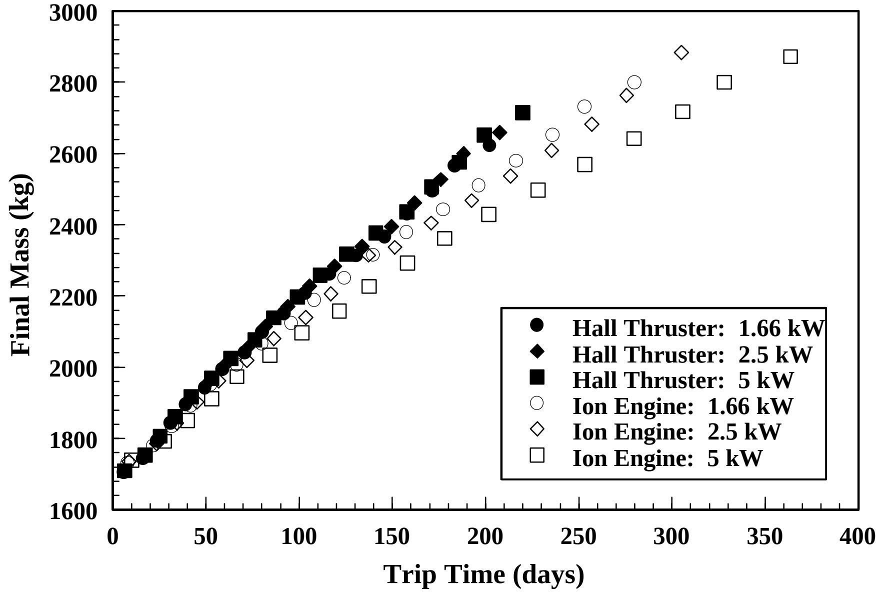

Figure A.21. Final Mass versus Trip Time, Power = 10 kW

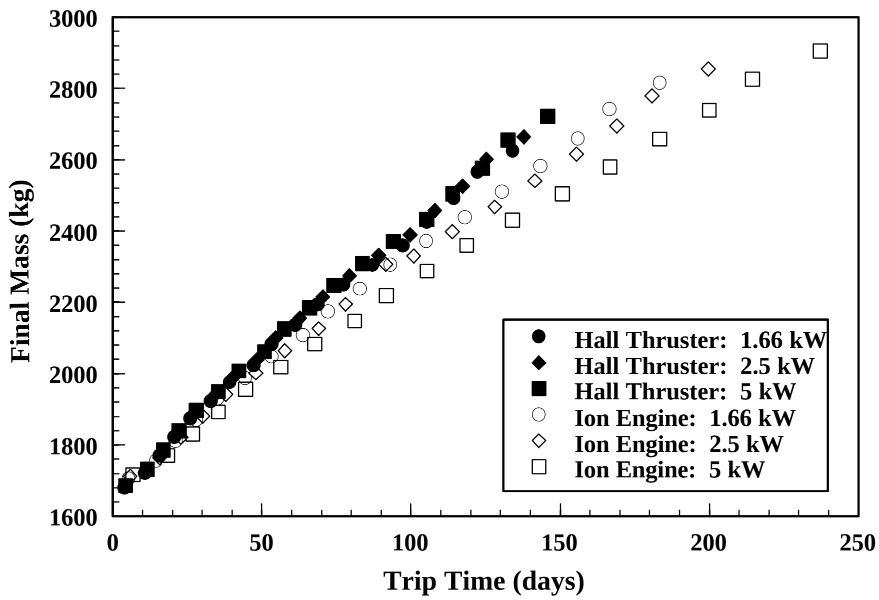

Figure A.22. Final Mass versus Trip Time, Power = 15 kW

The orbit topping scenario is power limited by fixing the amount of power available for the propulsion system. This differs from the two previous cases which were trip-time limited. By allowing trip time to vary, we see from Figure A.21 and Figure

A.22 that for a given amount of *DV*, ion engines can deliver more payload from the intermediate orbit to GEO, however they require more time to do so. The additional payload and longer trip time results from the fact that at a given input power, the ion engine has a higher specific impulse. From EQN A.4 and other basic rocket equations, we see that the higher specific impulse results in lower propellant mass (and thus higher payload mass) and longer trip times. Additionally, in both Figure A.21 and Figure A.22, there is a much larger spread between the power levels for the various ion engines than for the Hall thrusters. This spread is due to the larger increase in specific impulse in going from a 1.66 kW ion engine to a 5 kW ion engine, compared to the same change in power level for the Hall thrusters. Increasing power from 10 kW to 15 kW does not significantly affect the final mass delivered, but it does reduce trip time by approximately 33%.

We note that for trip times on the order of satellite check-out periods (~30 days) payload gains of over 100 kg can be achieved. For comparison, Oleson, et al. calculated that a system using all chemical propulsion for orbit transfer would have a mass of 1723 kg if it used SPTs for North-South Station Keeping (NSSK) and 1748 kg using ion engines.

The choice of thruster type for this mission will depend on the requirements of the user. For minimum trip time on a given mission (*DV* case), 1.66 kW SPTs or other low specific impulse Hall thrusters would be the best choice. However, if the user wants to maximize payload for a given mission, 5 kW or higher power ion engines would be the best thruster.

Reusable Orbit Transfer Vehicles:

The final mission examined in this study is a reusable orbit transfer vehicle (ROTV). The particular concept for ROTV studied in this paper is a modification of that proposed as part of a recent US Air Force study.[79] In that concept, there were two modules: a reusable power system composed of the solar arrays, bus, and docking module; and an expendable propulsion system - launched with the payload - comprised of thrusters (arcjets, resistojets, or ion engines), propellant tank, and power processing unit. In our study, the thrusters were changed to either Hall thrusters or ion engines, and the power processing unit was moved to the power system along with the thermal radiator.

For this study, it is assumed that the propulsion system/payload is launched on a Delta II, using the full payload capability. The power system is also launched on a Delta II, but due to the mass breakdowns of the system, the payload capacity of the second Delta II will not necessarily be used by the power system (the unused payload capability can be used in some cases for a second power system module, or for auxiliary payloads). The actual mass launched on the second Delta II is determined as a function of the trip time and the specific impulse of the thruster used.

The thrusters examined are Hall thrusters with specific impulses of 1600, 1900, 2200, and 2500 seconds and corresponding power levels from Figure A.1. The corresponding ion engine specific impulses were determined by matching the thruster input powers to those of the Hall thrusters.

Missions where the power system is used for up to five complete transfers from LEO to GEO and back were studied. Initial trip times of 180, 270, and 360 days each way were examined. Subsequent transfers will take more time due to solar array degradation.

The parameters for this mission are summarized in Table A.4. There are two differences between the ROTV and standard LEO-GEO transfer. First, due to the requirement of on-orbit coupling and decoupling of the power and propulsion systems, the adapter mass must be increased. There are three docking modules necessary in this concept: one to separate the payload and one each on the power system and propulsion system to dock the two together. It is assumed that each module comprises 5% of the total vehicle mass. This raises the primary structure fraction to 0.20 as compared to 0.06 for the other missions examined. Additionally, since the power system makes multiple trips through the Van Allen belts, the array degradation is cumulative. Therefore, f_{ave} is determined by multiplying the individual transfer power fractions (f_{avei}).

For the reusable orbit transfer scenario, the initial masses were computed by determining the mass breakout of the system between the expendable payload and propulsion system and the reusable power system. The ratio of expendable component mass to reusable component mass was lower for the ion engine than for the Hall thruster. Since it was assumed that the expendable/payload launcher is a full capacity Delta II, this results in a more massive reusable power system for the ion engine and thus a larger overall starting mass in LEO.

The mass transported to GEO includes both the satellite payload and the propellant for the return trip. Satellite payload fractions are shown in Table A.6 for the thruster configurations studied, both Hall thrusters and ion engines. These fractions represent the satellite payload mass (not including the propellant for the return trip), divided by the overall starting mass in LEO.

Thruster	Initial Trip Time (days)	Satellite Mass Percentage
Hall Thrusters		
1600 s, 1.04 kW	180	---
	270	3.56 %
	360	10.5 %
1900 s, 2.45 kW	180	---
	270	12.5 %
	360	18.7 %
2200 s, 5.08 kW	180	2.95 %
	270	16.6 %
	360	22.9 %
2500 s, 9.59 kW	180	5.09 %
	270	19.1 %
	360	25.7 %
Ion Engines		
1930 s, 1.04 kW	180	---
	270	---
	360	1.22 %
3195 s, 2.45 kW	180	---
	270	17.3 %
	360	25.7 %
4100 s, 5.08 kW	180	---
	270	18.2 %
	360	27.5 %
5092 s, 9.59 kW	180	---
	270	15.8 %
	360	26.5 %

Table A.6. ROTV Delivered Satellite Masses

Cases with no payload listed are ones for which the payload capacity was insufficient to transport enough fuel to return the ROTV in the specified trip time even with zero payload.

The other critical parameter is the power required for these cases. Due to solar array degradation, the available power will be highest for the first transit; subsequent trips will have less power available. Since payload is considered constant, the trip time must therefore increase for subsequent round trips. The initial power required is shown in Table A.7 and the trip time increase is shown in Figure A.23. (We note that for any given round trip, the downward leg can be made in the same amount of time or less than the upward, since the mass transported has been decreased by the mass of the payload and the fuel used in the upward trip. Therefore, the power required is lower. This analysis assumes that the downward trip time is the same as the upward leg.).

Thruster	Initial Trip Time (days)	Power Required
Hall Thrusters		
1600 s, 1.04 kW	180	---
	270	27.8 kW
	360	19.7 kW
1900 s, 2.45 kW	180	---
	270	29.1 kW
	360	20.7 kW
2200 s, 5.08 kW	180	55.3 kW
	270	31.7 kW
	360	22.4 kW
2500 s, 9.59 kW	180	61.8 kW
	270	34.8 kW
	360	24.5 kW
Ion Engines		
1930 s, 1.04 kW	180	---
	270	---
	360	25.3 kW
3195 s, 2.45 kW	180	---
	270	49.1 kW
	360	33.4 kW
4100 s, 5.08 kW	180	---
	270	64.4 kW
	360	42.6 kW
5092 s, 9.59 kW	180	---
	270	86.9 kW
	360	55.1 kW

Table A.7. ROTV First Transit Array Output Power

From Table A.6 we see that for equivalent thruster power and trip time, the ion engine delivers a higher satellite payload fraction than the Hall thrusters at high specific impulses. The overall mass fraction delivered to GEO (satellite plus return trip fuel) is lower for the ion engine, but since it operates at higher specific impulses it requires a lower propellant fraction for the return trip, allowing a higher satellite payload fraction. In Table A.7, we see that for equivalent cases the power required for the initial round trip is much higher for the ion engine than for the Hall thruster, due to their higher specific impulse and initial payload. Since the power per thruster is fixed, this means that ion engine systems will require more thrusters (assuming present day designs) than Hall thruster systems. Finally, from Figure A.23 we see that the trip time increase for subsequent transfers is more substantial for the Hall thruster than for the ion engine.

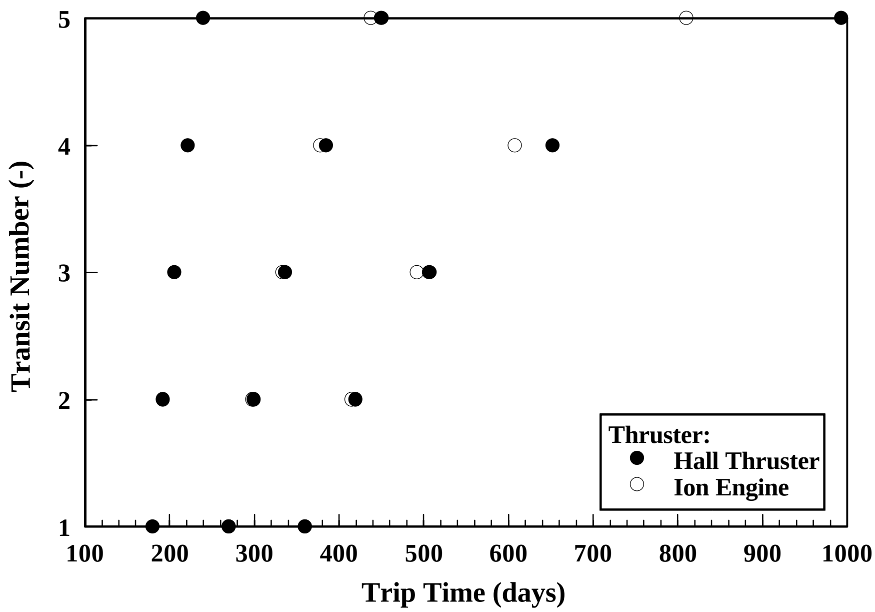

Figure A.23. ROTV Trip Times with Transit Number

Comparing the payload fraction data in Table A.6 to the standard LEO-GEO transfer as shown in Figure A.8, payload capability is less for ROTV's because of the need to carry propellant for the return trip. Figure A.23 shows that in spite of the use of highly resilient concentrator arrays, for initial trip times greater than 180 days, array degradation quickly drives the trip time to unacceptable levels for round trip number two and beyond.

CONCLUSIONS

The analysis in this study shows that if the trip time for a mission is fixed, then Hall thrusters can deliver higher payload fractions, due to their higher specific power. If, however, the power for a mission is fixed and trip time is allowed to vary, ion engines can deliver greater payload since they typically operate at higher specific impulses.

Examining all four missions and taking into account power and trip time requirements, the mission that seems most practical at this time would be orbit topping. Significant payload gains could be made for 10 or 15 kW systems with trip times of the order of 30 days, which is approximately the on-orbit check-out time for most satellites. Also practical in the near term would be small orbit transfers for LEO constellations, since they offer high payload fractions with short trip times.

A full, all electric propulsion, LEO-GEO transfer is practical using today's technology, as long as the user is willing to accept the long transfer times. However, by performing the shorter term orbit topping and LEO constellation type missions, the user can be introduced to the benefits of electric propulsion transfers without immediately suffering the large trip time penalties.

The same comments apply to an even greater extent to reusable orbit transfer vehicles. Though there can be payload benefits compared to chemical systems, the trip time penalties are much more severe than expendable LEO-GEO systems. Other issues to consider for ROTVs include: increased power requirement and logistical concerns (autonomous control is probably necessary for a practical system). These combine to make ROTVs the most long term of the missions examined here.

For all of these missions, there are concerns with regards to thruster size and payload faring volume. This is especially true for ion engine systems since they require a higher number of thrusters and ion engines are typically physically larger than Hall thrusters.

It is important to note that all of the analysis in the paper is based on the current generation of ion engines and Hall thrusters. Future thrusters that operate at higher specific powers and thruster power to specific impulse ratios, could increase system performance. Work has already been done in this area, such as the 50 cm and larger ion engines that have been tested by NASA[80,81] and Hall thruster designs such as the SPT-N series.[14] Advanced thrusters such as these also offer other improvements including higher efficiency and lower beam divergence.

Improvements in other areas can also improve electric propulsion capability. Solar array technology continues to improve, with increases in specific power and material density that will make performance improvements for both Hall thrusters and ion engine systems possible. Improvements in the cryogenic storage of xenon can benefit both types of thruster by reducing the tankage fraction.

ACKNOWLEDGEMENTS

The authors would like to thank Mr. Craig Claus of Atlantic Research Corporation and Mr. James Sovey of the NASA Lewis Research Center for their information about stationary plasma thruster and ion engine development respectively; Dr. J. Messerole from Boeing Defense and Space Group for his assistance with the analytical engine; and the other engineers and scientists of the Phillips Lab Electric Propulsion Laboratory for their input and suggestions.

APPENDIX B ***

ASSEMBLY DRAWINGS FOR UNIVERSITY OF MICHIGAN/UNITED STATES AIR FORCE P5 5 kW LABORATORY MODEL HALL THRUSTER

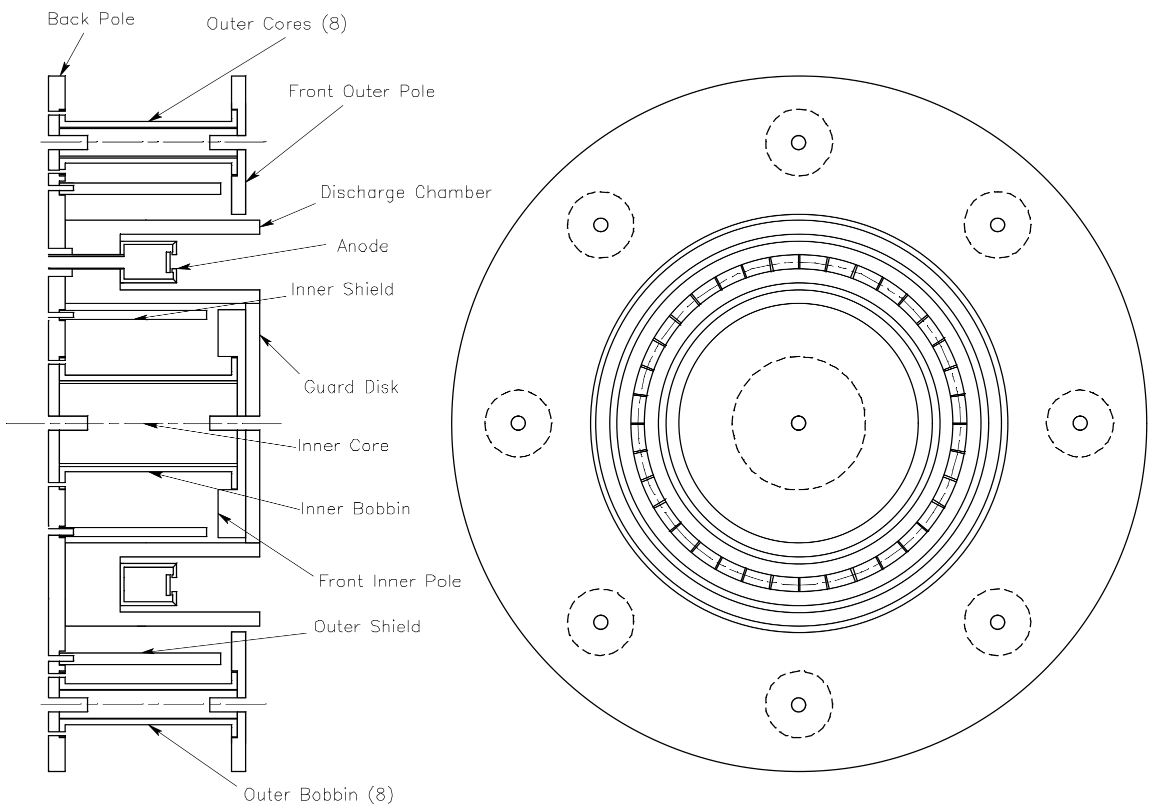

*** Note: Dimensions in this Appendix are presented in inches.

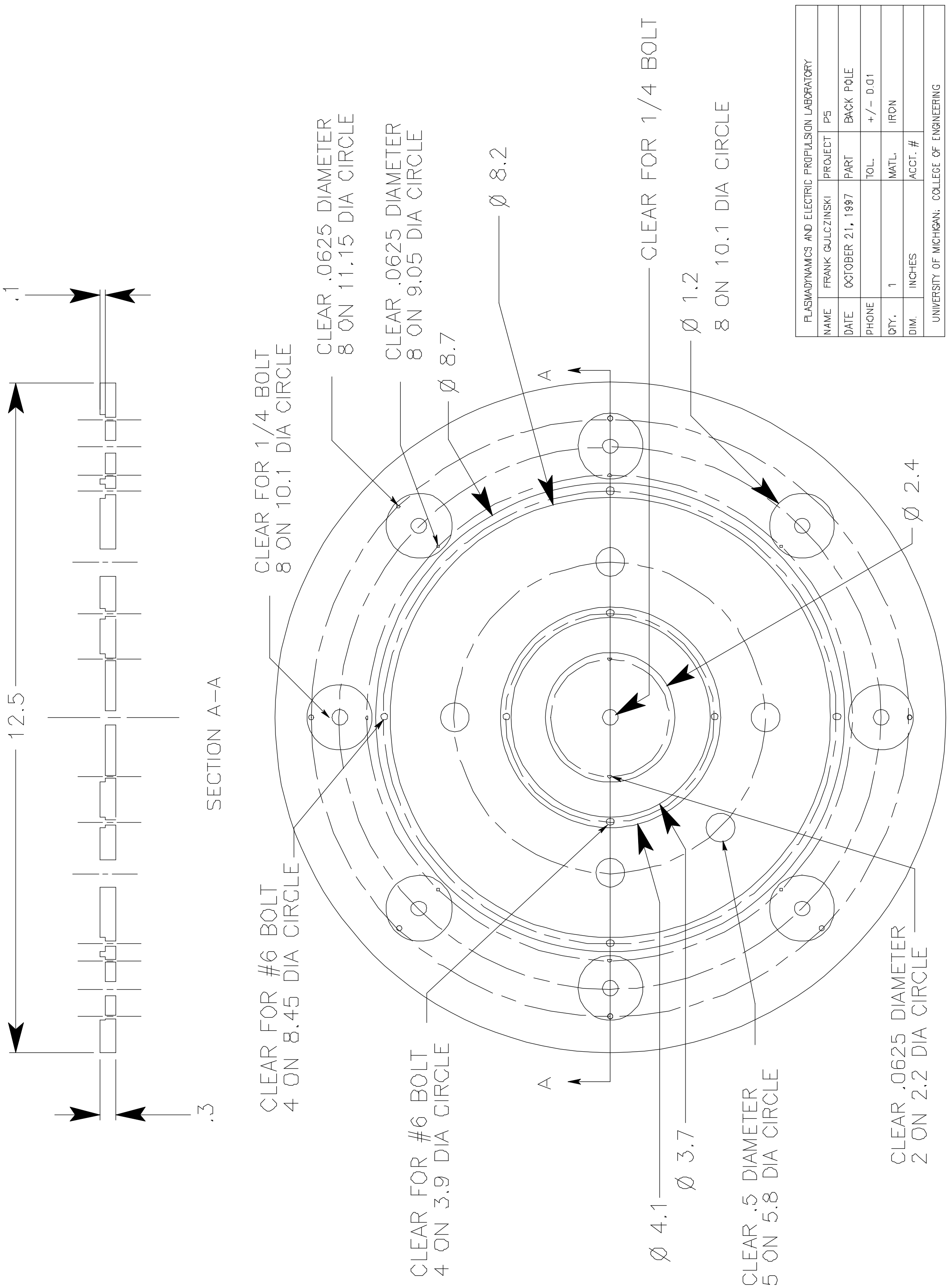
CLEAR FOR 1/4 BOLT
8 ON 10.1 DIA CIRCLE
CLEAR .0625 DIAMETER
8 ON 11.15 DIA CIRCLE
CLEAR .0625 DIAMETER
8 ON 9.05 DIA CIRCLE
Ø 8.7
Ø 8.2
CLEAR FOR 1/4 BOLT
Ø 1.2
8 ON 10.1 DIA CIRCLE
Ø 2.4
A
A
.1
12.5
.3
SECTION A-A
CLEAR FOR #6 BOLT
4 ON 8.45 DIA CIRCLE
CLEAR FOR #6 BOLT
4 ON 3.9 DIA CIRCLE
Ø 4.1
Ø 3.7
CLEAR .5 DIAMETER
5 ON 5.8 DIA CIRCLE
CLEAR .0625 DIAMETER
2 ON 2.2 DIA CIRCLE
PLASMADYNAMICS AND ELECTRIC PROPULSION LABORATORY
NAME FRANK GULCZINSKI PROJECT P5
DATE OCTOBER 21, 1997 PART BACK POLE
PHONE TOL. +/- 0.01
QTY. 1 MATL. IRON
DIM. INCHES ACCT. #
UNIVERSITY OF MICHIGAN, COLLEGE OF ENGINEERING

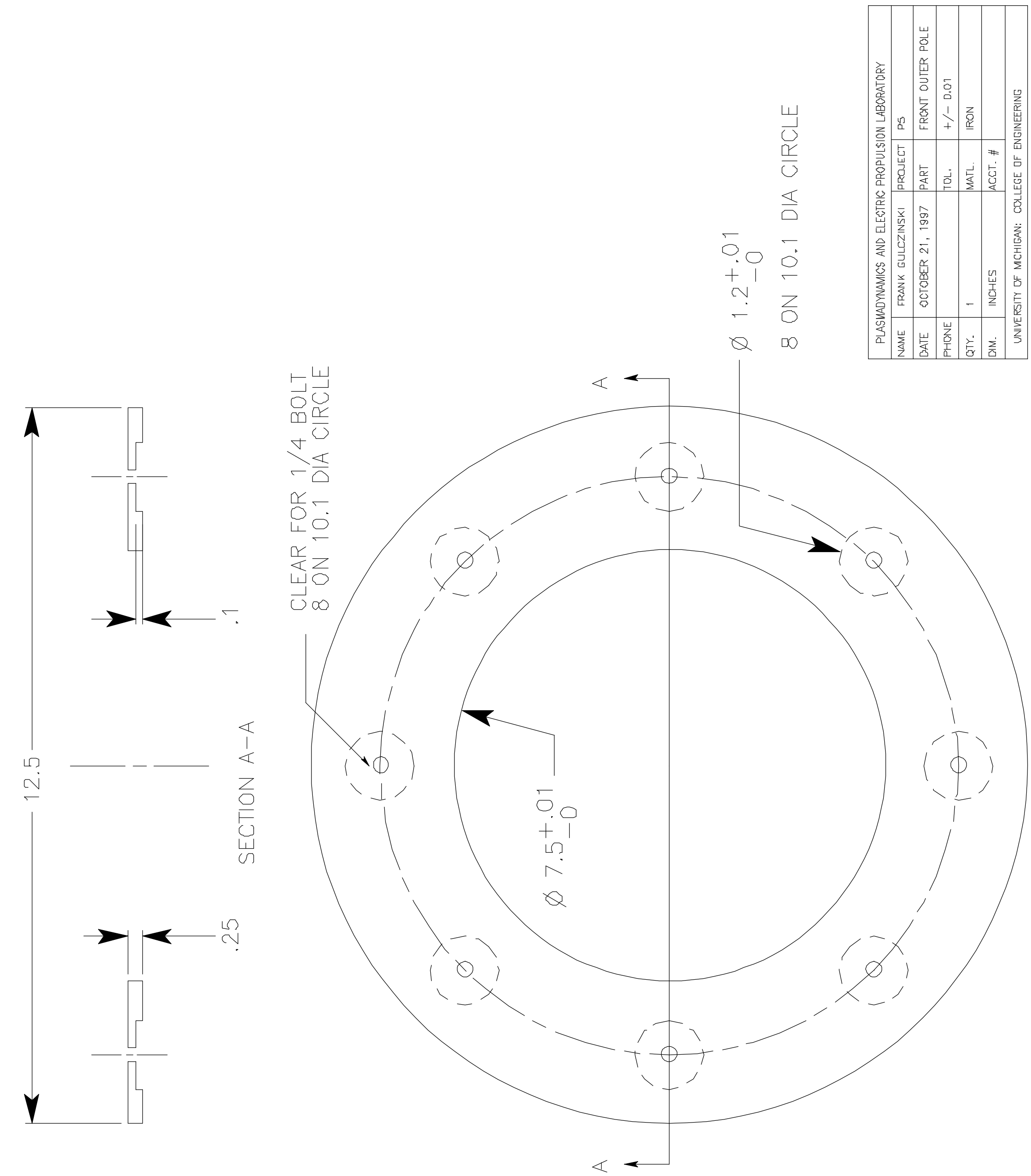
PLASMADYNAMICS AND ELECTRIC PROPULSION LABORATORY
NAME FRANK GULCZINSKI PROJECT P5
DATE OCTOBER 21, 1997 PART FRONT OUTER POLE
PHONE TOL. +/- 0.01
QTY. 1 MATL. IRON
DIM. INCHES ACCT. #
UNIVERSITY OF MICHIGAN: COLLEGE OF ENGINEERING
Ø 1.2 +.01 −0
8 ON 10.1 DIA CIRCLE
CLEAR FOR 1/4 BOLT
8 ON 10.1 DIA CIRCLE
Ø 7.5 +.01 −0
A
A
SECTION A-A
12.5
.1
.25

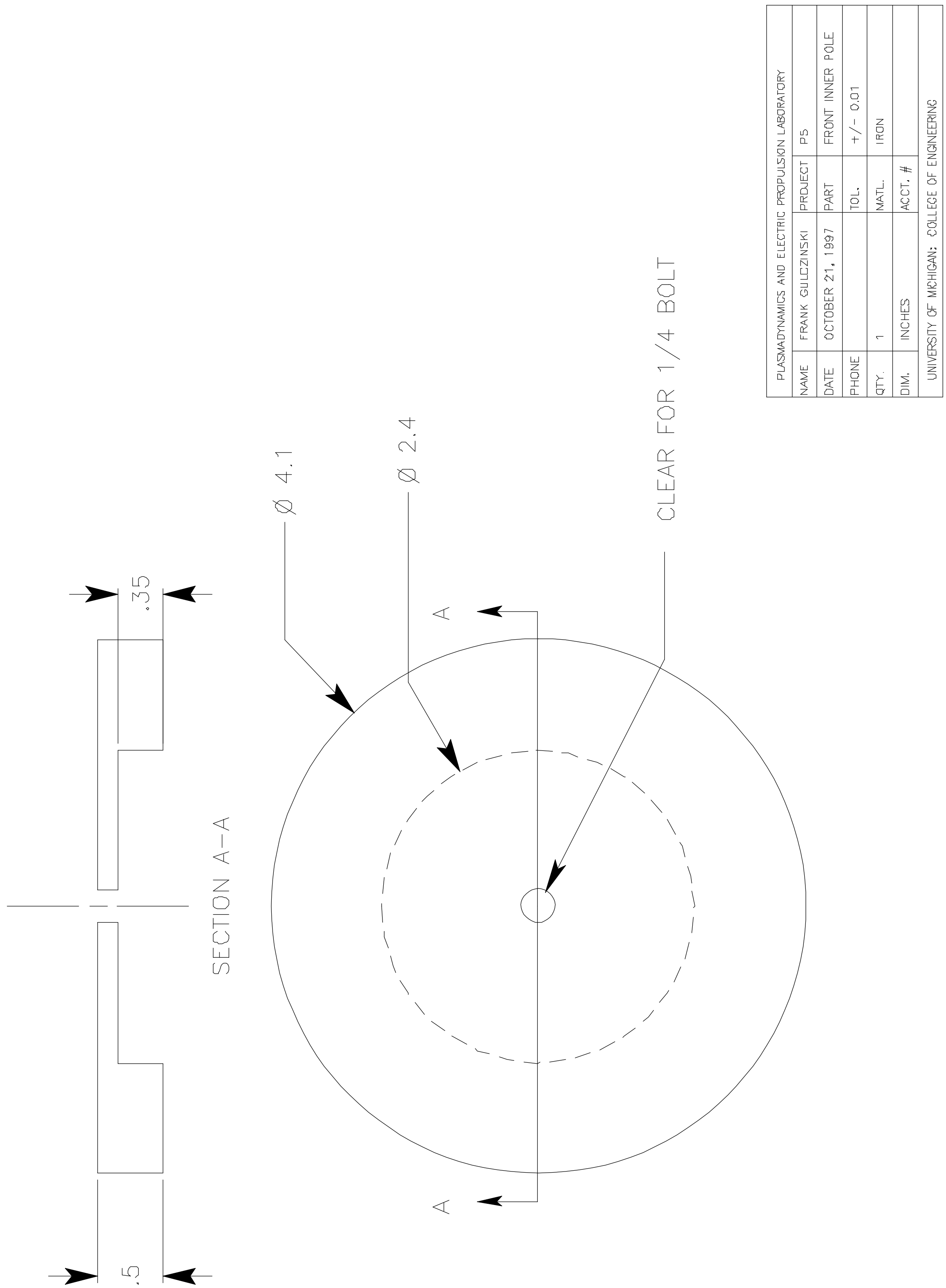
PLASMADYNAMICS AND ELECTRIC PROPULSION LABORATORY
NAME
FRANK GULCZINSKI
PROJECT
P5
DATE
OCTOBER 21, 1997
PART
FRONT INNER POLE
PHONE
TOL.
+/- 0.01
QTY.
1
MATL.
IRON
DIM.
INCHES
ACCT. #
UNIVERSITY OF MICHIGAN: COLLEGE OF ENGINEERING
CLEAR FOR 1/4 BOLT
Ø 2.4
Ø 4.1
A
A
.35
.5
SECTION A-A

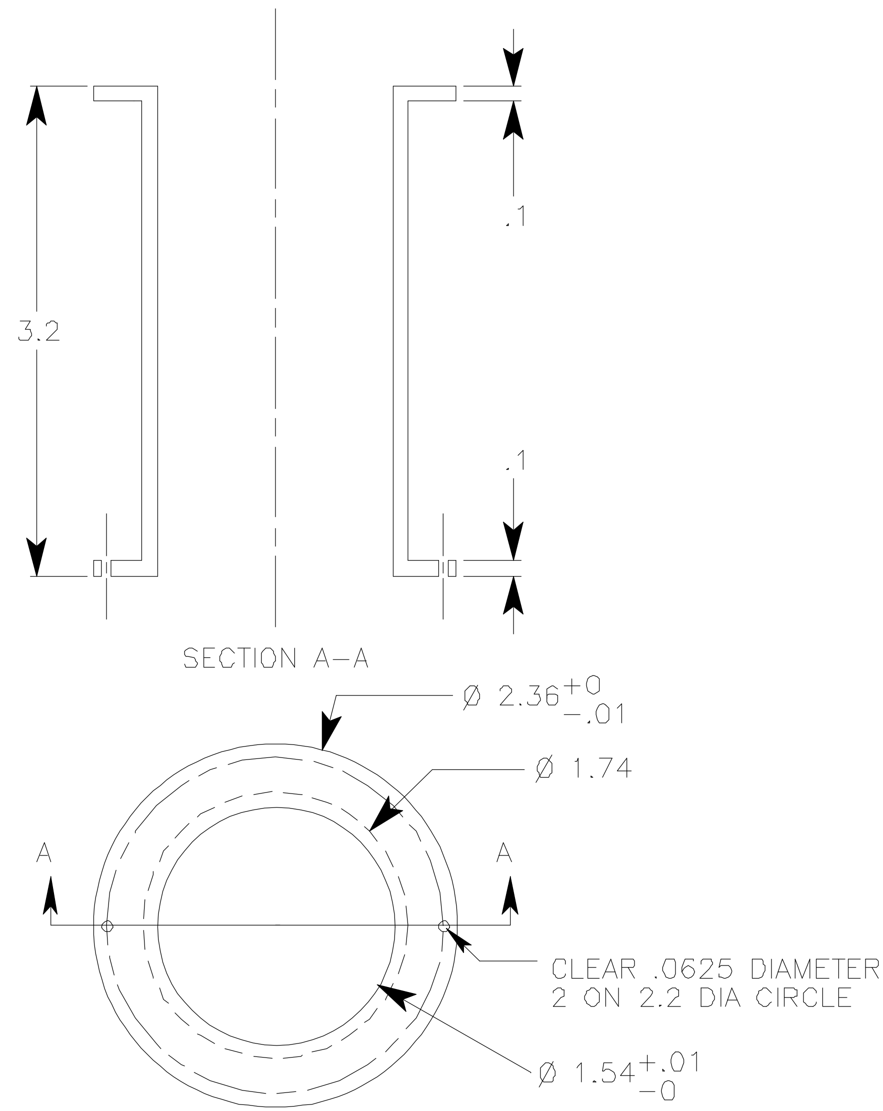

PLASMADYNAMICS AND ELECTRIC PROPULSION LABORATORY			
NAME	FRANK GULCZINSKI	PROJECT	P5
DATE	OCTOBER 21, 1997	PART	INNER BOBBIN
PHONE		TOL.	+/- 0.01
QTY.	1	MATL.	316 STAINLESS STEEL
DIM.	INCHES	ACCT. #	
UNIVERSITY OF MICHIGAN: COLLEGE OF ENGINEERING			

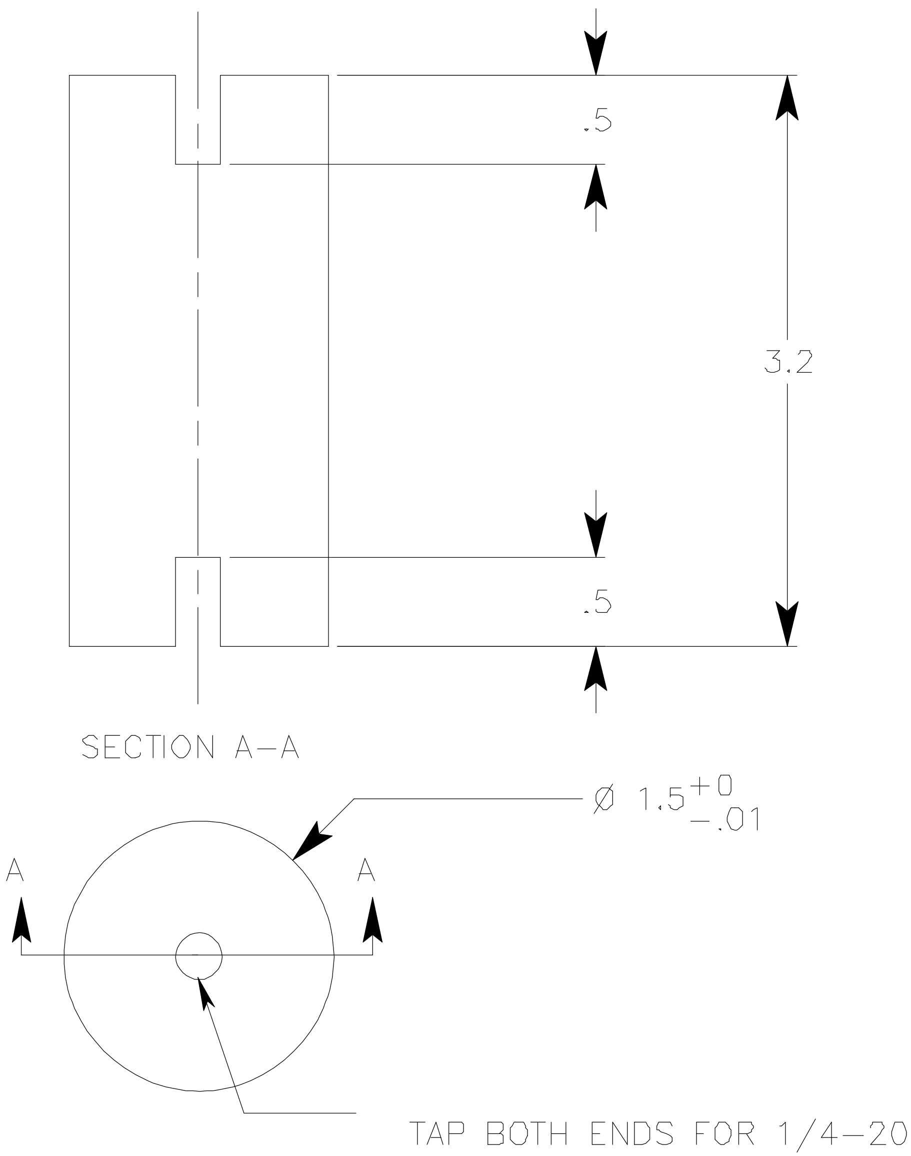

PLASMADYNAMICS AND ELECTRIC PROPULSION LABORATORY			
NAME	FRANK GULCZINSKI	PROJECT	P5
DATE	OCTOBER 21, 1997	PART	INNER CORE
PHONE		TOL.	+/– 0.01
QTY.	1	MATL.	IRON
DIM.	INCHES	ACCT. #	
UNIVERSITY OF MICHIGAN: COLLEGE OF ENGINEERING			

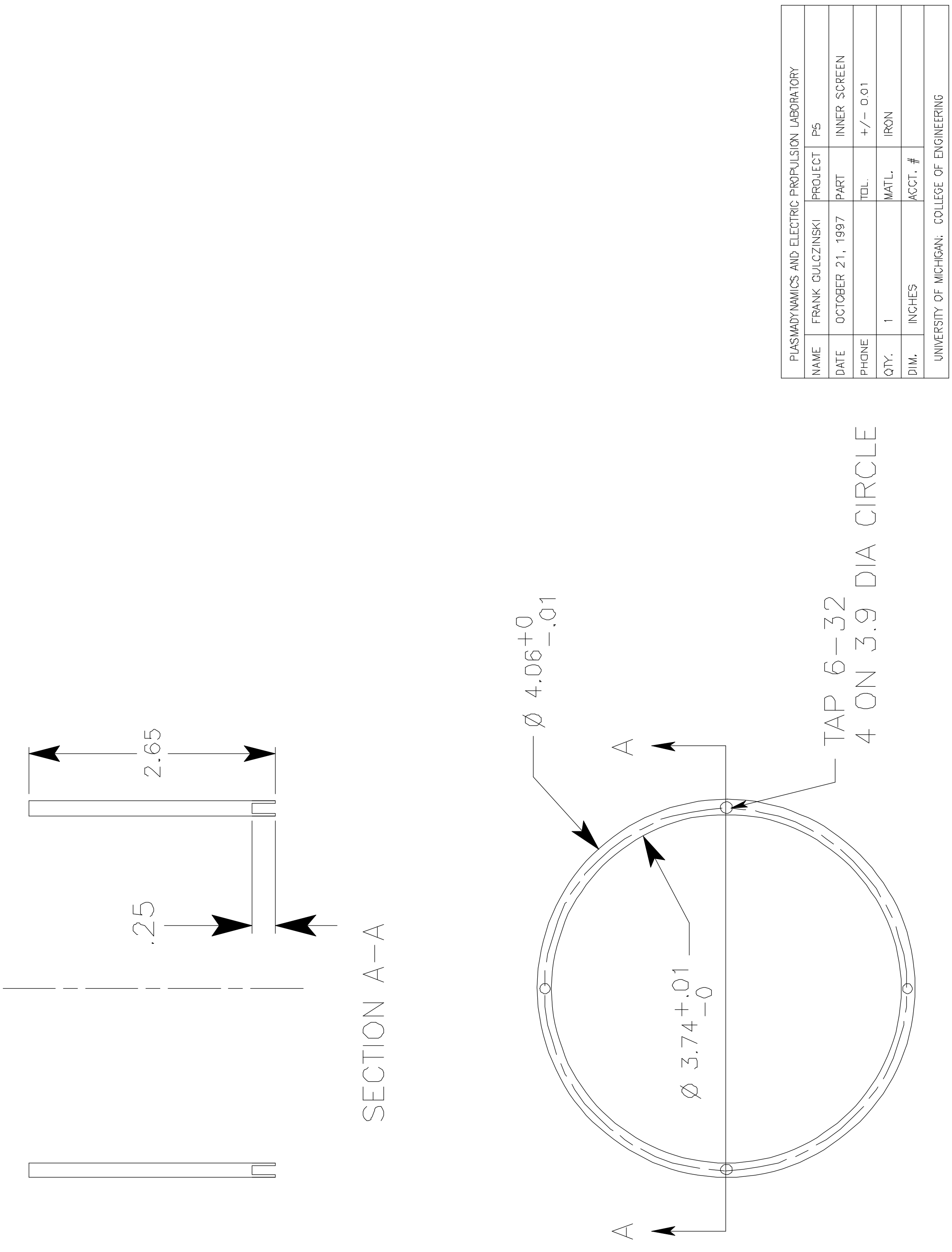
PLASMADYNAMICS AND ELECTRIC PROPULSION LABORATORY
NAME FRANK GULCZINSKI PROJECT P5
DATE OCTOBER 21, 1997 PART INNER SCREEN
PHONE TOL. +/- 0.01
QTY. 1 MATL. IRON
DIM. INCHES ACCT. #
UNIVERSITY OF MICHIGAN: COLLEGE OF ENGINEERING
2.65
.25
SECTION A-A
Ø 4.06 +0 -.01
Ø 3.74 +.01 -0
TAP 6-32
4 ON 3.9 DIA CIRCLE
A
A

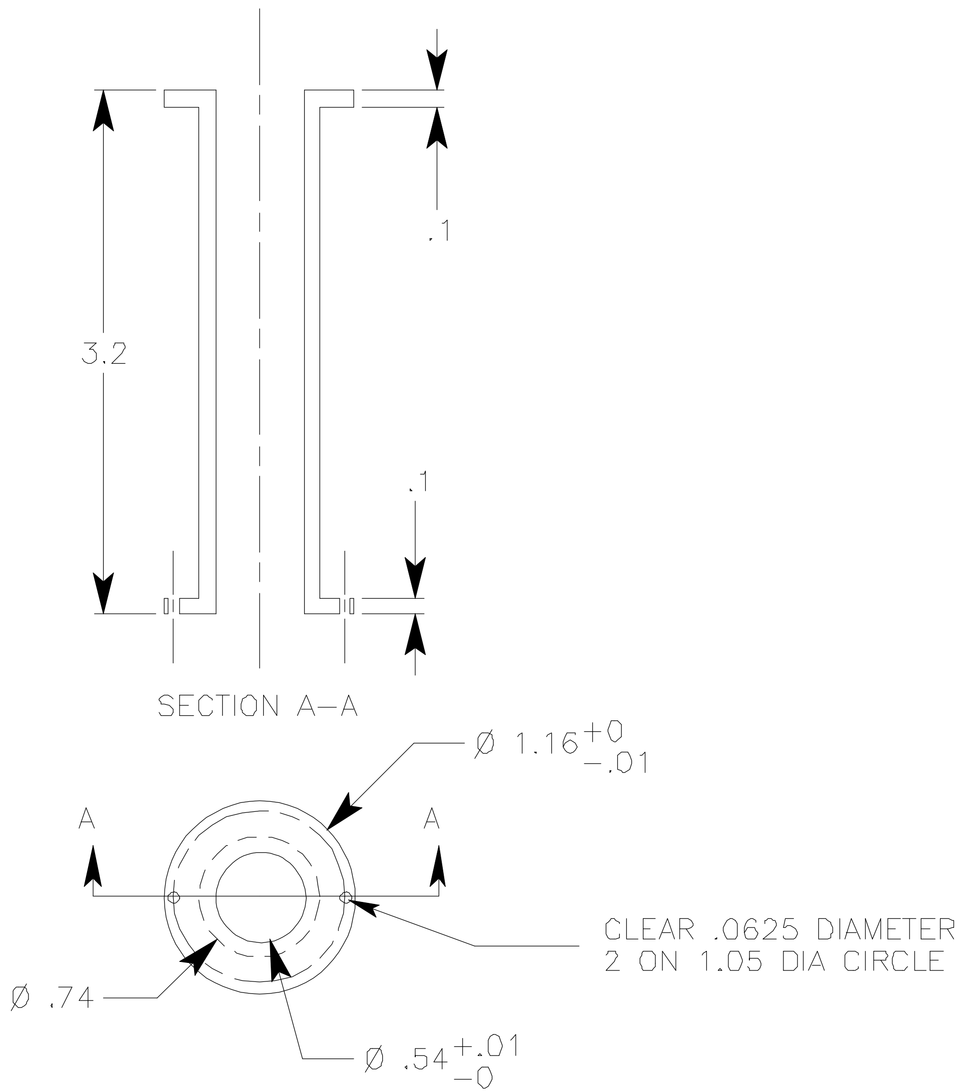

PLASMADYNAMICS AND ELECTRIC PROPULSION LABORATORY			
NAME	FRANK GULCZINSKI	PROJECT	P5
DATE	OCTOBER 21, 1997	PART	OUTER BOBBIN
PHONE		TOL.	+/− 0.01
QTY.	8	MATL.	316 STAINLESS STEEL
DIM.	INCHES	ACCT. #	
UNIVERSITY OF MICHIGAN: COLLEGE OF ENGINEERING			

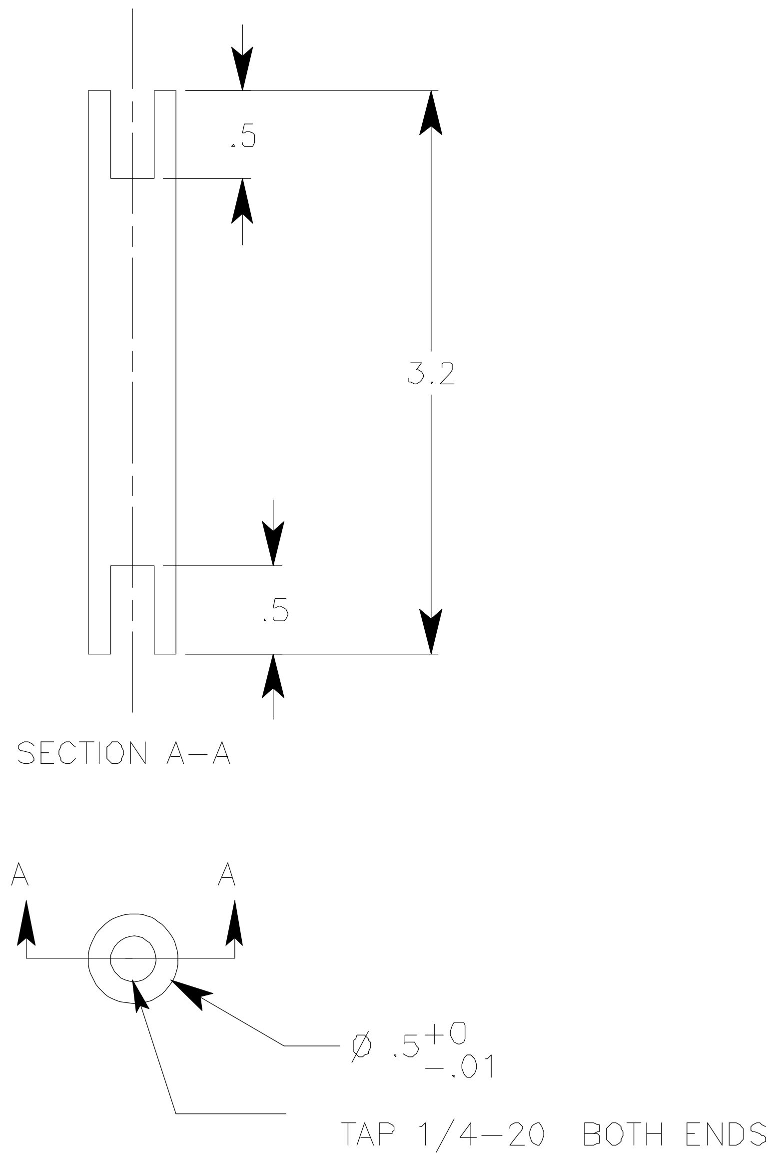

PLASMADYNAMICS AND ELECTRIC PROPULSION LABORATORY			
NAME	FRANK GULCZINSKI	PROJECT	P5
DATE	OCTOBER 21, 1997	PART	OUTER CORE
PHONE		TOL.	+/− 0.01
QTY.	8	MATL.	IRON
DIM.	INCHES	ACCT. #	
UNIVERSITY OF MICHIGAN: COLLEGE OF ENGINEERING			

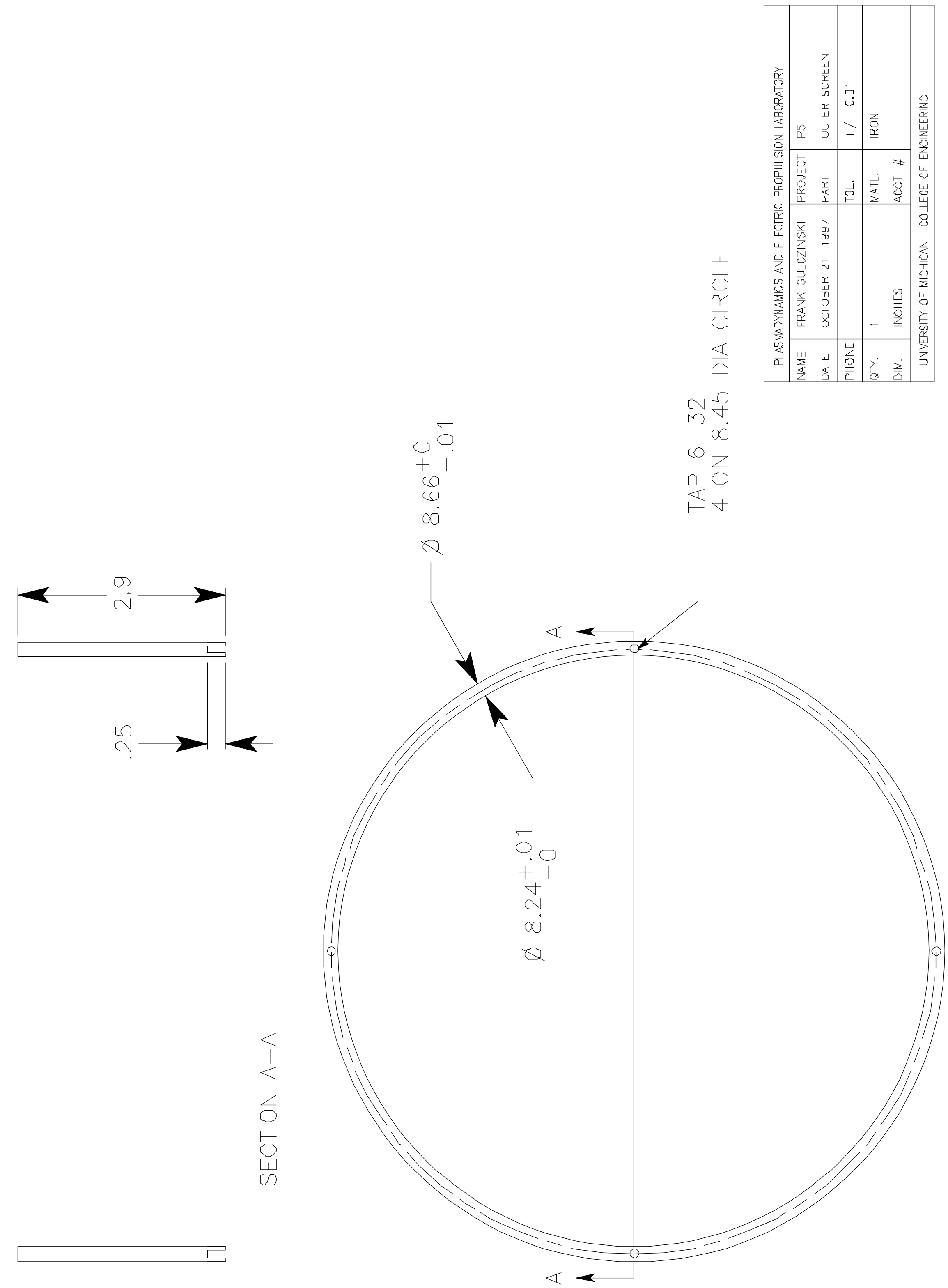
PLASMADYNAMICS AND ELECTRIC PROPULSION LABORATORY
NAME FRANK GULCZINSKI
PROJECT P5
DATE OCTOBER 21, 1997
PART OUTER SCREEN
PHONE
TOL. +/- 0.01
QTY. 1
MATL. IRON
DIM. INCHES
ACCT. #
UNIVERSITY OF MICHIGAN: COLLEGE OF ENGINEERING
TAP 6-32
4 ON 8.45 DIA CIRCLE
Ø 8.66 +0 -.01
Ø 8.24 +.01 -0
2.9
.25
A
A
SECTION A-A

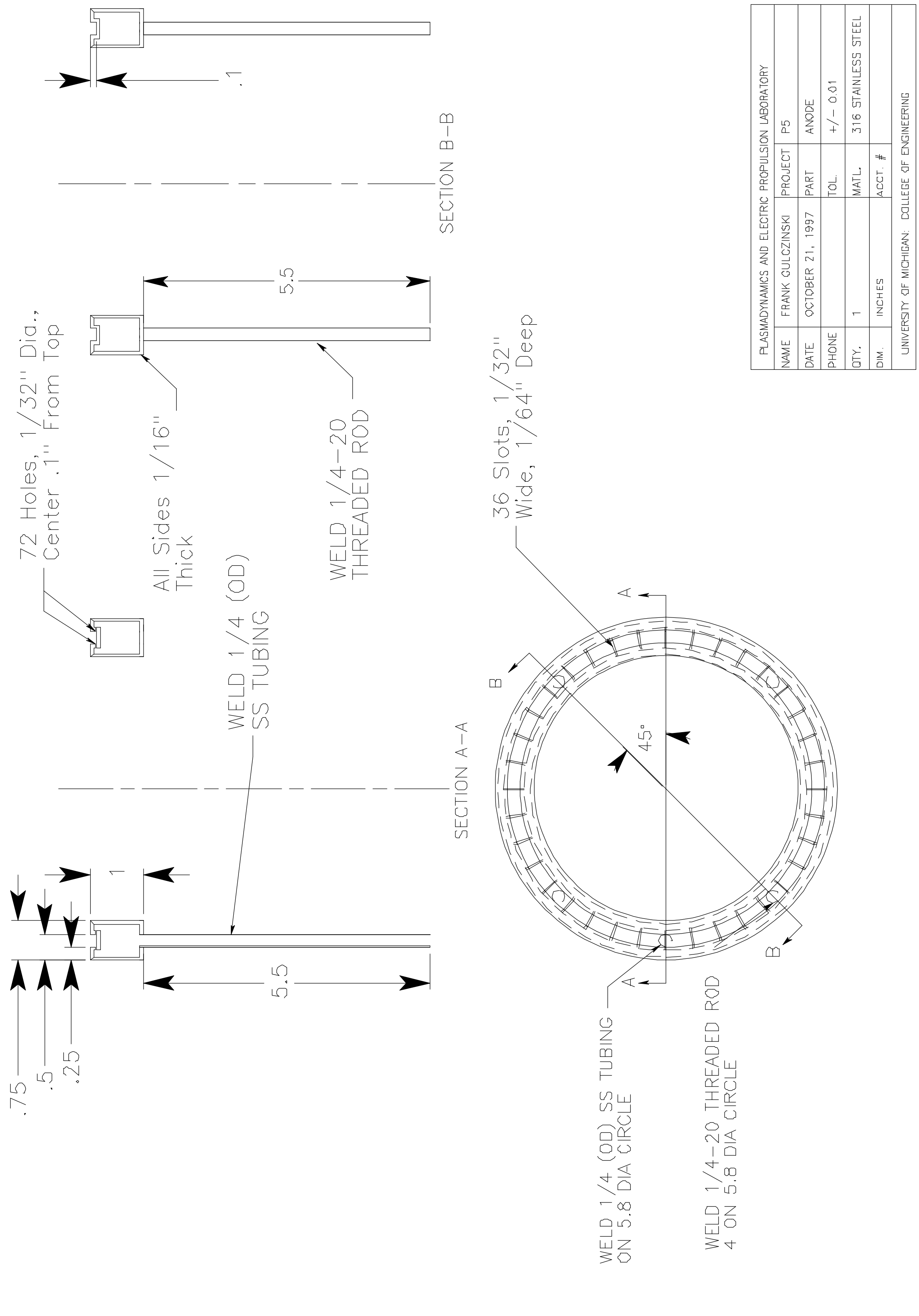
72 Holes, 1/32" Dia., Center .1" From Top
All Sides 1/16" Thick
WELD 1/4-20 THREADED ROD
WELD 1/4 (OD) SS TUBING
36 Slots, 1/32" Wide, 1/64" Deep
SECTION A-A
SECTION B-B
.1
5.5
5.5
1
.75
.5
.25
45°
A
A
B
B
WELD 1/4 (OD) SS TUBING ON 5.8 DIA CIRCLE
WELD 1/4-20 THREADED ROD 4 ON 5.8 DIA CIRCLE
PLASMADYNAMICS AND ELECTRIC PROPULSION LABORATORY
NAME FRANK GULCZINSKI
PROJECT P5
DATE OCTOBER 21, 1997
PART ANODE
PHONE
TOL. +/- 0.01
QTY. 1
MATL. 316 STAINLESS STEEL
DIM. INCHES
ACCT. #
UNIVERSITY OF MICHIGAN: COLLEGE OF ENGINEERING

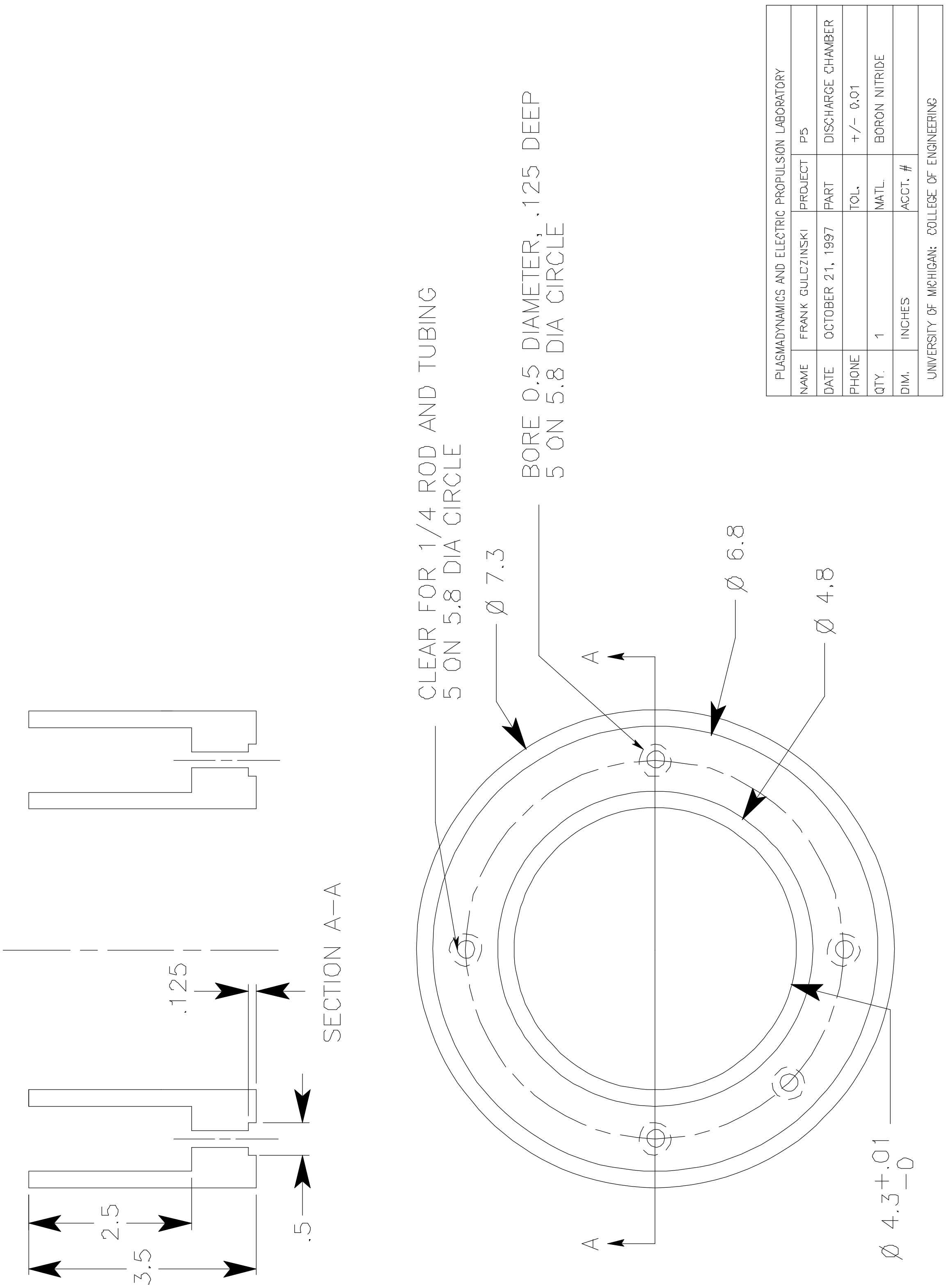
PLASMADYNAMICS AND ELECTRIC PROPULSION LABORATORY
NAME FRANK GULCZINSKI
PROJECT P5
DATE OCTOBER 21, 1997
PART DISCHARGE CHAMBER
PHONE
TOL. +/- 0.01
QTY. 1
MATL. BORON NITRIDE
DIM. INCHES
ACCT. #
UNIVERSITY OF MICHIGAN: COLLEGE OF ENGINEERING
CLEAR FOR 1/4 ROD AND TUBING
5 ON 5.8 DIA CIRCLE
BORE 0.5 DIAMETER, .125 DEEP
5 ON 5.8 DIA CIRCLE
Ø 7.3
Ø 6.8
Ø 4.8
Ø 4.3 +.01 −0
A
A
SECTION A–A
.125
.5
2.5
3.5

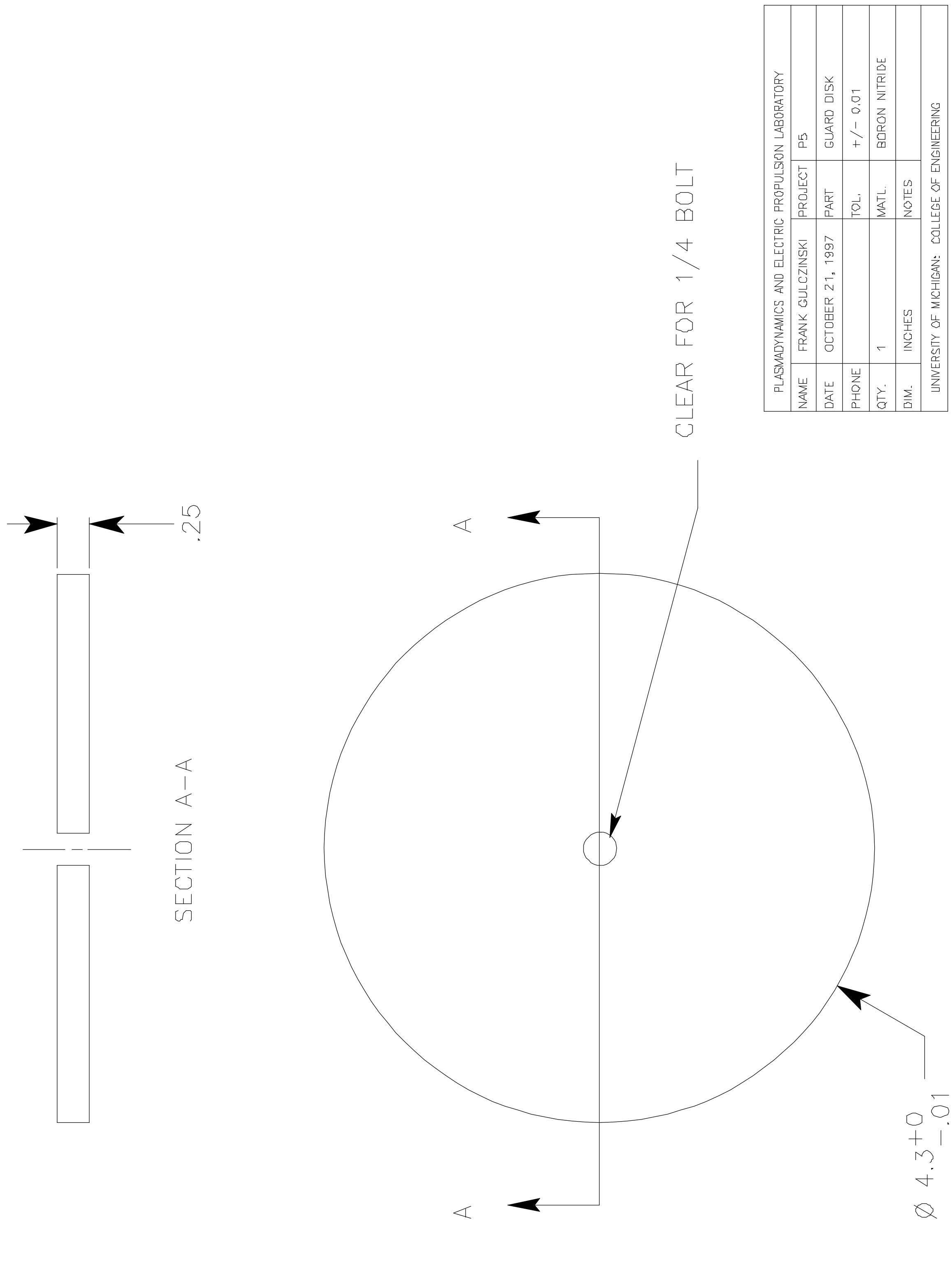
PLASMADYNAMICS AND ELECTRIC PROPULSION LABORATORY
NAME FRANK GULCZINSKI
PROJECT P5
DATE OCTOBER 21, 1997
PART GUARD DISK
PHONE
TOL. +/- 0.01
QTY. 1
MATL. BORON NITRIDE
DIM. INCHES
NOTES
UNIVERSITY OF MICHIGAN: COLLEGE OF ENGINEERING
CLEAR FOR 1/4 BOLT
A
A
Ø 4.3 +0 −.01
.25
SECTION A–A

BIBLIOGRAPHY

BIBLIOGRAPHY

[1] Stuhlinger, E., *Ion Propulsion for Space Flight*, McGraw-Hill Book Company, New York, 1964.

[2] Gulczinski, F.S. and Spores, R.A., "Analysis of Hall-Effect Thrusters and Ion Engines for Orbit Transfer Missions," AIAA 96-2973, 32nd Joint Propulsion Conference, July 1996.

[3] "Ion Thruster Operation," *NASA Spacelink - An Electronic Information System for Educators*, http://spacelink.msfc.nasa.gov/ NASA.Projects/ NASA.Launch.Vehicles/ Proposed.Systems/ Ion.Propulsion.Engine/ Ion.Thruster.Operation, April 1996**.**

[4] Polk, J.E., et al., "Validation of the NSTAR Ion Propulsion System on the Deep Space One Mission: Overview and Initial Results," AIAA 99-2274, 35th Joint Propulsion Conference, June 1999.

[5] Kaufman, H.R., "Technology of Closed-Drift Thrusters," *AIAA Journal*, Vol. 23, No. 1, 1985, 78-86.

[6] Zhurin, V.V., Kaufman, H.R., and Robinson, R.S., "Physics of Closed Drift Thrusters," IEPC 97-191, 25th International Electric Propulsion Conference, August 1997.

[7] Bober, A.S., et al., "State of Work on Electrical Thrusters in the USSR," IEPC 91-003, 22nd International Electric Propulsion Conference, October, 1991**.**

[8] Sankovic, J., Hamley, J., Haag, T., "Performance Evaluation of the Russian SPT-100 Thruster at NASA LeRC," IEPC 93-094, 23rd International Electric Propulsion Conference, September 1993.

[9] Garner, C.E., et al., "Cyclic Endurance Test of a SPT-100 Stationary Plasma Thruster," AIAA 94-2856, 30th Joint Propulsion Conference, June 1994.

[10] Morozov, A.I., "On Equilibrium and Stability of Flows in Accelerators with Closed Electron Drift and Extended Acceleration Zone," *Plasma Accelerators* (a collection of papers from I All-Union Conference on Plasma Accelerators, Moscow, Mashinostroenie, 1973.

[11] Gallimore, A.D., et al., "Preliminary Characterization of a Low Power End-Hall Thruster," AIAA 94-3012, 30th Joint Propulsion Conference, June 1994.

[12] Maslenikov, N.A., Russian Electric Propulsion Seminar, Massachusetts Institute of Technology, 1991**.**

[13] Day, M., Rogers, W., Maslinekov, N., "SPT-100 Subsystem Development Status and Plan," AIAA 94-2853, 30th Joint Propulsion Conference, June 1994**.**

[14] Clauss, C., "High-Power Stationary Plasma Thruster Propulsion Systems," Atlantic Research Corporation Memorandum, October 1995.

[15] "Hall Effect Plasma Thrusters, Internationally Developed Technology: High Efficiency, High Specific Impulse System," Space Power, Inc. and Keldysh Research Center, June 1998.

[16] Messerole, J.S., "Launch Costs to GEO Using Solar-Powered Orbit Transfer Vehicles," AIAA 93-2219, 29th Joint Propulsion Conference, June 1993.

[17] Brophy, J.R., "Ion Thruster Performance Model," NASA CR-174810, December 1984.

[18] Gallimore, A.D., et al., "Near and Far-Field Plume Studies of a 1 kW Arcjet," *Journal of Propulsion and Power*, January-February 1996.

[19] Dushman, S., *Scientific Foundations of Vacuum Technique*, Vol. 4, John Wiley & Sons, Inc., New York, 1958.

[20] Manzella, D.H., et al., "Performance Evaluation of the SPT-140," IEPC 97-059, 25th International Electric Propulsion Conference, August 1997.

[21] Sankovic, J.M., Haag, T.W., and Manzella, D.H., "Performance Evaluation of a 4.5 kW SPT Thruster," IEPC 95-030, 24th International Electric Propulsion Conference, September 1995.

[22] Tverdokhlebov, S.O., and Garkusha, V.I., "High-Voltage Mode of a TAL Thruster Operation," IEPC 97-023, 25th International Electric Propulsion Conference, August 1997.

[23] King, D., et al., "Development of the BPT Family of U.S.-Designed Hall Current Thrusters for Commercial LEO and GEO Applications," AIAA 98-3338, 34th Joint Propulsion Conference, July 1998.

[24] Haas, J.M., et al., "Performance Characteristics of a 5 kW Laboratory Hall Thruster," AIAA 98-3503, 34th Joint Propulsion Conference, July 1998.

[25] Marrese, C.M., et al., "D-100 Performance and Plume Characterization on Krypton," AIAA 96-2969, 32nd Joint Propulsion Conference, July 1996.

[26] Gulczinski, F.S., et al., "Impact of Anode Layer Thruster Plumes on Satellite Communications, AIAA 97-3067, 33rd Joint Propulsion Conference, July 1997.

[27] Arkhipov, B., et al., "Extending the Range of SPT Operation: Development status of 300 and 4500 W Thrusters," AIAA 96-2708, 32nd Joint Propulsion Conference, July 1996.

[28] Garner, C.E., et al., "Evaluation of a 4.5 kW D-100 Thruster with Anode Layer," AIAA 96-2967, 32nd Joint Propulsion Conference, July 1996.

[29] Marrese, C.M., et al., "Development of a Single-orifice Retarding Potential Analyzer for Hall Thruster Plume Characterization," IEPC 97-066, 25th International Electric Propulsion Conference, August 1997.

[30] Manzella, D., "Stationary Plasma Thruster Ion Velocity Distribution," AIAA 94-3141, 30th Joint Propulsion Conference, June 1994.

[31] Keefer, D., Wright, N., and Hornkohl, J., "Multiplexed LIF and Langmuir Probe Diagnostic Measurements in the TAL D-55 Thruster," AIAA 99-2425, 35th Joint Propulsion Conference, June 1999.

[32] Cedolin, R., et al., "Laser Induced Fluorescence Study of a Xenon Hall Thruster," *Applied Physics B,* Vol. 65, 1997, 459.

[33] Manzella, D., "Stationary Plasma Thruster Plume Emissions, IEPC 93-097, 23rd International Electric Propulsion Conference, September 1997.

[34] King, L.B., *Transport Property and Mass Spectral Measurements in the Plasma Exhaust Plume of a Hall-Effect Space Propulsion System,* Ph.D. Thesis, University of Michigan Department of Aerospace Engineering, University Microfilms International, 1998.

[35] Rapp, D., and Francis, W., "Charge Exchange Between Gaseous Ions and Atoms," *Journal of Chemical Physics,* Vol. 37, No. 11, 1962, 2631-2645.

[36] Gombosi, T.I., *Gaskinetic Theory,* Cambridge University Press, 1994.

[37] Semenkin, A.V., and Chislov, H.O., "Study of Anode Layer Thruster Operation with Gas Mixtures," IEPC 95-078, 24th International Electric Propulsion Conference, September 1995.

[38] Kim, S.-W., and Gallimore, A.D., "Plume Study of a 1.35 kW SPT-100 Using an ExB Probe," AIAA 99-2423, 35th Joint Propulsion Conference, June 1999.

[39] Pollard, J.E., "Plume Angular, Energy, and Mass Spectral Measurements with the T5 Ion Engine," AIAA 95-2920, 31st Joint Propulsion Conference, July 1995.

[40] Osher, J., Institute of Physics Conference Series, No. 38 (5) 201, 1978.

[41] Whaley, D.R., *Multiply-Charged Ion Emission from a Cyclotron-Resonance-Heated Plasma Ion Source*, Ph.D. Thesis, University of Michigan Department of Nuclear Engineering, University Microfilms International, 1989.

[42] Grivet, P., et al., *Electron Optics*, Permagon, Oxford, 1965.

[43] Haas, J.M., Hofer, R.R., and Gallimore, A.D., "Hall Thruster Discharge Chamber Plasma Characterization Using a High Speed Reciprocating Electrostatic Probe," AIAA 99-2426, 35th Joint Propulsion Conference, June 1999.

[44] Hutchison, I.H., *Principles of Plasma Diagnostics*, Cambridge University Press, Cambridge, England, 1987.

[45] Brown, S.C., *Basic Data of Plasma Physics: The Fundamental Data on Electrical Discharges in Gases*, AIP Press, Woodbury, New York, 1994.

[46] Hasted, J.B. and Hussain, M., "Electron Capture by Multiply Charged Ions," *Proceedings of the Physics Society*, Vol. 83, London, 1964, 911-924.

[47] Zhurin, V.V., Kaufman, H.R., and Robinson, R.S., "Physics of Closed Drift Thrusters," IEPC 97-191, 25th International Electric Propulsion Conference, August 1997.

[48] Williams, G.J., et al., "Laser Induced Fluorescence Measurement of Ion Velocities in the Plume of a Hall Effect Thruster," AIAA 99-2424, 35th Joint Propulsion Conference, June 1999.

[49] Marrese, C.M., et al., "Analysis of Anode Layer Thruster Guard Ring Erosion," IEPC 95-196, 24th International Electric Propulsion Conference, September 1995.

[50] Bishaev, A., and Kim, V., "Local Plasma Properties in a Hall-current Accelerator with an Extended Acceleration Zone," Soviet Physics – Technical Physics, Vol. 23, September 1978, 1055 – 1057.

[51] King, L.B., and Gallimore, A.D., "Gridded Retarding Pressure Sensor for Neutral Particle Analysis in Flowing Plasmas," *Review of Scientific Instruments*, 68(2), February 1997.

[52] Marrese, C.M., et al., "Field Emission Array Cathodes for Electric Propulsion Systems," AIAA 98-3484, 34th Joint Propulsion Conference, July 1998.

[53] Kim, S.W., *Experimental Investigation of Plume Parameters and Species-Dependant Ion Energy Distributions in the Exhaust Plasma Plume of a Hall Thruster*, Ph.D. Thesis,

University of Michigan Department of Aerospace Engineering, University Microfilms International, 1999.

[54] Williams, G.J., et al., "Laser Induced Fluorescence Measurement of Ions Emitted from Hollow Cathodes," AIAA 99-2862, 35th Joint Propulsion Conference, June 1999.

[55] Smith, T.B., et al., "Velocity Distribution Deconvolution of Hall Thruster LIF Spectra," work in progress, July 1999.

[56] Ohler, S.G., *Space Electric Propulsion Plasma Characterization using Microwave and Ion Acoustic Wave Propagation*, Ph.D. Thesis, University of Michigan Department of Electrical Engineering and Computer Science, University Microfilms International, 1996.

[57] Gulczinski, F.S., Hofer, R.R., and Gallimore, A.D., "Near-field Ion Energy and Species Measurements of a 5 kW Laboratory Hall Thruster," AIAA 99-2430, 35th Joint Propulsion Conference, June 1999.

[58] Operational Effectiveness Cost Study (OECS) Final Report, Office of Aerospace Studies, December 1995.

[59] Grobman, F., PL/VT, Personal Communication, June 1996.

[60] Day, M., et al., "SPT-100 Subsystem Qualification Status," AIAA 95-2666, 31st Joint Propulsion Conference, July 1995.

[61] Pollard, J.E., et al., "Electric Propulsion Flight Experience and Technology Readiness," AIAA 93-2221, 29th Joint Propulsion Conference, June 1993**.**

[62] Patterson, M.J., and Foster, J.E. "Performance of a 'Derated' Ion Thruster for Auxiliary Performance," AIAA 91-2350, 27th Joint Propulsion Conference, June 1991.

[63] Beattie, et al., "Flight Qualification of an 18-mN Xenon Ion Thruster," IEPC 93-106, 23rd International Electric Propulsion Conference, September 1993.

[64] Rawlin, V.K., and Majcher, G.A., "Mass Comparisons of Electric Propulsion Systems for NSSK of Geosynchronous Spacecraft," AIAA 91-2347, 27th Joint Propulsion Conference, June 1991.

[65] Marcucci, M., "Overview of the NSTAR Program," 7th Advanced Space Propulsion Workshop, April 9, 1996.

[66] Ashley, S., "Electric Rockets Get a Boost," *Mechanical Engineering*, December 1995, 61-65.

[67] Beattie, J.R., et al., "Xenon Ion Propulsion Subsystem," *Journal of Propulsion and Power*, Vol. 5, No. 4, 1989, 438-444

[68] Beattie, J.R., et al., "Status of Xenon Ion Propulsion Technology," *Journal of Propulsion and Power*, Vol. 6, No. 2, 1990, 145-150.

[69] Groh, K.H., and Loebt, H.W., "State-of-the-Art of Radio-Frequency Ion Thrusters," *Journal of Propulsion and Power*, Vol. 7, No. 4, 1991, 573-579.

[70] Gledhill, K., Marvin, D., "Future Trends in Space Photovoltaics," AIAA 94-3970.

[71] Pollard, J.E., and Janson, S.W., "Spacecraft Electric Propulsion Applications," Aerospace Report Number ATR-96(8201)-1, The Aerospace Corporation, February 1, 1996.

[72] Jahn, R.G., *Physics of Electric Propulsion*, McGraw-Hill Book Company, New York, 1968.

[73] LeDuc, J.R., ESEX Project Engineer, Personal Communication, April 1996.

[74] Isakowitz, S.J., *International Reference Guide to Space Launch Systems,* Second Edition, AIAA Publication, 1991.

[75] Oleson, S.R., et al., "Advanced Propulsion for Geostationary Orbit Insertion and North-South Station Keeping," NASA TM-107018, July 1995.

[76] Fiedler, S., and Preiss, B., "Geosynchronous Space Based Radar Concept Development for Theater Surveillance," IEEE Aerospace Applications Conference Proceedings, Volume 4, 1996, 77-90.

[77] Free, B., "High Altitude Orbit Raising with On-Board Electric Power," IEPC 93-205, 23rd International Electric Propulsion Conference, September 1993.

[78] Spitzer, A., "Novel Orbit Raising Strategy Makes Low Thrust Commercially Viable," IEPC 95-212, 24th International Electric Propulsion Conference, September 1995.

[79] McFall, K.A., Electric Propulsion Laboratory Research Engineer, Personal Communication, March 1996.

[80] Rawlin, V.K., "Performance of Large Area Xenon Ion Thrusters for Orbit Transfer Missions," NASA TM-102049, May 1989.

[81] Sovey, J.S., et al., "Ion Thruster Development at NASA Lewis Research Center," NASA TM-105983, January 1993.